Aerodynamic and Structural Characterisation of a Hinged Folding Wingtip

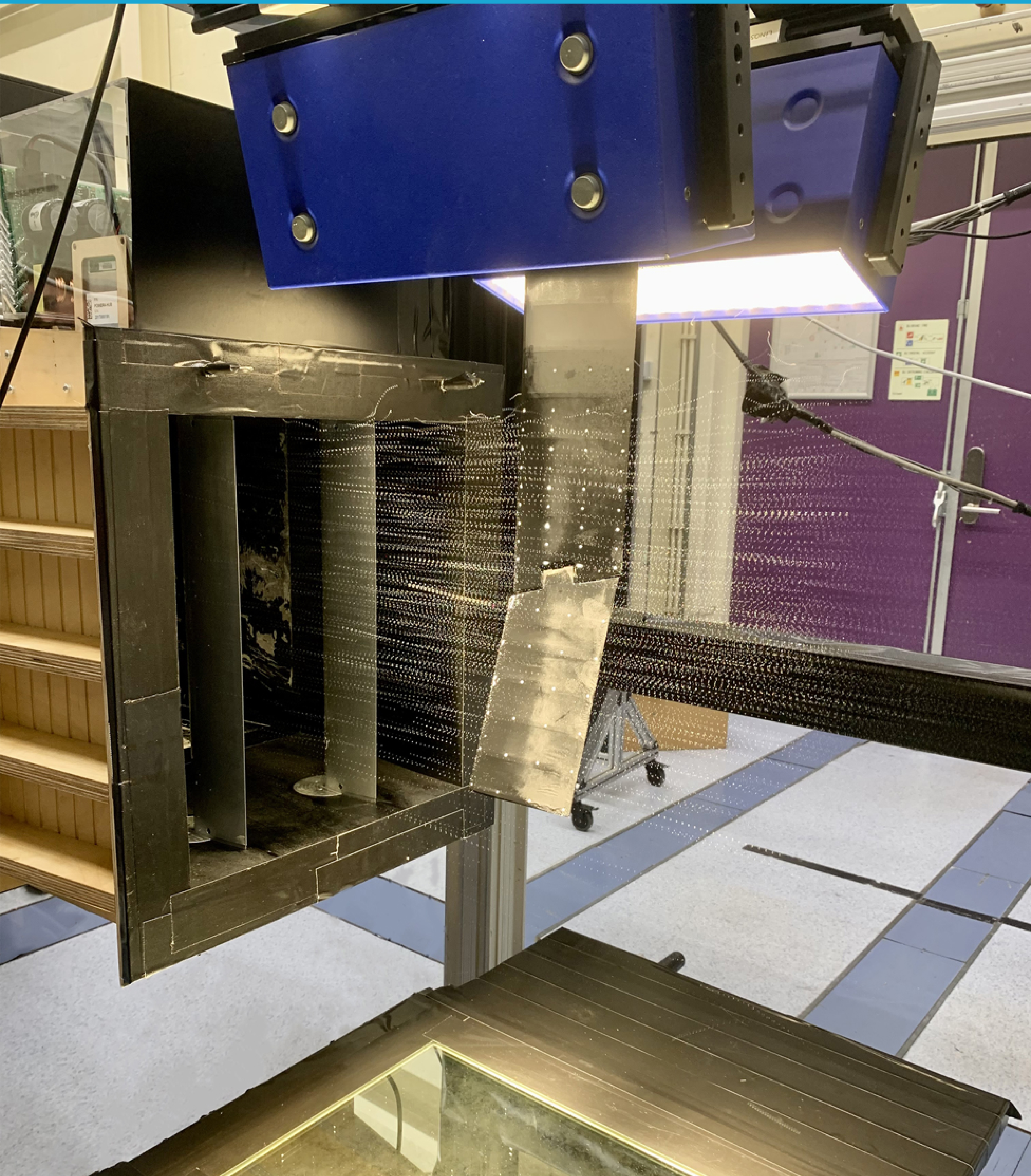

Fabio Taccaliti

TU Delft

AE5110: Thesis Aerodynamics and Wind Energy

Aerodynamic and Structural Characterisation of a Hinged Folding Wingtip By Means Instantaneous Large-Scale Particle Image Velocimetry

by

Fabio Taccaliti

Thesis Committee:	Dr.ir. B.W. van Oudheusden,	Chair;
	Dr. A. Sciacchitano,	Supervisor;
	Dr. J. Sodja,	Supervisor;
	Dr. ir. R. De Breuker	External Examiner;
	Ir. C. Mertens,	Daily Supervisor.

September 26, 2022

To obtain the degree of Master of Science,
at the Delft University of Technology,
to be defended publicly on October 24, 2022 at 10.

Student Number: 4490231
Thesis Duration: 11 October 2021 – 24 October 2022

An electronic version of this thesis is available at `https://repository.tudelft.nl/`.

TU Delft

Preface

This thesis report presents the work I performed during the nine-month-long Aerodynamics master's thesis project conducted at the Aerospace Engineering faculty of the Delft University of Technology, from the 11th of October 2021 to the 24th of October 2022.

A special thanks go to all my supervisors, Dr. Andrea Schiacchitano and Dr. Ir. Bas van Oudheusden and Dr. Jurij Sodja. They allowed me to perform this research in the state-of-the-art Particle Image Velocimetry (PIV) flow visualisation technique applied to a fascinating and promising topic like the Hinged Folding Wingtip (HFW), and whose supervision, advice and continuous feedback on this thesis was the key to the progress and success of my work. I hope this thesis research can contribute to achieving more accurate fluid-structure interaction wind tunnel experiments in the future and, more importantly, more sustainable aviation.

I would also like to thank my daily supervisor It. C. Mertens for the continuous support and all the time spent helping and explaining things to me. You constantly challenged and pushed me to accomplish all the steps needed for this research, overcoming all the issues and difficulties I encountered in these months. Working with a professional and open-minded person like Christoph was an honour. I think the success of this work and my graduation was not have been possible without you.

Grazie Giuseppe for all the support and help during these 6 years, sei sempre stato disponibile per me, sei un amico. Thanks also, Thomas and José, for all the time we shared; it was always great for me to work with you and study at my place after a plate of good Italian pasta. You were an inspiration for me to continuously achieve better results. Thanks, Xavi, for the help during the wind-tunnel experiment; even if your graduation was very close, you spent two full weeks working with Christoph and me at the W-tunnel. The work that you did in your thesis was stunning, and this made my life easier during these twelve months; I hope that I add something to your research.

Per ultimo ma non per importanza, vorrei ringraziare tutta la mia famiglia, Anahita, Francesca, Stella, Joceline, Gerardo e Roberto. Mi siete sempre stati vicini anche a più di 1500km di distanza. Mi avete sempre supportato ed aiutato a superare tutte le difficoltà, che solo noi sappiamo quante sono state in questi anni lontani da Sirolo e non mi avete mai fatto mancare nulla ne fatto sentire solo. Mi è molto difficile spiegare a parole quanto vi sono grato per tutto quello che avete fatto per me, per i vostri sacrifici, sforzi e per la vostra pazienza. Non potrò mai ringraziarvi abbastanza per ciò, spero di aver ricambiato almeno in una minima parte e di avervi reso orgogliosi con questi piccoli traguardi. Senza di voi tutto questo non sarebbe stato possibile. Grazie.

Fabio Taccaliti

Sirolo, July 2022

Abstract

In the last thirty years, massive improvements in flight operations and aircraft technology were implemented, reaching a 54% reduction in specific fuel consumption [1]. However, during the same period, the aviation market has tripled the number of flights per year with a consequent and direct increase in the emissions of greenhouse gasses. To fight against climate change due to the global rise in temperature, international policies are pushing towards a greener future for our society, setting specific objectives for reducing emissions, including aviation ones. In order to achieve the critical goal of climate neutrality by 2050, as stated by the European Green Deal [2], and since the number of total flights is valued will double by that year; significant development steps have to be taken in the aviation industry that has to become greener.

The best way to decrease aircraft emissions is to increase its aerodynamic efficiency, so increasing the wingspan of the wing in order to reduce the lift-induced drag. Unfortunately, this has two main problems, the increased total structural weight (that will therefore reduce the payload leading to an increase in the number of flights) and the limited wingspan due to existing airport gate requirements. These issues can be solved using a Hinged Folding Wingtip (HFW) that allows an aerodynamic efficient enormous wingspan during flight operations but will fold on the ground enabling the usage of existing gates. Furthermore, the hinge mechanism improves load alleviation capabilities, particularly during gusts, consequently reducing the bending moment transferred at the root of the wing, allowing beneficial lighter structure.

This thesis study focused on a precise aeroelastic characterisation (both aerodynamic and structural) of the hinged folding wingtip device using the instantaneous, non-intrusive and whole-field, large-scale Particle Image Velocimetry (PIV) technique, with the state-of-the-art Shake-The-Box (STB) Lagrangian Particle Tracking (LPT) algorithm in combination with Helium-Filled Soap Bubbles (HFSB) flow tracers and fiducial markers painted on the wing model. This new technique permits the avoidance of intrusive, conventional sensors used for aeroelastic evaluations, like strain gauges, piezoelectric accelerometers, potentiometers, and load cells that alter the structural properties of the tested object but also Pitot tubes that alter the flow behaviour. Furthermore, only pointwise measurements are possible with these devices.

Through a wind tunnel campaign at the W-tunnel facility at TU Delft, using a hinged folding wingtip model in both steady and unsteady conditions, it was shown that the implementation of this device shows very promising potential. Not only from an aerodynamic efficiency (due to the increased wingspan) and energy consumption efficiency (due to lower structural weight) points of view but more significantly in the gust alleviation capacities, indeed the peak load and the corresponding root bending moment can be reduced significantly applying a correct timing on the hinge release.

Contents

Preface i

Abstract iii

List of Figures viii

List of Tables xii

Nomenclature xiv

1 Introduction 1

2 Literature Review 4
2.1 Aeroelasticity . . . 4
2.2 Gust . . . 5
2.3 Gust Load Alleviation . . . 6
2.3.1 Concepts . . . 6
2.3.1.1 Passive Gust Load Alleviation Devices . . . 6
2.3.1.2 Active Gust Load Alleviation Devices . . . 7
2.3.2 Hinged Folding Wingtip Development Steps . . . 7
2.3.3 Hinged Folding Wingtip Results . . . 11
2.4 Tested Hinged Folding Wingtip Design Concept . . . 13
2.4.1 Model . . . 14
2.4.2 Numerical Results . . . 15
2.4.3 Experimental Results . . . 16
2.4.3.1 Steady Conditions . . . 17
2.4.3.2 UnSteady Conditions . . . 18
2.5 Particle Image Velocimetry . . . 21
2.5.1 Working Principle . . . 21
2.5.2 Development Steps . . . 22
2.5.3 Tomographic Particle Image Velocimetry . . . 23
2.6 Large-Scale Particle Image Velocimetry . . . 26
2.6.1 Helium-Filled Soap Bubble . . . 26
2.7 Lagrangian Particle Tracking . . . 27
2.7.1 Shake-The-Box . . . 27
2.8 Structural Characterisation . . . 29
2.8.1 Fiducial Markers Tracking . . . 29
2.9 Research Objective and Research Questions . . . 34

3 Experimental Set-Up and Procedures 37
3.1 Set-Up . . . 37
3.1.1 Facility . . . 37
3.1.2 Gust Generator . . . 38
3.1.3 Model . . . 38
3.1.4 Frame Structure . . . 39
3.1.5 Particle Image Velocimetry . . . 40
3.1.5.1 Seeding . . . 40
3.1.5.2 Illumination . . . 41
3.1.5.3 Camera . . . 41
3.1.5.4 Data Acquisition System . . . 42

3.1.6 Sensors Placed on the Wing . . . 42
3.2 Experiment Parameters . . . 43
3.2.1 Particle Image Velocimetry Parameters . . . 44
3.3 Data Acquisition Procedure . . . 45
3.3.1 Test Matrix . . . 45
3.3.2 Particle Image Velocimetry. . . . 46
3.3.2.1 Intensity Calibration . . . 46
3.3.2.2 Perspective Calibration. . . . 46
3.3.2.3 Free-Stream Measurements . . . 48
3.3.2.4 Wing Structure Measurements . . . 48
3.3.3 Conventional Sensors . . . 48

4 Data Analysis and Reduction Techniques **51**
4.1 Conventional Sensors Data Analysis . . . 51
4.2 Particle Image Velocimetry Data Analysis . . . 52
4.3 Flow-Field Visualisation . . . 53
4.4 Structural Characterisation . . . 60

5 Results and Discussion **68**
5.1 Steady Conditions . . . 68
5.1.1 Flow-Field Visualisation . . . 68
5.1.2 Structural Behaviour . . . 71
5.2 Unsteady Conditions. . . . 74
5.2.1 Flow-Field Visualisation . . . 74
5.2.2 Structural Behaviour . . . 81

6 Conclusions and Recommendations **89**
6.1 Conclusions. . . . 89
6.2 Recommendations . . . 91
6.2.1 Experimental Set-Up, Data Analysis and Reduction Techniques . . . 91

Bibliography **94**

A Appendix A **100**
A.1 Programmable Time Unit Connections. . . . 100

B Appendix B **102**
B.1 Image Pre-Processing . . . 102
B.2 Volume Self-Calibration . . . 105
B.3 Lagrangian Particle Tracking Operations . . . 106
B.3.1 Flow Post-Processing - Shake-The-Box . . . 106
B.3.2 Structure Post-Processing - Iterative Particle Reconstruction . . . 108

List of Figures

1.1 Drag and wing span relationship, with and without hinged folding wingtip for load alleviation [3]. . . 2

2.1 Collar's triangle [4]. . . . 4
2.2 Gusts directionality [5]. . . . 5
2.3 1-Cosine gust [6]. . . . 6
2.4 Passive twist wingtip device [7]. . . . 7
2.5 Hinged folding wingtip front-view [8]. . . . 7
2.6 Boeing 777X folding wingtip [9]. . . . 8
2.7 Hinged folding wingtip with positive flare angle [10]. . . . 8
2.8 Hinged folding wingtip model [11]. . . . 9
2.9 Hinged folding wingtip model and sensors location [12]. . . . 9
2.10 Hinged folding wingtip used in the wind tunnel experiment [13]. . . . 10
2.11 AlbatrossONE wingtip positions [14]. . . . 11
2.12 Flexible wingtip elastic bending deflection response to gust excitation [15]. . . . 11
2.13 Incremental wing root bending moment load envelope response to a 1-Cosine gust [10]. . . . 12
2.14 Fold angle and normalised wing root bending moment response to a 1-Cosine gust [12]. . . . 12
2.15 Normalised wing root bending moment load envelope response to a 1-Cosine gust [12]. . . . 13
2.16 Release response of the folding wingtip angle and wing root bending moment created [16]. . . . 13
2.17 Hinged folding wingtip model [17]. . . . 14
2.18 Model hinge mechanism (free-hinge condition) [18]. . . . 15
2.19 Locked-hinge, numerical wing root bending moment, peak load comparison [17]. . . . 15
2.20 Wind tunnel setup [18]. . . . 16
2.21 Wing sensors distribution [18]. . . . 17
2.22 Static bending moment coefficient and fold angle for plate B [17]. . . . 18
2.23 Relative peak load reduction respect to locked hinge condition for all gusts and plates, for $\alpha = 0°$ [17]. 19
2.24 Relative root mean square reduction respect to locked hinge condition for all gusts and plates, for $\alpha = 0°$ [17]. . . . 20
2.25 Planar 2-dimensional (2D) particle image velocimetry typical setup [19]. . . . 21
2.26 Stereoscopic particle image velocimetry typical setup [20]. . . . 23
2.27 Tomographic particle image velocimetry typical setup and working principle [21]. . . . 23
2.28 Object discretisation in voxels and imaging used for the reconstruction [22]. . . . 24
2.29 Multi-pass light amplification system [23]. . . . 25
2.30 **Left**: Front of the coaxial volumetric velocimetry, **Right**: Side measurement setup [24]. . . . 25
2.31 The coaxial volumetric velocimetry probe mounted on the robotic arm [25]. . . . 26
2.32 Miniaturised orifice-type generator for the helium-filled soap bubble formation [19]. . . . 26
2.33 Shake-the-box processing step and residual image [19]. . . . 28
2.34 Velocity comparison between conventional tomographic particle image velocimetry tracking algorithm (Left) and shake-the-box algorithm (Right) [26]. . . . 29
2.35 Plan view and side view of the digital image correlation and particle image velocimetry setup [27]. . . 30
2.36 Structural displacement and error comparison between particle image velocimetry and scanning vibrometer techniques [28]. . . . 31
2.37 Fitting procedure of measurements fiducial markers with reference marker grid [29]. . . . 31
2.38 Angle of attack and flap deflection position determination comparison between particle image velocimetry measurements and reference data [29]. . . . 32
2.39 Deflection comparison between finite element beam model and static particle tracking velocimetry measurements [30]. . . . 32
2.40 **Left**: Both flow and structure markers, **Center**: Just flow markers, **Right**: Just structure markers [31]. . 33

2.41 Polynomial curve fit chordwise-averaged displacement measurements [31]. 33
2.42 Reconstructed deformed wing [31]. 34

3.1 W-tunnel nozzle and exit [32]. 37
3.2 W-tunnel external ventilation system [32]. 38
3.3 Installed turbulence grid, gust generator and wing model. 39
3.4 Particle Image Velocimetry (PIV) set-up. 40
3.5 In-house Fluid Supply Units (FSU). 41
3.6 Helium-Filled Soap Bubble (HFSB) tracer particles seeder [33]. 41
3.7 Conventional sensors acquisition system set-up. 43
3.8 Perspective calibration views [34]. 46
3.9 Calibration plate settings. 47
3.10 Modified type 30 calibration plate. 47
3.11 Front side [35]. 48
3.12 Back side [35]. 48
3.13 Wind tunnel and data acquisition procedures. 49

4.1 Signal filtering effect. 51
4.2 Bending moment coefficient nomenclature. 52
4.3 Reduction Techniques Flow-Chart. 53
4.4 Suction and pressure side merging procedure. 54
4.5 Steady free condition, bin size sensitivity study (all time steps). 55
4.6 Steady free condition - Velocity change along the line (varying the bin size). 56
4.7 Unsteady free condition, bin size sensitivity study (50 time steps). 57
4.8 Unsteady free condition - Velocity change along the line (varying the bin size). 57
4.9 Unsteady free condition, time bin sensitivity study (15mm bin). 59
4.10 Unsteady free condition - Velocity change along the line (varying the time bin). 59
4.11 6 degrees of freedom, 3 rotations and 3 translations. 61
4.12 Fiducial markers fit. 62
4.13 Outliers removal results. 63
4.14 Wing Free-Body Diagram (FBD). 64
4.15 Cut wing Free-Body Diagram (FBD). 65

5.1 Flow field for the steady free condition, all time steps. 69
5.2 Flow field for the steady locked condition, all time steps. 70
5.3 3D flow field and wing reconstruction for the steady cases, all time steps. 70
5.4 Wingtip angle (θ) for the steady conditions measured with the potentiometer. 71
5.5 Bending moment coefficient (C_B) for the steady conditions measured with the strain gauges. 72
5.6 Wing reconstruction vs. IPR, $t/T_{ref} = 0$ [-]. 72
5.7 Wing reconstruction vs. IPR, $t/T_{ref} = 0.5$ [-]. 73
5.8 Wing reconstruction vs. IPR, $t/T_{ref} = 1$ [-]. 73
5.9 Markers average distance difference. 74
5.10 Flow field for the unsteady free condition, $t/T_{ref} = 0$ [-], (50 time steps). 75
5.11 Flow field for the unsteady locked condition, $t/T_{ref} = 0.5$ [-], (50 time steps). 76
5.12 Flow field for the unsteady pre-released condition, $t/T_{ref} = 1$ [-], (50 time steps). 77
5.13 Flow field for the unsteady 0% condition, $t/T_{ref} = 0$ [-], (50 time steps). 77
5.14 Flow field for the unsteady 50% condition, $t/T_{ref} = 0.5$ [-], (50 time steps). 78
5.15 Flow field for the unsteady 100% condition, $t/T_{ref} = 1$ [-], (50 time steps). 79
5.16 3D flow field and wing reconstruction for the unsteady cases. 81
5.17 Wingtip angle (θ) for the unsteady conditions measured with the potentiometer. 82
5.18 Bending moment coefficient (C_B) for the unsteady conditions measured with the strain gauges. . . . 82
5.19 Wing reconstruction vs. IPR. 84
5.20 Markers average distance difference. 85
5.21 Relative peak load comparison. 86

5.22 Relative Root-Mean-Square (RMS) comparison. 86
5.23 Velocity field at peak load time instant (15mm bin, 50 time steps). 87

B.1 Delete or change order of frames settings. 102
B.2 Unfiltered image. 103
B.3 Flow filtered image. 103
B.4 Structure filtered image. 103
B.5 Butterworth high pass filter Settings. 103
B.6 Minimum filter settings. 103
B.7 Structure image. 104
B.8 Subtract sliding. 104
B.9 Smoothing. 104
B.10 Intensity normalisation. 104
B.11 Multiply. 104
B.12 Geometric mask. 104
B.13 Subtract sliding settings. 104
B.14 Smoothing settings. 104
B.15 Intensity normalisation settings. 104
B.16 Multiply settings. 105
B.17 Geometric mask settings. 105
B.18 Volume self-calibration initial settings. 105
B.19 Volume self-calibration final settings. 105
B.20 Shake-the-box settings. 107
B.21 Iterative particle reconstruction settings. 108

List of Tables

2.1 Collars triangle components [4]. 4
2.2 Plates thickness and stacking sequence [17]. 15
2.3 Simulated and experimental flutter speed for $\alpha = 0°$ (free-hinge, steady conditions) [17]. 16
2.4 Test matrix [17]. 17

3.1 Wind tunnel flow conditions. 44
3.2 PIV parameter. 45
3.3 Test matrix. 45

4.1 Steady free condition - Velocity uncertainty - Bin size sensitivity study. 56
4.2 Unsteady free condition - Velocity uncertainty - Bin size sensitivity study. 58
4.3 Unsteady free condition - Velocity uncertainty - Time bin sensitivity study. 60
4.4 6 degrees of freedom. 61

5.1 Markers mean values of the average distance difference. 74
5.2 Markers mean values of the average distance difference. 84
5.3 Relative peak load and relative Root-Mean-Square (RMS). 86

Nomenclature

Abbreviations

2D	One-Dimensional
2D	Two-Dimensional
2D2C	Two-Dimensional Two Components
2D3C	Two-Dimensional Three Components
3D	Three-Dimensional
3D3C	Three-Dimensional Three Components
AC	Alternating Current
AFSB	Air Filled Soap Bubbles
AR	Aspect Ratio
BC	Boundary Condition
BFS	Bubble FLuid Solution
BNC	Bayonet Neill Concelman
CCD	Charge-Coupled Device
CFD	Computational Fluid Dynamics
CLPT	Classical Laminate Plate Theory
CV	Control Volume
CVV	Coaxial Volumetric Velocimetry
DIC	Digital Image Correlation
DMT	Derivative-Moment Transformation
DOF	Degrees Of Freedom
DSPIV	Dual-Plane Stereo Particle Image Velocimetry
DSR	Dynamic Spatial Range
EAS	Equivalent AirSpeed
EASA	European Union Aviation Safety Agency
FAA	Federal Aviation Administration
FBD	Free-Body Diagram
FE	Finite Element
FEM	Finite Element Method

FOV	Field Of View
FSI	Fluid-Structure Interaction
GLA	Gust Load Alleviation
DHPIV	Digital Holographic Particle Image Velocimetry
HD	Hard Disk
HFSP	Helium-Filled Soap Bubbles
HFW	Hinged Folding Wingtip
HPIV	Holographic Particle Image Velocimetry
EtherCAT	Ethernet for Control Automation Technology
IB	Interrogation Box
ICAO	International Civil Aviation Organization
IP	Internet Protocol
IPR	Iterative Particle Reconstruction
IR	Image Residual
LASER	Light Amplification by Stimulated Emission of Radiation
LCO	Limit Cycle Oscillation
LE	Leading Edge
LED	Light-Emitting Diode
LPT	Lagrangian Particle Tracking
MART	Multiplicative Algebraic Reconstruction Technique
NIC	Network Interface Controller
NS	Source Density
OJF	Open Jet Facility
OTF	Optical Transfer Function
PC	Personal Computer
PFV	Photron Fastcam Viewer
PIV	Particle Image Velocimetry
PPP	Particles Per Pixel
PPV	Particle Per Voxels
PS	Pressure Side
PSP	Pressure Sensitive Paint
PTU	Programmable Time Unit
PTV	Particle Tracking Velocimetry

RMS Root Mean Square

RPM Rotation Per Minutes

SAH Semi Aeroelastic Hinge

SS Suction Side

STB Shake-The-Box

STD Standard Deviation

SV Scanning Vibrometer

TE Trailing Edge

VSC Volume Self-Calibration

WI Wash-In

WO Wash-Out

WRBM Wing Root Bending Moment

Molecular Formulas

CO_2 Carbon Dioxide

He Helium

NO_x Nitrogen Oxides

SO_4^{2-} Sulphate

Symbols

A	Stream-Tube of Cross Section	[mm^2]
b	Wing Span	[m]
$b_{wingtip}$	Wing Span	[m]
C	Particles Concentration	[particles mm^3]
C_1	Strain Gauge Center Calibration Constant	[mV]
C_2	Strain Gauge Front Calibration Constant	[mV]
C_3	Strain Gauge Rear Calibration Constant	[mV]
C_B	Bending Moment Coefficient	[−]
C_d	Drag Coefficient	[−]
C_l	Lift Coefficient	[−]
C_p	Pressure Coefficient	[−]
d	Distance	[m]
D_i	Lift-Induced Drag	[N]
DR	Digital Image Resolution	[pixel mm^{-1}]
F	Dynamic Force	[N]

f	Frequency	[Hz]
$f_{\#}$	F-Stop	[−]
H	Gust Gradient Distance	[m]
I	Unit Tensor	[−]
L	Aircraft Lift	[N]
L	Lift	[N]
l_B	Bin Length	[mm]
M	Bending Moment	[N m^{-1}]
m	Magnification Factor	[−]
$\dot{N}$	Bubble Emitter Rate	[bubbles s^{-1}]
N_C	Camera Views	[-]
N_I	Particle Image Number Density	[−]
$N_{p_{min}}$	Minimum Number of Particles	[−]
N_{part}	Number of Particles	[-]
N_p	Number of Particles	[−]
N_{unc}	Number of Uncorrelated Measurement Samples	[-]
N	Load Factor	[−]
p	Static Pressure	[Pa]
P_0	Free-stream Total Pressure	[Pa]
p_∞	Free-Stream Static Pressure	[Pa]
P_{Lock}	Locked Peak	[-]
P_{Rel}	Relative Peak	[-]
q	Dynamic Pressure	[Pa]
RMS_{Rel}	Relative Root-Mean-Square	[-]
S	Wing Area	[m^2]
S_C	Strain Gauge Center Electric Signal	[N mm mV^{-1}]
S_F	Strain Gauge Front Electric Signal	[N mm mV^{-1}]
S_R	Strain Gauge Rear Electric Signal	[N mm mV^{-1}]
s	Penetration Distance	[m]
T	In-compressible Flow Viscous Stress Tensor	[−]
t	Time	[s]
t_B	Time Bin	[s]
t_{Rel}	Released Time	[s]

U	Maximum Gust Velocity	$[\mathrm{m\,s^{-1}}]$
u	Horizontal Instantaneous Velocity	$[\mathrm{m\,s^{-1}}]$
$u(s)$	Gust Velocity	$[\mathrm{m\,s^{-1}}]$
u_S	Body Wall Velocity	$[\mathrm{m\,s^{-1}}]$
U_∞	Free-Stream Velocity	$[\mathrm{m\,s^{-1}}]$
V	Aircraft Forward Velocity	$[\mathrm{m\,s^{-1}}]$
v	Vertical Instantaneous Velocity	$[\mathrm{m\,s^{-1}}]$
V_0	Potentiometer Electric Signal	[]
V_e	Effective Aircraft Velocity	$[\mathrm{m\,s^{-1}}]$
V_M	Measurement Volume	$[\mathrm{mm^3}]$
W	Aircraft Weight	[N]
w	Out-Of-Plane Instantaneous Velocity	$[\mathrm{m\,s^{-1}}]$
W_{ref}	Reference Gust Velocity	$[\mathrm{m\,s^{-1}}]$
x	Position Vector	[m]
α	Angle of Attack	[°]
β	Sideslip Angle	[°]
$\Delta\alpha_{WT}$	Angle of Attack Variation	[°]
Δt	Time Interval	[s]
Δx	Horizontal Coordinate	[pixel]
Δy	Vertical Coordinate	[pixel]
Δ_{pix}	Pixel Pitch	[mm]
ϵ	Twist Angle	[°]
ϵ_b	Bias Error	[−]
ϵ_r	Random Error	[−]
ϵ_u	Velocity Uncertainty	$[\mathrm{m\,s^{-1}}]$
γ	Heat Capacity	[−]
γ_b	Bound Vortex Strength	[−]
Λ	Flare Angle	[°]
$\mathcal{N}$	Space Dimension	[−]
μ	Dynamic Viscosity Coefficient	[−]
ν	Beam Deflection	[-]
ω	Vorticity Field	[−]
ρ_0	Sea-Level Air Density	$[\mathrm{kg\,m^{-3}}]$

σ	Normal Force	[N]
σ_a	Confidence Interval	[-]
τ	Viscous Stress Tensor	[−]
τ_p	Time Response	[s]
θ	Wingtip Fold Angle	[°]
θ_S	Beam Slope	[-]

1 INTRODUCTION

Thanks to government efforts and global policies to reduce greenhouse gas emissions and fight against climate change, the world is finally going towards a greener future. Aviation emission is one of the most critical parameters to be minimised since it consists of 3.8% of total CO_2 emissions, or 13.9% of the emissions if only the transport is considered, as stated in the European Green Deal [1], ranking in the top ten in terms of the emitters if it were a country. Furthermore, aviation also impacts climate change due to the release in the atmosphere of Nitrogen Oxides NO_x, water vapour, Sulphate SO_4^{2-} and soot particles. Based on the International Civil Aviation Organisation calculations, the total emission value will triple by 2050 [2]. To attenuate this problem and reach climate neutrality by 2050, the European Green Deal decided that aviation emission has to be reduced by 90% [1].

To reduce the emission created by the current aviation industry, there are several ways to tackle the problem. Firstly, combustion engines can be substituted with new engine types like hydrogen or electric-powered ones. Secondly, the structural weight has to be reduced using lighter material that will also reduce the energy needed (i.e. fuel consumption) to fly a particular payload, with the consequent reduction in the total number of flights. Moreover, the aerodynamic efficiency can be improved, maximising the lift over drag value, resulting in less energy consumption for a given flight. This can be reached by increasing the wing aspect ratio (AR) so the wingspan (b), since $AR = \frac{b^2}{S}$. Indeed, lift-induced drag D_i is approximately 40% of the total drag produced by an aircraft, which is inversely proportional to the wingspan (b) squared, as visible in the lift-induced drag D_i formula in Equation 1.1 [36].

$$D_{\mathrm{i}} = \frac{L^2}{\frac{1}{2} \cdot \rho_0 \cdot V_E^2 \cdot \pi \cdot b^2} \tag{1.1}$$

This span increase is unfortunately limited by the dimensions of the current gates (80m maximum in width [37]) that cannot meet these such extensive wingspan requirements. However, at the same time is also limited by the structural weight and by the aerodynamic loads that the fuselage can handle without encountering failure. For this reason, new solutions have been studied in recent years, and one of the most promising ones (coming from the naval aviation field) is the use of the Hinged Folding Wingtip. This will help increase the aircraft's wingspan during flight operations but can be folded and closed during taxiing to reduce the aspect ratio (AR) of the wing when the aircraft is on the ground. This increases the plane's handling capability and permits using the already existing airport gates without needing to construct new ones. As shown by Carrillo [17], the hinged folding wingtip has impressive Gust Load Alleviation (GLA) capabilities. Indeed, in case of a gust load hitting the wingtip, the hinge is released, letting the wingtip free to move. A moment created will force the wingtip to move up and down until a steady state is again reached (load equal to its weight). Since a hinge connection is present, this bending moment will not be transferred at the root of the wing, alleviating its peak value and permitting lighter structures. Furthermore, this design also increases the aircraft's roll capability during flight. An ideal relation (where the hinged wingtip compensates entirely for the increase in weight due to the extra span) between the aircraft drag and wingspan increase is plotted in Figure 1.1, for both a wingtip that folds only on the ground and one that is used in flight for gust alleviation purposes.

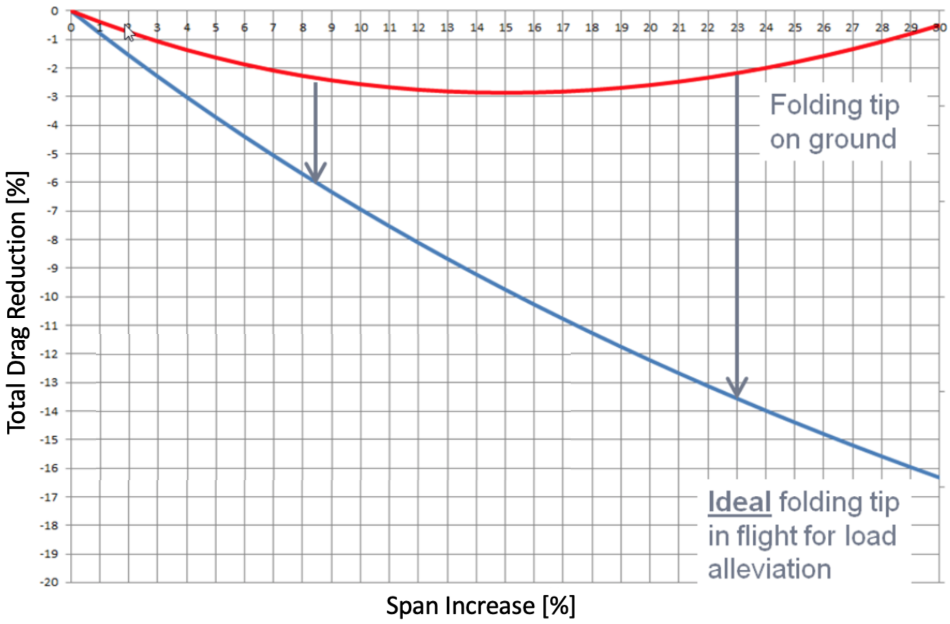

Figure 1.1: Drag and wing span relationship, with and without hinged folding wingtip for load alleviation [3].

Aerodynamic numerical simulation studies and, in particular, wind tunnel experiments (that do not need to model the complex structure and flow, giving more accurate results) are becoming increasingly critical in the aviation industry to achieve this reduction in fuel consumption. This to improve efficiency and make aircraft less polluting, but at the same time also as a way to verify and validate results obtained with other methods. Different measurement techniques can be used, from the most simple flow visualisation (oil flow visualisation, wall tufts, smoke lines and hydrogen bubbles), to pressure measurements using pressure taps and probes or hot-wire anemometry to measure the fluid velocities. Reaching the most advanced non-intrusive flow measurement technique, the so-called Particle Image Velocimetry (PIV), where the flow properties can be studied by recording with a camera the motion of the illuminated tracer particles in different instants in time.

Since this new Hinged Folding Wingtip (HFW) design is still not implemented in a real aircraft and since the result obtained are not always consistent between different studies. A precise aeroelastic characterised from both the aerodynamic and structural point of view is necessary, particularly in the presence of gusts (unsteady flow situations) when the hinge will be unlocked and the wingtip is let free to move. This will be achieved with a wind tunnel experiment, where the scaled model of the HFW is analysed with a state-of-the-art large-scale, whole field and non-intrusive PIV technique that takes 3D instantaneous measurements using six different digital cameras. These are used to record the movement of Helium-Filled Soap Bubble (HFSP) tracer particles and use the Shake-The-Box (STB) Lagrangian Particle Tracking (LPT) algorithm.

This thesis report will be structured as follows. Chapter 2 will summarise the literature review performed for this thesis project, including an overview of aeroelasticity and gusts, hinged folding wingtip and Particle Image Velocimetry, also presenting the formulated research objective and the research questions. In Chapter 3, the set-up and equipment used during the wind-tunnel campaign are presented and the experimental procedures performed before the test for the calibration and during it for the actual measurements, including the test matrix cases. Then, in Chapter 4, the methodology and techniques used for the post-process and processing analysis of the gathered data with both PIV and conventional sensors are given. Chapter 5 contains the final discussion on the found results. Finally, in Chapter 6, the conclusion and recommendations for future studies are drawn and presented. Then, in Appendix A, the Programmable Time Unit (PTU) connections with the six cameras are stated.

2
LITERATURE REVIEW

This chapter will introduce a summary of the literature review performed for the thesis project, including an overview of aeroelasticity and gusts, hinged folding wingtip and Particle Image Velocimetry. It also presents the formulated research objective and the research questions.

2.1 AEROELASTICITY

Implementing lightweight composite material in aviation is a direction the leading companies follow to achieve the sustainability goal set by the institutions. These structures are usually more flexible with respect to conventional metal-based ones so that they will be more impacted by the presence of gusts during flights. For this reason, aeroelastic studies are becoming very important to understand the structural response to such complex loads. Aeroelasticity defines all the interactions between the inertial, elastic, and aerodynamic forces due to the flow surrounding a structure. These subjects were studied independently and separately as discrete quantities in the past. Collars [4] instead showed that strong interconnections were present, and this field should be studied as an integrated quantity, where each event is connected to the different forces involved.

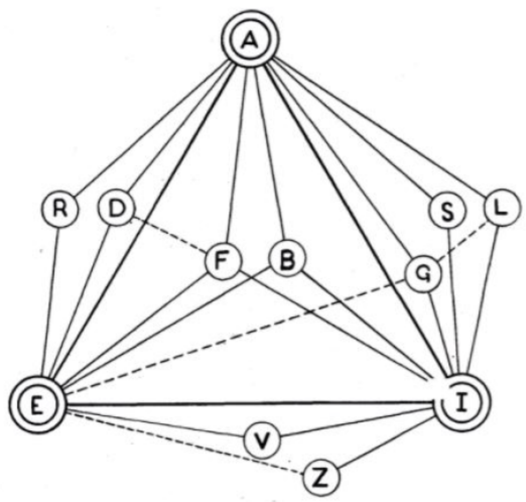

Figure 2.1: Collar's triangle [4].

All the interactions between the flow and the structure are represented in the Collar's Triangle visible in Figure 2.1 and listed in Table 2.1.

Table 2.1: Collars triangle components [4].

A	Aerodynamic Forces	**F**	Flutter	**D**	Divergence	**L**	Loading
E	Elastic Forces	**B**	Buffeting	**R**	Reversal of Control	**V**	Mechanical Vibrations
I	Inertial Forces	**S**	Stability & Control	**G**	Gusts	**Z**	Impacts

Aerodynamic forces are due to the structure interaction with the flow that creates differences in pressure distribution. Instead, the elastic forces are caused by the deformation of the structure and depend strongly on the structural properties. Finally, the inertial forces are generated by the accelerations acting on the structure mass.

2.2 GUST

When all three primary forces in the Collar's Triangle are involved and interact, the most interesting and challenging aeroelastic phenomena occur, like in the presence of gusts. Gusts are dynamic events encountered during flights caused by atmospheric currents turbulence that creates air-flow freestream velocity perturbations that decrease the flight dynamics performance of the aircraft [5]. The structure response and deformation of this kind of abrupt load variation (overload) are crucial in the presence of composite materials. They are an essential prerequisite in an aircraft's design and certification phases to avoid sudden and unexpected failures due to structural fatigue. To reduce these loads transferred from the wing to the connection with the fuselage, hinged folding wingtip solutions can be used, which also help to decrease the aircraft's structural weight, leading to a greener aviation future.

Gusts are very complex phenomena due to their non-uniformity. For this reason, several simplified models were constructed to characterise all the different types. The three main types, based on the incoming direction of the burst, are vertical, lateral and head-on gusts, visible in Figure 2.2. Where V is the forward flight mean speed of the aircraft, U is the velocity of the gust perturbation, and V_e is the effective total velocity of the aircraft. Each gust will cause an effect on the aircraft, on the angle of attack (α), sideslip angle (β) and dynamic pressure (q) change [5].

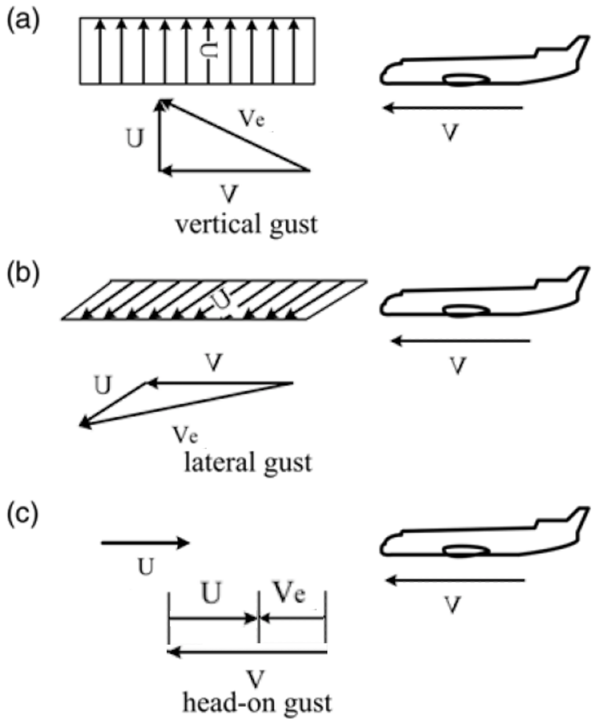

Figure 2.2: Gusts directionality [5].

An important parameter that defines the gusts is the load factor (n), calculated using Equation 2.1 [5] diving the aircraft lift (L) under a specific gust load by the aircraft weight (W), where Δn is the acceleration increment caused by the gust.

$$n = \frac{L}{W} = 1 \pm \Delta n \tag{2.1}$$

The gust most used for certification and unsteady-state flow simulation purposes is the 1-Cosine gust, modelled initially by Nasa [38] with a cosine shape curve velocity profile as illustrated in Figure 2.3.

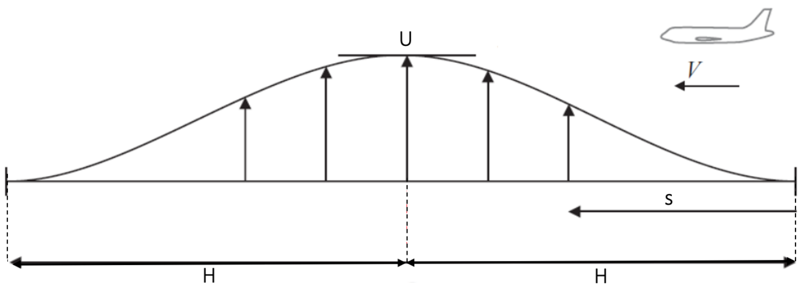

Figure 2.3: 1-Cosine gust [6].

1-Cosine gusts velocity profile $u(s)$ at any penetration distances s can be defined mathematically as Equation 2.2 [6]. Where U is the maximum gust velocity, and H is the gust gradient distance, or half of the gust wavelength (distance from the beginning to the end of the gust), that rages from 36m to 428m [39].

$$u(s) = \begin{cases} \frac{U}{2} \cdot \left(1 - \cos\left(\frac{\pi \cdot s}{H}\right)\right) & \text{if} \quad 0 < s < 2H \\ 0 & \text{elsewhere} \end{cases} \tag{2.2}$$

The maximum gust velocity U is given by Equation 2.3 [6]. Where W_{ref} is a reference gust velocity that varies from $17.07\,\mathrm{m\,s^{-1}}$ at sea level Equivalent Airspeed (EAS) to $6.36\,\mathrm{m\,s^{-1}}$ EAS at 18288m based on the Federal Aviation Administration (FAA) and European Union Aviation Safety Agency (EASA) regulations [39].

$$U = W_{\text{ref}} \cdot \left(\frac{H}{106.14}\right)^{1/6} \tag{2.3}$$

2.3 Gust Load Alleviation

This section presents an overview of the Gust Load Alleviation (GLA) devices, including the two main concepts. Then, the development steps of the active GLA category and the obtained results in terms of reduced wing root bending moment are given.

2.3.1 Concepts

As already stated, beyond the aerodynamic efficiency improvement, an advantage to implementing the hinged folding wingtip is the Gust Load Alleviation (GLA), a reduction in the peak load during a gust, resulting in a lower Wing Root Bending Moment (WRBM) that enable the implementation of lighter wing structures. Nowadays, research focuses on two primary GLA devices, active and passive. A hinged folding wingtip is included in the active GLA devices where the surface used to reduce the loads is actuated, while the passive ones do not need direct control.

2.3.1.1 Passive Gust Load Alleviation Devices

Passive GLA devices are based on the structural and aerodynamic forces to alleviate the gust loads. For example, a wing loaded due to a gust can deform so that it can alleviate the gust peak loads. Guo et al. [7] presented a passive twist wingtip concept (illustrated in Figure 2.4) where the wingtip is allowed to rotate around the wing axis due to a sprung shaft joint that connects it to the wing, this design can achieve a 21% reduction in the gust-induced wingtip deflection and 11% in wing root bending moment. The working principle is based on the wingtip aerodynamic centre (a.c.) position behind the shaft joint (between the wingtip and the wing). This allows that when a load increase occurs, the tip will offload instantly. Other concepts instead are based on aeroelastic tailoring, for example, using the composite material's directional stiffness properties to tailor the aeroelastic response of the wing, affecting in a positive way the aerodynamic and structural performance of that aircraft [40]. Furthermore, Kruger et al. [41] reached a 30% reduction in wing structural weight using anisotropic laminates with respect to the quasi-isotropic one. A downside of passive GLA devices is that they do not permit the wingtip to be closed, reducing the wingspan on the ground.

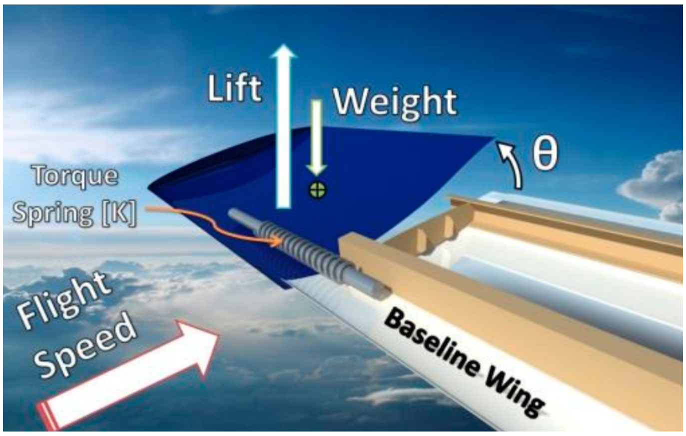

Figure 2.4: Passive twist wingtip device [7].

2.3.1.2 ACTIVE GUST LOAD ALLEVIATION DEVICES

Instead, active GLA devices are actuated structural surfaces used to decrease the peak loads. One of the most promising designs is the hinged folding wingtip (visible in Figure 2.5), which can bring a 19% lower wing root bending moment for the unsteady flow case compared to conventional wingtip [10]. This is due to the hinge that enables the wingtip to respond to a gust, more specific results are presented in subsection 2.3.3. Nevertheless, it introduces some disadvantages, like an increase in weight for the wing extension (additional span) and the hinge/actuation system. However, the gust load alleviation capabilities of the hinged folding wingtip caused a reduction in the wing root bending moment, enabling the use of a lighter wing-box structure. Since the wing mass has approximately a cubic increment with the wingspan, this results in a lower total wing mass with respect to a conventional wing [8], leading to a more lightweight, fuel-efficient and environmentally friendly aircraft. Furthermore, increasing the wingspan will help reduce lift-induced drag and improve the total aircraft aerodynamic efficiency. Overall, it is possible to state that active GLA devices and, in particular, hinged folding wingtips gave more positive results regarding peak load reduction with respect to the passive ones.

Figure 2.5: Hinged folding wingtip front-view [8].

2.3.2 HINGED FOLDING WINGTIP DEVELOPMENT STEPS

Regarding active Gust Load Alleviation (GLA) devices, Boeing [42] was the first aircraft manufacturing company that included a folding wingtip in its new model Boeing 777X (that will be introduced in 2024), to extend it by 7m. This is to increase the wing aspect ratio during the flights, intending to improve the aerodynamic performance via a reduction in lift-induced drag. However, this design will also be able to fold after landing during taxiing to have better manoeuvrability and comply with already existing gates avoiding the necessity to build bigger ones. On the European side, Airbus is working on a slightly different design of folding wingtip, including a hinge that allows the wingtip to rotate that will be released during flight to alleviate the increase in bending moment at the wing root. Indeed it is true that the wing will be heavier, enhancing the loads, but the free hinge of the wingtip will not transfer any moments at the root, and at the same time, this new wingtip can be used as gust alleviation.

Figure 2.6: Boeing 777X folding wingtip [9].

Castrichini et al. [43] did a preliminary analysis on the model visible in Figure 2.7 and showed in his study the influence of the flare angle (Λ) (angle between the aircraft longitudinal axis and the hinge rotation axis) on the gust alleviation capabilities. The greater the flare angle, the lower the wingtip mass and the hinge spring stiffness, and the greater the load alleviation due to the passive nose-down deflection in the geometric angle of attack (α). For a conventional airliner, with the hinge-axis perpendicular to the quarter chord of the wing, a positive fold angle (wingtip displacement about the hinge axis from the wing-level position) θ = 1° gives variation in the local angle of attack $\Delta\alpha_{WT}$ = -0.42°, using Equation 2.4 [43]. This is associated with an aerodynamic aircraft download that alleviates the load and helps reach static stability [3]. The best results were obtained by a 25° flare angle in steady-state, giving a wing root load reduced of 30% compared to the rigid hinge case, with higher root loads of just 4.36% respect to the reference model with no wingtips, despite a span increase of 25% [43].

$$\Delta\alpha_{WT} = -\tan^{-1}(\tan\theta \sin\Lambda) \tag{2.4}$$

Siddaramaiah et al. [10] using the same aeroelastic model (Figure 2.7), proved what obtained by Castrichini et al. [43], that the best load alleviation and reduction in wing root bending moment for a swept wing can be reached by the 25° flare angle.

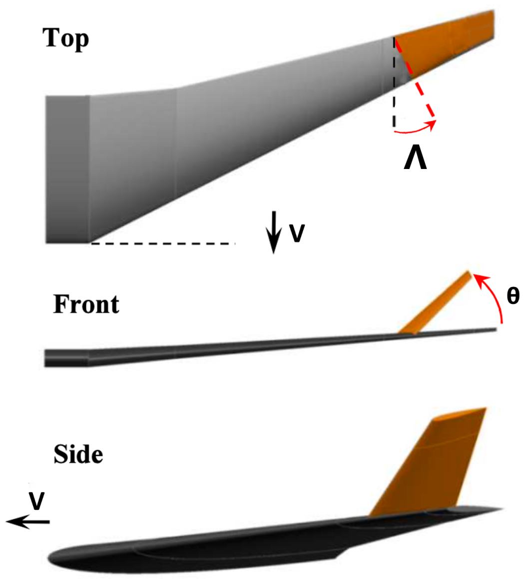

Figure 2.7: Hinged folding wingtip with positive flare angle [10].

Furthermore, the obtained results were confirmed by Cheung et al. [11] with a subsequent steady and unsteady (1-

Cosine gust) low-speed wind tunnel experiment using a 30° flare angle wingtip configuration. The model (shown in Figure 2.8) has a span of 0.7m, a chord (c) equal to 0.3m and uses a NACA0015 airfoil, force/torque sensors were used to measure the lift and bending moment, while a rotary magnetic encoder for the wingtip fold angle. A reduction of about 56% in the peak rolling moment increment during the generated gusts was observed, demonstrating gust alleviation capability.

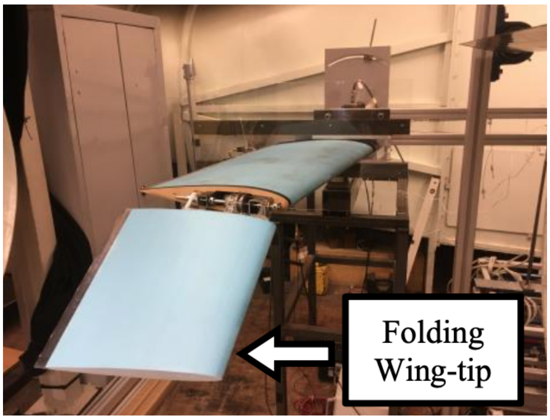

Figure 2.8: Hinged folding wingtip model [11].

Moreover, Cheung et al. [12] proposed and demonstrated that adding to the wingtip a second movable device (wingtip tab) that controls the wingtip orientation will keep the wingtip orientations stable throughout the different angles of attack (α) and wind tunnel speeds in steady conditions. Instead, in unsteady conditions, actively controlling this device and releasing it when the gust hits the wingtip will help reduce the peak in the bending moment at the root of the wing [12].

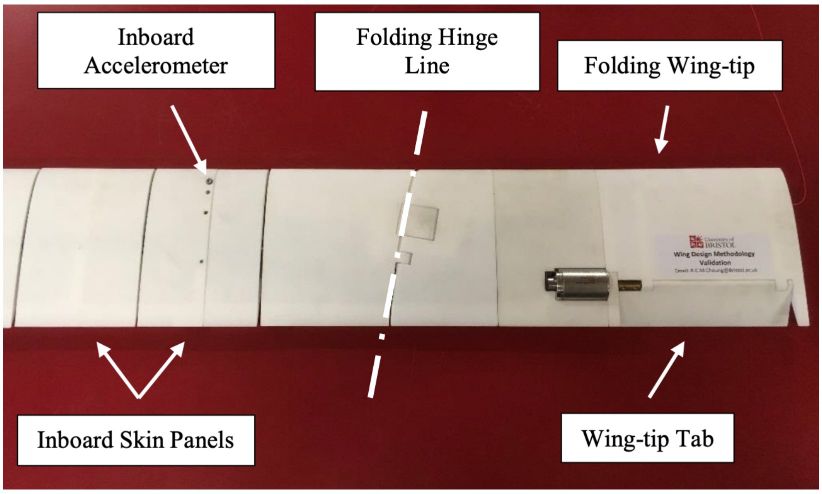

Figure 2.9: Hinged folding wingtip model and sensors location [12].

The hinge moment threshold to release the wingtip is an important parameter since it affects the gust load alleviation capability of the wingtip. The influence of this parameter was investigated by Castrichini et al. [44]. A non-zero low moment threshold value (3×10^5Nms) and low hinge stiffness (1Nmrad^{-1}) and hinge damping (1×10^5Nmsrad^{-1}) permit a fast rotation of the hinged wingtip when hit by a gust load, resulting in a decrease of the inertial loads with a consequent lower wing root bending moment respect to a baseline aircraft with a fixed wingtip. Instead, increasing the threshold using high values over-damp the system, worsening the load gust alleviation capabilities of the hinged wingtip due to the delayed onset rotation of the wingtip with a consequent reduction in the time available to alleviate the gust. The faster the initial wingtip rotation, the greater the inertial force as the maximum rotation angle is approached. The only limitation is that once the wingtip is released, having such a small hinge stiffness value, it will remain deflected even after the gust event during straight and level cruise flight due to the static trim loads; this will produce an undesirable effect that will be negative in terms of the aerodynamic performance and trim behaviour.

For a linear hinge, there is a conflict between the low spring stiffness value needed for good load alleviations and the high values needed to counteract static trim deflections and continuous oscillations. Castrichini et al. [45], with a subsequent study, to solve this issue, investigate the introduction of a passive non-linear hinge spring on a model with 20% more span with respect to the baseline, allowing the recovery of the wingtip to the original position after the gust. This hinge was designed with a high static low dynamic stiffness to be stiff enough statically to support the wingtip mass and avoid the wingtip deflecting during the cruise. At the same time, it has a low natural frequency (low dynamic stiffness). The results showed that using a passive non-linear spring device allowed a load alleviation improvement compared to the linear spring model due to the negative stiffness contribution of the oblique springs that allow the fastest wingtip deflections.

Then, Castrichini et al. [16] studied the effect of the so-called Semi Aeroelastic Hinge (SAH) to keep the wingtip in place in a clean position during the cruise and release it just when necessary (combining the free hinge with a lock and a clutched actuator). In this adaptive system, the hinge is kept in place by a mechanism that blocks it during cruising, but when the trigger event is detected, the wingtip is released and is left free to move, acting as a passive gust load alleviation device, driven just by the inertial and aerodynamic forces. When the gust is finished, an actuator will bring the wingtip to the initial position and then block it. Also, the time at which the hinge will be released was investigated. The results show that the capability to alleviate gust loads depends massively on the releasing timing and delay of the hinge with respect to the gust load episodes. Indeed, releasing the hinge early will result in the same load alleviation capabilities of a free-floating wingtip (best gust load alleviation) but decrease the flutter speed. This low flutter speed problem of the wing, caused by the free hinge of the wingtip, can be solved by adding tip mass [3].

Considering the aircraft handling, Dassault et al. [46] studied the effect numerically on a roll due to a folding wingtip. Successively, Healy et al. [13] on a rectangular, un-swept, untapered wing model (visible in Figure 2.10) demonstrated and validated experimentally that hinged folding wingtip improves aerodynamic performance due to the increased span, in particular, the aircraft roll performances due to the unloaded wingtip during the roll manoeuvre respect to a fixed wingtip design. Indeed, the aircraft's maximum roll rate is improved thanks to the reduced aerodynamic roll damping. Moreover, the wing angular acceleration peak is also increased, causing a decreased time to reach steady-state roll. This bigger span also involves an increase in the aircraft's moment of inertia, reducing the acceleration rate for a given aileron torque. This means that a larger span will imply a bigger aileron (not always structurally feasible to include) to avoid controllability issues like the occurrence of the aileron reversal phenomenon, so for this reason, roll dampers may be necessary.

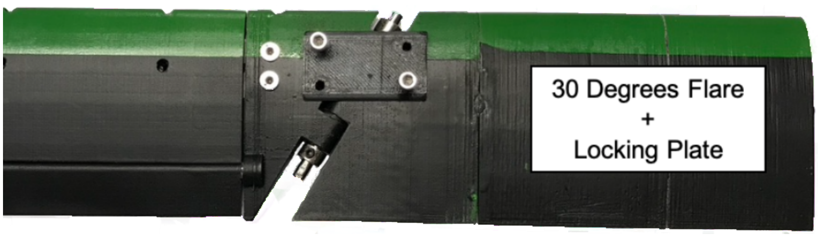

Figure 2.10: Hinged folding wingtip used in the wind tunnel experiment [13].

The SAH wingtip design was tested in the wind tunnel and in flight by Wilson et al. [47] using a small scale demonstrator aircraft (with a 3.7m span and $\Lambda = 15°$) based on an Airbus A321 called AlbatrossONE, visible in Figure 2.11. The first-ever flight of an aircraft with a SAH wingtip confirmed the wing load alleviation effect due to the free wingtip. The strain gauge measurements confirmed the reduced WRBM due to the load alleviation effect on the free wingtip. In this model, the wingtip flare angle (Λ) causes an effective sideslip (β), and the fold angle (θ) have a non-linear proportionality with the angle of attack (α).

(a) Folding wingtips in vertical position during taxiing

(b) Folding wingtips in horizontal position during cruise

(c) Folding wingtips released for gust load alleviation

Figure 2.11: AlbatrossONE wingtip positions [14].

2.3.3 Hinged Folding Wingtip Results

The gust response of aircraft incorporating Hinged Folding Wingtip devices has been the subject of many recent studies (both numerical and experimental). This is due to the more common usage of composite material that implies a more flexible structure that will deform under such non-linear phenomena with peak loads.

Fazelzadeh et al. [15] simulated a flexible aircraft's wingtip numerically bending deflection response when encountering a stochastic continuous gust, visible in Figure 2.12, where the dotted line indicates the quasi-steady situation modelled, while the continuous line the unsteady one. When the high-frequency gust hits the structure at $t = 10$s, the wingtip results in high frequency bending deformation. At $t = 15$s, when the gust effect ceases, the high-frequency elastic oscillations are entirely damped out by the structural damping of the flexible wing for the unsteady case; instead, for the quasi-steady one, low-frequency oscillations are still present.

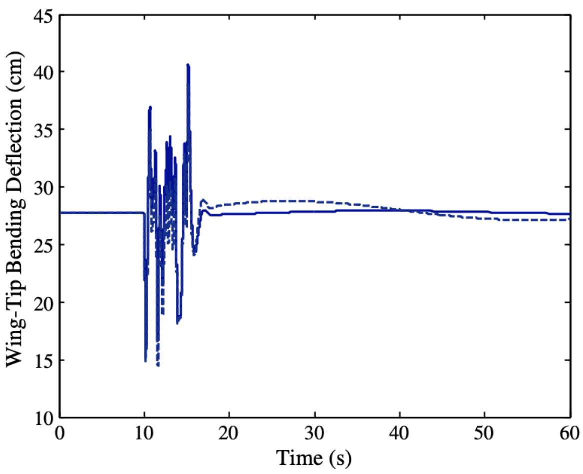

Figure 2.12: Flexible wingtip elastic bending deflection response to gust excitation [15].

Siddaramaiah et al. [10] found that the wingtip's flare angle affects the root bending moment compared to a conventional fixed wingtip. Indeed, the best results in terms of load alleviation were obtained (using a numerical elastic model) with the 25° flare angle with a consequent 15% reduction in static load circumstances (1-g level flight), while 19% for the unsteady case (1-Cosine gust), this is visible in Figure 2.13, for the flight case considered ($M = 0.8$ and $H = 30000$ ft).

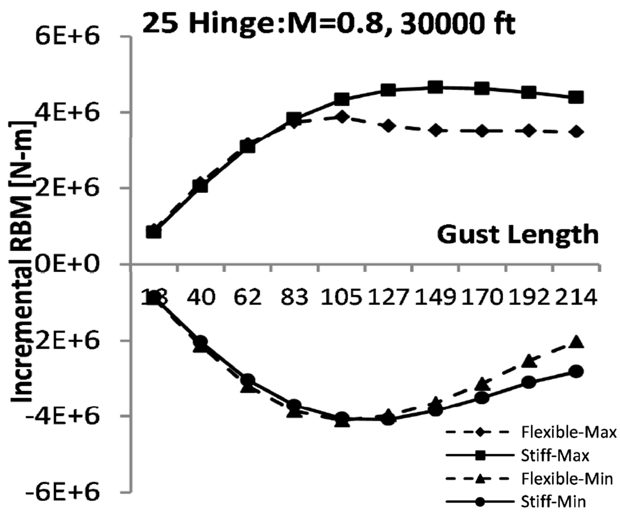

Figure 2.13: Incremental wing root bending moment load envelope response to a 1-Cosine gust [10].

Cheung et al. [12] perform several low-speed wind tunnel experiments on a flexible high AR wing with a hinged folding wingtip to study the Wing Root Bending Moment (WRBM) response to a 1-Cosine gust long 12m at $\alpha = 5°$ with an $18\,\mathrm{m\,s^{-1}}$ wind tunnel free-stream velocity. Looking Figure 2.14 with the results obtained for both locked-hinge and free-hinge configurations, where the WRBM (calculated with four strain gauges) was normalised with its steady value, it is possible to state that a peak reduction in WRBM for the free-hinge occurs respect to the locked one, showing the hinged folding wingtip load alleviation capabilities.

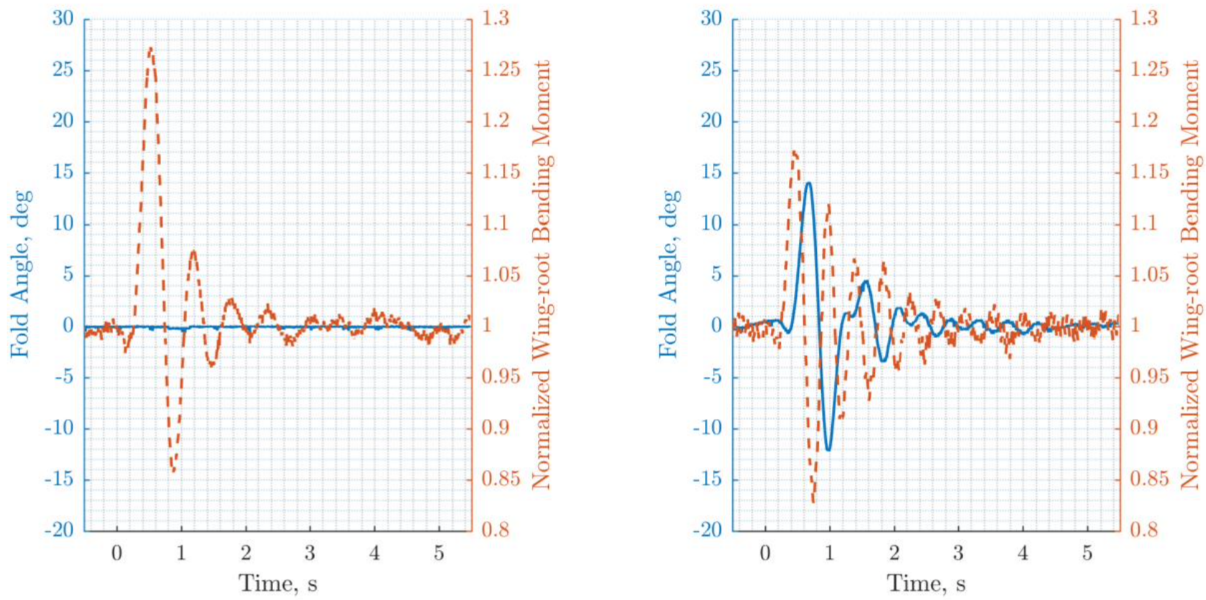

(a) Locked-hinge configuration. (b) Free-hinge configuration.

Figure 2.14: Fold angle and normalised wing root bending moment response to a 1-Cosine gust [12].

Figure 2.15 represents the normalised WRBM response variation for the 1-Cosine gust excitation length range. Overall, the reduction in the WRBM was reduced using the free-hinge configuration. The best results are obtained with a gust length of 18m, achieving a reduction in WRBM of 11% with respect to the reference case (locked-hinge).

With lower gust lengths, between 4m and 7.2m, this alleviation effect decreases, resulting in a WRBM reduction of just from 4% to 6%. This can be attributed to the gust effective excitation frequency close to the frequency of one of the wing bending modes causing a response from the most-inner wing part [12].

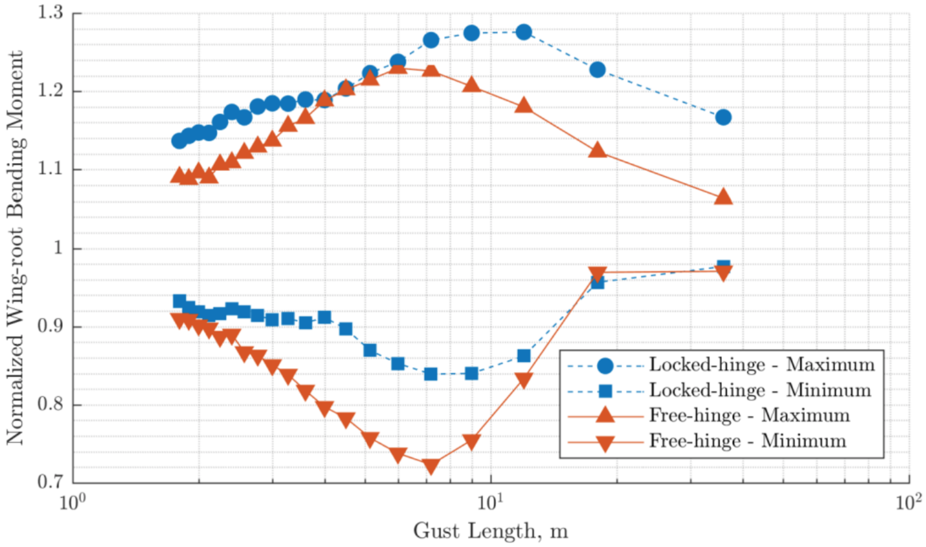

Figure 2.15: Normalised wing root bending moment load envelope response to a 1-Cosine gust [12].

Castrichini et al. [16] studied the influence of the release time of the hinge wingtip. In Figure 2.16, the folding angle and WRBM response using a Semi Aeroelastic Hinge (SAH) when the wingtip is released during a gust. The solid black line represents the SAH, the red dashed line indicates the free-floating hinge, and the blue dashed line is the fixed hinge. The graph below shows that the best results are obtained with the SAH. Indeed, when the hinge is released, the peak of the gust load is reduced with the 1*g* load contribution compared to the other hinge. Then, advancing with time, the loads stabilise, reaching a steady state at a lower level with respect to the fixed hinge. Please note that steady loads are present both before and after the release. The same observations are also valid for the wingtip folding angle.

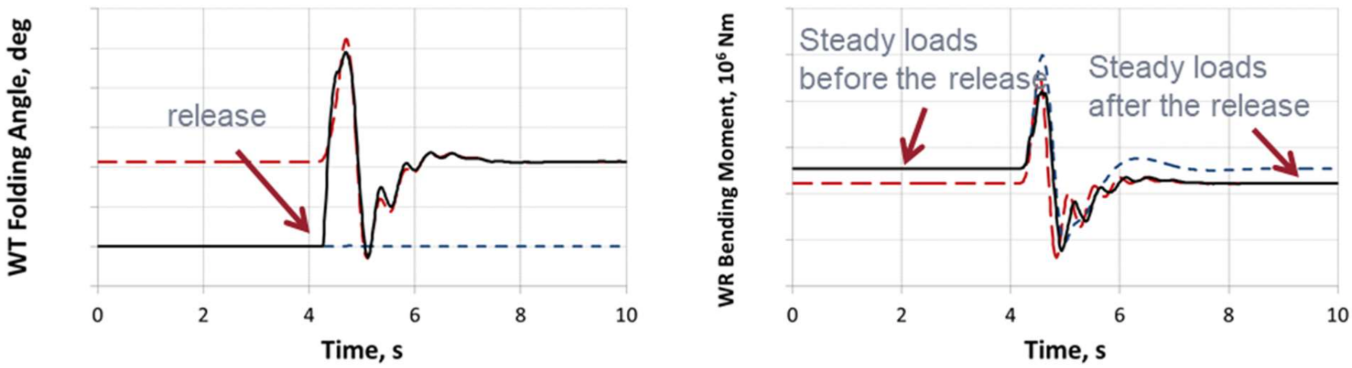

(a) Folding wing-tip angle

(b) Wing root bending moment

Figure 2.16: Release response of the folding wingtip angle and wing root bending moment created [16].

2.4 TESTED HINGED FOLDING WINGTIP DESIGN CONCEPT

This thesis research is based on the Hinged Folding Wingtip (HFW) model, visible in Figure 2.17, developed by Carrillo et al. [17] in his thesis study where the effect of wing stiffness properties and the Semi Aeroelastic Hinge (SAH) release threshold were investigated on a hinged folding wingtip aeroelastic model used for Gust Load Alleviation (GLA) purposes. From his design and results presented in this section, an integrated aerodynamic and structural analysis is conducted in this thesis using the Particle Image Velocimetry (PIV) technique.

2.4.1 MODEL

This model was designed to be in scale with the AlbatrossONE [47], the rectangular wing has a semi-span of 700mm including the 200mm long HFWT (with 15° flare angle), the chord is long 100mm and the airfoil is the symmetric NACA0018, the Aspect Ratio (AR) is 14 (on the full wing span). To have large deformation and easily vary the wing's stiffness property, the Pazy wing concept, introduced by Avin et al. [48], was used. A composite plate (that controls the wing structural properties) acting as a spar designed to carry all the loads is inserted in the 3D printed chassis that contains all the ribs and is covered by a foil.

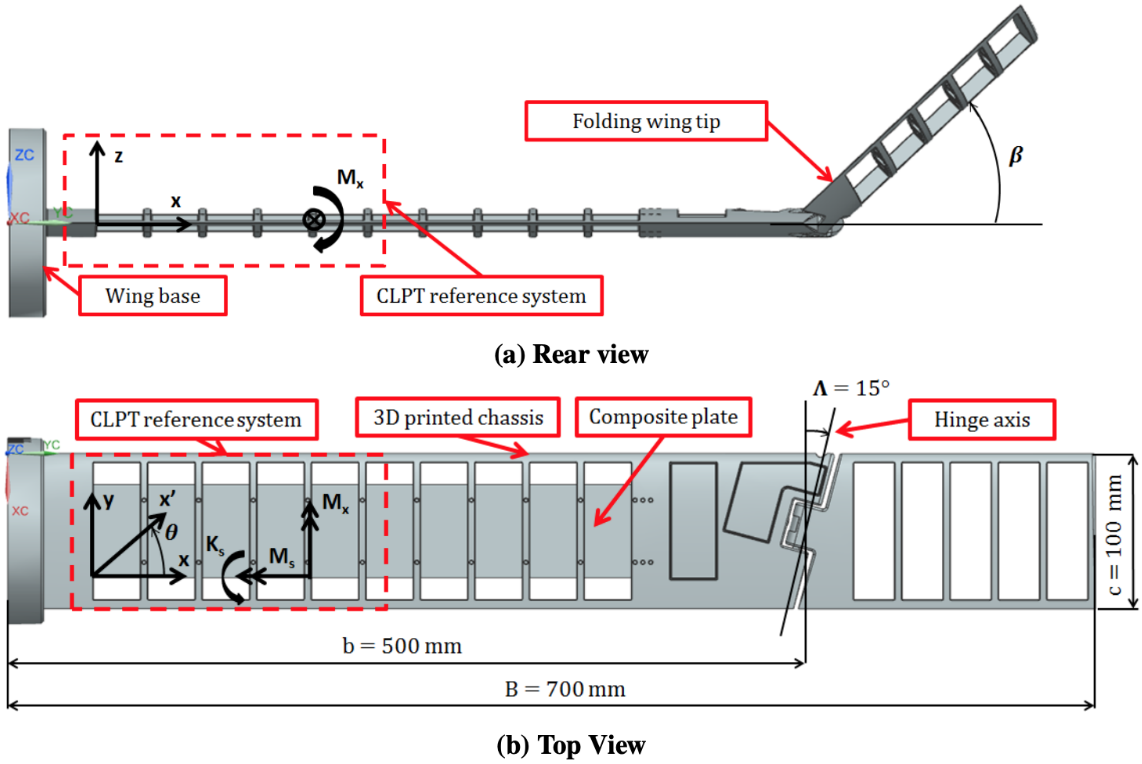

Figure 2.17: Hinged folding wingtip model [17].

Five plates were tested, and three were designed to investigate how the different bending stiffness influence the GLA performances (plates A, B and C, where A is the less stiff and C the stiffest). The last two instead are tailored plates (Wash-In (WI) load enhancing and Wash-Out (WO) load alleviation response) designed to check how the HFWT interacts with an aeroelastic tailoring structure. For the first three plates, the special balanced laminate (with only 0°, 45° and 90° fibre orientations) is used with a stacking sequence antisymmetric with respect to the mid-plane and each half again symmetric about its mid-plane. This, to do not have in the ABD matrix, of the Classical Laminate Plate Theory (CLPT), the bending-twisting coupling, resulting in a quasi-isotropic material [49]. The stiffness changes between the three plates were achieved by adding $[0°\ 90°]_s$ layers between the middle plane but losing the in-plane quasi-isotropic behaviour. Instead, for the tailoring plates (B_{WI} and B_{WO}), plate B was taken as a reference, but now a symmetric laminate is used (with also 15°, 30°, 45° and 75° fibre orientations), to maximise and minimise the bending-twisting coupling term (D_{16} in the ABD matrix), to reach the Wash-In and Wash-Out desired effects. Their stacking sequence is listed below in Table 2.2.

Table 2.2: Plates thickness and stacking sequence [17].

Plate	Thickness [mm]	Stacking Sequence
A	1.2	$[0,45,90,-45]_s[0,90,90,0]_s[0,-45,90,45]_s$
B	1.6	$[[0,45,90,-45]_2]_s[[0,-45,90,+45]_2]_s$
C	2	$[[0,45,90,-45]_2]_s[0,90,90,0]_s[[0,-45,90,+45]_2]_s$
B_{WI}	1.2	$[-30,-15,-45,-15,-15,75,-30,30,90,-75,30,15,-75,45,45,15]_s$
B_{WO}	1.2	$[30,15,45,15,15,-75,30,-30,90,75,-30,-15,75,-45,-45,-15]_s$

The folding wingtip is released by the Semi-Aeroelastic Hinge (SAH) mechanism shown in Figure 2.18 [17]. An active servo-actuated mechanism was used, where a pin connected to an actuator controlled by an Arduino UNO microcontroller is locking the wingtip rotation pressing against the hinge axle. When the Arduino receives the trigger, it releases the pressure at the pin, allowing the wingtip free movement.

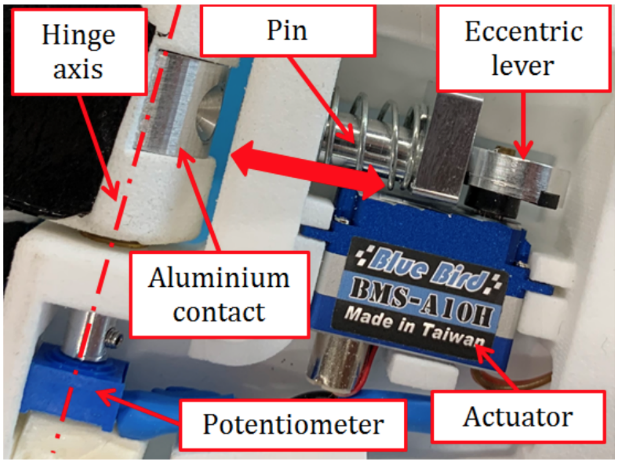

Figure 2.18: Model hinge mechanism (free-hinge condition) [18].

2.4.2 NUMERICAL RESULTS

Due to the model's limitations, simulations were possible just for small fold angles θ. Furthermore is not possible to simulate the hinge released based on the load threshold. In Figure 2.19, the WRBM peak load for the locked-hinge situation for a range of gusts shows that it decreases with the wing bending stiffness, plate A has the highest, with plate C the lowest. For the tailoring plates, plate B_{WI} behave like plate A, while B_{WO} has better GLA alleviation capabilities, with a peak lower than plate C.

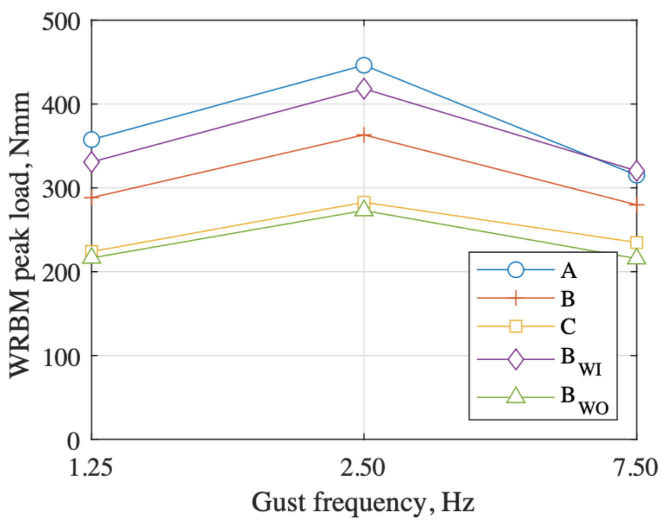

Figure 2.19: Locked-hinge, numerical wing root bending moment, peak load comparison [17].

2.4.3 EXPERIMENTAL RESULTS

The wind tunnel experiment was conducted in the W-tunnel at the Aerospace Faculty of the Delft University of Technology, an open-jet tunnel with a square 0.4m x 0.4m outlet. It can reach a maximum velocity equal to 35m s^{-1} with minimum achievable turbulence level of 0.5% [50]. The test was performed at a low freestream velocity equal to 10m s^{-1}(instead of the 15m s^{-1} decided before) to avoid the fluttering of the wing (since from experiments they result 40% lower than the simulated ones, listed in Table 2.3).

Table 2.3: Simulated and experimental flutter speed for $\alpha = 0°$ (free-hinge, steady conditions) [17].

Plate	A	B	C	B_{WI}	B_{WO}
Simulation [m s^{-1}]	19.9	21.1	23	20.4	22.9
Experiment [m s^{-1}]	12	16	17	15	18

A gust generator was installed at the nozzle's exit, creating 1-Cosine gusts with a fixed time interval. After the gust generator, the wing was placed vertically to reduce the increase in the flutter speed, avoiding the dominance of the weight force instead of the aeroelastic forces. The setup used is illustrated in Figure 2.20.

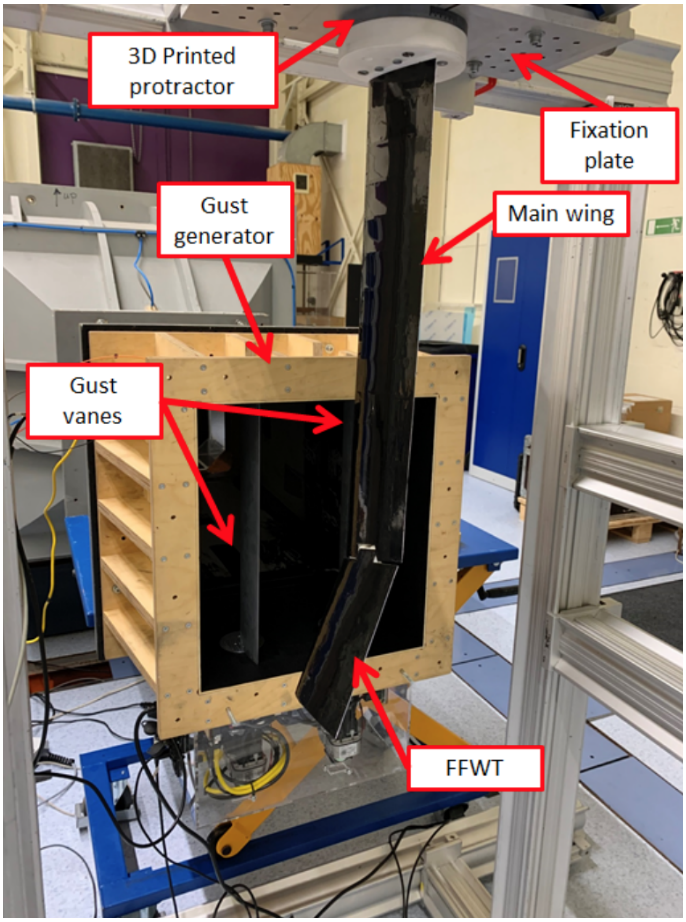

Figure 2.20: Wind tunnel setup [18].

Several sensors were installed on the model to collect the wanted physical quantity during the experiment. This is visible in Figure 2.21. The Wing Root Bending Moment (WRBM) is measured with two tri-axial 0°/90°/45° strain gauges rosette placed on both sides of the plate. Then, the main tip displacement is checked with two uniaxial accelerometers. Finally, the wingtip fold angle is recorded with a potentiometer.

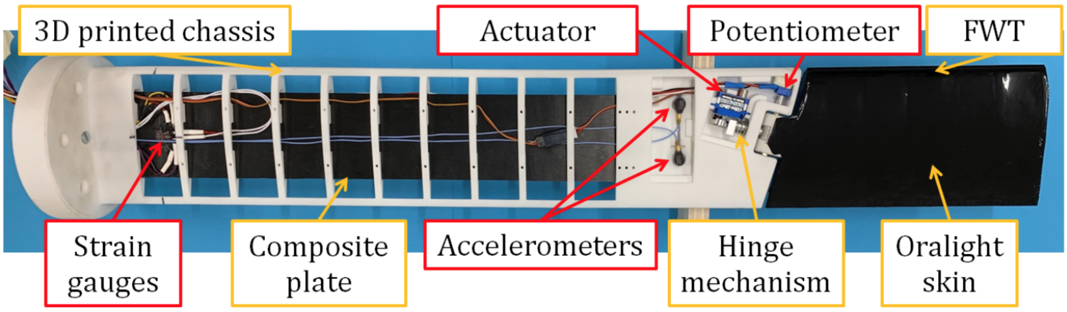

Figure 2.21: Wing sensors distribution [18].

The different wings were tested in both steady and unsteady conditions. For the steady condition experiments, the angle of attack (α) was changed with steps of 1° between -6° and 14°. Instead, for the unsteady condition experiment, using the 1-Cosine gust, α was set to be equal to 0° for dynamic load representation (since the airfoil is symmetric, no lift is produced with a null angle of attack), instead, equal to 5° for static and dynamic load representation. To have a good range of natural gust frequencies, it was decided to use 0.5Hz, 5Hz, 8Hz (maximum required for the CS 25 regulations [39]), the first natural frequency in the locked-hinge configuration, called 1st Bending, and the first natural frequency in the free-hinge configuration, called 1st Flapping (that is the same for all the wing, 1.33Hz), found with an impact test. Since the gust generator is producing gusts with steps of 0.5Hz, the 1st Flapping frequencies were rounded to 1.5Hz for all the plates, while the 1st Bending were rounded to 3.5Hz for plate C while 3Hz for the rests. The different hinge released conditions and load threshold variations are studied, testing six different cases: free hinge, locked-hinge, hinge released with the gust generator trigger signal, before the gust hit it (called pre-released), hinge released when the gust hit it (called 0%), hinge released when the gust load is at 50% (called 50%) and finally hinge released at the gust peak load (called 100%) [17]. The experiment was done ten times for the unsteady tests to have better consistency between results. The complete test matrix of the wind tunnel experiment is visible in Table 2.4.

Table 2.4: Test matrix [17].

Parameter	Steady Condition	UnSteady Condition
Plate	A, B, C, B_{WI}, B_{WO}	A, B, C, B_{WI}, B_{WO}
Hinge Condition	Free, Locked, Pre-Released, 0%, 50%, 100%	Free, Locked, Pre-Released, 0%, 50%, 100%
Angle Of Attack [°]	[-6, 14]	0, 5
Gust Amplitude [°]	-	2.5
Gust Frequency [Hz]	-	0.5, 5, 8, 1st Bending, 1st Flapping

2.4.3.1 Steady Conditions

The bending moment coefficient (C_B) and fold angle (θ) polars, for the steady condition case, are displayed in Figure 2.22 for plate B. For the other plates, a similar trend results. This shows that the different plates do not play a role in moment alleviation. The fold angle (θ) polars shows how the wingtip rotates to maintain an equilibrium state. C_B) was calculated with Equation 2.5 [36], where M is the bending moment and S the wing area.

$$C_B = \frac{M}{\frac{1}{2} \cdot \rho \cdot S \cdot b \cdot V^2} \tag{2.5}$$

The reduced slope of the bending moment line for the free hinge configuration confirms the Gust Load Alleviation (GLA) capabilities of the Hinged Folding Wingtip (HFW) design. For high angles of attack (close to 15°), the measurement deviation increase while the bending moment coefficient decrease; the stall phenomenon causes this.

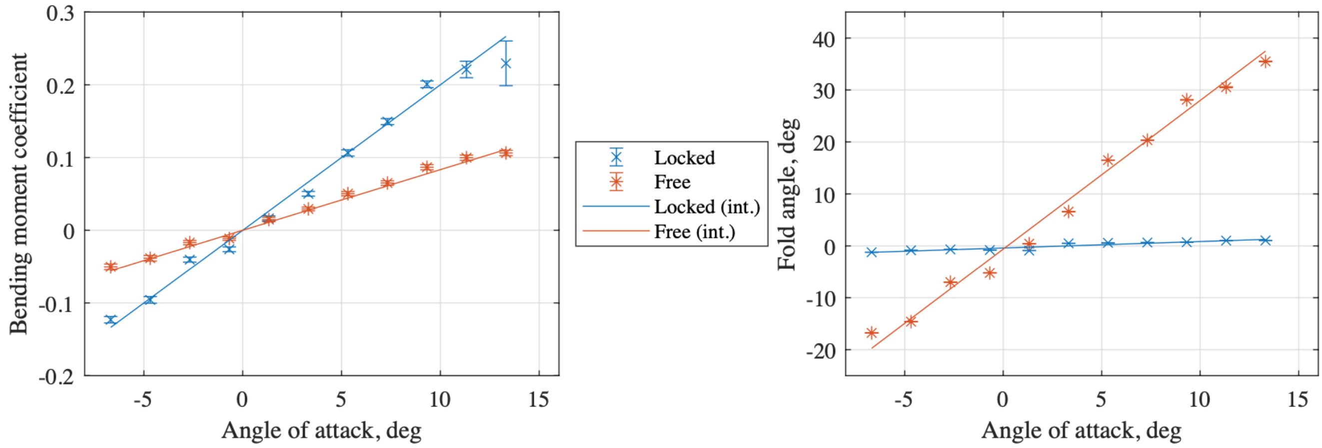

Figure 2.22: Static bending moment coefficient and fold angle for plate B [17].

2.4.3.2 UNSTEADY CONDITIONS

Studying the hinged folding wingtip in unsteady conditions, it was noticed that the timing of the hinge released appears to have a massive impact on the performance. Unfortunately, two different time delay sources were found that affected the results. The first one is caused by the delay of the Arduino in releasing the hinge after the input is given (2ms). While the second one is between the input sent to the actuator and the wingtip starting moving (50ms) [17]. These errors are more pronounced for high-frequency gusts (short gusts) since they represent an essential source of error.

Looking Figure 2.23, that represents the relative peak load reduction with respect to the locked hinge condition for all gusts frequencies and different plates for $\alpha = 5°$ (static and dynamic loads). The peak load reduction is worsened, increasing the delay of the release since higher loads are achieved before the wingtip is allowed to be released, reaching the 100% release state where the loads are higher than the locked hinge condition. When the hinge is released before (pre-released and 0% load threshold), the peak load is reduced by up to 90%. Also interesting to see how the load alleviation reduces with gust frequency for the 50% release case. This is due to the system time delays that increase the load threshold and increase the frequency this error becomes more dominant. The results for all the plates are in line with just minor differences. Exciting the plates at their natural frequency (1st Bending and 1st Flapping) does not influence the Gust Load Alleviation (GLA) performances.

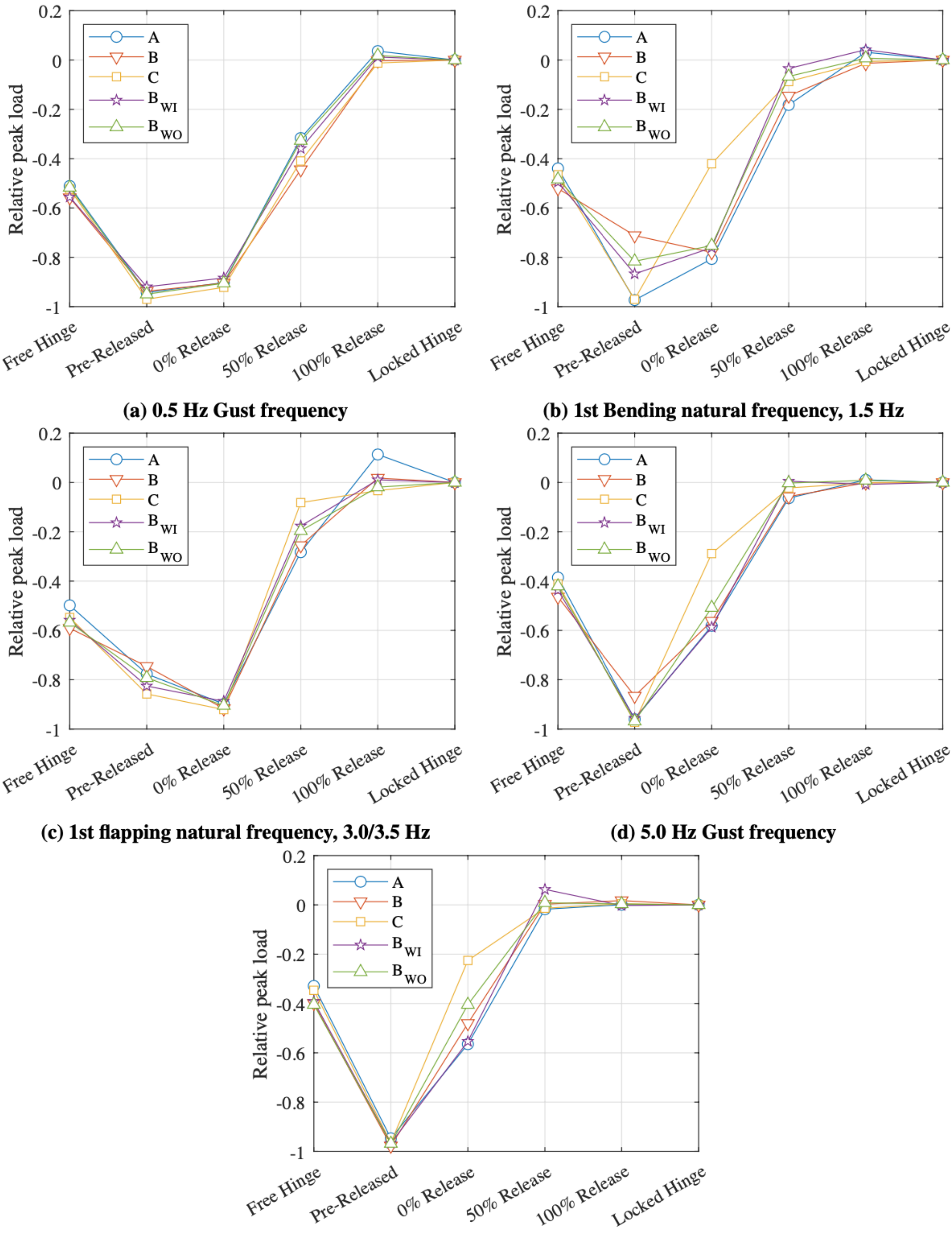

(a) 0.5 Hz Gust frequency

(b) 1st Bending natural frequency, 1.5 Hz

(c) 1st flapping natural frequency, 3.0/3.5 Hz

(d) 5.0 Hz Gust frequency

(e) 8.0 Hz Gust frequency

Figure 2.23: Relative peak load reduction respect to locked hinge condition for all gusts and plates, for $\alpha = 0°$ [17].

Instead, it Figure 2.24 the Root Mean Square (RMS) of the signals is displayed for $\alpha = 5°$, and it is used to study the impact of the release on the wingtip oscillation. Looking at the figure, three main considerations can be made. Firstly, at the 1st bending natural, 0.5Hz, 1.5Hz, 5Hz, and 8Hz gust frequency, the differences between the wings can be detected. Indeed, the lowest RMS reduction is experienced by wing A while the highest by wing B; both the tailored wings achieve higher RMS reduction with respect to wing B. Secondly, the natural frequency excitation impacts the RMS response. Indeed the corresponding RMS reduction at the pre-released condition is lower with respect to the 0% threshold case. Finally, the RMS for the 50% and 100% threshold cases is higher with respect to the locked hinge condition.

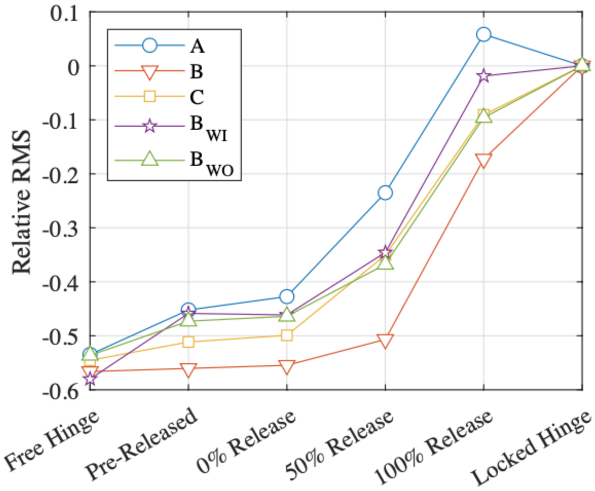

(a) 0.5 Hz Gust frequency

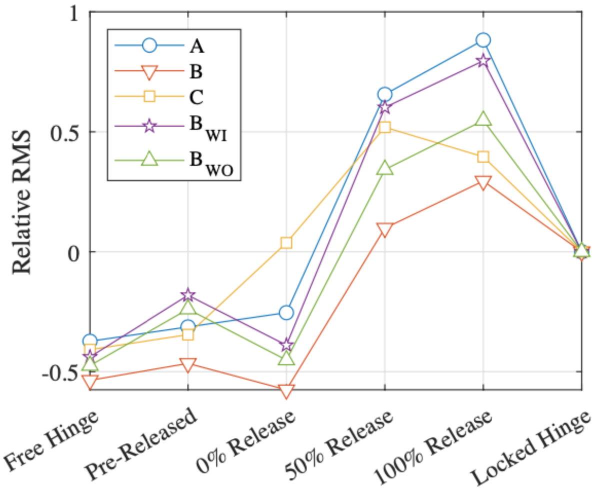

(b) 1st Bending natural frequency, 1.5 Hz

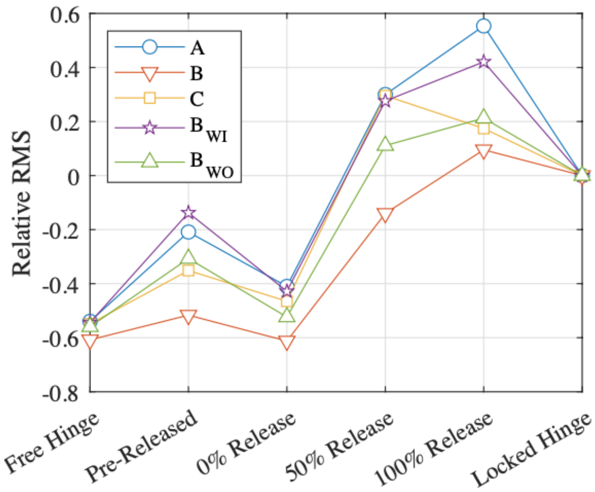

(c) 1st flapping natural frequency, 3.0/3.5 Hz

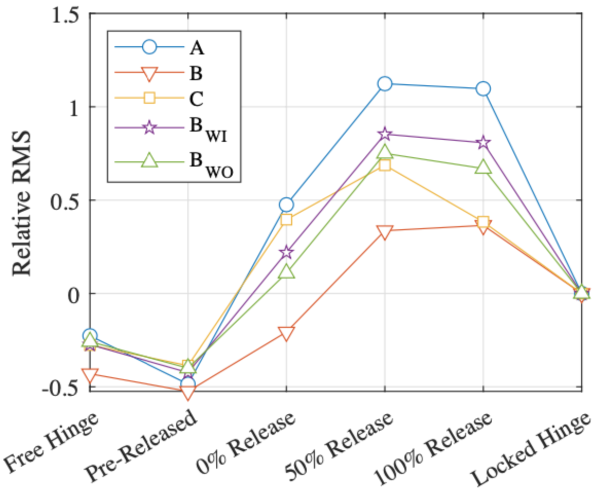

(d) 5.0 Hz Gust frequency

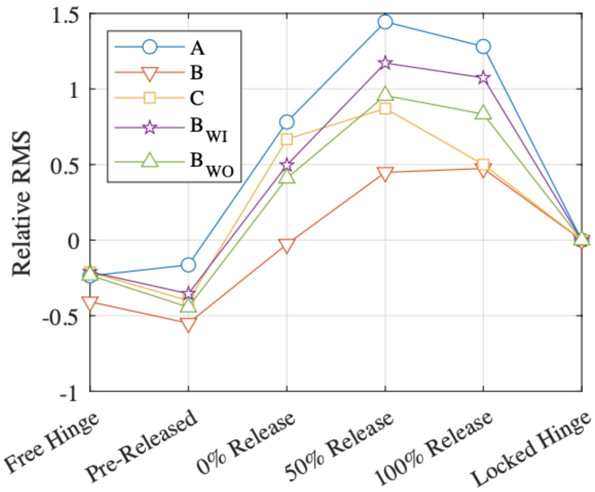

(e) 8.0 Hz Gust frequency

Figure 2.24: Relative root mean square reduction respect to locked hinge condition for all gusts and plates, for α = 0° [17].

It can be concluded that there is no connection between peak load alleviation and plate stiffness. The only influent parameter is the hinge release time; indeed, the hinge has to be released when the gust is detected to have the best

GLA performances. If the hinge is released with a time delay, the peak load will be higher than the locked-hinge conditions and oscillations are introduced that persist for quite some time also after the gust disappears. This can cause fatigue issues on the wing and winglet structure.

2.5 PARTICLE IMAGE VELOCIMETRY

Particle Image Velocimetry (PIV) is the state-of-the-art technique for flow visualisation. Indeed, it is a whole field, non-intrusive method that, with modern development, can be used to study the 3D flow around an object during a wind tunnel experiment.

2.5.1 WORKING PRINCIPLE

The Particle Image Velocimetry (PIV) technique is based on the displacement measurements of small tracer particles added to the wind tunnel flow and transported without altering their behaviour. These tiny particles are illuminated homogeneously by a short, thin light sheet usually generated by a pulsed laser system and shaped by lenses/mirrors. Then, an imaging optics, usually a Charge-Coupled Device (CCD) camera placed normal to the measurement plane and connected to a computer, will record the light scattered by the illuminated particles at two successive instants in time, t and $t + \Delta t$ (from two consecutive light pulses). The typical planar (2D) setup is illustrated in Figure 2.25.

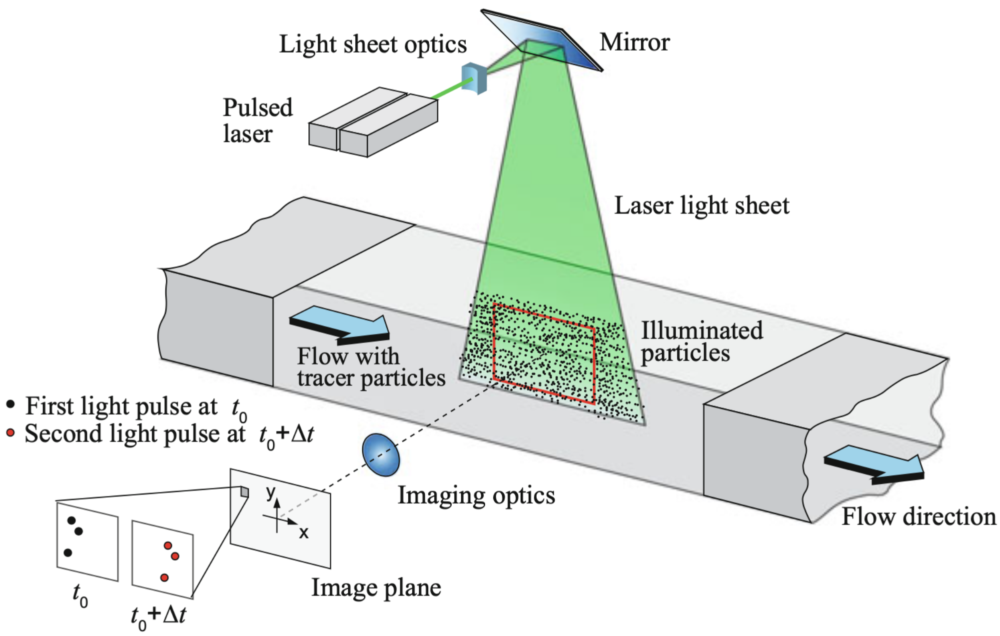

Figure 2.25: Planar 2-dimensional (2D) particle image velocimetry typical setup [19].

To evaluate the motion of the tracer particles, the images are divided into smaller domains called interrogation windows (that contain at least 10 tracer particles [51]). Using the windows of two successive exposures, using Equation 2.6 [51], the statistical analysis process called cross-correlation is performed, used to find the degree of matching of the particles in the two interrogation windows, which returns a map whose peaks show the average displacement of the tracers.

$$\phi(m,n) = \frac{\sum_{i,j=1}^{I,J} I(i,j) \cdot I'(i+m,j+n)}{\sqrt{\mathrm{stdev}(I) \cdot \mathrm{stdev}(I')}} \tag{2.6}$$

The highest peak will be selected due to the tracer particles' mean motion, while the others are discarded since they formed just from noise or the non-paired particle correlation. To have sub-pixel accuracy of the position of this highest peak, a Gaussian fit interpolation scheme is usually used, applying Equation 2.7 [51] that uses Equation 2.8 [51] and Equation 2.8 [51].

$$f(x) = \phi_0 \cdot e^{-\frac{(x-x_0)^2}{\sigma^2}} \tag{2.7}$$

$$x_0 = i + \frac{\ln\phi(i-1,j) - \ln\phi(i+1,j)}{2\ln\phi(i-1,j) - 4\ln\phi(i,j) + 2\ln\phi(i+1,j)} \tag{2.8}$$

$$y_0 = j + \frac{\ln\phi(i,j-1) - \ln\phi(i,j+1)}{2\ln\phi(i,j-1) - 4\ln\phi(i,j) + 2\ln\phi(i,j+1)} \tag{2.9}$$

The peaks coordinates calculated (Δx and Δy) are then divided by the product of the Magnification Factor (M) (that is, the ratio between sensor size and object size) and the time interval (Δt) between the two light pulses to derive the horizontal and vertical components of the instantaneous velocity, using Equation 2.10 [20] and Equation 2.11 [20].

$$u(x,y) = \frac{\Delta x}{M \cdot \Delta t} \tag{2.10}$$

$$v(x,y) = \frac{\Delta y}{M \cdot \Delta t} \tag{2.11}$$

The planar instantaneous velocity field can be visualised during this process and repeated for all the interrogation windows.

2.5.2 Development Steps

In recent years, the state-of-the-art technique for flow visualisation techniques for instantaneous velocity field measurements during wind tunnel experiments has become Particle Image Velocimetry (PIV). This is due to the non-intrusiveness (no probe needs to be inserted in the flow, it only requires optical access for both the laser and the camera) and also because it is a whole-field quantitative method (with a big spatial resolution). Instead, the only drawbacks are the complex setup, the low temporal resolution and the fact that it is an indirect measurement system (the flow velocity is obtained by measuring the tracer particle's velocity).

The setup shown in Figure 2.25 is for the conventional planar PIV (2D2C) that uses only one digital camera to record the light scattered by the moving tracer particles. This permits the record of only the two velocity components of the velocity vector projection into the plane of the light sheet (in-plane), of the tracer particles, in a 2D domain, missing all the information on the out-of-plane velocity components and the out-of-plane velocity gradient.

To overcome this limitation, the Stereoscopic PIV method (2D3C) was introduced by Arrayo et al. [52] using two digital cameras (both with a different view angle, usually 90° to allow the same measurement uncertainty for all velocity components), visible in Figure 2.26. These will record simultaneous but distinct off-axis views of the same region of interest, resulting in the also obtain of the out-of-plane velocity component (relying on the perspective distortion of a displacement vector viewed from different directions [19]), also permitting to eliminate the prospective errors. The method used to determine the out-of-plane velocity component is based on reconstructing the 3D displacement field from the two projected planar displacement fields.

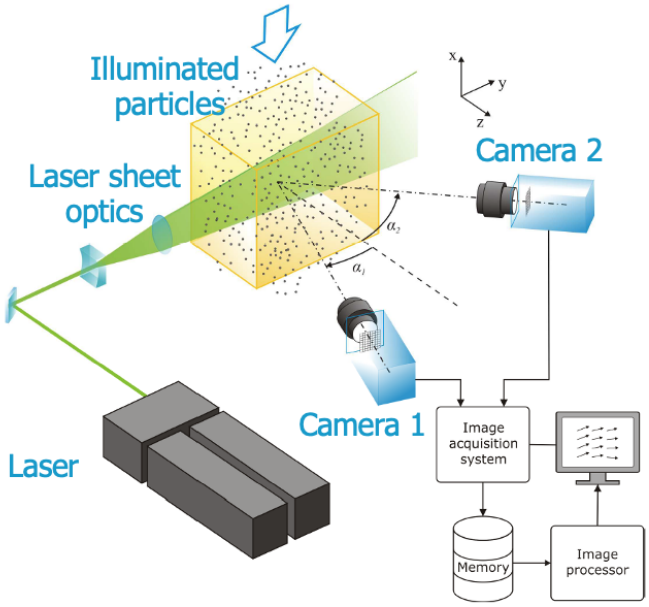

Figure 2.26: Stereoscopic particle image velocimetry typical setup [20].

2.5.3 Tomographic Particle Image Velocimetry

The state-of-the-art technique that allow the complete characterisation of the velocity field ($u(x, y, z)$, $v(x, y, z)$, $w(x, y, z)$) in three dimensions (3D3C) was achieved using tomographic Particle Image Velocimetry technique, introduced by Elsinga et al. [21], visible in Figure 2.27. This allows instantaneous flow field measurements combining the simple optical arrangement of 3D Particle Tracking Velocimetry (PTV) with the volume reconstruction method that is not based on particle identification. To achieve this, an additional camera, in a non-collinear view, was added (now three at least are present) that help to model the measurement domain as a 3D volume regardless of the flow velocity. Lasers are the most used light source methods for tomographic PIV since their beam is collimated (electromagnetic radiation with parallel rays) and has high energy and short duration. Consequently, the tracer particle density is higher than 3D PTV, reaching values of 0.05 particles per pixels [21] (for a four-camera setup), allowing more velocity vectors to be present in the other 3D PIV techniques.

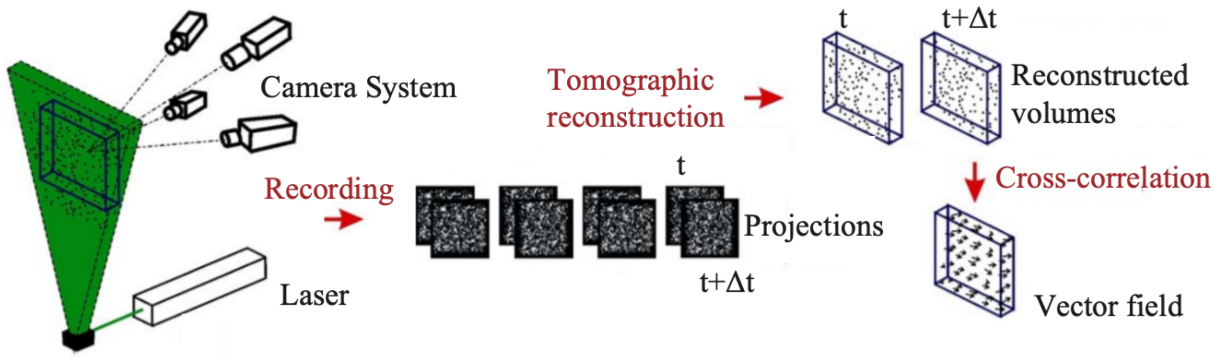

Figure 2.27: Tomographic particle image velocimetry typical setup and working principle [21].

A calibration procedure is needed to find a relation between the projection coordinates and the physical space. It is done by recording a calibration target (usually a planar plate with a grid of markers that are detectable easily when the images are processed) at different viewing directions for each camera, resulting in the field of view and the viewing direction. Indeed, the reconstruction technique is based on the triangulation of the camera's views; an accuracy of a fraction of the particle size is necessary for a correct particle reconstruction.

To 3D reconstruct the instantaneous velocity field of the particles (from the displacement of the recorded particles), an algebraic tomographic 3D cross-correlation algorithm is used on interrogation volumes at two different exposures in short successions, with an iterative multigrid volume (window) deformation technique, called Multiplicative Algebraic Reconstruction Technique (MART) that was introduced by Herman et al. [53]. This is an inverse problem where the solution is underdetermined, meaning that different reconstruction results can be obtained from a single set of projections. It requires that the line of sight of all the cameras intersect precisely to avoid distortions. It is based on the mapping function (M) between the image planes $p_i' = (x, y)$ and the 3D physical space $P(X, Y, Z)$ that contains the object (particle distribution), represented in Equation 2.12 [19].

$$\left(x_i, y_i\right) = M_i(X, Y, Z) \tag{2.12}$$

An array of voxels (3D pixels considered that have a non-zero value inside and zero outside) that discretise the physical space with coordinates (X, Y, Z) and intensity $E(X, Y, Z)$ is used as a mathematical representation of the intensity distribution, as visible in Figure 2.28.

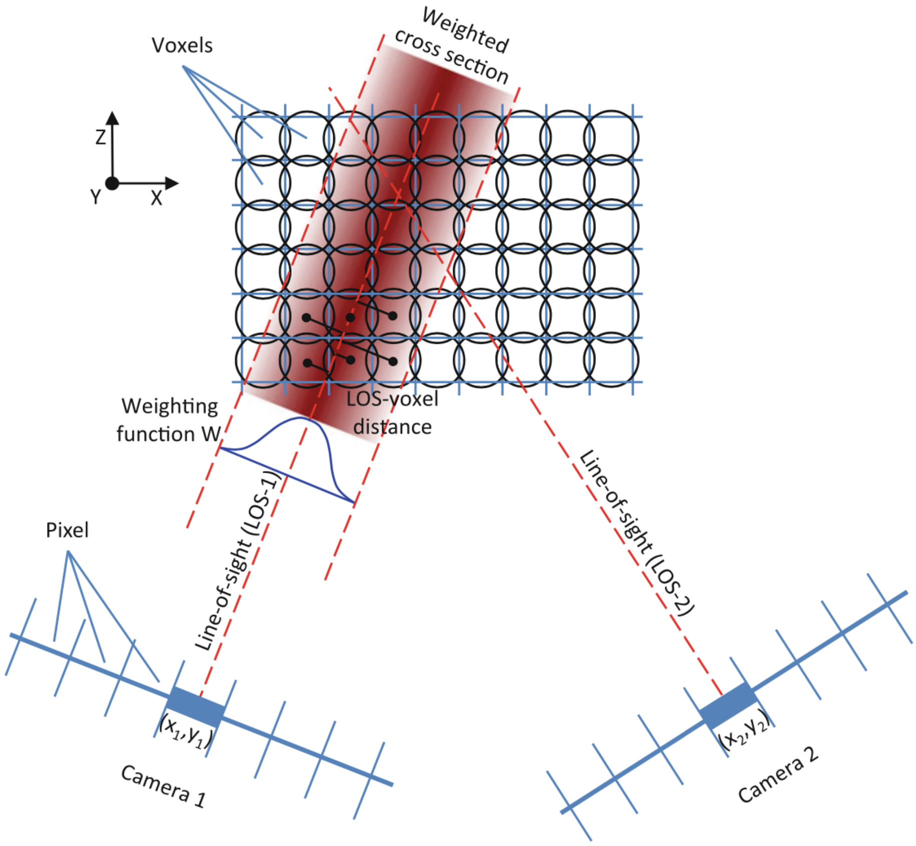

Figure 2.28: Object discretisation in voxels and imaging used for the reconstruction [22].

The reconstruction quality depends on the number of independent camera views N_C, the particle tracers' concentration and diameter, and the angular aperture. The spatial resolution depends on the concentration of tracers. Typically for accurate and robust reconstructed results, it has to be between 5 and 10 for each Interrogation Box (IB), resulting in a Source Density (NS) (fraction of image occupied by particles) lower than 0.5 [19]. Increasing the concentration will decrease the image contrast caused by optical transmission loss in the seeded medium. The optimum source density is calculated with Equation 2.13 [19], where PPV = $\frac{C}{D_R^3}$ is number of particle per voxel (with C is the particle concentration), W the width of the measurement volume (V_M), $D_R = \frac{M}{\Delta_{\text{pix}}}$ the digital image resolution (with Δ_{pix} the pixel pitch) and d_τ^* is the particle image diameter normalized by the pixel size.

$$N_S = PPV \cdot W \cdot D_R \cdot \frac{\pi}{4} \cdot d_\tau^{*2} \tag{2.13}$$

Using an excessive tracer concentration leads to loss of image contrast and accuracy. The drawback of this technique is that the obtained Field Of View (FOV) (the maximum area of a sample that a camera can image) was pretty small due to the small F-stop ($f_\#$) (ratio of the camera focal length to the diameter of the aperture). This was required by the tiny camera lens aperture but also due to the energy density of the light that is inversely proportional to the light beam thickness. Indeed, the light intensity is also reduced because the illumination system is now used to illuminate a volume region and not a plane anymore. This issue is overcome using mirrors for a multiple-pass system in combination with a beam expander (that expands the light to the required measurement volume), visible in Figure 2.29, and knife-edge filters to cut the light externally of the measurement volume. It resulted in a light amplification gain factor of 7 times compared with the single-pass systems [23].

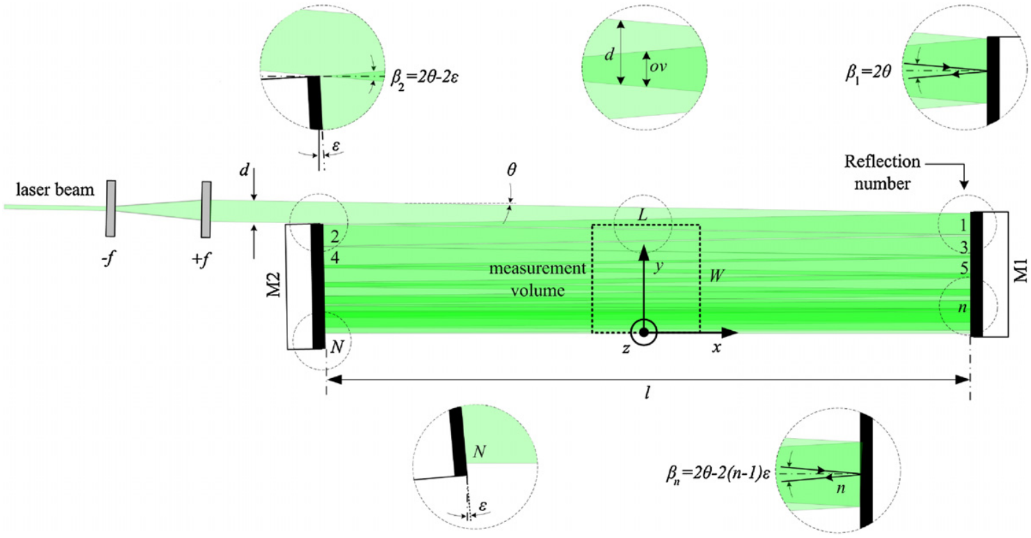

Figure 2.29: Multi-pass light amplification system [23].

Schneiders et al. [24] introduced a new and different approach that combines Coaxial Volumetric Velocimetry (CVV) with a robot arm to perform time-averaged large-scale measurements around complex objects. The CVV PIV is integrated into a single module composed of a multi-camera system (typically four) that subtends an aperture angle by just a few degrees and an extended focal depth, as visible in Figure 2.30. The laser light is in the camera view direction to reduce the optical access requirement (requiring the optical access only from one measurement direction) of the system and expanded to illuminate the entire FOV of the cameras.

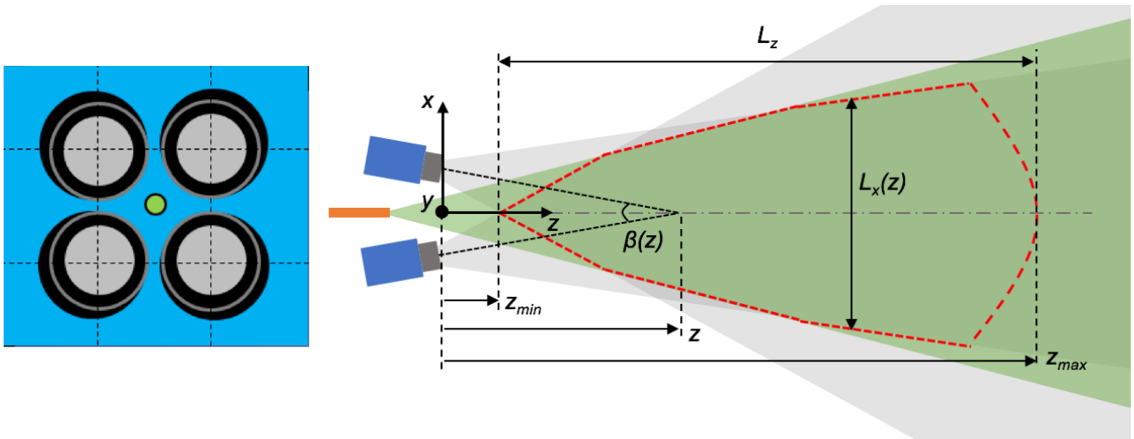

Figure 2.30: Left: Front of the coaxial volumetric velocimetry, **Right**: Side measurement setup [24].

Due to the compactness of this PIV module, the measurement volume can be expanded (up to several cubic metres) using a robotic arm to move the CVV arrangement. This was done by Jux et al. [25]. A 6 degree of freedom robotic arm was used to control the CVV probe orientation and position (as illustrated in Figure 2.31) to perform a complete aerodynamic 3D characterisation around a full-scale cyclist model (including hidden regions between the arms and the legs) to access the near-wall velocity. To perform this experiment on the 2m^3 domain, the superposition of 450 different views was necessary. Helium Filled Soap Bubbles (HFSB) were used as tracer particles, and the Lagrangian particle tracking technique Shake-The-Box (STB) was adopted. The advantage of this system is that it provides improved optical access, and calibration is no longer required after repositioning the CVV measurement probe. In contrast, the disadvantages are the low accuracy in the depth direction and the capacity only to measure the flow statistics. So, for this reason, it was decided not to use the CVV probe in this thesis experiment.

Figure 2.31: The coaxial volumetric velocimetry probe mounted on the robotic arm [25].

2.6 LARGE-SCALE PARTICLE IMAGE VELOCIMETRY

Initially, the 3D3C measurements conducted with Tomographic Particle Image Velocimetry were limited to small volumes. To increase it, several techniques were introduced in recent years, particularly the use of helium-filled soap bubbles (HFSB) tracer particles, which will be explained in this section.

2.6.1 HELIUM-FILLED SOAP BUBBLE

Since the light scattered by the tracer particles is a crucial parameter to increasing the volume measured, and since the pulse energy of the light source is not a scalable quantity. Big-size tracer particles like the Helium Filled Soap Bubbles (HFSB) were developed and introduced by Bosbach et al. [54]. Using this new technology, they were able to investigate the convective flow in an aircraft cabin of a 7m^2 volume. These tracer particles are capable of scattering light several orders of magnitude greater than with respect to conventional smaller tracers [19] (thanks to the greater scatter efficiency) but still maintaining the neutral buoyancy (balancing the soap film weight with the helium-filled bubble volume), and the mechanical properties [55]. On the other hand, to track the flow motion in a good way, the tracers should be small. For this reason, a trade-off in particle size is necessary to maintain a well-scattered light with an accurate tracking fidelity. With this technique, Schneiders et al. [56] increased the measurement domain by two orders of magnitude larger with respect to PIV using conventional tracers. A representation of the formation of these tracers is presented in Figure 2.32. This is based on regulating the air and helium pressures and the Bubble Fluid Solution (BFS) flow rate. Correct proportions are necessary to achieve the neutral buoyancy condition, essential to behave like an ideal flow tracer and result in correct PIV measurements. BFS consists of a mixture of soap, glycerine and water.

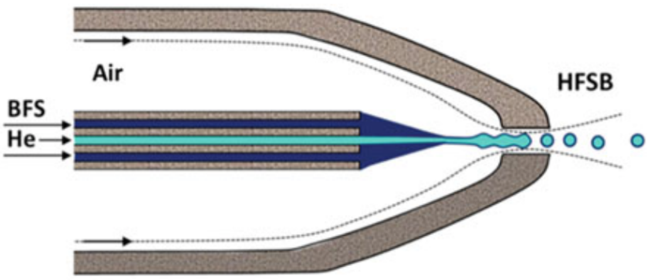

Figure 2.32: Miniaturised orifice-type generator for the helium-filled soap bubble formation [19].

The time response (time after the $1-e^{-1} = 63\%$ of the flow velocity step variation $\Delta U_{1-2} = U_1 - U_2$ [51]) change of the particle velocity of changes in flow velocity of sub-millimetre HFSB (in the range 1-5mm) is around 10μs [55] (with 10% of bubble density respect to the density of the surrounding air [57]), demonstrating the HFSB applicability for PIV wind tunnel experiments. The drawbacks of HFSB are that the bubble's lifetime is about 1/2 minutes, and the experiments are limited to low speed. Since in tomographic PIV, the spatial resolution depends on the tracer concentration, the production rate should be as high as possible, but at the same time, it is also true that also the number of ghost particles will increase. The spatial resolution can be represented with the Dynamic Spatial Range (DSR) that is expressed in terms of the particle's production rate, as Equation 2.14 [58]. Where L is the length of the field of view, N_I is the particle image number density (number of particles per interrogation volume), U is the flow velocity, A is the stream-tube of cross-section, and finally, $\dot{N} = C \cdot A \cdot U$ the bubble emitter rate, with C the number of tracers per unit of volume. Using HFSB, Scarano et al. [55] managed to reach a production rate of approximately 50000 bubbles s^{-1}.

$$DSR = L\left(\frac{\dot{N}}{N_I \cdot A \cdot U}\right)^{\frac{1}{3}} \cong \left(\frac{L \cdot \dot{N}}{N_I \cdot U}\right)^{\frac{1}{3}} \tag{2.14}$$

The HFSB particle's volume size is directly proportional to the volume flow-rates ratio of helium He and air and the orifice size, while the bubble production rate increases linearly with the flow rate of the air volume and with the inverse of the orifice diameter [57].

When these big tracer particles are used, instead of laser light, the adoption of high-power Light-Emitting Diode (LED) introduced by Willert et al. [59], was investigated as an alternative to laser-based illumination to increase the illuminated volume, reaching measurements volume of several meters square. Operating these LEDs with a short light duration can decrease the operation cost significantly and, at the same time, is less dangerous due to the un-collimated light. Furthermore, the repetition rate of the pulse can be varied freely since LEDs do not need to be operated at specific pulsing frequencies.

2.7 LAGRANGIAN PARTICLE TRACKING

Conventional tomographic PIV cross-correlation-based reconstruction techniques like MART require high memory and computational time. They are just applicable with a low particle image density (0.05 particles per pixel) since an increased density will lead to overlapping ghost particles that will decrease the accuracy of the reconstruction [19]. This is due to the individual treatment of every time instants, where the intensity distribution is represented as a 3D interrogation box. The voxels on which a cross-correlation procedure is applied to reconstruct the velocity field. Furthermore, the applied spatial average on the voxels will cause the impossibility of visualising the smallest structures, flattening the spatial gradients. For this reason, a new and superior algorithm that overcomes these problems, based on Lagrangian particle tracking, was developed, like the Shake-The-Box (STB), which employs spatial and temporal information to predict the particle's trajectory at successive time steps from the PIV recorded images. Moreover, correct the found tracer positions' shaking' the tracked particles inside the measurement box, leading to a robust particle tracking algorithm usable for high-density tracer particle images that also discards a good amount of ghost particles.

2.7.1 SHAKE-THE-BOX

To solve the drawbacks of the MART technique, a new and more efficient algorithm called Shake-The-Box (STB) was introduced by Schanz et al. [26] that actuates the particle tracking on time-resolved tomographic data using advanced triangulations. Differently from MART, where the measurements of each time instant are considered independently, this algorithm treats both spatial and temporal information. Indeed, knowing the particle position at the time instant t_n, STB allow predicting the positions in the measurement volume of the tracer particles on subsequent time instants t_{n+1} using the temporal information directly in the reconstruction process, leading to results valid also for large measurement volume with high-concentration of seeding particles (around 0.1 ppp), above the thresholds for tomographic PIV. Without ghost particles, this avoids spatial filtering and smoothing of the velocity gradients and ensures fast and accurate particle positions. Schanz et al. [60] to develop this algorithm assumed that knowing the particle's trajectory will permit to have the 3D position of the tracer particles in the following time steps and that the tracer particle cannot disappear in the interrogation volumes between time steps (actuating a suppression of ghost particles due to their shorter lifetime compared to real tracer particles).

This algorithm can be divided into three main steps [60]. The initialisation is the first one, applied to the first four time-steps, where the particle tracks information are not available. The identification of the tracer particle positions in the first images is done with the volumetric Iterative Particle Reconstruction (IPR) distribution method [61], using the calibrated Optical Transfer Function (OTF). A search radius is defined and applied to each reconstructed particle to find a possible match in the next time steps. Subsequently, a second-order polynomial is fit in the last four positions of the tracked particle to validate the tracer tracks found.

Then, after the initial time step, where the particles are tracked correctly, the convergence phase follows where the tracer particles' temporary' positions at successive time step t_{n+1} are predicted along all found tracks evaluating the fitted polynomial and determining the Wiener filter coefficients [62]. The reconstruction process also goes back in time to previous time steps to increase the accuracy of the result. This predicted particle intensity and 3D position (usually off by a fraction of pixels) are shifted to the correct position with an iterative image shake matching scheme techniques (that cover larger accelerations of the spars particles distribution in 3D space) until a position that minimises the local Image Residual (IR) for all camera projections, eliminating the prediction error.

When all particles are tracked, convergence is reached, and the converged phase begins, where many tracers are already tracked. In this phase, the particles entering the measurement volume are searched (using triangulation on the residual images), and particles that leave the interrogation volume are ended together with the ones that have an intensity below a set threshold value, which are assumed to be lost. Some tracks are also ended thanks to an outlier detector applied. Then, all the particles are shaken again until convergence is reached. This process is repeated for all the time steps of the entire time domain, with the system pre-solved after each prediction step. The procedure for one time-step in the converged state and the computation step effects on the residual image (for just one camera) are illustrated in Figure 2.33.

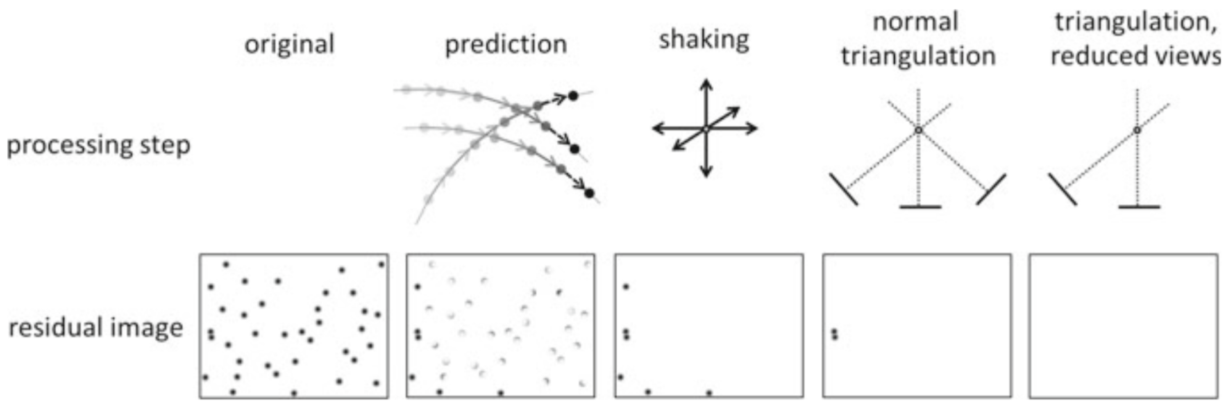

Figure 2.33: Shake-the-box processing step and residual image [19].

Afterwards, knowing the temporal sequence of location (estimated) for each tracked tracer particle, a smoothing fitting method called TrackFit [19] is used to reduce the noise in the measurements. This is based on a cubic B-spline function computed from the positions of the particles taking the noise into account. Assuming that the position errors are not correlated between different time steps, leading to an estimate of the Standard Deviation (STD) of the position, velocity and acceleration errors. Since the velocity and acceleration of the particles are known just at the position of a specific time interval, spatial interpolation is actuated to have a spatially continuous representation (at any point) of the velocity and acceleration of the particles. This is done with the FlowFit [19] method, which represents the velocity field as a superposition of evenly spaced 3D base B-spline function, avoiding any spatial smoothing.

The application of the STB algorithm on a time-resolved high-resolution dataset obtained experimentally proved a robust and reliable tracking of the most tracers particle for the whole length of stay inside the measurement volume. Achieving results more accurately than the ones obtained with other 3D cross-correlation algorithms [60], reaching tracer particle image densities up to 0.2 ppp, without ghost particles. Since the STB data size needed is smaller than the voxel-based algorithms, it results in low computational cost and faster computational time between 3 to 20 times.

As visible in Figure 2.34, which represents the reconstructed velocity field of a jet for conventional voxel-based tomographic PIV algorithm and the new STB algorithm, the latter method outcomes in a more accurate result with also the smaller flow structure reconstructed. This is due to the avoidance of spatial filtering and the smoothing of the velocity gradients, the ghost particles removal and better position accuracy.

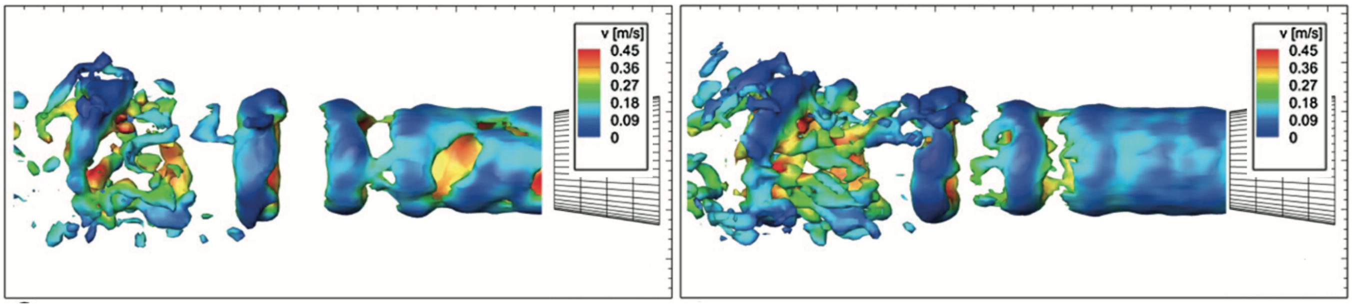

Figure 2.34: Velocity comparison between conventional tomographic particle image velocimetry tracking algorithm (Left) and shake-the-box algorithm (Right) [26].

2.8 Structural Characterisation

Particle Image Velocimetry (PIV) can not just be used to identify the aerodynamic behaviour and forces of the studied model but can also be used to conduct aeroelastic structural characterisation of the body. Indeed, recently it was shown that the structural dynamics behaviour and displacement could be found tracking a grid of small circular fiducial markers painted on the model. This will help to replace intrusive point-wise techniques like strain gauges and accelerometers.

2.8.1 Fiducial Markers Tracking

Nowadays, the structural characterisation of a model (position, displacement, deformation, deflection and strain) is usually performed by whole field optical non-intrusive technique like Digital Image Correlation (DIC) introduced by Pan [63] or photogrammetric point tracking reviewed by Baqersad et al. [64] that replace the need of intrusive techniques like strain gauges and accelerometers. DIC has a high spatial resolution of the structural displacement and deformation measurements with the downside of a dense pattern needed on the surface. Instead, photogrammetric point tracking is more suitable for large-scale studies where such high measurement density is not needed since it only gives information where the cameras are pointing, resulting in a reduced time for the model preparation. So firstly, the combination of 2D PIV and 3D DIC was performed to have both aerodynamics and structure deformation, as done by Timpe et al. [65] where the wing displacement on tiny wing regions was recorded with planar (2C2D) flow-field measurements, Bleischwitz et al. [66] instead extended the DIC measurement on the full-span wing. To record all the three velocity components on an airfoil, Marimon Giovannetti et al. [27] added an extra camera to Take stereoscopic PIV measurements, as visible in Figure 2.35.

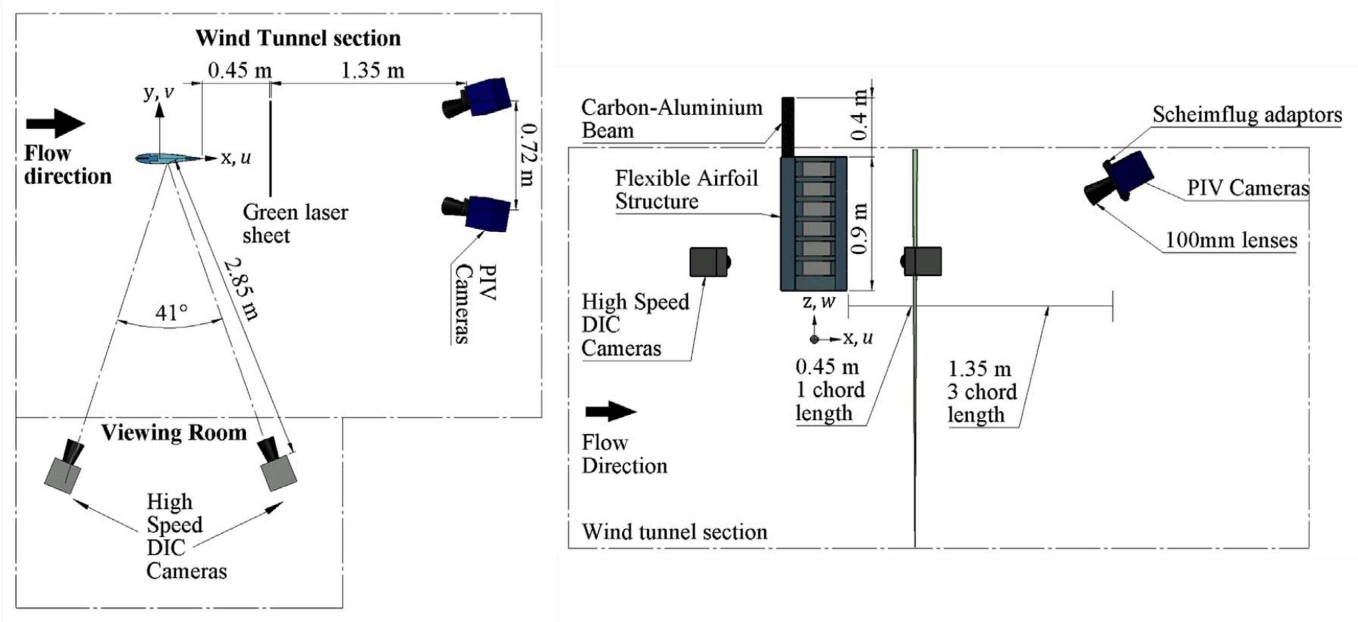

Figure 2.35: Plan view and side view of the digital image correlation and particle image velocimetry setup [27].

Recently, studies focused on using just a single measurement system to perform both measurements. Indeed, a new PIV technique was introduced where a grid of fiducial markers is painted in the tested model and tracked using the STB algorithm that allows the simultaneous aerodynamic and structural characterisation of a highly flexible and moving object (tracking simultaneously also the HFSB flow tracer). This has the disadvantage of only providing information at the location of these fiducial markers, resulting in lower information results densities than DIC.

This approach was first used by Mitrotta et al. [28], where a Robotic Volumetric PIV approach was used to track the aerodynamic and the structural response simultaneously to a Fluid-Structure Interaction (FSI) problem composed of a large-scale flexible plate hit by a periodic gust. The displacements of the fiducial markers from the images recorded for the flow-field characterisation were verified and compared with the displacement calculated from the laser Doppler scanning vibrometer technique. To separate the flow and structure information from the recorded images and obtain images with only structural markers, a low-pass filter is used, assuming that the structural fiducial markers move slower with respect to the flow tracer particles. To calculate the displacement of the markers, the LPT STB algorithm [26] [60] was applied to the structure images, also using the volume self-calibration procedure [67] and an Optical Transfer Function (OTF) [68]. At each time instant of the wanted phases, the marker displacements are interpolated, and the displacements of the same phase are averaged. As visible in Figure 2.36, the PIV technique gives results accurate and in line with the ones calculated with Scanning Vibrometer (SV), having a bias error of just $\epsilon_b = -0.258$mm and a random error of $\epsilon_r = 0.718$mm, demonstrating the ability of PIV to characterise both the aerodynamic and structural behaviour of an aeroelastic FSI problem.

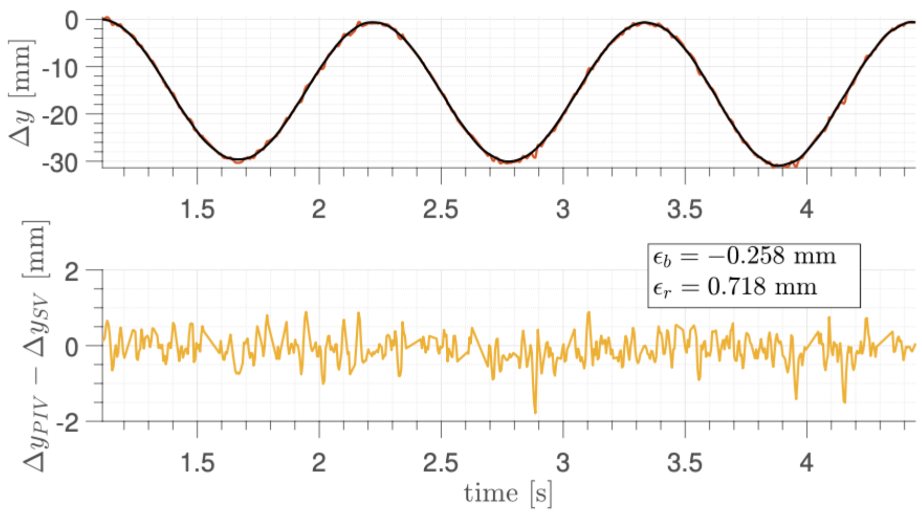

Figure 2.36: Structural displacement and error comparison between particle image velocimetry and scanning vibrometer techniques [28].

This simultaneous measurements PIV technique that involves the tracking of fiducial markers painted on the model surface was also used by Mertens et al. [29] to visualise the structural position in space and the unsteady flow-field of a pitching airfoil with an actuated flap giving very reliable results. The fiducial marker tracking data fitted a rigid body model to calculate the model's unsteady position and flap deflection. This takes into account the motion degrees of freedom of the model. Again, after the filtering procedure on the recorded images, the Lagrangian particle tracking STB algorithm is used for image processing, considering the fiducial markers painted on the airfoil surface. A rotation matrix $\vec{R} = \vec{R}_z(\Psi) \cdot \vec{R}_y(\Theta) \cdot \vec{R}_x(\varphi)$ (given in Equation 2.15 [29]), is applied to perform a coordinate transformation of the measured fiducial marker positions obtained in the laboratory reference frame (X, Y, Z) to the airfoil reference frame (Ψ, Θ, φ) around the x, y, z axis.

$$\vec{R} = \begin{bmatrix} \cos\Psi & -\sin\Psi & 0 \\ \sin\Psi & \cos\Psi & 0 \\ 0 & 0 & 1 \end{bmatrix} \cdot \begin{bmatrix} \cos\Theta & 0 & \sin\Theta \\ 0 & 1 & 0 \\ -\sin\Theta & 0 & \cos\Theta \end{bmatrix} \cdot \begin{bmatrix} 1 & 0 & 0 \\ 0 & \cos\varphi & -\sin\varphi \\ 0 & \sin\varphi & \cos\varphi \end{bmatrix} \tag{2.15}$$

The outliers (caused by reflection) were eliminated using a threshold for the spatial distance between two near fiducial markers. Then, the position in the space of the airfoil was found by fitting the fiducial marker position measured on the static airfoil to reference the marker grid painted on the airfoil, as illustrated in Figure 2.37.

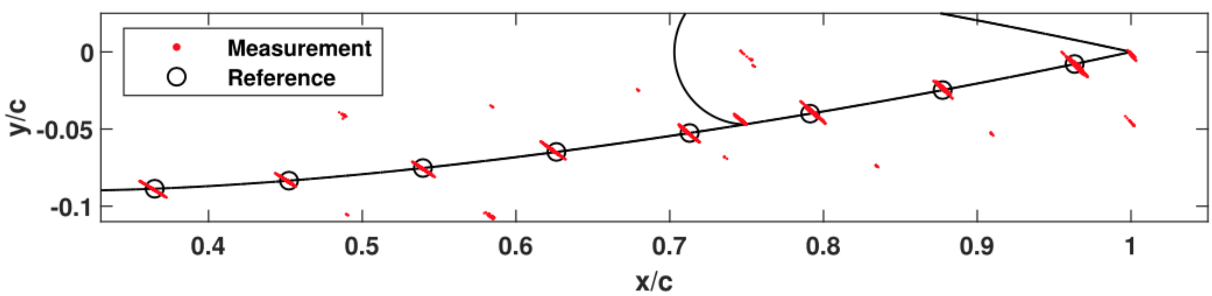

Figure 2.37: Fitting procedure of measurements fiducial markers with reference marker grid [29].

In Figure 2.38, the results obtained with the fiducial markers PIV technique are compared to the reference data. For the angle of attack, the pitching motion imposed by the pitching mechanism is set as a reference. While for the flap deflection, the reference is the control signal value received by the servomotor (the mechanism) that actuates the flap. The results obtained agree very well with the reference ones, with a Root Mean Square (RMS) of the difference of just 0.03° for the angle of attack and 0.44° for the flap deflection. This higher RMS is present due to random noise generated by the flap actuator servo motor operating at its power limit (while the Alternating Current (AC) motor of the pitching mechanism operates at lower power).

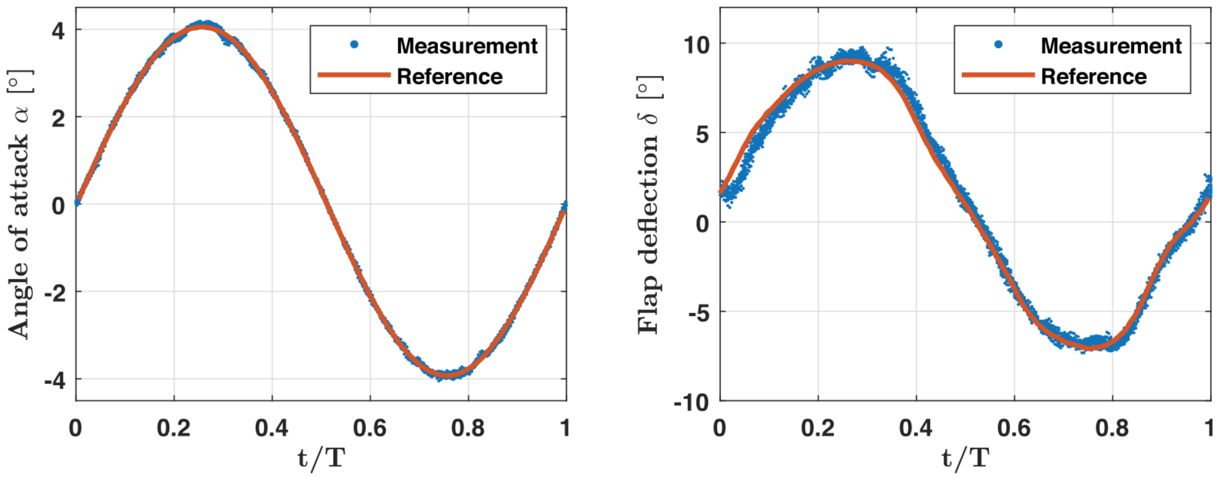

Figure 2.38: Angle of attack and flap deflection position determination comparison between particle image velocimetry measurements and reference data [29].

Overall it is possible to state that this technique is suitable for the structural study of an object that deforms under applied loads if this deformation can be characterised only by a few degrees of freedom; like in the Mertens et al. [29] study where the airfoil/flap motion was based only on two degrees of freedom (Ψ and δ).

In the Mertens et al. [30] successive study, the determinations of the three force components in the Collar's triangle (aerodynamic, elastic and inertial) Figure 2.1, fully characterising the response of a flexible wing was achieved with this integrated simultaneous technique using just a CVV probe mounted on a robotic arm for both steady and unsteady conditions. Attaching a rectangular grid of white circular markers on the wing, both the aerodynamics and structural images dataset were post-processed with the STB algorithm, resulting in an agreement between the deflection calculated from the Finite Element (FE) model and the PTV measurement, with an RMS value of just 0.1mm, as shown in Figure 2.39.

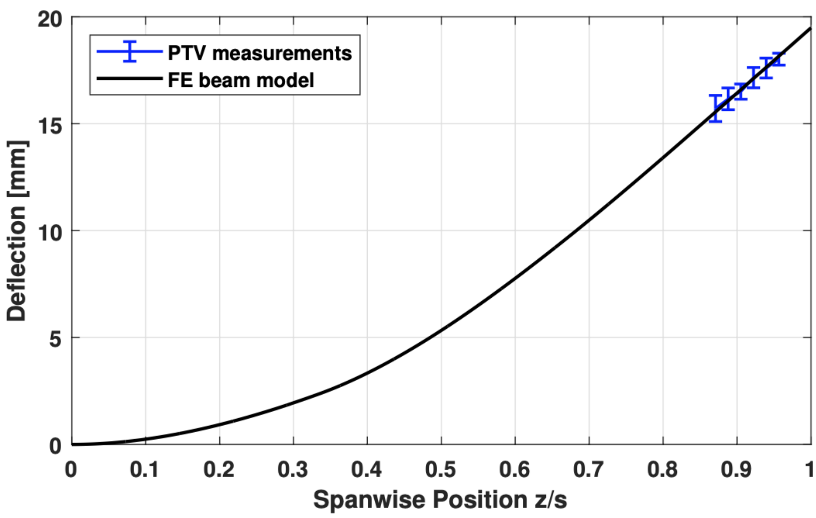

Figure 2.39: Deflection comparison between finite element beam model and static particle tracking velocimetry measurements [30].

In both the studies reported above ([29], and [30]), the PIV system used a CVV probe mounted on a robotic arm, resulting in applications limited to periodic or repeatable phenomena. This can be overcome using a fixed multi-camera PIV system that simultaneously records the flow field in the entire measurement volume. This was achieved with another study by Mertens et al. [31], performing an aeroelastic characterisation of a highly flexible wing in steady and unsteady conditions using three high-speed cameras. The fiducial markers painted in the wing are used to transform the coordinate measurement system in the wind tunnel coordinate system and to calculate the wing's deformation, validated with a Finite Element Method (FEM) model. After separating the structural and flow information from the recorded images, as illustrated in Figure 2.40, the STB algorithm is applied, resulting in the position, velocity and acceleration of each tracer particle in time for both the structural markers and the flow tracers.

Figure 2.40: Left: Both flow and structure markers, **Center**: Just flow markers, **Right**: Just structure markers [31].

After the coordinate system is transformed to the wind tunnel one, the fiducial marker position is used to compute the deformation of the wing, averaging each position of the markers and using a fourth-order polynomial curve fit through all of them. With the coefficients calculated through an optimisation process, displayed in Equation 2.16 [31], the phase averaged characterisation of the entire wing deformation is shown. This curve fitting technique was applied after a phase-averaged was performed for the unsteady flow case. Indeed different time periods measurements $T = 1/f_g$ are averaged at the respective same time as a fraction of the period t/T [31].

$$d(z) = Az^4 + Bz^3 + Cz^2 \tag{2.16}$$

The results of the polynomial curve fit to the fiducial marker measurements for each span-wise section are given in Figure 2.41.

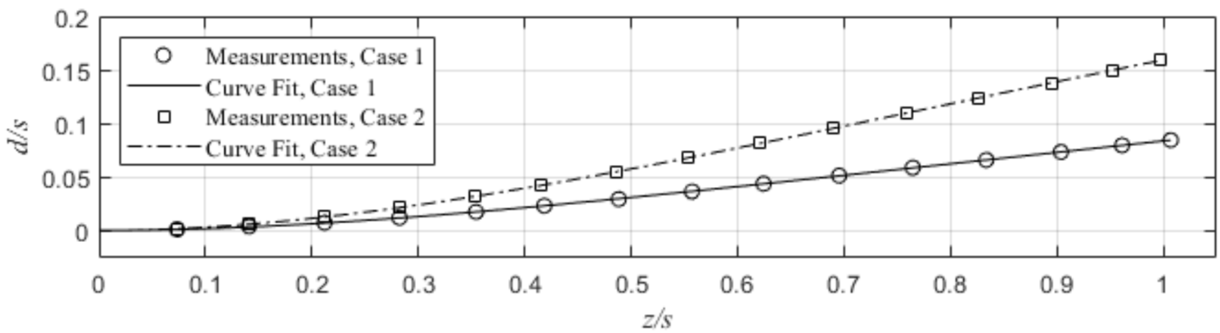

Figure 2.41: Polynomial curve fit chordwise-averaged displacement measurements [31].

To structurally characterise the deformed wing, the wing twist angle ε is calculated using the average displacement of the two fiducial markers at the Leading Edge (LE) and the Trailing Edge (TE), with the formula Equation 2.17 [31], assuming that the wing is not twisting due to deformation.

$$\varepsilon = \tan^{-1}\left(\frac{y_{TE} - y_{LE}}{x_{TE} - x_{LE}}\right) \tag{2.17}$$

The final reconstructed wing shape and marker measurements are illustrated in Figure 2.42.

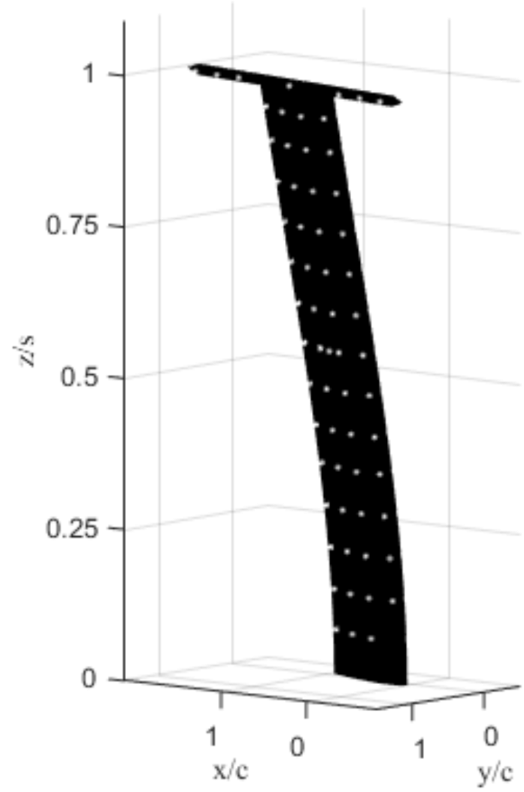

Figure 2.42: Reconstructed deformed wing [31].

The same approach was used by Mertens et al. [69] in a successive study on the same wing model for the gridless determination of aerodynamic loads.

2.9 Research Objective and Research Questions

From the review of state-of-the-art literature, it can be concluded that the results obtained from the Hinged Folding Wingtip capabilities are not always in line with each other. For this reason, a complete aeroelastic characterisation (both aerodynamic and structural) of this model, which was never investigated before, is needed to accurately understand this device's behaviour, eventually contributing to improving more sustainable aviation. This type of study was never performed mainly due to the model's small dimensions that cannot provide enough space to place all the sensors needed for the structural measurements. So, an alternative method to study the Fluid-Structure Interaction (FSI) has to be used. For this reason, the instantaneous large-scale tomographic Particle Image Velocimetry (PIV) flow measurement technique was chosen. Indeed, the need for a whole field, non-intrusive and precise method that can track in a holistic way both together the aerodynamic and structural properties of the hinged folding wingtip is identified as a gap in the scientific and academic knowledge. For this reason, this thesis will focus on this gap and try to 'fill' it. To close this knowledge gap and contribute, at the same time to improving this aviation industry problem, the following research objective of this thesis work is defined.

> **Research Objective**
>
> Study the aerodynamic and structural behaviour of a hinged folding wingtip in both steady and unsteady conditions by means of an instantaneous large-scale particle image velocimetry wind tunnel experiment.

Four sub-objectives are identified from the main objective already stated to simplify the problem into more straightforward tasks.

OB1 Establish, set-up and calibrate the experiment measurement equipment.

OB2 Acquire instantaneous 3D measurement of the aeroelastic model.

OB3 Analyse the flow field around the wingtip.

OB4 Characterise the structural response of the model.

To provide steering to the research process, ensure that suitable activities are performed, and, in the end, check that the goal of the research objective has been achieved, the following research questions and subquestions are set.

Research Questions

Q.1 How does the flow behave around the hinged folding wingtip?

- Q.1.1 Can flow separation on the wingtip be observed for steady conditions?
- Q.1.2 Can flow separation on the wingtip be observed for unsteady conditions?
- Q.1.3 Can flow separation on the wing be observed for steady conditions?
- Q.1.4 Can flow separation on the wing be observed for unsteady conditions?

Q.2 What is the wing root bending moment response for the different hinge conditions of the folding wingtip?

- Q.2.1 What is the accuracy of the wing root bending moment computed using particle image velocimetry for steady conditions?
- Q.2.2 What is the accuracy of the wing root bending moment computed using particle image velocimetry for unsteady conditions?

Q.3 What is the wing structural response to the different hinge conditions of the folding wingtip?

- Q.3.1 What is the accuracy of the wing structural displacement computed using particle image velocimetry for steady conditions?
- Q.3.2 What is the accuracy of the wing structural displacement computed using particle image velocimetry for unsteady conditions?
- Q.3.3 Can this particle image velocimetry technique be a replacement for the conventional sensors for aeroelastic measurements?

3
Experimental Set-Up and Procedures

This chapter presents the experimental facility, model and set-up used for both Particle Image Velocimetry (PIV) and conventional sensors. The data acquisition system is explained with also the test matrix cases studied.

3.1 Set-Up

The set-up and components/devices used for both the Particle Image Velocimetry (PIV) and conventional sensors used during the wind tunnel experiment are illustrated in this section.

3.1.1 Facility

The wind-tunnel campaign is conducted in the W-tunnel at the Aerodynamic department of the Aerospace Engineering faculty of the Delft University of Technology, visible in Figure 3.1. This wind tunnel is an open-loop, open jet wind tunnel with a square exit, including an interchangeable contraction. For this test, a 0.4m x 0.4m was selected since it is the only one that permits the installation of the used gust generator. The test was performed by setting the revolutions per minute of the centrifugal fan to 10000, corresponding to a flow velocity of $10\,\mathrm{m\,s^{-1}}$ with a turbulence level of around 0.5% [50] (without considering the aluminium turbulence grid installed). The wind tunnel is composed in order by a plenum, a centrifugal fan, a diffuser, a settling chamber, a contraction, a nozzle and finally, the exit.

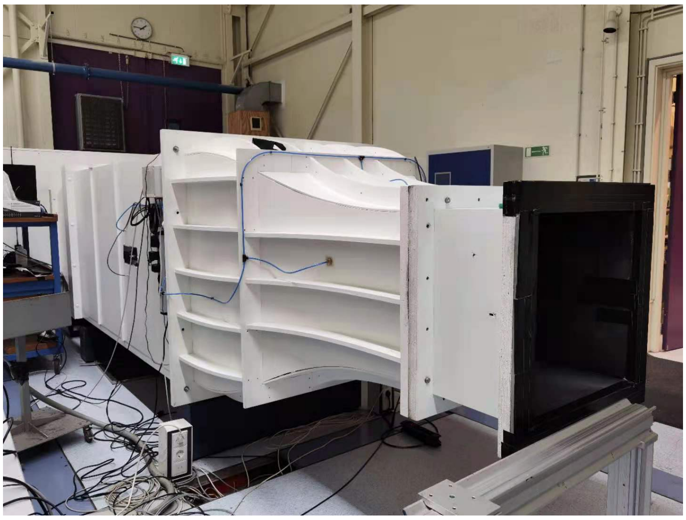

Figure 3.1: W-tunnel nozzle and exit [32].

During the Particle Image Velocimetry (PIV) experiment Helium-Filled Soap Bubbles (HFSB) trace particles are added to the flow, and an external ventilation system is used to filter the added particles out of the air, shown in Figure 3.2.

Figure 3.2: W-tunnel external ventilation system [32].

3.1.2 GUST GENERATOR

The test campaign includes both measurements in steady and unsteady conditions. For this reason, to generate unsteady inflow conditions with a cross-flow velocity component, a gust generator controlled by an external laptop was installed at the exit of the wind tunnel (as visible in Figure 3.3). It is an in-house wood-made wind-tunnel extension with an exit diameter of 0.353m x 0.4m and two aluminium wings placed vertically and controlled electrically by a motor. It can generate sine and 1-cosine gusts (the latter used during the experiment) with an amplitude between 0° and 7.5° and frequency between 0Hz and 12Hz. Due to the different exit with respect to the one from the wind tunnel, using the continuity equation (assuming constant air density ρ) $A_1 \cdot V_1 = A_2 \cdot V_2$ (where A is the exit area and V the flow velocity at 1 the wind tunnel exit and 2 the gust generator exit), it is possible to find that the flow was accelerated to $11.331\,\mathrm{m\,s^{-1}}$. However, an aluminium turbulence grid was placed before the wind tunnel nozzle to spread the Helium-Filled Soap Bubbles (HFSB) tracer particle more uniformly, which blockage caused the flow to slow down to around $9.7\,\mathrm{m\,s^{-1}}$. These values result from the ensemble average process of the free-stream measurements without the wing installed in the test section. The gust generator is connected to the Computer that controls it with a USB cable, to the SCADAS, and to the PTU x with a BNC cable.

3.1.3 MODEL

The model tested during the wind tunnel experiment is the one produced by Carrillo [18] and shown in Figure 2.17, but entirely covered with the oralight skin. It is a rectangular wing with a semi-span of 700mm including the 200mm long HFWT (with 15° flare angle), the chord is long 100mm and the airfoil is the symmetric NACA0018, the Aspect Ratio (AR) is 14 (on full wing span).

The composite plate (that acts as a spar and is designed to carry all the loads in the Pazy wing concept) tested during the wind tunnel experiment was decided to be the type C (the particular balanced laminate stacking sequence is visible in Table 2.2). Since it is the stiffest one (thicker one and with more 0° fibre orientation that improves the bending stiffness), it results in the highest experimental flutter speed (17 m/s). Allowing a wind tunnel experiment with higher velocity (without any safety problem) and Reynolds Number (Re = 6.85×10^4) that is more relevant in terms of the wanted research since this HFW has to be applied to real aircraft that experience high velocity (high Re). This choice was also dictated by the fact that the other wings are 'open' and not ready to be used since some wiring problems occurred during the previous experiment done by Carrillo et al. [17].

Furthermore, since the skin was glossy black, it was decided to spray-paint it with matt black to minimise any unwanted reflection during the PIV recordings, which decreased the accuracy of the results. To be able to track also the wing structure deformation and the fold angle variation of the wingtip, a pattern of 1.5 ± 0.2mm white circular fiducial markers were painted on the part of the wing immersed in the flow and on the entire wingtip

(35cm from the tip). This uses a laser-cut wood stencil with a pattern of holes separated by 30mm in chordwise direction and by 30mm in spanwise one, leaving a 5mm distance from the leading edge and wingtip. To have more markers on the wing (near the hinge), allowing better tracking, it was decided to half the distance of the markers in the spanwise direction, using the same stencil two times, resulting in a spacing of 15mm. The total number of markers was 24 disposed in 4 (chordwise) x 6 (spanwise) dots in the wingtip, while 36 in the wing disposed in 4 (chordwise) x 9 (spanwise) dots. The top (closer to the wing-root) spanwise row is not visible in the images acquired.

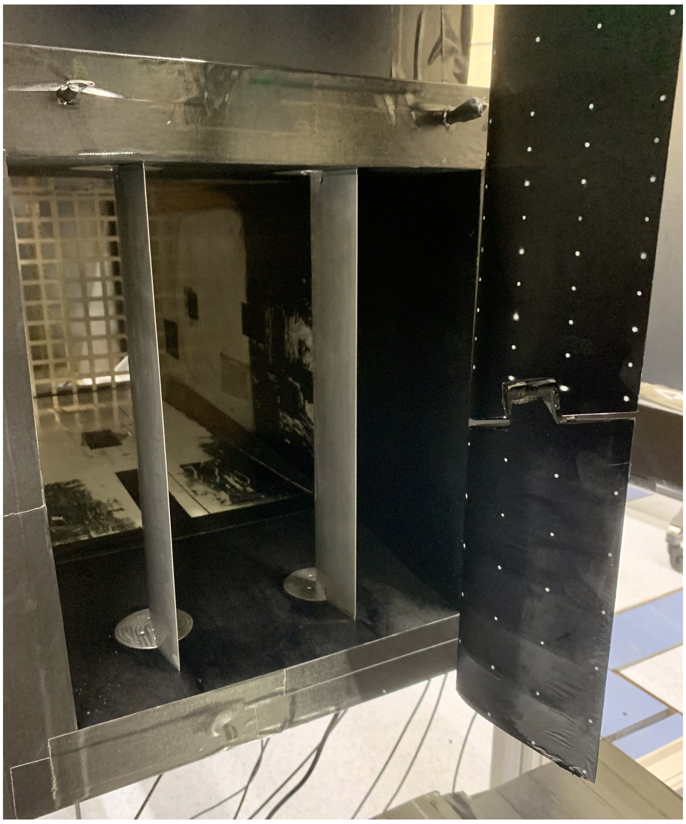

Figure 3.3: Installed turbulence grid, gust generator and wing model.

As done by Carrillo et al. [17], the wing was attached to the structure through a 3D printed spacer that includes an angular mask to measure the geometrical angle of attack. The wing is placed vertically to increase the flutter speed, avoiding the dominance of the weight force instead of the aeroelastic forces. The gust vane is placed at the exit of the W-tunnel just during the unsteady experiments, while the HFSB generator nozzle is included inside the W-tunnel (upstream of the gust vane). The wing was placed distant from the gust generator by 20cm and at a height from its bottom side of 10cm, allowing the entire wingtip to be immersed in the flow. Still, more importantly, immersed in the HFSB generated by the seeder; indeed it was found that the bottom 10cm of the flow do not contain any bubbles due to the 25cm height of the first nozzle row of the HFSB seeder from the floor of the wind tunnel.

3.1.4 FRAME STRUCTURE

To attach and place all the needed devices and instrumentation (wing model, cameras, LED, etc..), a structure made of aluminium X95 beams and rails was constructed at the exit of the wind tunnel with the following dimensions (l x w x h) 160 x 130 x 170cm, visible in Figure 3.4. It is based on a square made of beams on the top (with the other two in the middle to allow the wing model and LEDs placement), connected with four vertical beams to two horizontal beams placed on the ground, with two additional beams fixed at half height for stiffness purposed. As visible, most of the beams were covered with black tape to avoid any unwanted reflection from the glossy aluminium. While at the sides of the structure, four 2 x 3m black screens were placed to avoid recording external disturbances.

3.1.5 Particle Image Velocimetry

The final Particle Image Velocimetry (PIV) set-up is displayed in Figure 3.4, and the different devices employed in this set-up are presented here. All the instruments used for the PIV measurements are enumerated in the figure and listed here.

1. Photron Fastcam camera (35mm lens);
2. Photron Fastcam camera (50mm lens);
3. PTU X;
4. Gust generator;
5. LED;
6. Black screen;
7. Mirror;
8. Aluminium turbulence grid;
9. Wing model;
10. Pantograph trolley.

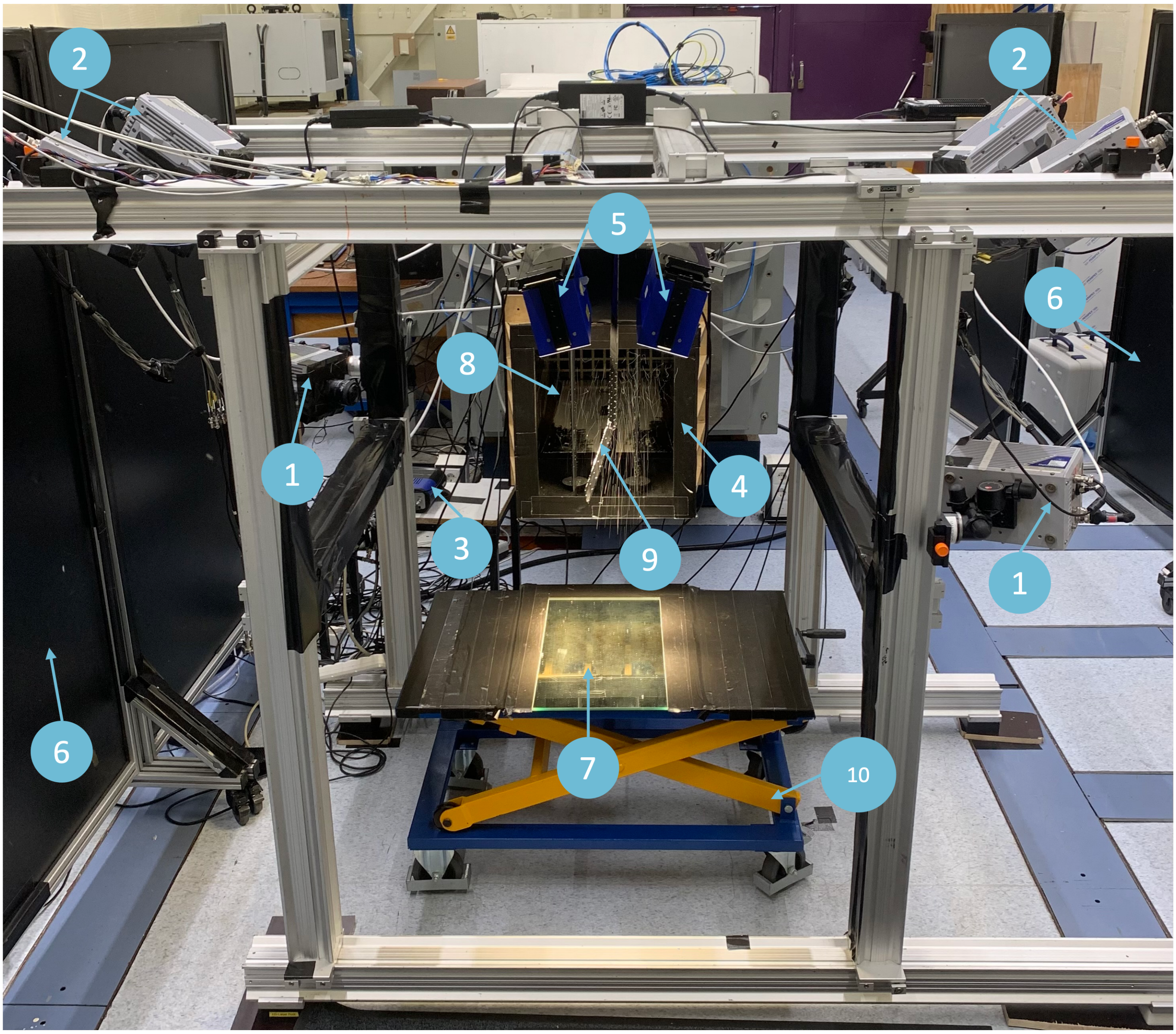

Figure 3.4: Particle Image Velocimetry (PIV) set-up.

3.1.5.1 Seeding

The seeding production includes a Fluid Supply Unit (FSU) and the tracer particle seeder, visible in Figure 3.5 and Figure 3.6, respectively. The FSU was built in-house at TuDelft in 2019 by Dennis Bruikman [70]. It is operated manually and includes three inlets for air, helium and soap, each with a pressure regulator that can be adjusted. In the experiment the following pressures were used, 2.5bar for soap, 1.8bar for helium and 2bar for air. Also, the seeder was built in-house at TuDelft, and it is 80cm high and 50cm wide and includes 200 nozzles evenly distributed in 2-level columns with a symmetric airfoil shape. The production rate is 3×10^4 bubbles x s [58]. Since the seeder is placed in the settling chamber of the wind tunnel, the contraction will also reduce the cross-section of the seeding resulting in a final height of 27.71cm and an exit width of 16.814cm. Four 0.3l bottles of soap were used during the entire wind tunnel experiments.

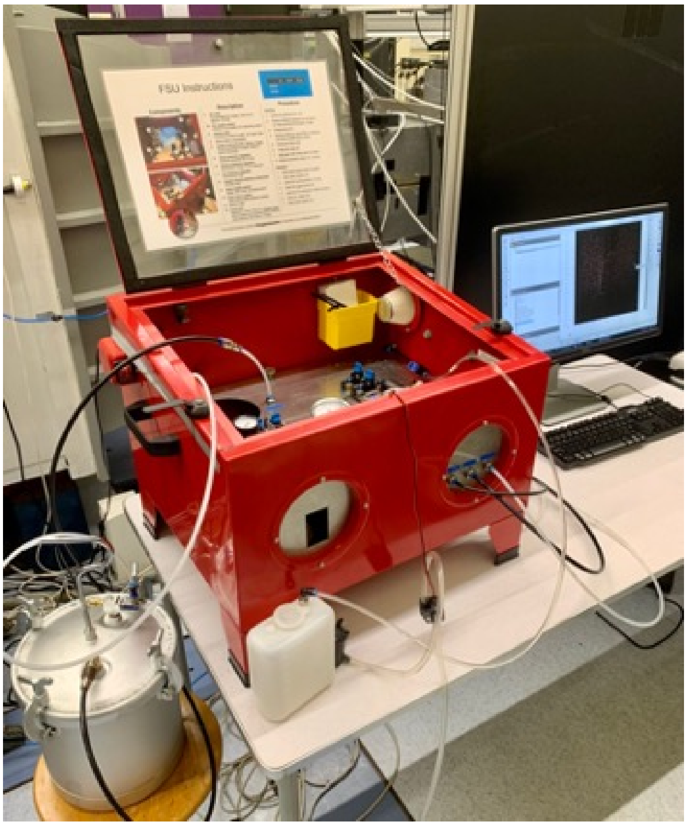

Figure 3.5: In-house Fluid Supply Units (FSU).

Figure 3.6: Helium-Filled Soap Bubble (HFSB) tracer particles seeder [33].

3.1.5.2 ILLUMINATION

As visible in Figure 3.4, the Helium-Filled Soap Bubbles (HFSB) were illuminated with two Lavision LED-Flashlight 300, placed on the top of the wing at the edge of the gust generator top side and tilted 15° towards the wing. The LEDs unit contain 72 high-power LEDs in an area of 300 x 100mm^2 capable to provide constant homogeneous brightness white light intensity with a light pulse trigger between 0 and 20Hz [71]. They were operated in free trigger mode that allows an operation with constant illumination (100% duty cycle) or can be triggered by an external signal. To increase the light intensity, a 60 x 40cm^2 mirror was placed on the bottom side of the measurement volume at a high of 53cm from the ground. It was lain down over a pantograph trolley to adjust the height freely. The mirror size and positioning, with also the positioning of the LEDs (considering the opening angle of 10° ± 5°) [72] were decided to permit the maximum tracer particles illumination but at the same time to avoid any reflection during the acquisition phase. The LEDs are triggered and synchronised with the cameras using a Programmable Time Unit X (PTU).

3.1.5.3 CAMERA

The experiment used six high-speed LaVision Photron Fastcam to capture the moving tracer particles. Four of them are owned by the Aerodynamic department of the Aerospace Faculty of TUDelft. They are the model SA1.1 [73], while the remaining two were on loan by the Netherlands Aerospace Centre (NLR) and are the model SA5. There are no significant differences in specification, but it was essential to select the correct model during the hardware set-up in DaVis before the acquisition phase. The two SA1.1 are mounted at the same height of the wingtip, at a distance of 70cm, while the four on the top are mounted with a distance equal to 110cm (these distances are indeed a bit different from the optimum ones calculated in Table 3.2. Still, unfortunately, they were limited by the structure size; however, correctly setting the lens focus was enough to have good images with these object distances). At the same time, this final position of the camera results after several modifications and adjustments during the set-up phase to avoid any unwanted reflections of the wing and wingtip during the recording. The vertical distance between the lower and upper-level cameras is 50cm, while the horizontal distance between the two cameras on the top was 80cm. All the cameras are attached to the structure made of X95 beams with gimbal supports that allow a completely 3D positioning of the cameras. Furthermore, all the cameras are connected on the side and hanging to use their weight for stabilisation purposes and not be affected too much by vibrations or small position changes. The cameras have a sensor size of 1024 x 1024 px [74], resulting in 5.4kHz maximum acquisition frequency during the experiment to capture the duration of 2s of the flow, the acquisition frequency used was equal to 2.7kHz with a total number of images of 5457. On the cameras, different lenses are mounted; on the two cameras at the same height of the wingtip, a 35mm lens is mounted, while on the four on the top, 50mm lenses are selected, this allows to place the cameras at different distances from the tested object. The $f_{\#}$ was set to 16 to have a depth of field of 0.25m. The interchangeable lenses are mounted directly on the G type F-mount on the cameras, but for the two NLR cameras, an additional device is present after the G type F-mount. This is used to avoid the change of the $f_{\#}$, so it was set to open for the entire experiment, so it was easy to change this value during the calibration and acquisition phase. After several tests, the exposure time was set to 83μs to have the right amount of light in the images.

To communicate with the Programmable Time Unit X (PTU), the cameras are cabled using Bayonet Neill Concelman (BNC) cables to the I/O connector located at the centre back of the camera. While transferring the recorded images to the PC, Ethernet cables are used. Since the size of the images is very big (more than 1.5TB of images), the Ethernet cables used are the ones with a CAT 8.1 allowing a maximum transmission speed of 40GB$\,s^{-1}$ at 100m and a maximum bandwidth of 2000MHz [75]. The two cameras from NLR are connected to a Gigabit Ethernet switch that is then attached to the PC with another Cat 8.1 cable, while the other four cameras are connected directly to the computer Network Interface Controller (NIC) ports of the PC (with the high-speed card installed), to do this some additional steps were necessary. Indeed, using the Photron Fastcam Viewer (PFV) software, each camera's Internet Protocol (IP) address was changed and set to 192.168.X.10, with X being 10 for the first camera until 13 for the fourth one. At the same time, the IP address of each NIC port is changed in the Windows Network Properties from 192.168.Y.1, with Y being 1 first one to 4 for the fourth one [76]. Also, the IP address of the switch was set to 192.168.1.Z, with Z different from the X of the NIC ports. Furthermore, the windows firewall was turned off; the Jumbo Packet was set up to 9014Bytes. Then, to test that all the cameras and ethernet switches were set and connected correctly, the command prompt was opened, and the text ping followed by the IP address of each device was typed. After this process, all the cameras were added to the hardware set-up in DaVis 10.2, assigning the name Camera 1 to the camera with the lowest IP address and so on. This allows a total saving time of around 50min for each acquisition run.

3.1.5.4 DATA ACQUISITION SYSTEM

The acquisition computer C with the LaVision DaVis 10.2 software was used to store the data gathered by the cameras. This software was used for the acquisition of the images but also in the image pre-processing and post-process phase for the STB and IPR algorithms. A LaVision Programmable Time Unit X (PTU) was connected to the computer with a USB cable and used to trigger the LEDs and the six cameras in a synchronised way with the signal coming from the gust generator control PC. The connection used to connect the six cameras, the 2 LEDs and the trigger are listed in Appendix A. The images were stored directly in two different 4TB hard disks (HD), one that will be connected afterwards to the Aerodynamic server 7 that allowed the remote post-processing of the images. At the same time, the other one was stored for backup reasons.

3.1.6 SENSORS PLACED ON THE WING

The final conventional sensors set-up is displayed in Figure 3.7, and the different devices employed are presented here. All the instruments used for the traditional sensor measurements are enumerated in the figure and listed here.

1. Laptop;
2. SCADAS;
3. Arduino;
4. Power supply;
5. cRIO.

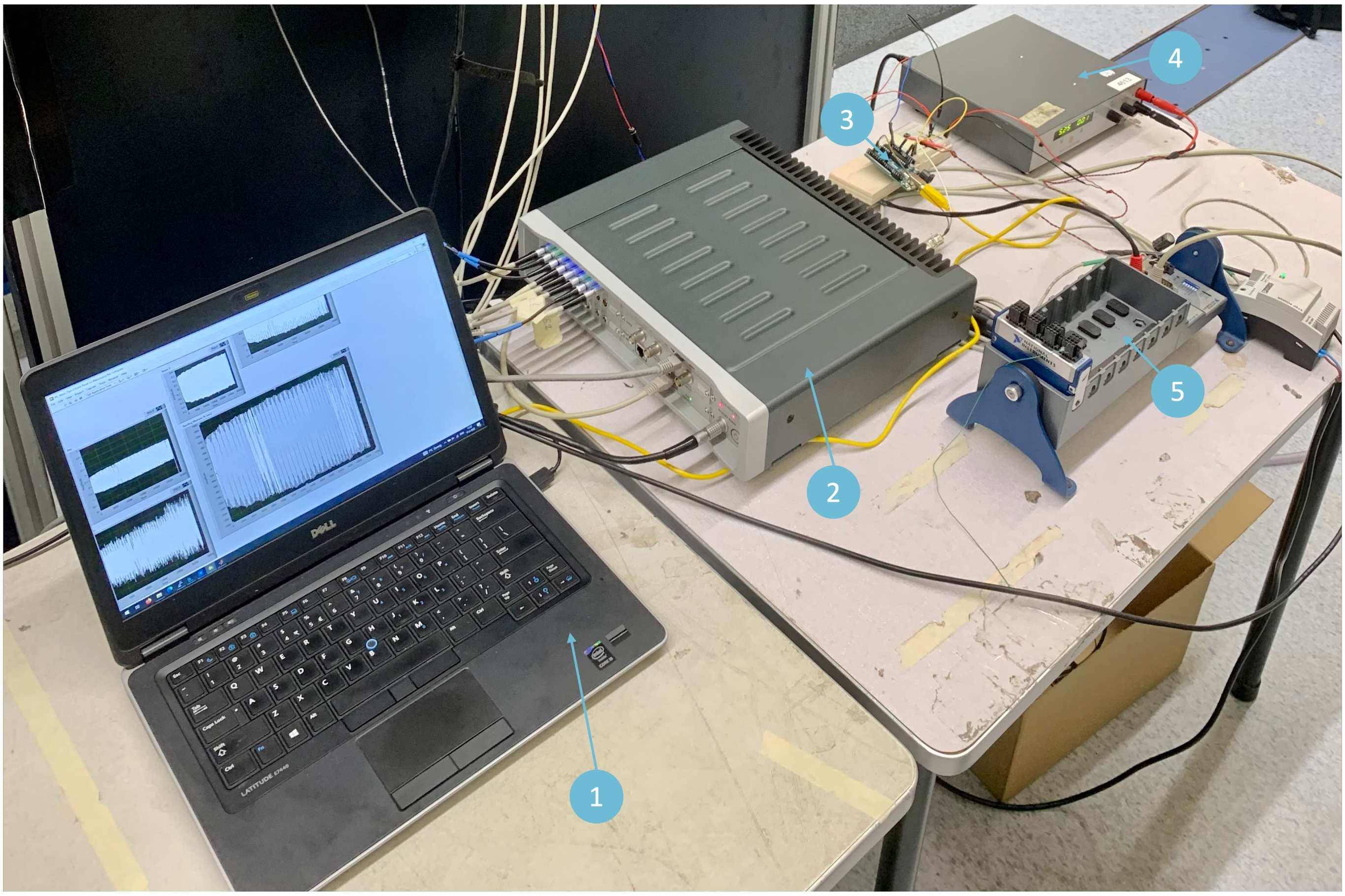

Figure 3.7: Conventional sensors acquisition system set-up.

It includes a laptop **(1)** that controls the gust generator using the PuTTY program. It sends the information to the gust generator like the type of gust (sine or 1-cosine), amplitude, frequency, number of gusts and delta time between each gust. A power supply **(4)** was used for the actuator; only the Arduino can power it, but it has a minimum current output, so an external power supply was preferred. The Arduino UNO microcontroller **(3)** that, controlled by the laptop, released the wingtip hinge mechanism when it received the trigger signal (in the form of an electric pulse) from the gust generator after a set delta time to achieve the desired load threshold. After a specific set time, the mechanism is locked again. The same trigger signal from the gust generator is also sent to the Siemens Simcenter SCADAS Mobile 8 **(2)** that is in charge of the data acquisition from all the sensors mounted on the wing (two rosettes of Kyowa KFGS-10-120-D17-164 triaxial 0°/90°/45° strain gauges for the root bending moment, a Bourns 3310C-125-203L potentiometer for the wingtip fold angle and the two PCB 352A24 uniaxial accelerometers for the tip displacement). The Arduino is instead sending to the SCADAS a control signal for the actuator motion. All the information stored in the SCADAS are then sent cyclically to the National Instruments cRIO-9744 9 **(5)** using the Ethernet for Control Automation Technology (EtherCAT) communication between the two. The cRIO reads these electrical signal from the SCADAS and then process them by converting and correcting them, using the calibration constants computed by Carrillo [18], saving after the test in the laptop in a .txt file.

3.2 Experiment Parameters

The wind tunnel flow conditions are presented in Table 3.1. Where the wing chord (c) is based on the tested model, the air density (ρ) is calculated based on the testing air temperature (20°) using the engineering toolbox [77]. The free-stream velocity (V) will be the one used by Carrillo et al. [17] $10\,\mathrm{m\,s^{-1}}$, and the air dynamic viscosity (μ) is calculated based on the air air temperature (20°), using the engineering toolbox [78]. The Reynolds Number (Re) and Mach Number (M) can be derived from these.

Table 3.1: Wind tunnel flow conditions.

Parameter	Symbol	Equation	Value	Unit
Wing Chord	c	-	0.1	m
Air Density	ρ	-	1.204	$\mathrm{kg\,m^{-3}}$
Air Temperature	T	-	293.15	K
Freestream Velocity	V	-	10	$\mathrm{m\,s^{-1}}$
Air Dynamic Viscosity	μ	-	1.803×10^{-5}	$\mathrm{Pa\,s}$
Reynolds Number	Re	$\mathrm{Re} = \frac{\rho \cdot V \cdot c}{\mu}$	6.68×10^{4}	-
Gas Constant	R	-	287.057	$\mathrm{J\,kg^{-1}\,K^{-1}}$
Ratio of Specific Heat	γ	-	1.4	-
Speed of Sound	a	$a = \sqrt{\gamma R T}$	343.236	$\mathrm{m\,s^{-1}}$
Mach Number	M	$M = \frac{V}{a}$	0.0291	-

Since this thesis's focus and principal object is the application of Particle Image Velocimetry (PIV) for instantaneous large-scale aeroelastic measurements, it was decided not to use wind tunnel corrections (like wall corrections). This is also because these corrections do not significantly impact the improvement of the results. Indeed, the wing doesn't fit entirely in the wind tunnel flow exiting from the nozzle. This demonstrates that this thesis study is based on the investigation of only the release timing of the hinge without focusing on a quantitative evaluation of other involved parameters.

3.2.1 PARTICLE IMAGE VELOCIMETRY PARAMETERS

The PIV parameters needed for the experiment are given in Table 3.2. The pixel size (d_{px}) and the number of pixels ($\#px$) are from high-speed Photron Cameras sensor [73], the Field of View (FOV) is decided based on the maximum area that a camera can image (considering the 200mm long wingtip and 400mm squared W-tunnel exit [50]). The focal length (f) is the lens's angle of view (the longer the focal length, the narrower its angle of view), so to have the same FOV, the object distance should be increased. It is based on the lenses installed on the cameras; a 35mm is used for the two cameras closer to the winglet and 50mm for the four on the top farther away, so the results in Table 3.2 are for both these lenses. Also, the depth of field (range in which the particles are on focus) is calculated based on the FOV and on the $f_{\#}$, which equals 0.245m. The wavelength of the LED-Flashlight 300 is 600μm (yellow colour) at the absolute maximum [72]. Finally the Helium Filled Soap Bubbles (HFSB) tracer particle geometric diameter (d_{geom}) generated by the in-house build Fluid Supply Units (FSU) [70] is 300μm [79]. Knowing these, all the other parameters can be derived. Please note that in reality, the object distances used for both lens types were increased to 70cm and 110cm respectively, due to structure size limitations, which results in a greater FOV.

Table 3.2: PIV parameter.

Parameter	Symbol	Equation	35mm Lens	50mm Lens	Unit
Pixel Size	d_{px}	-	2×10^{-5}		m
Number of Pixel	$\#px$	-	1024		-
Field of View	FOV	-	0.35		m
Focal Length	f	-	35	50	mm
F-Stop	$f_\#$	-	16		-
Magnification Factor	M	$M=\frac{d_{px}\cdot\#px}{FOV}$	0.059		-
Wave Length	λ	-	600		μm
Depth of Field (Focal Depth)	δ_z	$\delta_z=4.88\cdot\lambda\cdot f_\#^2\cdot\left(\frac{M+1}{M}\right)^2$	0.245		m
Lens Aperture Diameter	D	$D=\frac{f}{f_\#}$	0.002	0.003	m
Object Distance	d_o	$d_o=\frac{f\cdot(M+1)}{M}$	0.633	0.904	m
Image Distance	d_i	$d_i=M\cdot d_o$	0.037	0.053	m
Geometric Diameter	d_{geom}	-	300		μm
Effective Particle Diameter	d_p	$d_p=\frac{d_{geom}}{M}$	0.005		m
Diffraction Limit	d_{diff}	$d_{diff}=2.44\cdot\lambda\cdot(1+M)\cdot f_\#$	2.479×10^{-5}		m
Resulting Particle Image Diameter	d_τ	$d_\tau=\sqrt{d_{\text{geom}}^2+d_{\text{diff}}^2}$	3.01×10^{-4}		m

3.3 Data Acquisition Procedure

This section explains the data acquisition procedure to record the images with PIV and gather the data from the conventional sensor. Furthermore, the experiment test matrix is presented.

3.3.1 Test Matrix

The test matrix investigated during the wind tunnel experiment is shown in Table 3.3, where DPN indicate the Data Point Number. The first two DPN are for comparing free and fixed hinge in steady cases. Instead, from DPN 3 to DPN 8, the unsteady cases with the 1-cosine gust (with 8Hz gust frequency and 2.5° gust amplitude) are performed to investigate the hinge timing influence on the wing root bending moment reduction due to a gust. For all the DPN, the angle of attack is equal to 5° for static and dynamic load representation, and the free-stream velocity was $10\,\mathrm{m\,s^{-1}}$. A repetition of the measurements was not performed due to the long saving time of the images (around 50 min for each DPN).

Table 3.3: Test matrix.

DPN [-]	Condition	α [°]	β [°]	V [m/s]	Hinge Condition [-]	Gust Frequency [Hz]	Gust Amplitude [°]
1	Steady	5	-	10	Free	-	-
2	Steady	5	-	10	Fixed	-	-
3	Unsteady	5	-	10	Free	8	2.5
4	Unsteady	5	-	10	Fixed	8	2.5
5	Unsteady	5	-	10	Pre-Released	8	2.5
6	Unsteady	5	-	10	0%	8	2.5
7	Unsteady	5	-	10	50%	8	2.5
8	Unsteady	5	-	10	100%	8	2.5

The time at which the peak load appears is measured for the DPN 4 (unsteady fixed hinge) and then is used for the hinge release for the unsteady cases (DPN 5-8). The hinge is released simultaneously as the trigger from the gust generator for the pre-released. For the 0%, the hinge is released at the minimum of the peak load (95ms), for 50%, the hinge is released at half the maximum peak load (128ms), while at 100% the hinge is released at the maximum peak load (at 165ms). For all of them, the two delays presented and discovered by Carrillo [18] are considered. Indeed, both the delay from the Arduino processing time of 2ms and the delay between the signal sent and the movement of the actuator equal to 50ms are into account and subtracted by the time set in the Arduino program listed above. For a 8Hz short gust the 2ms a relative delay of 1.6% while the 50ms represents a relative delay of 40%.

3.3.2 PARTICLE IMAGE VELOCIMETRY

For Particle Image Velocimetry, the calibration of the cameras plays a significant role in achieving good results. For this reason, a considerable amount of time and effort was put into it during the experiment.

3.3.2.1 INTENSITY CALIBRATION

After each position or setting (exposure time, frame rate or $f_{\#}$ modification on the camera or lenses, the first step is intensity calibration. This requires the cap mounted on the lens and takes just a few seconds. The aim is to subtract an offset dark image to create a transform function that relates the image intensity sampled with the camera to the known standard values that may have a nonlinear relationship [80].

3.3.2.2 PERSPECTIVE CALIBRATION

Then, after the intensity calibration, the next step is perspective calibration (volume calibration). This is done by removing the wing model and recording 100 images of a calibration plate in seven different independent positions in the measurement volume, as illustrated in Figure 3.8. The different views are: in the middle of the measurement volume, rotated clockwise 30°, rotated counterclockwise with the same angle, tilted 15° vertically towards one side of the measurement volume, inclined by the same angle towards the other side, then moved 5cm forth, and finally the same movement but back.

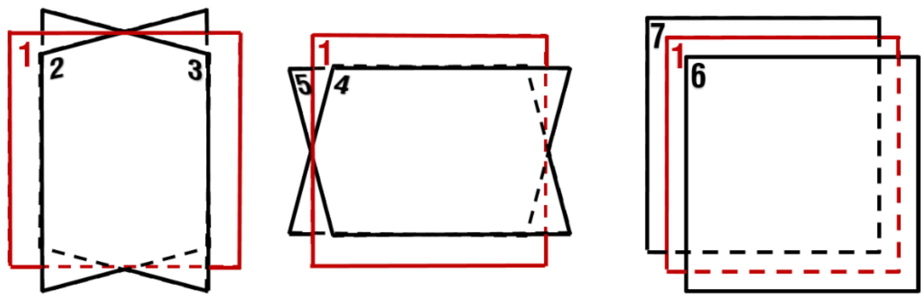

Figure 3.8: Perspective calibration views [34].

The used calibration plate is the modified type 30 3D plate (visible in Figure 3.10 with its properties in Figure 3.9) with the white dots calibration marks on a black background separated by a plane distance dz [34].

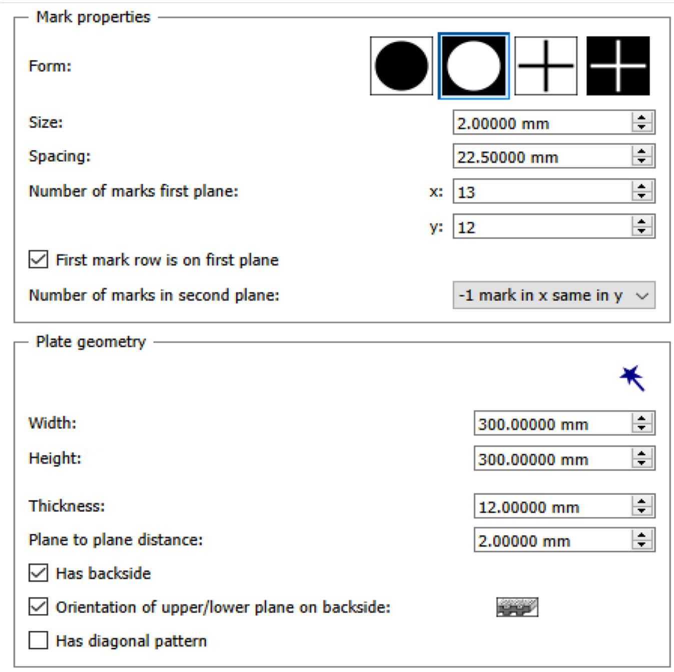

Figure 3.9: Calibration plate settings.

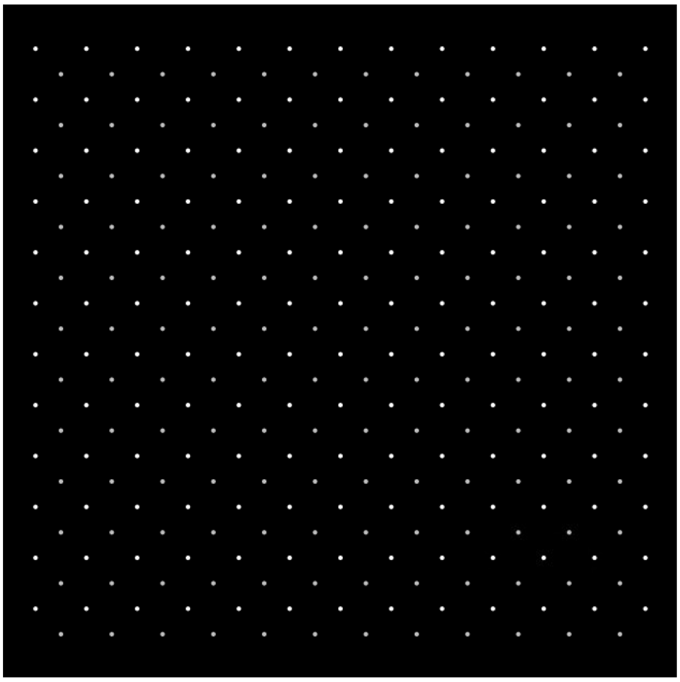

Figure 3.10: Modified type 30 calibration plate.

The cameras set up for this phase are the following $f_{\#} = 4$ (large aperture to allow enough light to be recorded, since in this phase the LEDs are turned off), with an extensive exposure time (shutter speed) 100ms. The pinhole fit was used during this phase to map the world points to the camera sensor. When all the images are recorded, the average processing is done for each view, and all the pictures are appended to one data set. Since the calibration plate is a modified version of Type 30, the automatic search function for the markers was disabled by LaVision. For this reason, for each view and each camera, the central marker (origin), the direct neighbour mark of the origin (that defines the x-axis), and the direct neighbour mark of the origin at 90° define the y-axis [35], have to be selected manually. Since the plate is double-sided, the selection scheme will be different for each side of the plate to ensure the proper orientation of the coordinate system in the corrected image. For the front side (with the Type label on the bottom right), which is visible by the first three cameras after the central markers, the one on the left and then the one above have to be clicked (as shown in Figure 3.11), while for the back side (visible from the last three cameras) the one on the left and then the one above are clicked (as visible in Figure 3.12). Please note that in the used calibration plate, no triangular or rectangular shape markers were painted.

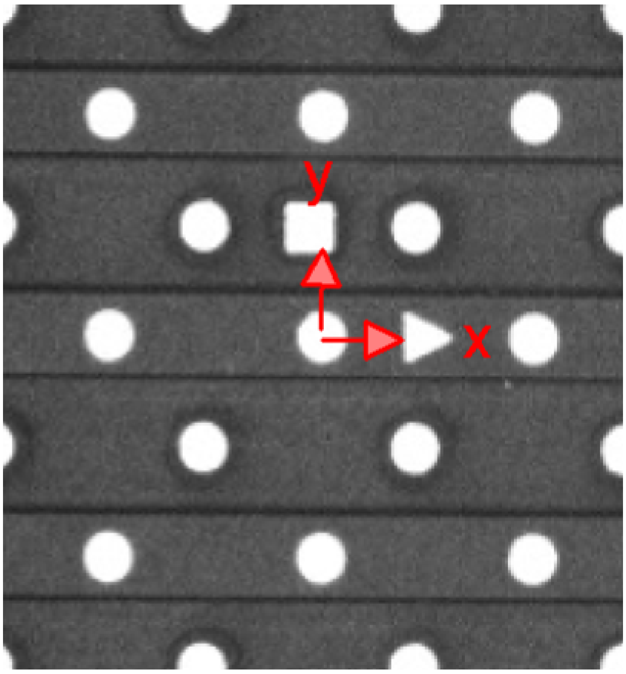

Figure 3.11: Front side [35].

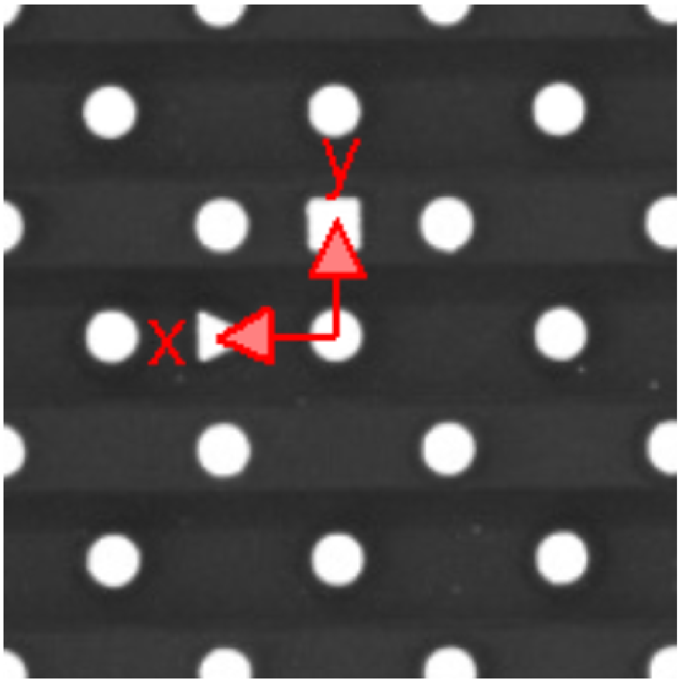

Figure 3.12: Back side [35].

Then DaVis will start searching for all markers painted on both sides of the plate. When the process is finished, the perspective geometrical calibration is stored and can be used for the volume self-calibration phase presented in section B.2.

3.3.2.3 Free-Stream Measurements

After both the intensity and perspective calibration, the cameras are ready to start the real and effective recordings of the measurement volume. Firstly, free-stream measurements are done; the idea was to use these images later for volume-self-calibration purposes; two sets of free-stream images were taken (before DPN 1 and before DPN). This running the wind tunnel at $10\,\mathrm{m\,s^{-1}}$ in steady state. So the camera settings are switched to the ones used for the entire experiment to have 2s of recordings (that will be enough to capture the entire 8Hz gust) with an image rate of 2.7kHz, the maximum number of images allowed was 5457. The exposure time was decreased to 83ms, and the $f_{\#}$ increased to 16 (smaller camera aperture) due to the current presence of the LEDs, which resulted in less light needed by the camera's sensor. Using the same settings, a free-stream with the gust was recorded before DPN 3 (using a 1-cosine 8Hz gust with a 2.5° amplitude) to have the possibility to visualise the 1-cosine gust without the wing in the middle in the post-processing phase.

3.3.2.4 Wing Structure Measurements

Then, the wing was mounted on the frame structure attached to the 3D-printed angular mask that allows the change in the angle of attack. It was set with an angle of attack of 5°, and all the conventional sensors were attached. Images without the wing flow are recorded to have a baseline for the structure deformation and wingtip folding angle variation. One set was recorded before DPN 1 to have images of the straight wing position.

3.3.3 Conventional Sensors

The calibration is not required for the conventional sensors since it was already done by Carrillo [18], so the same calibration constants (for the strain gauges) are also used in this experiment. Instead, zero measurements are taken to use in the following post-process phase. Indeed, zero measurements are done (without the flow) to use in the post-processing phase to subtract from the actual recorded value and remove any disturbances from the data recorded. This was done for both the winglet locked and unlocked.

After all these processes, the measurement of the test cases presented in the test matrix listed in Table 3.3 can start, and the method used for the wind tunnel set-up and data acquisition procedure is presented in Figure 3.13.

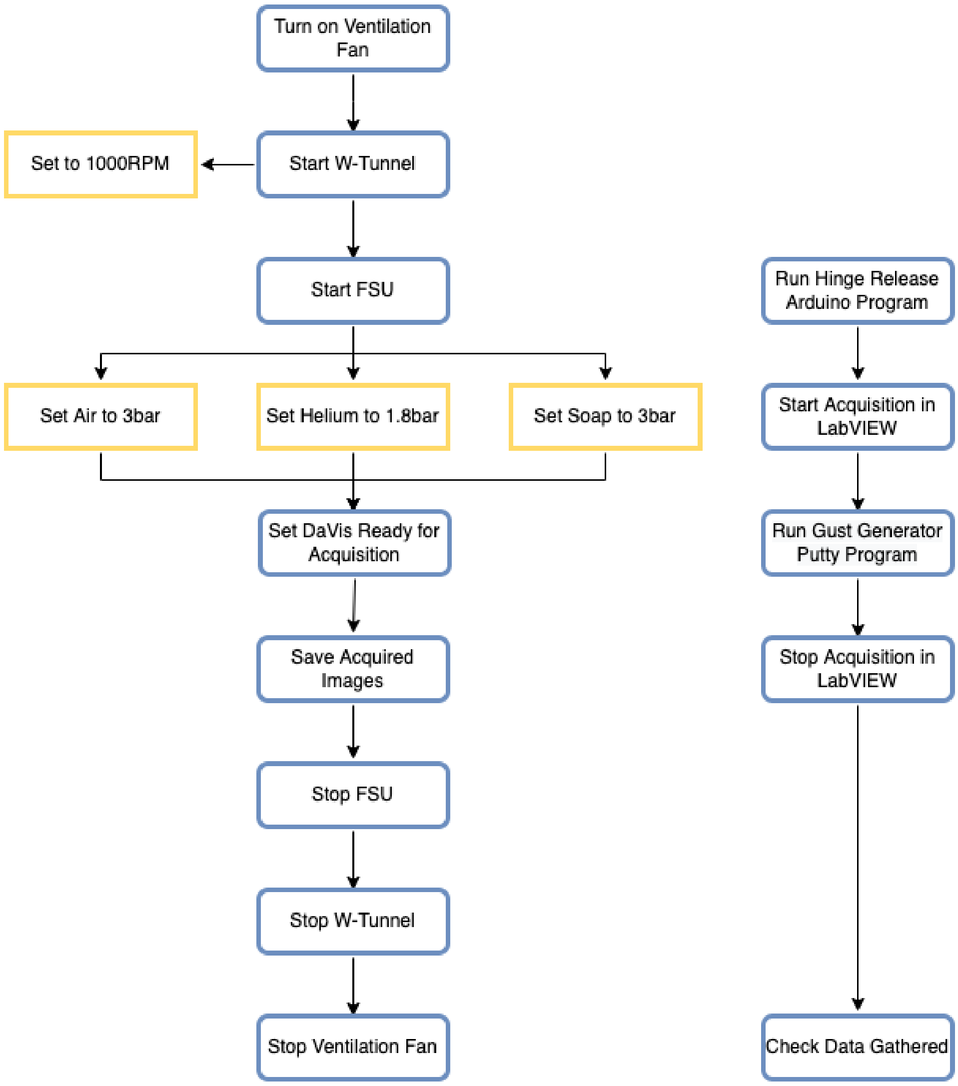

Figure 3.13: Wind tunnel and data acquisition procedures.

4
Data Analysis and Reduction Techniques

This chapter presents the reduction techniques used for the data analysis of conventional sensors and Particle Image Velocimetry (PIV). Then the flow field visualisation and structural characterisation procedure are explained.

4.1 Conventional Sensors Data Analysis

This section presents the conventional sensor data analysis and reduction techniques. The dynamic response of the wing hit by the 1-cosine gust is studied to characterise the wingtip gust load alleviation based on the hinge's release conditions. To assess this, two important parameters based on the bending moment coefficient (C_B) are taken into account, the peak load (ΔC_B) and the Root Mean Square (RMS). Firstly, the bending moment from the strain gauge electric signals was obtained using the calibration constants on the strain gauge electric signals, S_C from the centre, S_F from the front, S_R from the rear. These calibration constants were obtained by Carrillo [18] applying a know shear force using a fixed weight that hangs from the pulley to the clamped wing. These are called C_1, C_2 and C_3 in Equation 4.1 and are equal to -639.469, 188.082, -83.509 respectively. Please note that the values for S_C, S_F and S_R were already updated, subtracting the same from the zero measurements.

$$M = C_1 \cdot S_C + C_2 \cdot S_F + C_3 \cdot S_R \tag{4.1}$$

Then, the bending moment coefficient (C_B) is computed using Equation 4.2.

$$C_B = \frac{M}{\frac{1}{2} \cdot \rho \cdot S \cdot b \cdot V^2} \tag{4.2}$$

Knowing the value of the bending moment for each time interval, a filtering procedure was actuated to decrease the amount of noise coming from the electric signal recorded. This was done using the Matlab digital filter function *designfilt* and selecting a low-pass filter, with a filter order of 8, a passband frequency of 10Hz, a passband ripple of 0.2dB and an average sampling rate of 465Hz. The result for the Unsteady case with the free-hinge is illustrated in Figure 4.1. Please note that the filtered bending moment coefficients (C_B) are used for the rest of the thesis.

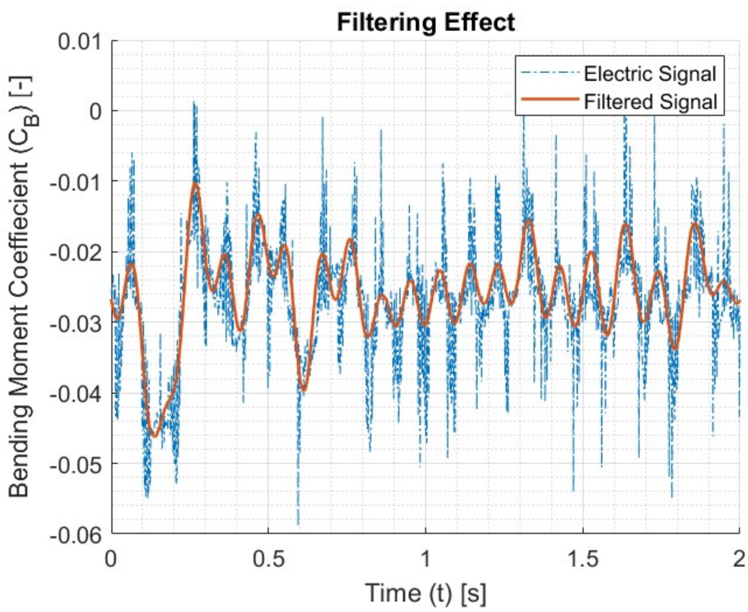

Figure 4.1: Signal filtering effect.

The peak load is defined as the difference between the maximum load ($C_{B_{max}}$) and the static load before the gust hits the wing, the so-called pre-released steady-state load ($C_{B_{pre}}$), visible in Figure 4.2. While the RMS was selected since it gives the load signal oscillation persistence (higher RMS indicates a longer oscillation in time) or, more simply, how much the signal deviates from the steady load value.

The peak load and the RMS are studied relatively compared with the wing in the locked hinge condition, as visible in Equation 4.3 and Equation 4.4.

$$P_{Rel} = \frac{P - P_{Lock}}{P_{Lock}} \tag{4.3}$$

$$RMS_{Rel} = \frac{RMS_{\tilde{C}_B} - RMS_{\tilde{C}_{B_{Lock}}}}{RMS_{\tilde{C}_{B_{Lock}}}} \tag{4.4}$$

Where the peak (P) is $C_{B_{Max}} - C_{B_{Pre}}$ and $\tilde{C}_B$ is given with Equation 4.5, and is split in before and after the released time (t_{rel}), since there are two steady states, corresponding to the locked-hinge (before t_{rel}) and free-hinge conditions (after t_{rel}).

$$\tilde{C}_B = \begin{cases} C_B - C_{B\,\mathrm{Pre}} & 0 < t < t_{\mathrm{Rel}} \\ C_B - C_{B\,\mathrm{Post}} & t > t_{\mathrm{Rel}} \end{cases} \tag{4.5}$$

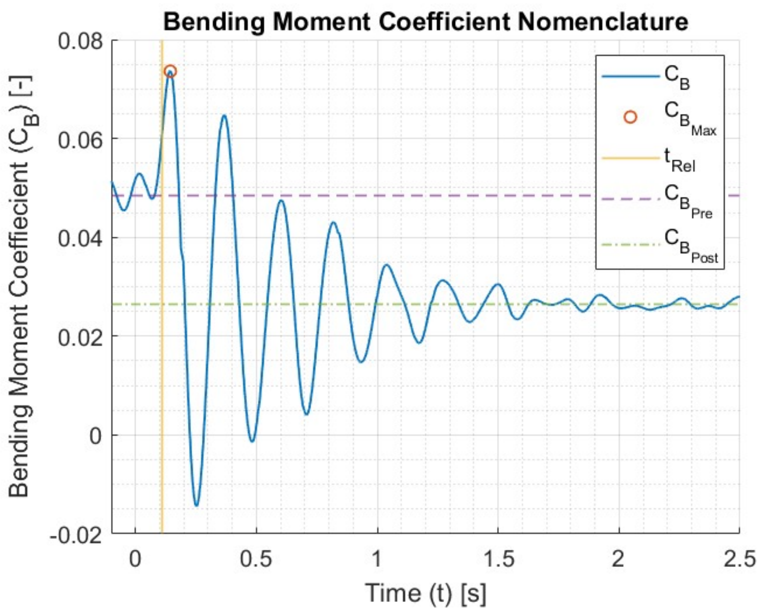

Figure 4.2: Bending moment coefficient nomenclature.

Instead for the wingtip fold angle (θ) variation the calibration formula in Equation 4.6 is used. Where m_V is the calibration constant equal to 0.0208 and V_0 is the potentiometer fold angle electric signal from the zero measurements, and V is the same for the actual test case. Also, in this case, the same low-pass filtering procedure was actuated. Please note that the filtered fold angles (θ) are used for the rest of the thesis.

$$\theta = \frac{V - V_0}{m_V} \tag{4.6}$$

4.2 Particle Image Velocimetry Data Analysis

Data analysis and reduction techniques are also needed for the particle image velocimetry recorded images. Indeed image pre-processing is necessary before executing the tracers and markers tracking. At the same time to allow good results, Volume Self-Calibration (VSC) is required. Then, the post-processing phase can be executed when the flow and structure information are separated. The processing operations from the recorded raw images until the wing geometry reconstruction and the flow field visualisation are summarised in the flow-chart visible in Figure 4.3.

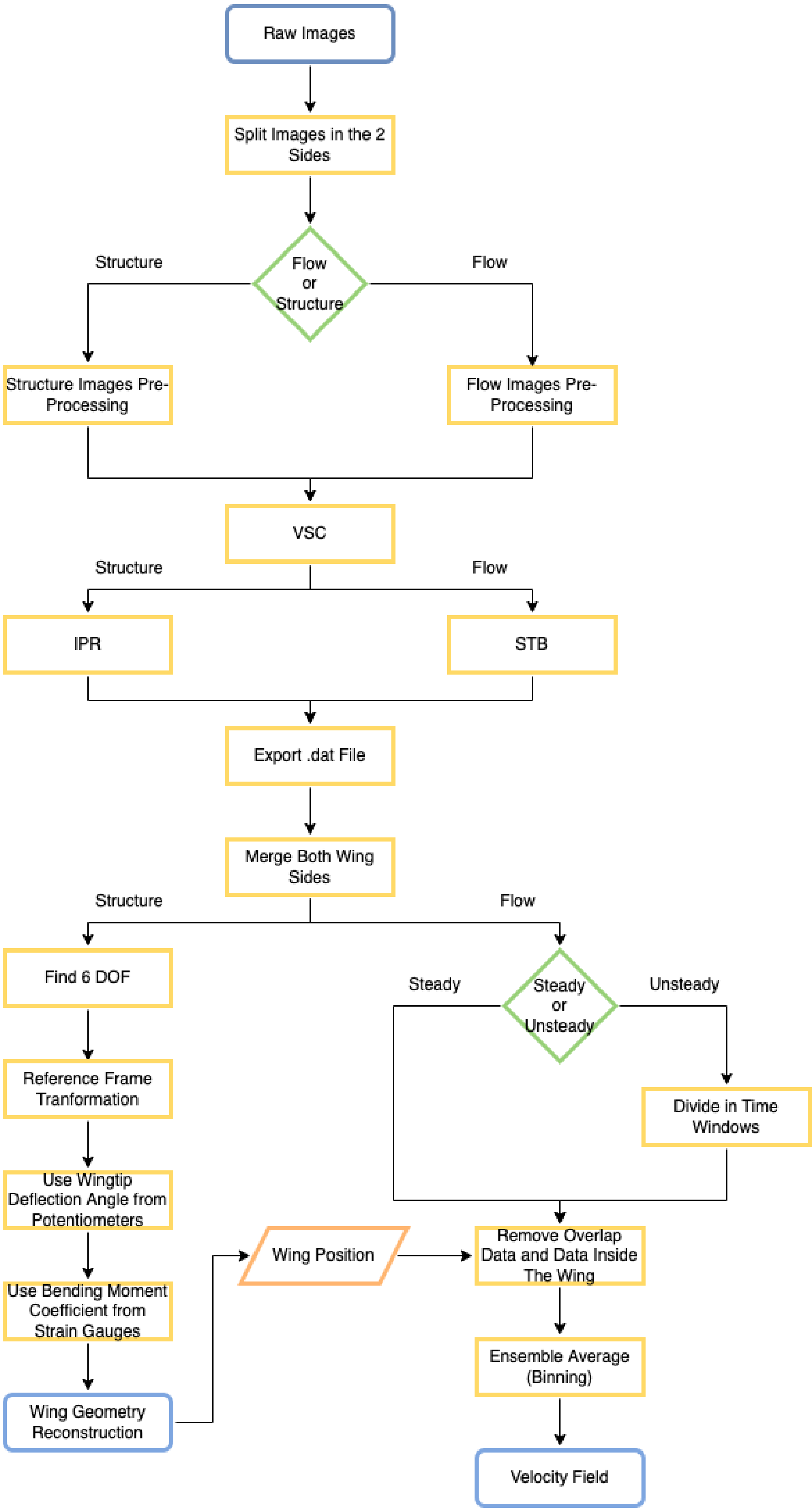

Figure 4.3: Reduction Techniques Flow-Chart.

All the steps presented in the flow chart above are detailed described in Appendix B.

4.3 Flow-Field Visualisation

For the flowfield visualisation around the wing and wingtip, an ensemble-averaging binning code was used on the Shake-The-Box (STB) .dat file exported previously with the Export to Tecplot command from DaVis. These data files (saved initially in two different parts from DaVis, for Side 1 and Side 2) were merged, considering that the STB measurements of the same time instants have to stay together. However, also, as illustrated in Figure 4.4, taking from each side only the measurements until the wing surface (knowing the Leading Edge (LE) and Trailing Edge (TE) from the wing reconstruction results) and the extended chord line (discarding the overlap region), to avoid regions with two different measurement sets and have better results. This ensemble averaging process transforms the flowfield STB data from the Lagrangian format (particle position and velocity known over time) to an Eulerian structured grid format description of the flow. This is done by dividing the measurement volume into small cells with cubical shapes (bins), which contain several particles with known position and velocity and then computing the statistical moments from the velocity vectors within sub-volumes.

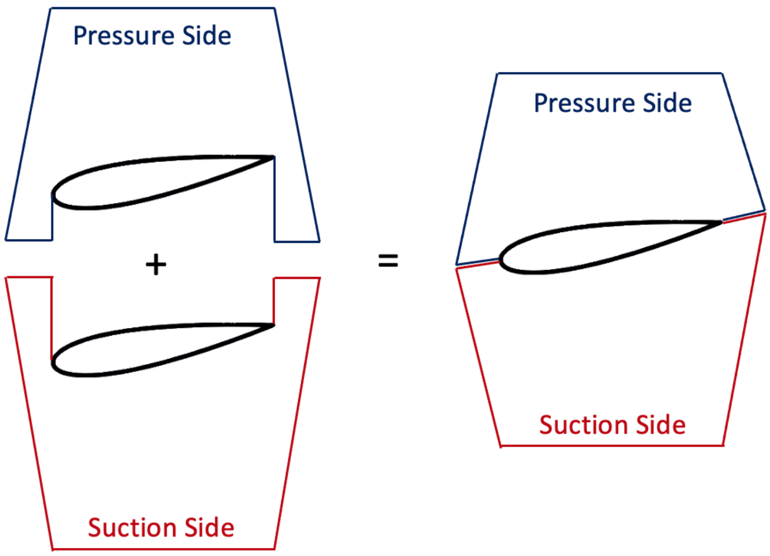

Figure 4.4: Suction and pressure side merging procedure.

For the binning code, the following settings were used. A bin-size (l_B) for the ensemble averaging (interrogation windows) of 15mm, with an overlap factor of 0.75 (75%) between neighbouring bins. The minimum number of particles ($N_{p_{min}}$) in each spatio-temporal bin was set to be equal to 1 to use all the interrogation windows that contain at least one particle (larger values were tried but resulted in a significant missing of flow information.). Minimising the uncertainty of the reconstructed velocity flow field, have a smaller probability of experiencing valid empty bins while simultaneously avoiding data gaps resulting from the incapability of certain interrogation windows to meet the concentration requirements. While the volume of interest spans $-175\,x\,175$mm in x-coordinate, $-125\,x\,125$mm in y-coordinate and $-175\,x\,175$mm in z-coordinate (same as the measurement volume in DaVis). The tophat filter-mode method for the ensemble averaging was selected to retrieve each spatio-temporal bin velocity statistic from the contained particles. More advanced higher-order ensemble 3D methods are available, like the one presented by Agüera et al. [81], that is, using a polynomial fit for accounting for the spatial variations of velocity distributions within each bin in the least square sense. This method can be extended to the temporal dimension for phase-average conditions, becoming a spatio-temporal ensemble averaging method. However, it was decided to do not use them since the measurements are not fully static, and the computational cost would be increased without improving the accuracy of the process since it cannot be proven that the dimension of the position errors is much smaller in magnitude to the selected bin size. Indeed, during a single PIV measurement, the wing and the six cameras position can be slightly different due to some vibrations/oscillations induced by the flow, introducing particle positioning errors in the reference frame. Furthermore, additional random measurement errors arise from the software during the reconstruction process. These settings were giving good results for both the time-average static cases and for the phase-average dynamic ones.

The bin size (l_B), spatial discretisation resolution windows of the velocity field, of 15mm that defines the smallest resolvable length scale, was selected (equal to $\frac{20}{3}$ of the 100mm wing chord), to allow a proper flow visualisation. Based on this, a Cartesian mesh grid spanning the volume occupied by the tracked particles during the acquisition time is generated. Each point node of this grid represents the centroids of an interrogation window bin used for the ensemble averaging process. Then this value was checked with some calculations, indeed knowing that the images were taken with a sample rate $f = \frac{1}{T} = 2.7\text{kHz}$, $T = \frac{1}{f} = \frac{1}{2700} = 0.37\mu\text{s}$, and knowing the wind-tunnel freestream velocity $V = \frac{d}{T} = 9.7\text{m}\,\text{s}^{-1}$. The maximum distance travel in one time step is $d = V \cdot T = 9.7 \cdot 3.7 \times 10^{-4} = 3.589\text{mm}$, that is indeed lower respect to 15mm selected. Smaller bin sizes were tested but gave more noisy results due to a lower number of particles inside the bin leading to an increase in the uncertainty level of the velocity. On the contrary, a bigger bin size was also tested but gave some overlap issues with the wing surface and a less refined velocity field. For this reason, the 15mm one was kept for all the ensemble-averaging processes. The bin size (l_B) sensitivity study conducted for the steady free condition (using all time steps at the middle plane of the wingtip $z/b = 0.85$ or $z/b_{wingtip} = 0.5$) is visible in Figure 4.5.

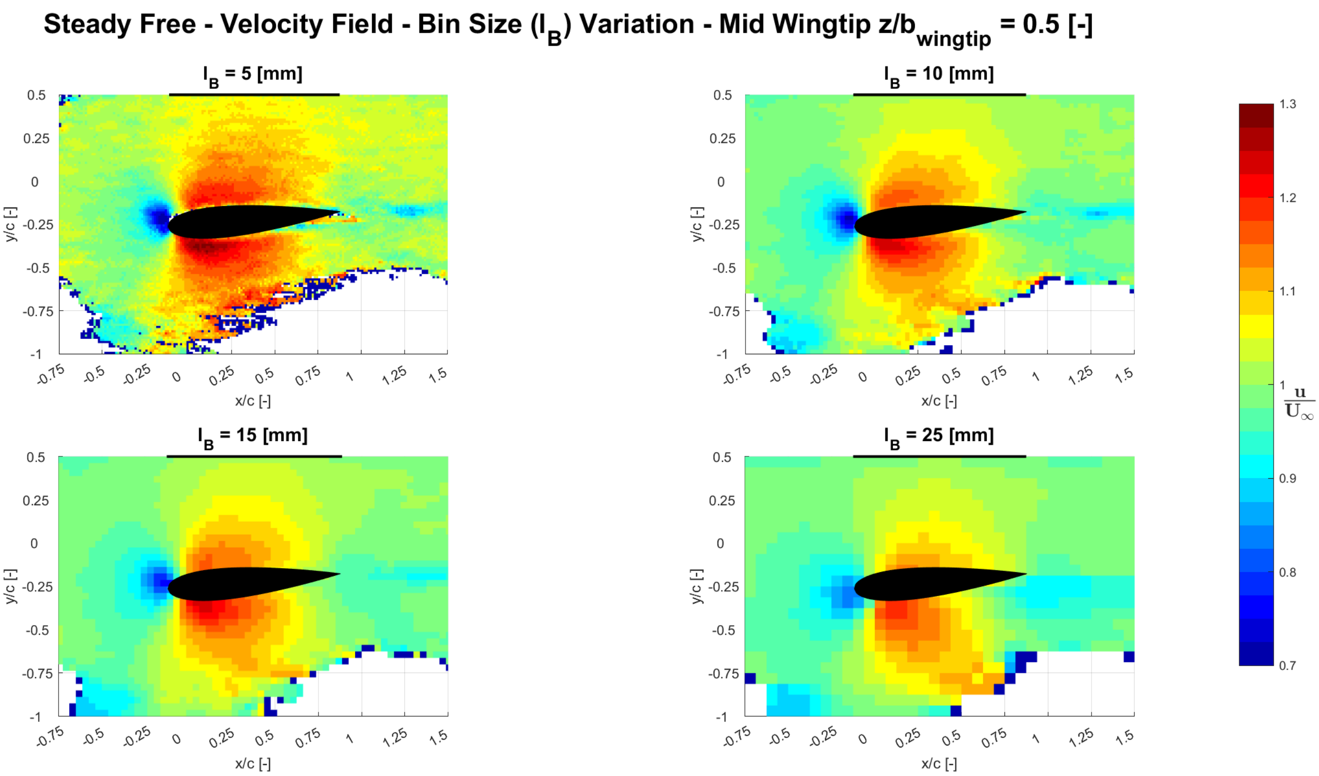

Figure 4.5: Steady free condition, bin size sensitivity study (all time steps).

To quantify the difference in velocity, change the bin size (l_B), a line that spans the chord length of the airfoil at $y = 75\text{mm}$ ($y/c = 0.5$) on top of the Pressure Side (PS) of the airfoil was considered (as visible in Figure 4.5), and the velocity (normalised by the mean velocity of each measurement plane, around $9.7\text{m}\,\text{s}^{-1}$ for all the conditions) is plotted in Figure 4.6. Based on these results, the 5mm presents higher velocities, so, for this reason, it was not considered. While all the others are quite smooth and very close, a slight decrease is experienced when the bin size (l_B) increases. Only for $l_B = 5\text{mm}$ and 10mm some velocity information are missing at low values of x/c. Discarding also the bigger bin size (from a graphical/qualitative point of view), the two options remaining were the 10mm and the 15mm. Even if the 10mm results in a slightly better spatial resolution, the 15mm was selected since it gave the best results for the unsteady cases, and a direct comparison was then possible.

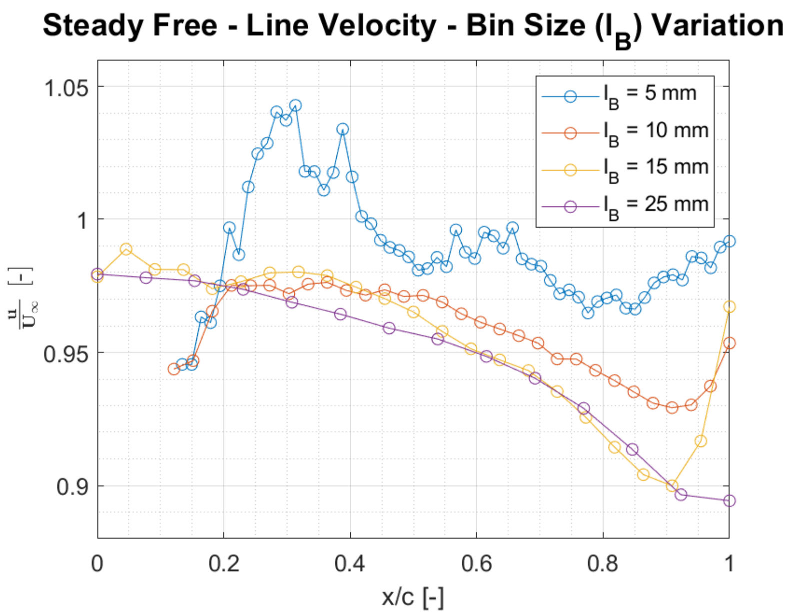

Figure 4.6: Steady free condition - Velocity change along the line (varying the bin size).

The bin size (l_B) is related to the uncertainty of the time-averaged mean velocity level (ϵ_u) computed by the ensemble averaging process. Indeed it defined the smallest length scale that is resolvable during the binning process and determines the spatial resolution of the velocity field resulting. Ideally, the value has to be as small as possible to avoid spatial modulation of measurement data. At the same time, reducing the cell size results in fewer particles per bin cell, so it should allow to include of several samples inside each bin that do not increase the velocity uncertainty level (ϵ_u) that is calculated using Equation 4.7 as introduced by Jux [82].

$$\epsilon_u = \frac{z_a \cdot \sigma_u}{\sqrt{N_{unc}}} \tag{4.7}$$

Where N_{unc} is the number of uncorrelated measurement samples inside each cell, estimated conservatively to be equal to the number of particles contained in each bin (N_{part}) as done by Cordero [83]. σ_u is the velocity standard deviation computed from the flowfield phase average. While z_a is the coverage factor, to have a confidence interval of 95% of the normal Gaussian distribution, a $z_a = 2$ was selected.

This was computed for the bin that contains the first point of the line considered in Figure 4.5. So the velocity uncertainty for the different bin sizes considered in the sensitivity study can be computed as a percentage of the mean velocity equal to 9.7m s^{-1}.

Table 4.1: Steady free condition - Velocity uncertainty - Bin size sensitivity study.

l_B = 5 [mm]	l_B = 10 [mm]	l_B = 15 [mm]	l_B = 25 [mm]
8.187%	1.974%	0.976%	0.395%

As it is possible to extract from the values in Table 4.1, which are in line with the previous results; the relative velocity uncertainty decreased, increasing the bin size (l_B), due to the more uncorrelated measurements samples (particles) included in each bin. Indeed the 25mm bin size will allow considering 125 times the number of particles included in the 5mm bin. The selected bin size equal to 15mm has a velocity uncertainty of 0.976%, indicating that the bins are big enough to allow many samples inside, leading to small uncertainty values. Increasing it more will allow better compliance of the flowfield with the wing's geometry (due to lower uncertainty levels). Still, it can also lead to an overlap between the flowfield and the reconstructed wing surface.

The same sensitivity study was also conducted for the unsteady free case, taking a time bin size of 50 steps. Also, in this case, using small bin sizes gave more noisy results (with a velocity distribution way higher than all the other bin size cases), while increasing it results in a loss in spatial resolution.

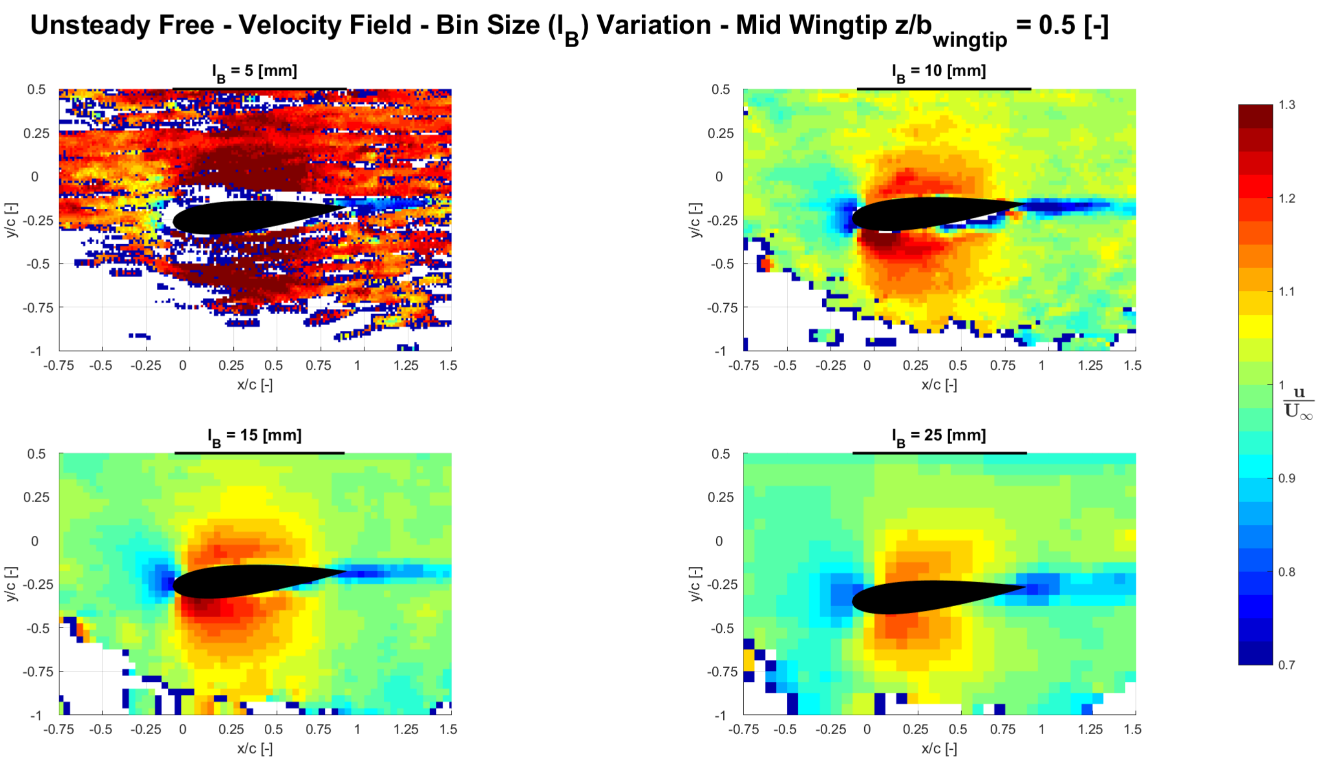

Figure 4.7: Unsteady free condition, bin size sensitivity study (50 time steps).

Looking at the velocity (normalised by the mean velocity of each measurement plane) at the same line on top of the airfoil pressure side and plotted in Figure 4.8, it is possible to visualise that at a bin size equal to 5 and 10mm, the velocity fluctuates massively. At the same time, all the others are smoother, so for this reason, these two bin sizes were discarded. Also, in this case, a velocity decrement is experienced when the bin size (l_B) is increased, and a lower spatial resolution results. The 15mm bin size is also used to analyse the unsteady cases.

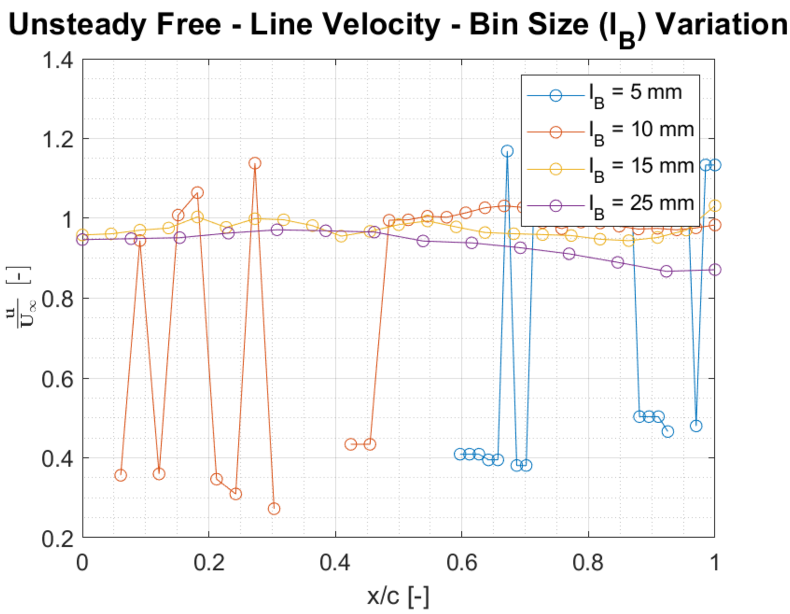

Figure 4.8: Unsteady free condition - Velocity change along the line (varying the bin size).

The uncertainty analysis was also conducted for this sensitivity study; the velocity uncertainty found at the same location as before (bin containing the first point of the line in Figure 4.7) are listed in Table 4.2.

Table 4.2: Unsteady free condition - Velocity uncertainty - Bin size sensitivity study.

$\mathbf{l_B}$ **= 5 [mm]**	$\mathbf{l_B}$ **= 10 [mm]**	$\mathbf{l_B}$ **= 15 [mm]**	$\mathbf{l_B}$ **= 25 [mm]**
51.142%	10.489%	4.654%	1.66%

With respect to the steady case, now the uncertainty is higher for all the bin sizes selected. This is due to the lower amount of particles in the bin, 13.5 times less than those in the previous sensitivity study (for the 15mm bin size). This is caused by the time kernel used in the phase-average approach introduced for the unsteady measurements, while for the steady conditions, all the time instants were considered. For the selected bin size (15mm), the uncertainty level is 4.654%.

Indeed, two methods were used for the ensemble average process based on the two temporal characteristics of the test cases measurement, respectively, for the steady and unsteady measurements. For the steady ones, the analysis was conducted in a spatial-average sense, where the .dat files are used entirely, and the binning process is done for all time steps together, spanning the entire acquisition time. Contrary, for the unsteady ones, the analysis is conducted in a phase-averaged sense (spatio-temporal), where the ensemble average is done for the particle tracks for each cycle phase, and three different time-phase instants of the gust cycle were considered (time window centred on a considered phase). Respectively $t/T_{ref} = 0$, $t/T_{ref} = 0.5$ and $t/T_{ref} = 1$ (where the time t is considered as a fraction (non-dimensionalised by) of the total reference period T_{ref}), this to have a common temporal reference frame from particles of different PIV acquisitions. Based on these, to improve the accuracy by having more data for the binning process and letting some time for the unsteady gust process to adjust and be visible. The selected time step was combined with a non-dimensional time window equal to the next and previous twenty-five time steps (creating a wanted time bin), extended symmetrically. For the $t/T_{ref} = 1$ case, the previous fifty time steps (t_B) were instead selected, while for the case $t/T_{ref} = 0$ the successive fifty time steps. Indeed, all the particles tracked that belong to this time window (time bin) are used for the ensemble averaging process. Considering the 8Hz 1-cosine gust employed in the unsteady cases, it has a period equal to $T = \frac{1}{f} = \frac{1}{8} = 0.125$s, then from total acquisition period equal to 2s it is possible to compute that the selected time windows is around the 15% of the total gust time ($T_{time,bin} = \frac{2}{5457} \cdot 50 = 0.018$s, $\frac{0.018}{0.125} \cdot 100 = 14.66\%$) and around 1% of the total acquisition time ($\frac{50}{5457} \cdot 100 = 0.916\%$). This number of successive time steps was decided after an evaluation of different values and gave the best results in terms of flow field visualisation with a consequent good statistical convergence of the results. Smaller values resulted in missing information and noisy flow field distribution due to the small number of particles tracked in such a small time bin. Also, higher values were tried, resulting in a loss in temporal resolution (without increasing the quality of the results). Indeed, this value can be increased until the time of transit of the flow tracers particles over the wing chord remains much smaller with respect to the period of oscillation of the wing. This means that the flow field is frozen, and several time steps (included in this time bin) can be used for the ensemble averaging without losing temporal resolution. Since the selected temporal bin size is larger than the separation time between two consequent images, more particles that belong to the same track are allowed to be part of the ensemble averaging process, so for this reason, the particles are strongly correlated in time. The time bin (t_B) sensitivity study for the ensemble average process (which represents the number of time intervals for the ensemble averaging process), conducted for the unsteady free condition (using $l_B = 15$mm at the middle plane of the wingtip $z/b_{wingtip} = 0.5$ or $z/b = 0.85$) is visible in Figure 4.9. Respectively a $t_B = 5$ corresponds to a $t_{integration}/T_{ref} = \frac{5}{5457} = 9.162 \times 10^{-4}$, while $t_B = 25$ corresponds to a $t_{integration}/T_{ref} = \frac{25}{5457} = 4.581 \times 10^{-3}$, then $t_B = 50$ corresponds to a $t_{integration}/T_{ref} = \frac{50}{5457} = 9.162 \times 10^{-3}$ and finally $t_B = 100$ corresponds to a $t_{integration}/T_{ref} = \frac{100}{5457} = 1.832 \times 10^{-2}$.

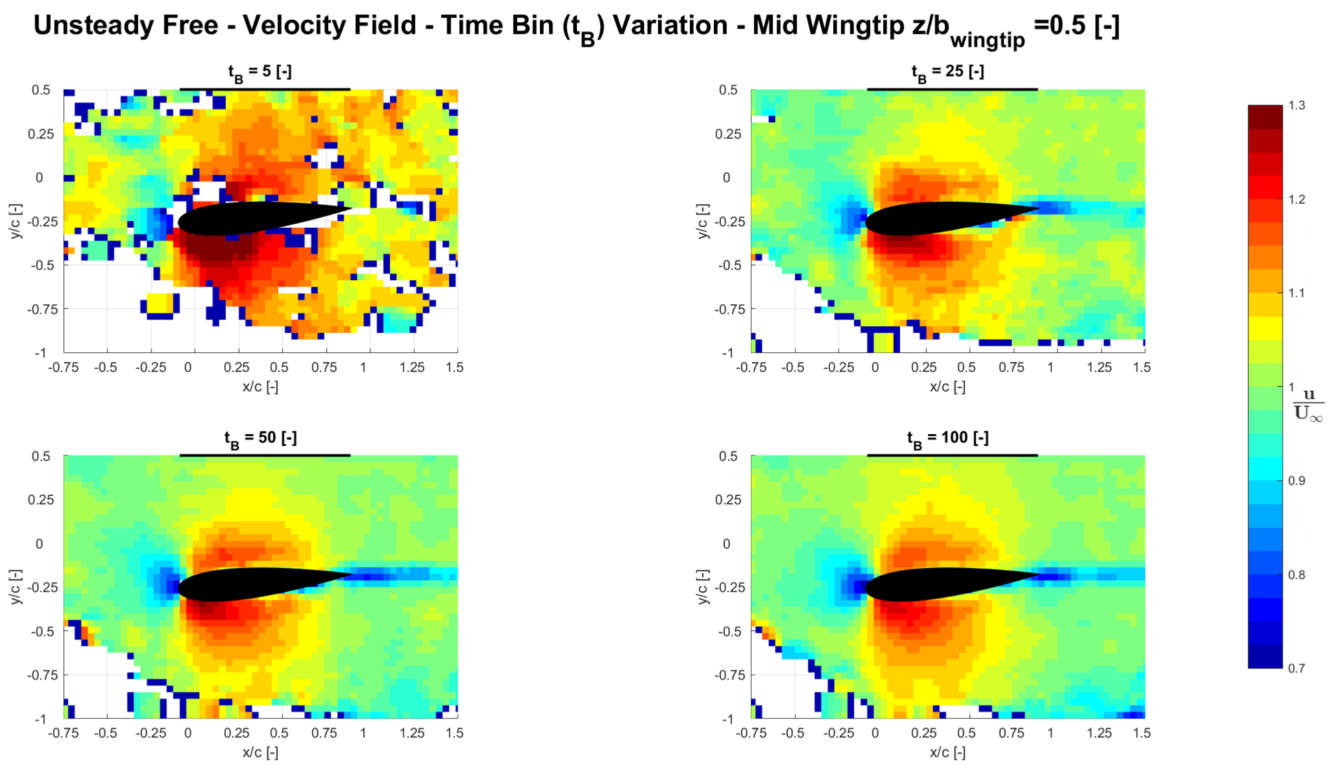

Figure 4.9: Unsteady free condition, time bin sensitivity study (15mm bin).

Again, to quantify the difference in terms of velocity, changing the time bin (t_B), the same line is considered, and the velocity (normalised by the mean velocity of each measurement plane) that results were plotted in Figure 4.10. Based on these results, it was decided to discard the smaller time bin since it presents a fluctuating velocity distribution. While for the others, all the velocities are pretty smooth and very close to each other, with the velocity slightly decreasing while increasing the time bin (t_B) size, so the final decision to use the value 50 was based on a graphical point of view, since increasing further to 100 time steps is not adding more information. In contrast, taking 100 time steps will decrease the temporal resolution (it spans 29.32% of the total gust duration).

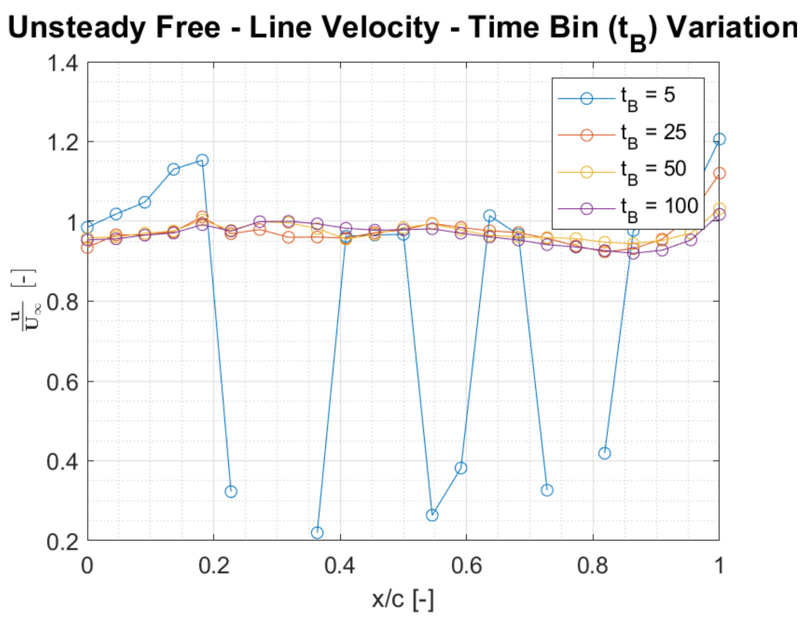

Figure 4.10: Unsteady free condition - Velocity change along the line (varying the time bin).

Finally, the uncertainties that arise from the time bin selected are listed in Table 4.3.

Table 4.3: Unsteady free condition - Velocity uncertainty - Time bin sensitivity study.

t_B = 5 [-]	t_B = 25 [-]	t_B = 50 [-]	t_B = 100 [-]
29.938%	7.439%	5.138%	3.035%

Decreasing the time bin will lead to a higher velocity uncertainty due to the lower amount of particles in the bin. For the selected time bin (50), the velocity uncertainty level is 5.138%.

A factor affecting the uncertainty (due to an uneven particle concentration in the measurement volume) is the irregular seeding from the FSI that generates the HFSB. This affected equally all the cases considered for the sensitivity study. Fixing this issue is a way to decrease the velocity uncertainty. Moreover, two additional options are possible, the time bin and the bin size can be increased; these will help to increase the number of particles inside each bin but will reduce the flowfield spatial resolution.

For each condition, it was decided to visualise the 2D flowfield distributions in four different spanwise locations. At the last part of the wing ($z/b = 0.7$), at the beginning of the wingtip ($z/b = 0.78$ or $z/b_{wingtip} = 0.25$), in the middle part of the wingtip ($z/b = 0.85$ or $z/b_{wingtip} = 0.5$) and at the end of the wingtip ($z/b = 0.92$ or $z/b_{wingtip} = 0.75$). This was decided to have a complete overview and better insight into the wingtip, the most interesting region of the entire wing. These different heights were selected after the six degrees of freedom calculated were used to transform the coordinates from the laboratory reference frame to wing one, the values (three rotations and three translations) used are listed in Table 4.4. To better visualise, it was also decided to normalise the velocity distribution values by the mean velocity in the plane of each measurement (around $9.7\,\mathrm{m\,s^{-1}}$ for all the conditions). Then the colourmap limit was set from 0.7 to 1.3 $\frac{u}{U_\infty}$. The airfoil is positioned correctly for each instant based on the known position of the painted fiducial markers from the structural characterisation reconstruction explained in the next section.

Instead, for the Fluid-Structure Interaction (FSI) events 3D visualisation figures, all four planes are plotted together with the marker positions from the wing reconstruction code. For the steady cases, the position of the wing was averaged for all the time steps. While for the unsteady cases, the position is averaged using for the temporal resolution only the 50 time steps at the beginning, middle or end of the measurement, based on the time instant t/T_{ref} that was intended to be represented.

4.4 STRUCTURAL CHARACTERISATION

For the structural behaviour characterisation, the first step was to find the six Degrees Of Freedom (DOF) necessary for the rigid body transformations (translations and rotations) to convert from the laboratory reference system to the wing one. First, the separated datasets (Side 1 and Side 2) containing the tracked fiducial markers painted on the wing are put together in one enormous array. Then, the six degrees of freedom are found using an optimisation algorithm (using the Matlab built-in constrained nonlinear optimisation algorithms *fmincon*). Through a minimisation process, the distance between the coordinates of the tracked and painted markers matched the markers tracked through the IPR process with the nearest one painted on the wing in reality (minimising the average distance between these two sets). This uses the static dataset of the wing without any flow from the wind tunnel (assuming fully structural staticity neglecting any vibration or oscillation caused by uncontrolled external factors). The selected reference frame of reference was with the origin coinciding at the root Leading Edge (LE) point of the wing with the positive x-axis pointing in the chordwise direction, the positive y-axis pointing in the cross-flow direction, away from cameras 1/2/3 (pointing toward the left side of the wing looking in the front view from the exit of the wind tunnel) and the positive z-axis pointing in the spanwise direction. The six degrees of freedom are respectively the rotations (computed firstly) and translations in all three directions (x, y and z). Respectively, the rotation with respect to the vertical z-axis (spanwise direction) corresponds to changes in the wing pitch angle. Instead, the rotation with respect to the transverse y-axis (cross-flow direction) is equivalent to the modifications in the wing sweep angle. Finally, the rotation with respect to the longitudinal x-axis (chordwise direction) is comparable to adjustments in the wing dihedral angle. These are listed and plotted below in Figure 4.11 and Table 4.4. Please note in the figures that the grey dashed line indicates the mean degree of freedom in the entire period, these values, also reported in the table, will be used for the coordinates system correction.

In all the figures, a big 'jump' is present at 0.3s and 1.5s; this is due to the summing up of numerical error during the optimisation procedure, while the noisy results before 0.4s are due to images with a low number of markers recorded.

Table 4.4: 6 degrees of freedom.

x Rotation [°]	y Rotation [°]	z Rotation [°]	x Translation [mm]	y Translation [mm]	z Translation [mm]
0.564	-0.298	-0.321	44.289	-34.28	592.617

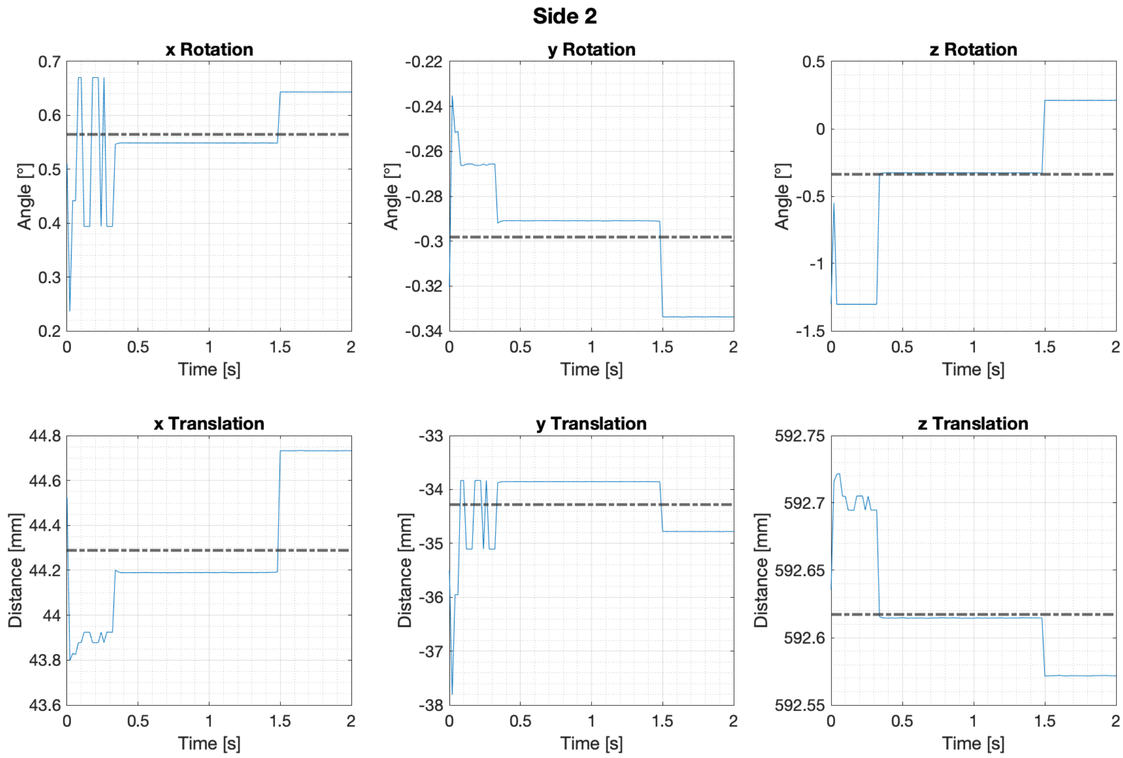

Figure 4.11: 6 degrees of freedom, 3 rotations and 3 translations.

Then, knowing these six degrees of freedom, the coordinates of the markers tracked by the IPR process are corrected to get the markers in the wing reference frame. This was done by adding the 3 found translations and multiplying them with a rotation matrix that includes the 3 rotation angles).

$$\mathrm{R} = \mathrm{R}_z(Rot_x)\cdot R_y(Rot_y)\cdot R_x(Rot_z) = \begin{bmatrix} \cos(Rot_x) & -\sin(Rot_x) & 0 \\ \sin(Rot_x) & \cos(Rot_x) & 0 \\ 0 & 0 & 1 \end{bmatrix} \cdot \begin{bmatrix} \cos(Rot_y) & 0 & \sin(Rot_y) \\ 0 & 1 & 0 \\ -\sin(Rot_y) & 0 & \cos(Rot_y) \end{bmatrix} \cdot \begin{bmatrix} 1 & 0 & 0 \\ 0 & \cos(Rot_z) & -\sin(Rot_z) \\ 0 & \sin(Rot_z) & \cos(Rot_z) \end{bmatrix} \tag{4.8}$$

Looking at the results displayed in Figure 4.12, it is possible to state that the match is very good, particularly at the wingtip, where all the IPR tracked markers coincide with the 48 fiducial markers painted. While on the wing, a consistent number of markers are missing due to the IPR process that was unable to track them. Indeed out of 64, just 19 were tracked (in particular, the ones closer to the root were missing). Overall this was not a big problem since the optimisation worked very well. The NACA 0018 airfoil is placed at each marker row spanwise position by implementing its relative thickness equation.

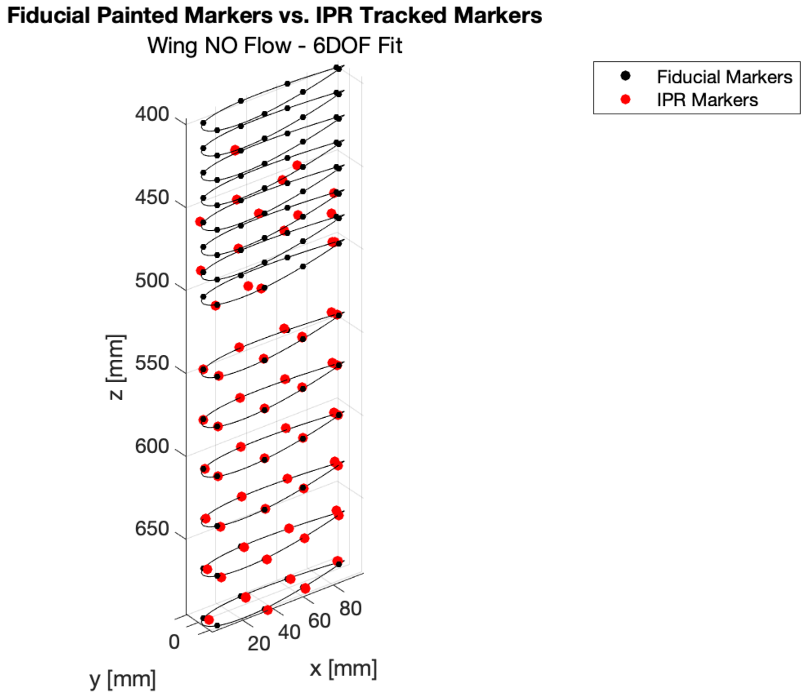

Figure 4.12: Fiducial markers fit.

As visible in Figure 4.13, the outliers present in the dataset were removed after the first fitting procedure setting as a threshold for the distance to the nearest reference marker; four times the mean Euclidean norm; indeed, no outliers were present in this 6 degrees of freedom optimisation fit. Furthermore, another outlier removal method was also used in the last step of the wing reconstruction phase. Indeed, a distance with a radius of 5mm was set as a threshold from the position of each marker painted on the wing at each time instant. All the markers outside were removed. In addition, if more than one marker were present in that radius threshold, only the one closer to the real painted marker is kept, with all the others discarded.

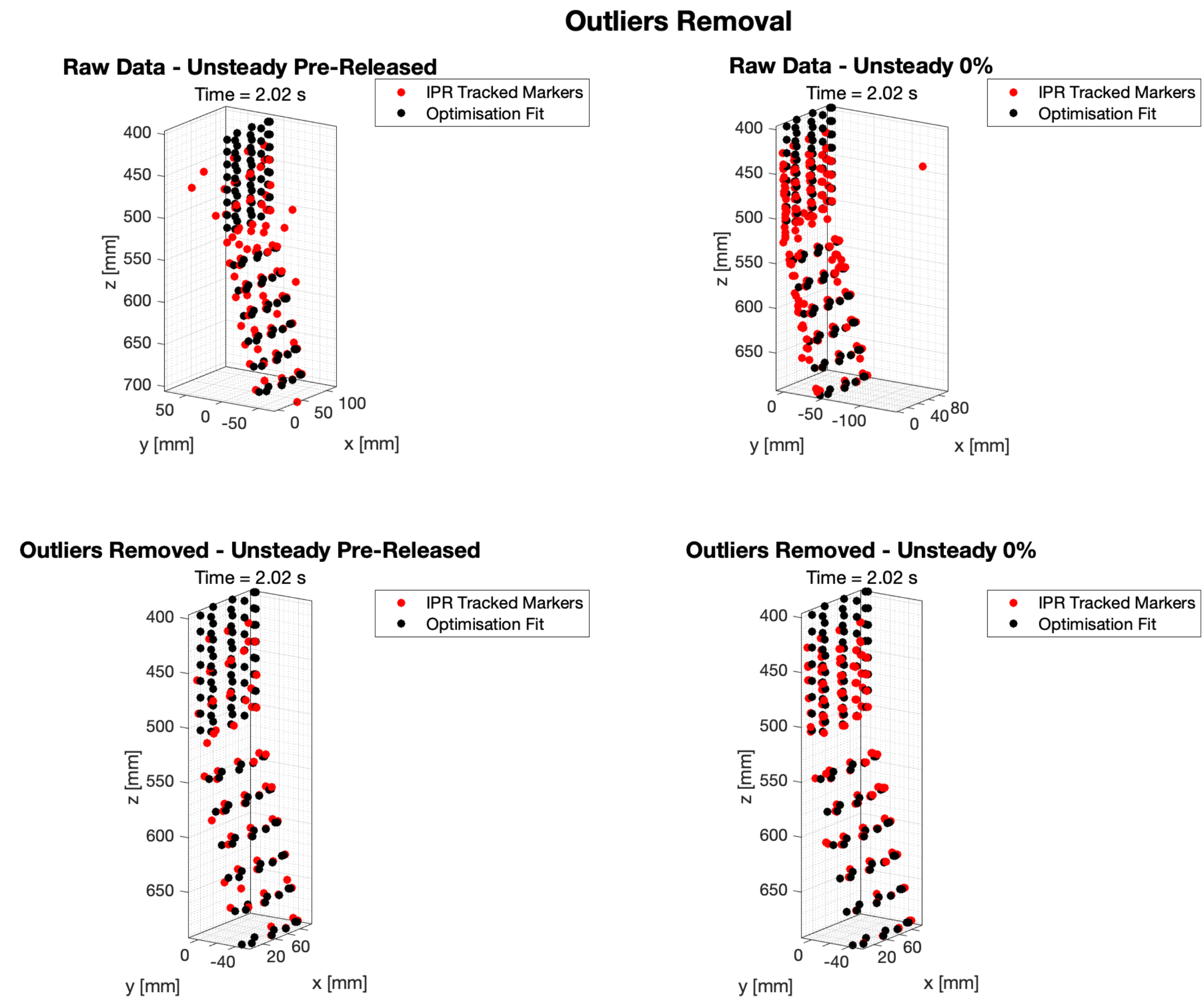

Figure 4.13: Outliers removal results.

After this, the next step was to find the last two missing 'degrees of freedom', the wingtip deflection angle (θ) and the bending moment coefficient (C_B), respectively. For these, the measurements recorded with the conventional sensors are used. Indeed, as explained in section 4.1, the wingtip fold angle and the bending moment coefficient can be derived from the recorded information of the potentiometer and strain gauges, respectively. These two parameters were used in the optimisation fit procedure to deflect the wingtip and bend the wing fiducial markers painted on the wing to match the ones found through the IPR process. Also, the flare angle of the wingtip was taken into account, meaning that as the wingtip deflects, the airfoil sections experience a rotation that causes a change in z-coordinate.

A wing model with the wingtip angle (θ) and bending model coefficient (C_B) as inputs and the final position of the wing/wingtip as output was constructed to give a 3D visualisation of the wing reconstruction technique. To do so, the wingtip angle from the potentiometer was used directly. While for the bending moment coefficient (C_B), a different method was used, indeed the wing was bent, fitting a third-order polynomial through the markers in the spanwise direction, using for the coefficient A of the cubic bending function stated in Equation 4.9 the value of the Bending Moment Coefficient (C_B) recorded by the strain gauges. This determines the bending (y-coordinate) displacements and the consequent spanwise (z-coordinate) displacement. To confirm that this approach has a physical meaning, a derivation was done (visible below) to prove that the polynomial order chosen was high enough to bend the wing realistically.

$$d(z) = A \cdot z^3 + B \cdot z^2 + C \cdot z + D \tag{4.9}$$

Where C and D are equal to 0 due to the zero slope (θ_S) (first derivative $d'(z = 0) = 0$) and zero deflection (v) ($d(z = 0) = 0$) at the root of the wing (assumed to be a One-Dimensional (1D) beam clamped at the root), illustrated in front view (looking from inside the wind-tunnel) in Figure 4.14. To be able to directly use the Bending Moment Coefficient (C_B) from the strain gauges inside the third-order polynomial without the need for a second coefficient, the B term was assumed to be equal to zero. This model follows the simplified structural model and the tip point force load assumption of the Euler-Bernoulli beam theory as presented by Wang et al. [84]. A beam is deflected (assuming small deformation) in the direction perpendicular to the wing chord (dominant motion degree of freedom) by a lateral point force assuming no effects from rotatory inertia and shear torsional deformation (very small compared to bending effects), with the remaining degrees of freedom neglected. The wing/wingtip free-body diagram represents only the wing as a beam of length L where a force F_B is applied at the tip (point B). This represents the lift due to the positive angle of attack (5°. Ideally, the lift is distributed with an elliptical shape along the entire finite wing span, but for a simplified representation, here is considered a point force at its tip. In contrast, at the root (point A), the reaction forces and moment are A_y, A_z (positive on the positive y and z directions) and M_A (positive counterclockwise). The weight of the wing w is represented at the root (point B), pointing towards a positive z coordinate.

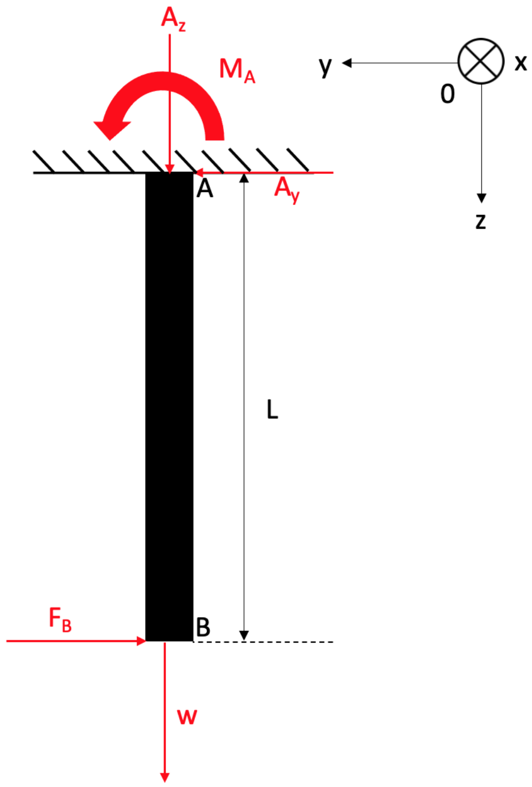

Figure 4.14: Wing Free-Body Diagram (FBD).

To calculate the reaction forces and moment at the point A, the sum of forces and moments are done around this point:

$$\sum F_z = 0 \quad \Rightarrow \quad A_z + w = 0 \quad \Rightarrow \quad A_z = -w \tag{4.10}$$

$$\sum F_y = 0 \quad \Rightarrow \quad A_y - F_B = 0 \quad \Rightarrow \quad A_y = F_B \tag{4.11}$$

$$\sum M_A = 0 \quad \Rightarrow \quad M_A + F_B \cdot L = 0 \quad \Rightarrow \quad M_A = -F_B \cdot L \tag{4.12}$$

Then, doing a cut normal to the beam, the remaining part (with length z) is illustrated in Figure 4.15. At the cutting line (point C), the normal force σ, shear force τ and the moment M appear.

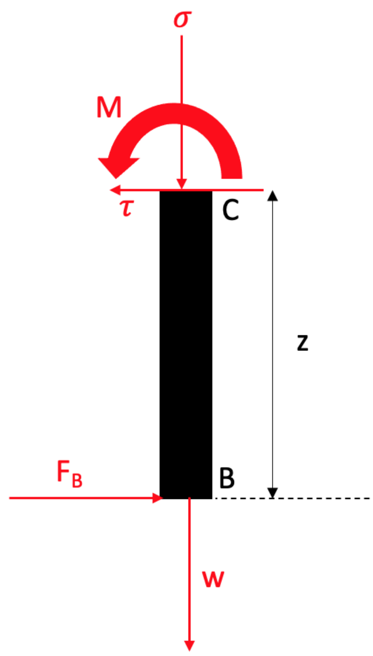

Figure 4.15: Cut wing Free-Body Diagram (FBD).

Also, in this case, the sum of moments around the cutting line (point C) was done to find a relation of the internal moment with the lift force F_B.

$$\sum M_C = 0 \quad \Rightarrow \quad M + F_B \cdot z = 0 \quad \Rightarrow \quad M = -F_B \cdot z \tag{4.13}$$

Now the moment-curvature relationship can be derived, where the flexural rigidity (EI) is the product of the material modulus of elasticity (E) that is a function of how stiff a material is and the elements' second moment of area (I) that is a function of the element shape.

$$M = -EI \cdot \frac{\partial^2 v}{\partial^2 z} \quad \Rightarrow \quad -F_B \cdot z = -EI \cdot \frac{\partial^2 v}{\partial^2 z} \quad \Rightarrow \quad \frac{\partial^2 v}{\partial^2 z} = \frac{F_B \cdot z}{EI} \tag{4.14}$$

Doing the integral of this equation, the slope (θ_S) relationship results, where C_1 is an integration constant:

$$\int_z \frac{\partial^2 v}{\partial^2 z} dz = \frac{F_B \cdot z}{EI} \quad \Rightarrow \quad \frac{\partial v}{\partial z} = \frac{F_B \cdot z^2}{2 \cdot EI} + C_1 \quad \Rightarrow \quad \theta_S = \frac{F_B \cdot z^2}{2 \cdot EI} + C_1 \tag{4.15}$$

To obtain the displacement relationship, another integral was computed, where C_2 also, in this case, is an integration constant.

$$\int_z \frac{\partial v}{\partial z} dz = \frac{F_B \cdot z^2}{2 \cdot EI} + C_1 \quad \Rightarrow \quad v = \frac{F_B \cdot z^3}{6 \cdot EI} + C_1 \cdot z + C_2 \tag{4.16}$$

Applying the Boundary Conditions (BC) at the root of the wing ($z = 0$), where the deflection (v) and the slope (θ_S) are equal to zero, results that both integration constants (C_1) and (C_2) are equal to zero.

$$0 = \frac{F_B \cdot 0^2}{2 \cdot EI} + C_1 \quad \Rightarrow \quad C_1 = 0 \tag{4.17}$$

$$0 = \frac{F_B \cdot 0^3}{6 \cdot EI} + C_1 \cdot 0 + C_2 \quad \Rightarrow \quad C_2 = 0 \tag{4.18}$$

Knowing this, the two final equations can be derived. Respectively the wing slope (θ_S) and deflection (v) in the function of the span z of the wing.

$$\theta_S = \frac{F_B \cdot z^2}{2 \cdot EI} \quad (4.19) \qquad v = \frac{F_B \cdot z^3}{6 \cdot EI} \quad (4.20)$$

This deflection coefficient (v) related to the cube of the z-coordinate proves that the third-order polynomial selected for the fitting model was indeed accurate. So the coefficient A used in the third-order deflection equation displayed in Equation 4.9 was directly substituted with the Bending Moment Coefficient (C_B) recorded from the strain gauges applied at the root of the wing. Another method that uses directly Equation 4.20 to compute the deflection at each wing z location was investigated. Where the force F_B can be retrieved from the strain gauges recorded signal. Unfortunately, due to the unavailability of the wing model's flexural rigidity value (EI), this last equation cannot be used directly to compute the deflection. Indeed, the value of EI can be retrieved using a FEM model, but it was beyond the scope of this thesis. Furthermore, the wing/wingtip was modelled with a more realistic constant distributed lift along the entire span. However, the deflection equation was still dependent on the cube of the coordinate z, proving the accuracy of the selected polynomial deflection equation again.

5
Results and Discussion

This chapter presents the results for all the test matrix cases that were investigated with Particle Image Velocimetry (PIV) and conventional sensors, and a discussion about it is given.

5.1 Steady Conditions

For the steady conditions (no gust employed), the aerodynamic and structural results for the two different hinge conditions, free and fixed, are illustrated in the following subsections.

5.1.1 Flow-Field Visualisation

The 2D velocity (stream-wise component u) field distributions for both Steady Free and Steady Fixed conditions, considering all the time steps, are visible in Figure 5.1 and Figure 5.2, these for four different plane locations, one at the end the wing ($z/b = 0.7$, 495mm from the wing root) and three on the wingtip (start $z/b = 0.78$, mid $z/b = 0.85$ and end $z/b = 0.92$. Correspondingly 50mm, 100mm and 150mm from the hinge or $z/b_{wingtip} = 0.25$, $z/b_{wingtip} = 0.5$ and $z/b_{wingtip} = 0.75$. The black mask representation of the wing section surface (airfoil) at each different plane has been reconstructed and positioned, knowing the tracked fiducial markers information.

Looking at the velocity field that results from the steady free conditions, all the main linear aerodynamic flow field features are visible. Indeed, the flow hits the airfoil and decelerates from the freestream velocity at the stagnation point (blue dot), the point where the flow velocity is equal to 0 at the Leading Edge (LE) of the airfoil Pressure Side (PS). Instead, at the Suction Side (SS) of the airfoil (bottom side), the flow accelerates (more extensive red region) going over the airfoil surface (due to the angle of attack (α)) and finally, after it leaves the Trailing Edge (TE) again slows down (blue line region) and it forms a wake (non-linear aerodynamic effect). Furthermore, non-linear flow field features are also present; at the end wing location, a region of separated flow on the second half of the chord on the airfoil PS is visible; this is not present in the wingtip slices.

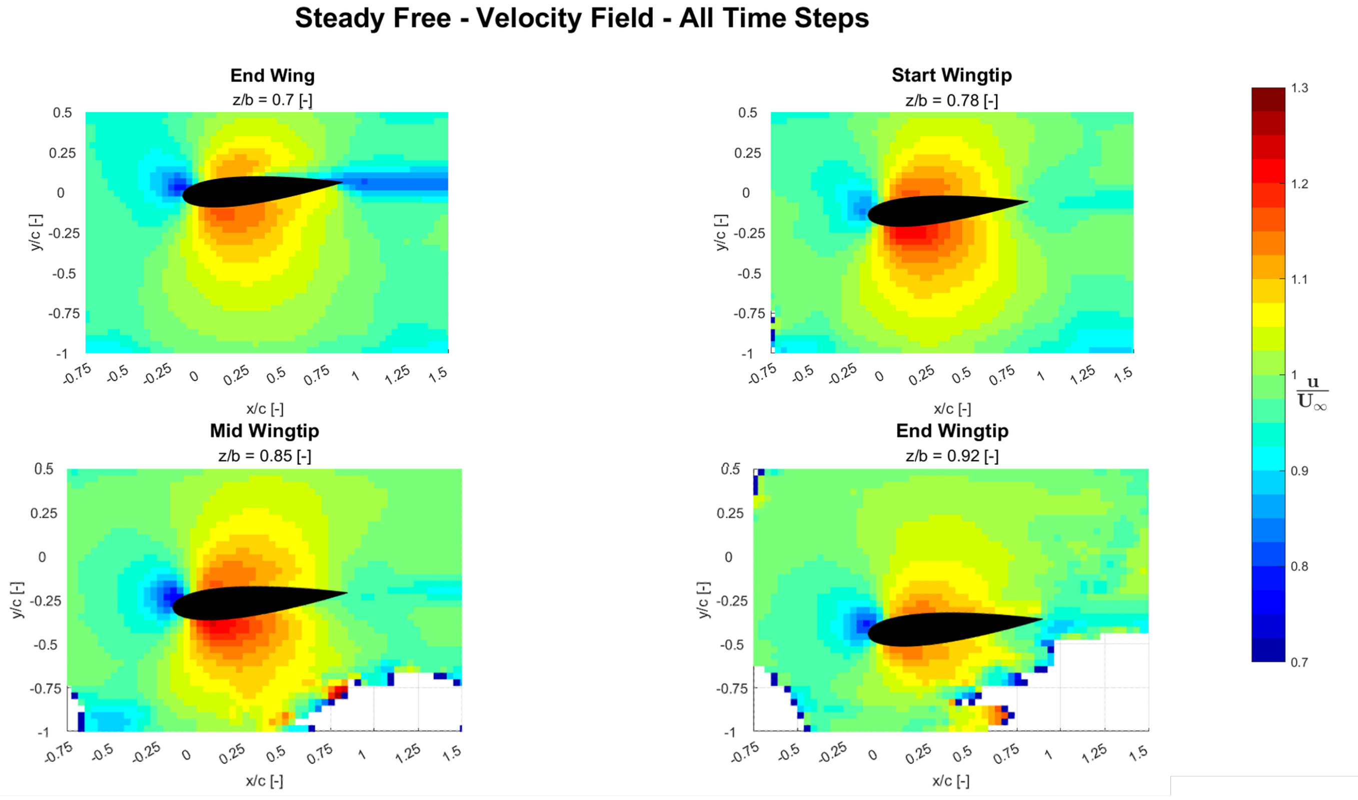

Figure 5.1: Flow field for the steady free condition, all time steps.

The same as above is experienced in the steady locked condition. Here some more missing data are visible (white region), particularly at the higher z/b values (near the end of the wingtip). This is due to the failure to fulfil the particle concentration requirement ($N_p < N_{p_{min}}$) inside each interrogation window (so no particles are present at all since $N_{p_{min}}$ was set to be equal to 1), but also caused by the non-uniform seeding produced during the wind tunnel experiment caused by some blocked HFSB nozzles. Again, separated flow is present only at the end of the wing on the PS; this proves the good design of the wingtip. Indeed for this wingtip, it is essential to have an attached flow allowing a lower pressure drag without decreasing the high aerodynamic efficiency of the hinged-folding wingtip.

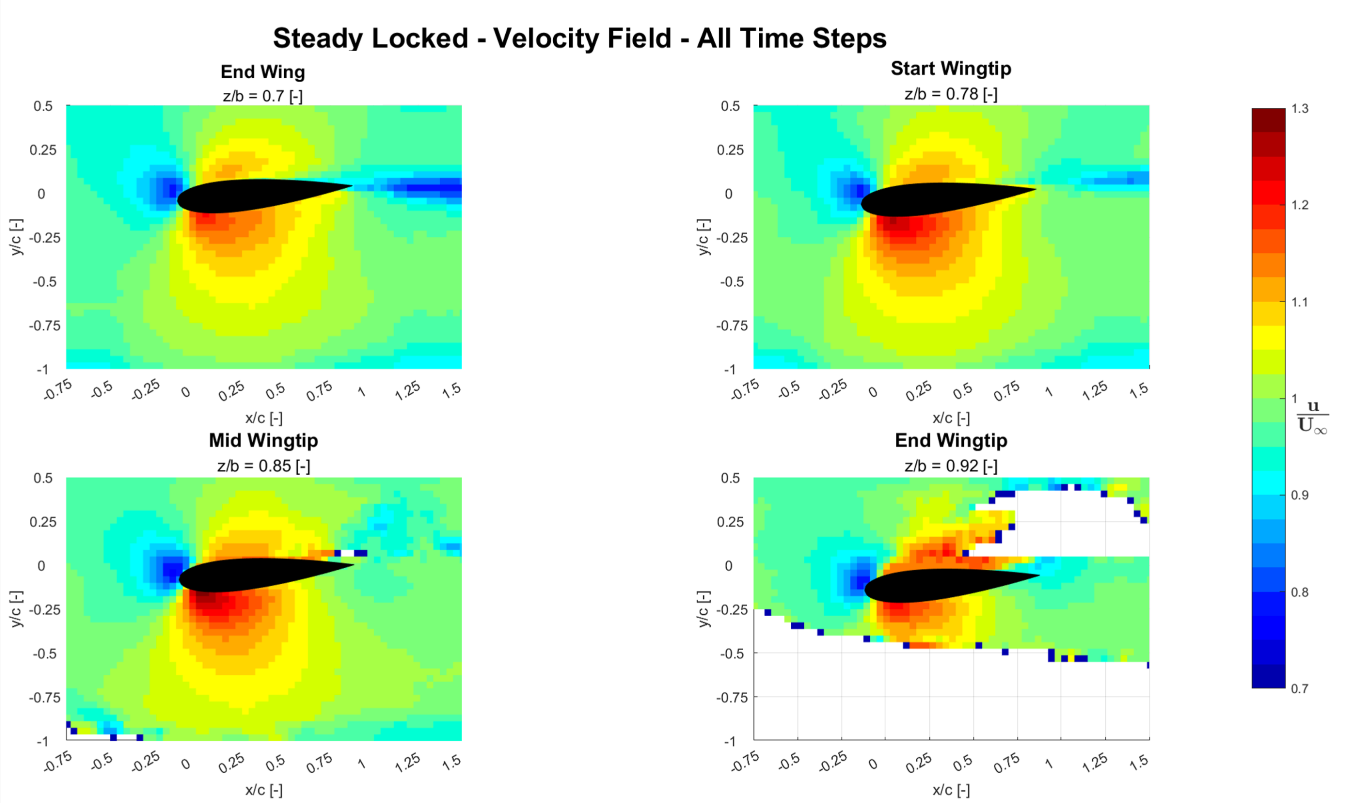

Figure 5.2: Flow field for the steady locked condition, all time steps.

Figure 5.3 represents the 3D visualisation of the wing/wingtip structural position (averaged for all time steps) and the flow field distribution at the four planes displayed above. Overall, the match of the wing reconstructed (average position for all time steps) and the flow is very good. Indeed, all the flow features illustrated above follow the wing surface geometry position.

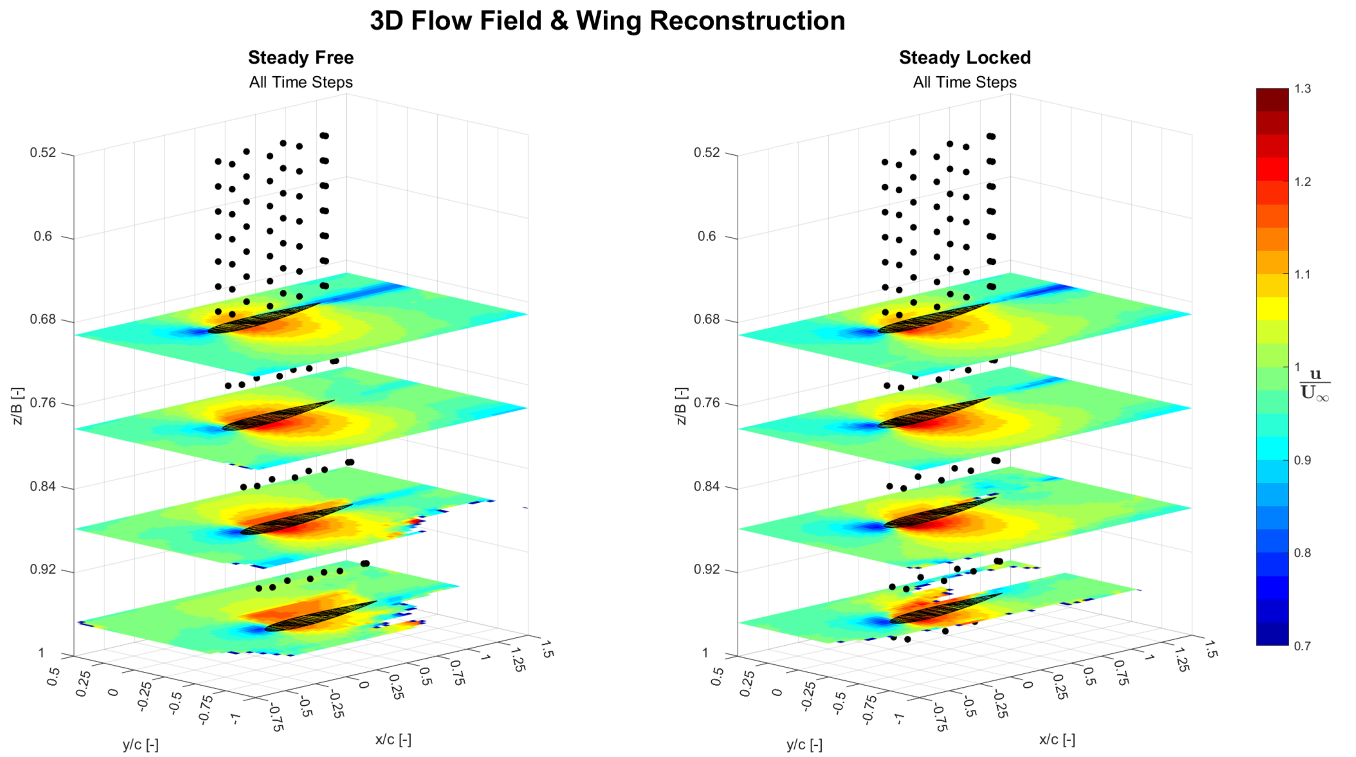

Figure 5.3: 3D flow field and wing reconstruction for the steady cases, all time steps.

5.1.2 STRUCTURAL BEHAVIOUR

Regarding the structural behaviour of the wing, the two found degrees of freedom by the conventional sensors are presented. Indeed, in Figure 5.4, the wingtip deflection angle (θ) recorded by the potentiometer placed on the hinge of the wing is displayed.

For the free case, it is possible to see that the wingtip angle starts at 10°, oscillating in the transient phase (reaching peak values of 15.4°) and stabilising at around 12.8° after it. This is due to the flow from the wind tunnel that is deflecting the wingtip before the start of the experiment (due to the already released hinge). While for the locked case where the hinge is not released, it is constant around 0.91° in the transient phase and then stays at 0.82° in the steady region. The first part of the graphs (more oscillatory), until a time equal to 3s, represents the transient response of the wingtip, while after this period, the wingtip angle reaches a steady state.

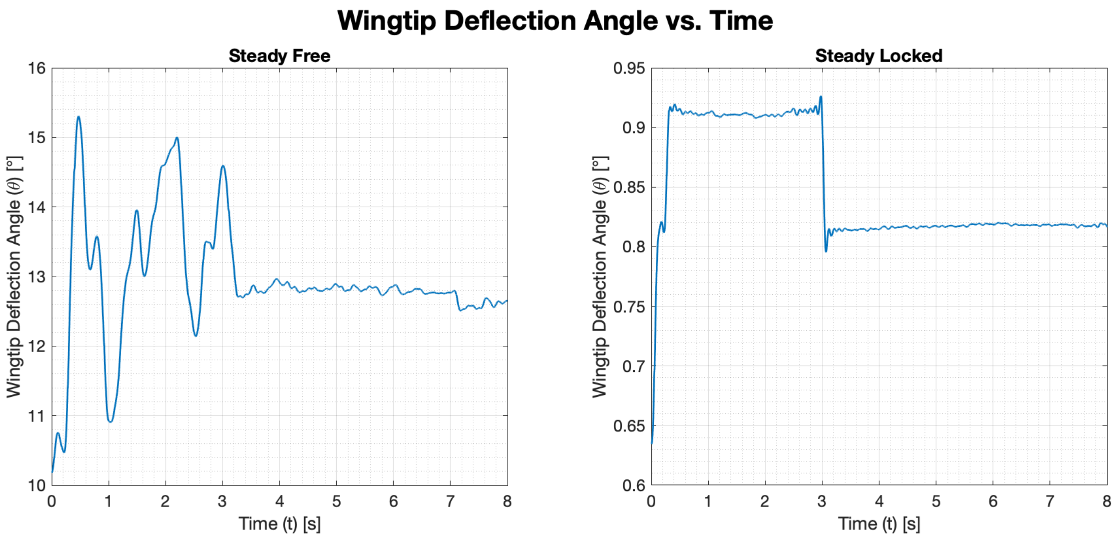

Figure 5.4: Wingtip angle (θ) for the steady conditions measured with the potentiometer.

Then, the last 'degree of freedom' missing, the bending moment coefficient (C_B) recorded by the strain gauges applied at the root of the wing and computed using Equation 4.2 is illustrated in Figure 5.5. As it is possible to see, the free case where the wingtip is allowed to move is more oscillatory in the transient phase with respect to the locked, while after, it remains constant at values closer to 0.025. Instead, the recorded values are higher for the locked case and oscillate around 0.064. This is due to the locked hinge and the aerodynamic force from the flow that creates a higher moment at the root of the wing. Overall, the moment coefficient measurements are noisier with respect to the wingtip angles (particularly in the plateau region) due to the vibrations induced by the HFSB hitting the wing.

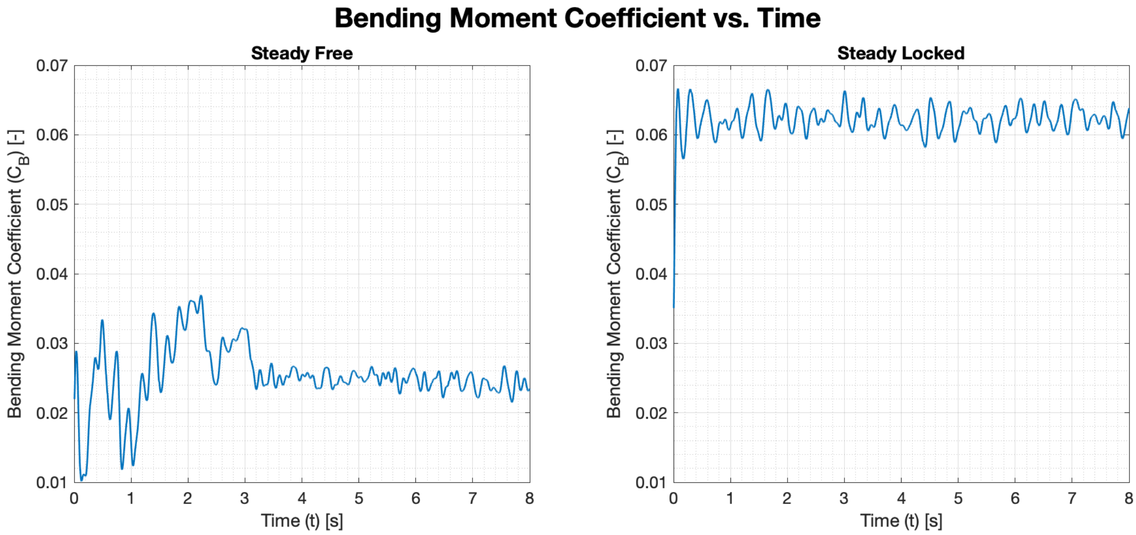

Figure 5.5: Bending moment coefficient (C_B) for the steady conditions measured with the strain gauges.

Then, the two degrees of freedom shown before are used to bend the wing and deflect the wingtip to visualise the behaviour of the complete 3D wing compared with the actual fiducial painted markers tracked with the IPR process. This is shown in Figure 5.6, Figure 5.7 and Figure 5.8. Respectively for $t = 0$s ($t/T_{ref} = 0$ [-]), $t = 0.49$s ($t/T_{ref} = 0.5$ [-]) and $t = 0.99$s ($t/T_{ref} = 1$ [-]), using $T_{ref} = 1$s for both free and locked hinge condition. Looking at these figures is possible to say that the match between the wing reconstruction model using the two missing degrees of freedom from the potentiometer and the strain gauges is accurate with the fiducial markers painted on the wing and tracked with the fiducial markers painted on the IPR process. Indeed, the reconstruction seems to be good from a qualitative point of view, with a wingtip deflection close to zero at the wing root and progressively increasing towards the end of the wingtip. Some differences can be attributed to disturbances or reflections during the wind tunnel experiment. Still, for all the different periods (start, middle and end of the experiment), both the wingtip angle (θ) and the bending of the wing (based on C_B) are represented correctly.

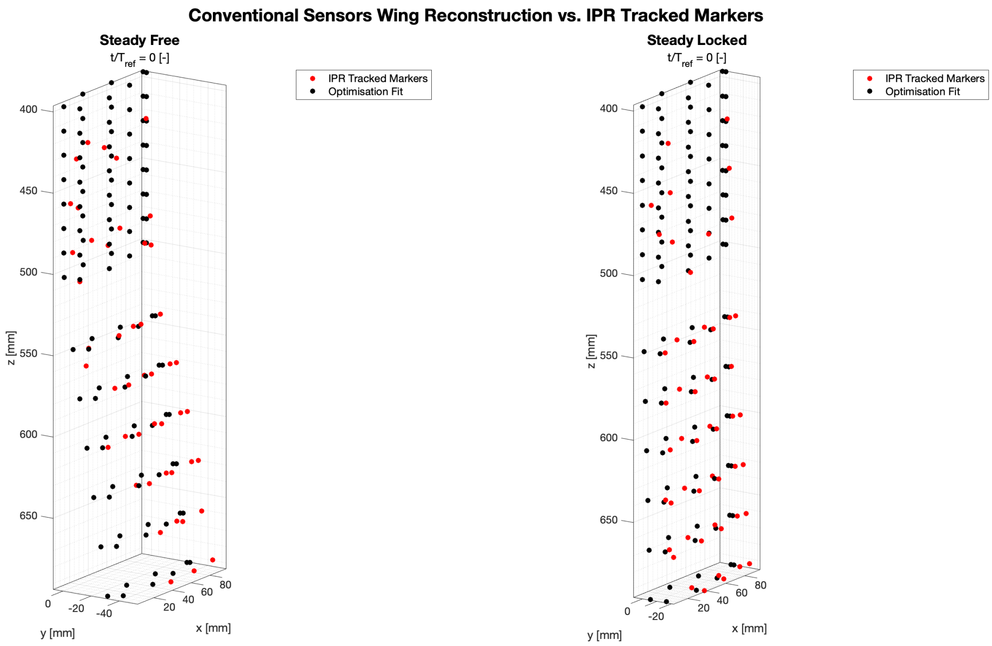

Figure 5.6: Wing reconstruction vs. IPR, $t/T_{ref} = 0$ [-].

Most 112 painted fiducial markers (56 per side of the wing) are tracked continuously over the entire acquisition time. However, for some of them, the tracking is interrupted due to uncontrolled events like the movement of painted markers out of the measurement volume, the alteration of the imaged marker's shape and their particle light intensity and the positional uncertainty from the tracking procedure due to other setup limitations.

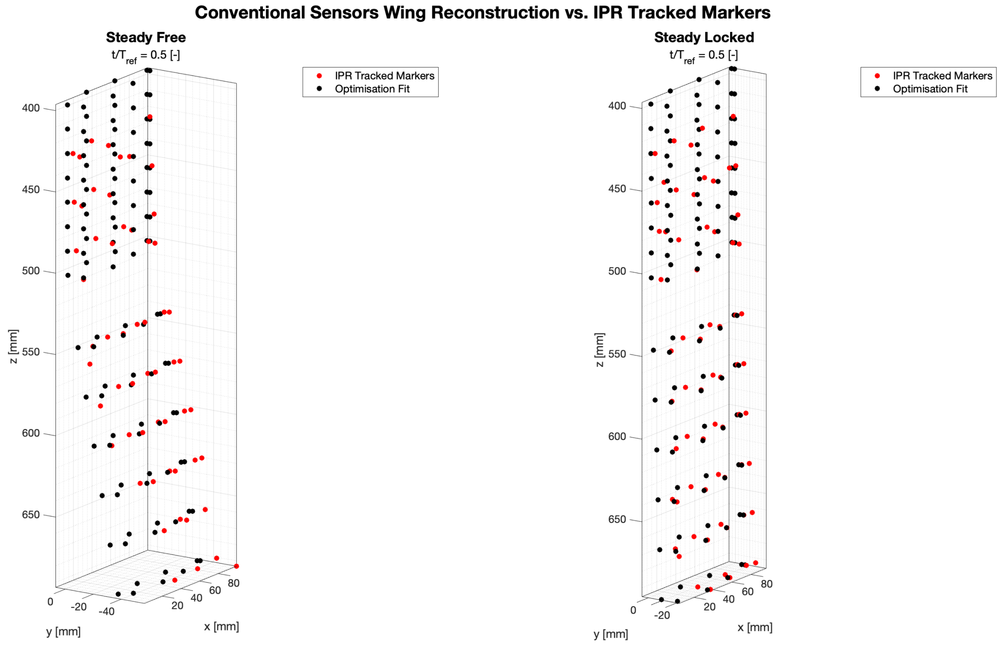

Figure 5.7: Wing reconstruction vs. IPR, $t/T_{ref} = 0.5$ [-].

Overall, on the wing, where only the bending degree of freedom is used in the reconstruction process, the match with the IPR tracked markers is very accurate. On the wingtip, instead, beyond the bending, the wingtip deflection angle is also used for the optimisation fit. Indeed, here, a slightly more deviation is visible than the tracked markers, particularly at the end of the wingtip. This is due to the combination of these two degrees of freedom causing some uncertain errors.

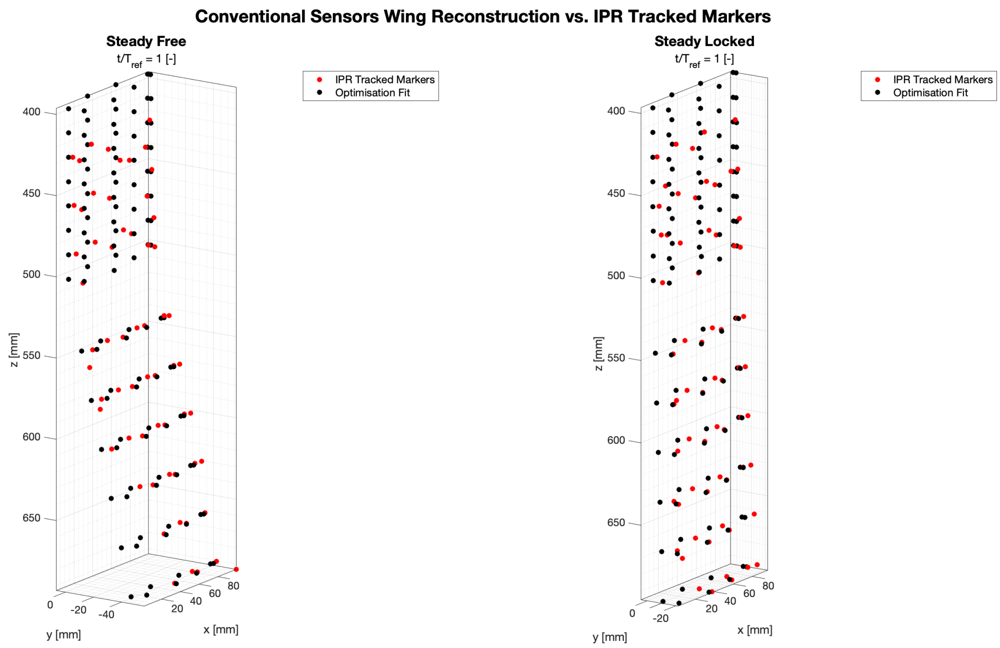

Figure 5.8: Wing reconstruction vs. IPR, $t/T_{ref} = 1$ [-].

To quantify the difference between the wing reconstruction through the data gathered from the conventional sensors (potentiometer and strain gauges) and the fiducial markers painted on the wing, tracked with the IPR process; the average distance between the two sets of markers for each hinge condition for both the wing and the wingtip was found. The closer tracked marker was selected for each painted marker, and the average distance from it (considering all 3-coordinates) was computed. This was done for each time step, and the total average was calculated. The average distances results are illustrated in Figure 5.9, while the total averages are listed in Table 5.1.

Table 5.1: Markers mean values of the average distance difference.

	Steady Free	Steady Locked	Unit
Wing	0.583	0.525	mm
Wingtip	1.885	0.834	mm

Looking at the plots, it is possible to state that for the average wing distance, the steady locked case presents a better correlation between the IPR markers with the painted ones with a total average distance of 0.525mm compared with the 0.583mm of the steady free case. The same trend but amplified for the wingtip, where the steady free case is experiencing a more considerable difference with a value equal to 1.885mm with respect to the 0.834mm of the steady locked; this was expected due to more uncertainties that are generated with the movement of the wingtip (steady free case) respect to the locked case where it is kept fixed.

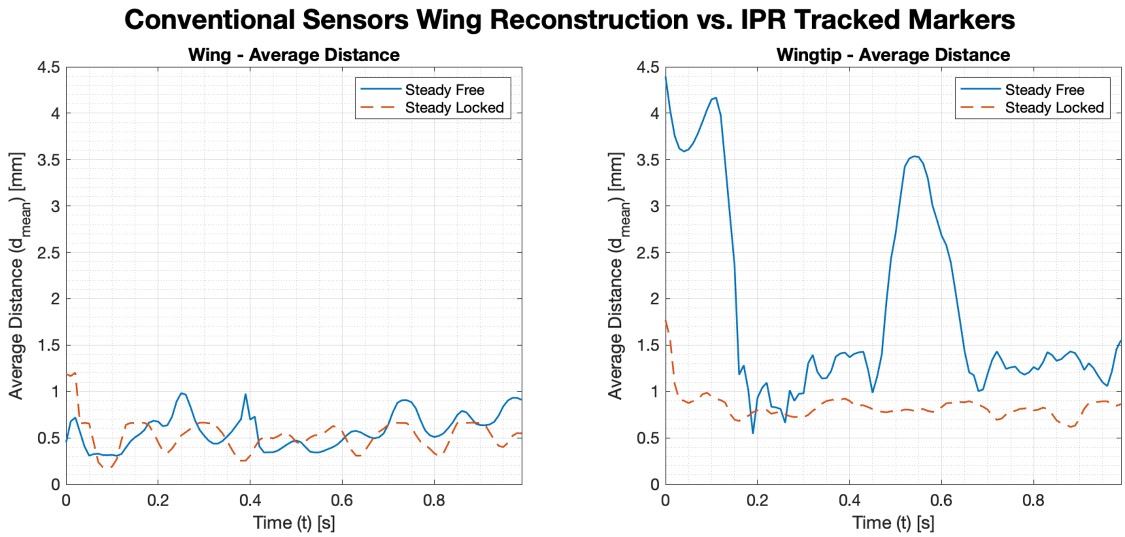

Figure 5.9: Markers average distance difference.

All these presented results show that the fiducial marker and HFSB tracking information acquired with the instantaneous large-scale PIV system and processed with IPR and STB can successfully be used to reconstruct the structural kinematics response of the wing and simultaneously study the aerodynamic performances.

5.2 Unsteady Conditions

In this section, the flow-field visualisation and structural behaviour characterisation are displayed for the unsteady cases where the 8Hz gust (with 2.5° amplitude) was employed. This is for all the six different hinge release conditions: free, locked, pre-released, 0% release, 50% release and 100% release.

5.2.1 Flow-Field Visualisation

Figure 5.10, Figure 5.11, Figure 5.12, Figure 5.13, Figure 5.14 and Figure 5.15 show the flow-field distribution at four different wing locations for all the unsteady cases, free, fixed, pre-released, 0% release, 50% release and 100% release. Respectively, the time instant $t/T_{ref} = 0$ is represented for the free hinge and 0% hinge release, the time instant $t/T_{ref} = 0.5$ for the cases locked hinge and 50% hinge release and finally $t/T_{ref} = 1$ for the pre-released hinge and for the 100% hinge release condition.

All the aerodynamic features already visualised in the steady cases are visible also here (with the same morphology (thickness and location)), in particular the stagnation point at the Leading Edge (LE) of the Pressure Side (PS) of the airfoil (top side). The flow acceleration on the airfoil Suction Side (SS), the wake formed after the end on the Trailing Edge (TE) and the separated flow on the PS at the end of the wing. However, some differences are visible. Indeed, for these unsteady conditions, the region around the stagnation point presents lower velocity and is more marked (the bluer region at the LE). The flow accelerates more on the top of the SS surface (redder areas), and the wake afterwards is more pronounced with respect to the steady cases (bluer line). These differences can be attributed to the gust that, when it encounters the wing/wingtip, forces the flow to accelerate more on the SS, and then when the airfoil surface is finished, it slows down completely to form a wake. Indeed, this effect is noticeable at $t/T_{ref} = 0.5$ and $t/T_{ref} = 1$, while at $t/T_{ref} = 0$ where the gust is still not generated, this is not visible.

Overall, the flow-field results are less accurate with respect to the steady ones (in particular at high z/b values, end of the wingtip). This lower statistical convergence is associated with the phase averaging method used for the binning process (compared to the spatial average used for the steady cases); but also by the gust that is causing some missing information during the STB process (indeed, this is more pronounced at $t/T_{ref} = 0.5$, where the gust hit the wing). Furthermore, this can also be associated with the non-uniform seeding produced during the wind tunnel experiment was caused by some blocked HFSB nozzles. Indeed, the level of random error is increased compared to the steady conditions due to the lower number of particles tracked, on average, 13.5 times less. This is also due to the difference between all-time steps selected for the steady cases against the 50 time steps ($\frac{50}{5457} \cdot 100 =$ 0.92% time span of the total period) for the unsteady ones. It is also true that even if the tracer tracks for each side were selected until the wing surface; the STB process detected some tracks that were penetrating the wing surface, causing uncertainty errors in the velocity field visualisations closer to the surface with the velocity field going into the surface (not visible in the flow field images since the black airfoil is plotted on top of those). Another reason that can cause some regions of permeation between the flow and the wing structure is the ensemble-averaging binning process. Indeed even if only the particles from the correct side of the airfoil and until its surface are used, cubic interrogation bins spanning across the airfoil surface and having the centroid beyond it may result in permeating cells when particles fall inside the part of the bin on the portion of the airfoil surface and overlap.

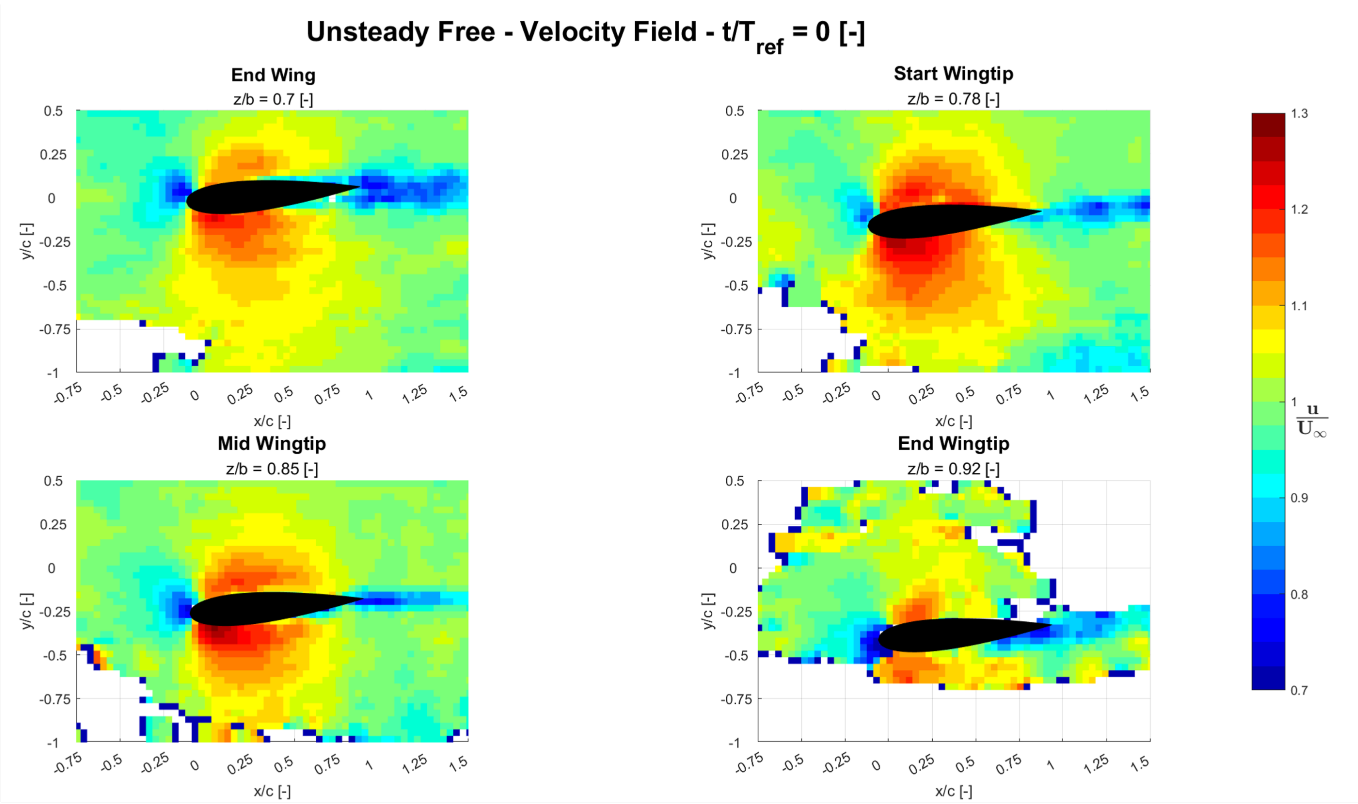

Figure 5.10: Flow field for the unsteady free condition, $t/T_{ref} = 0$ [-], (50 time steps).

The very pronounced low-velocity region around the stagnation point (blue region) at the LE can also be caused by the high particle concentration near the leading edge due to the soap accumulation during the wind tunnel experiment, which creates false particles during the STB and binning process.

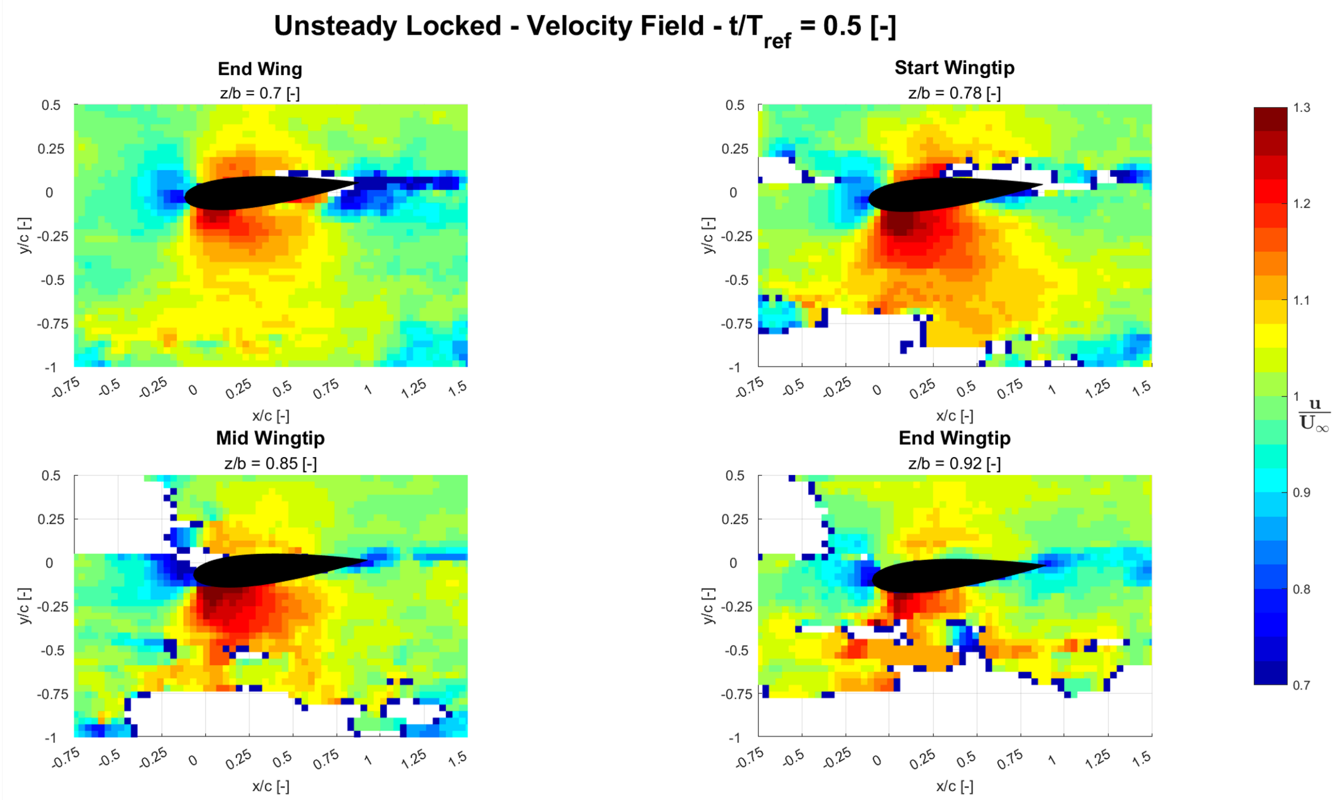

Figure 5.11: Flow field for the unsteady locked condition, $t/T_{ref} = 0.5$ [-], (50 time steps).

In these figures, several particle tracks have a velocity different from the closer local average. This is attributed to measurement noise and random error from the PIV data acquisition and uncertainty introduced by the STB post-processing due to the way it detects the markers in the images and positions them in space. However, more importantly, these measurements are affected by random errors due to the low statistical convergence of the phase average method used for the binning process. Such deviations can also be caused by significant numerical errors arising from uncontrolled phenomena like big Helium-Filled Soap Bubbles not matching the buoyancy requirements. At the same time, some small uncontrolled inflow velocity changes can also occur, causing an inconstant flow velocity behaviour along the test section.

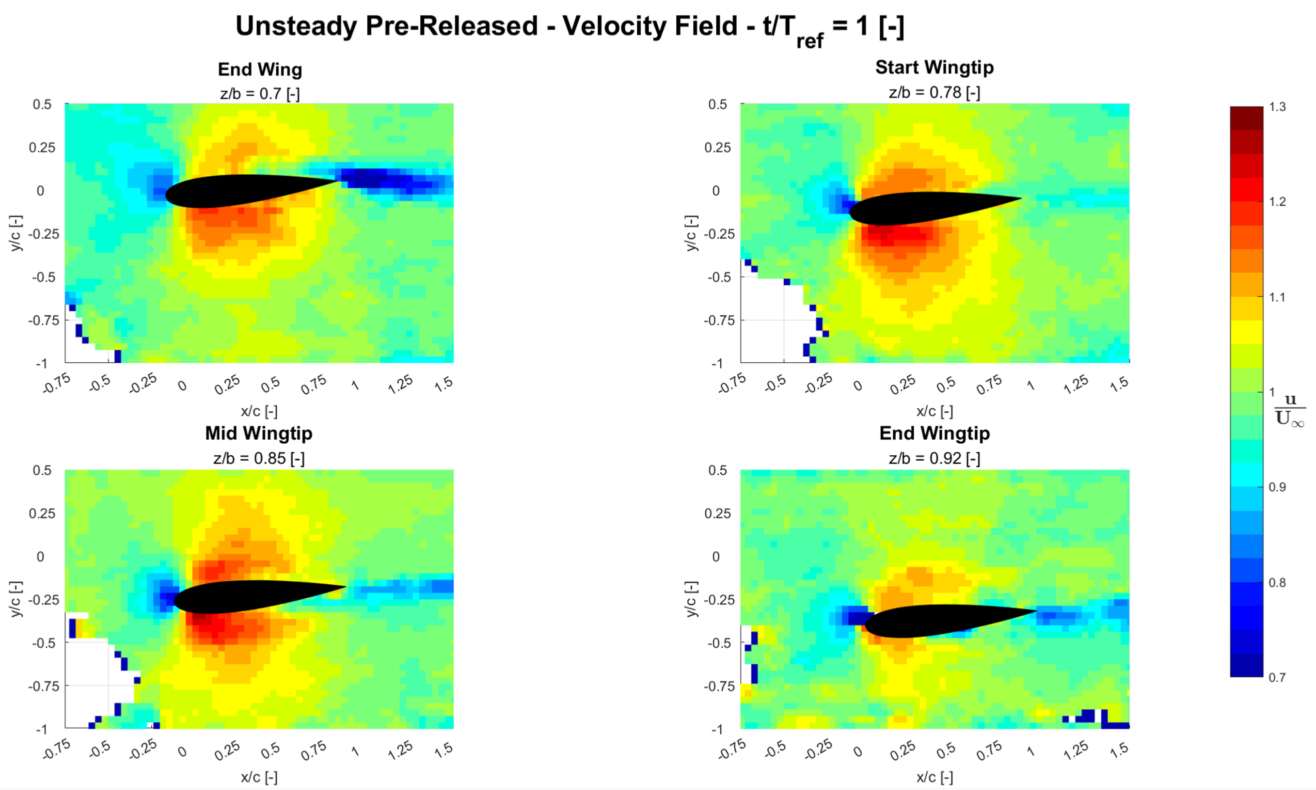

Figure 5.12: Flow field for the unsteady pre-released condition, $t/T_{ref} = 1$ [-], (50 time steps).

It is essential to state that there are some spatial discontinuities in the merging line between the different sides of the wing.

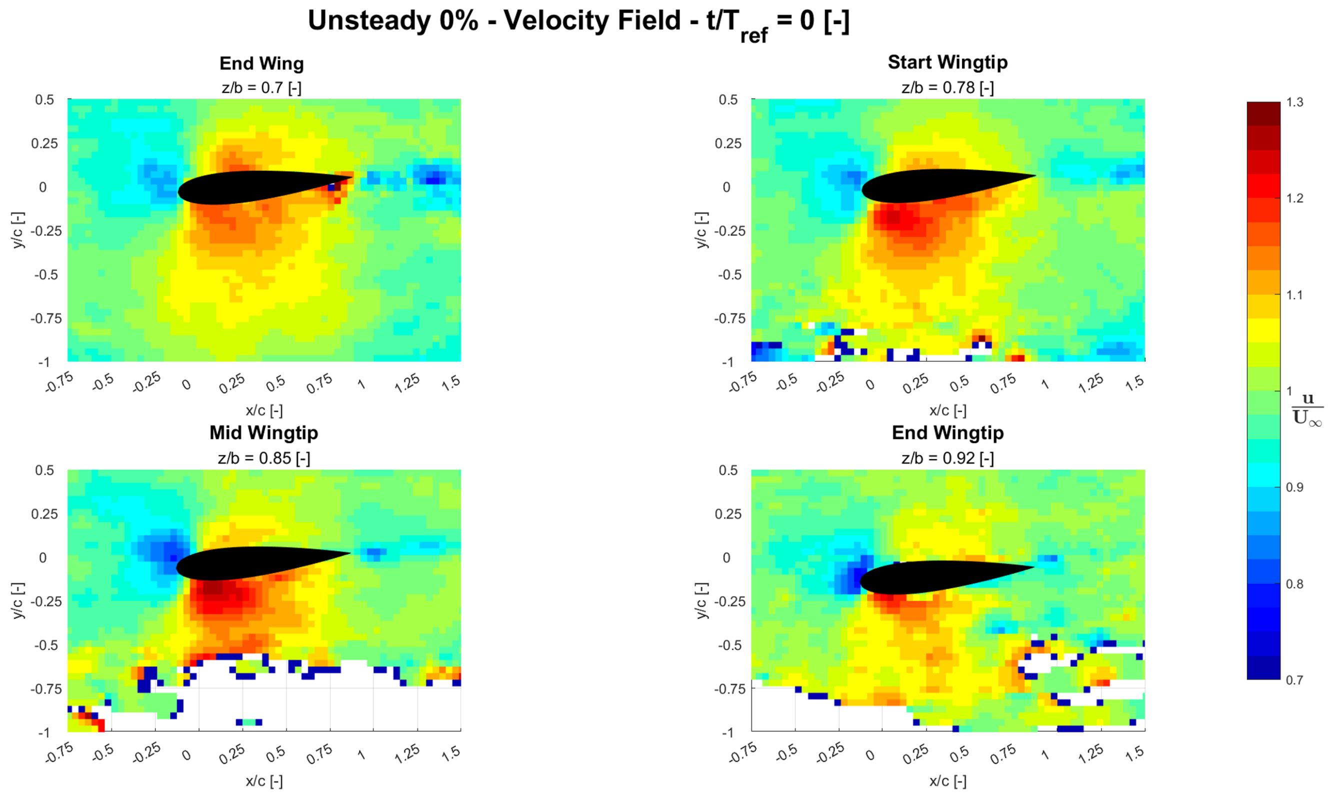

Figure 5.13: Flow field for the unsteady 0% condition, $t/T_{ref} = 0$ [-], (50 time steps).

The effect of the gust generated during these measurements is also visible looking the differences between the three time-phase instants ($t/T_{ref} = 0$, $t/T_{ref} = 0.5$ and $t/T_{ref} = 1$). Indeed, at $t/T_{ref} = 0.5$ where the gust hit the wing/wingtip, an enlarged region of acceleration is visible on the SS of the wing airfoil, while at $t/T_{ref} = 0$ (before the gust hit) and at $t/T_{ref} = 1$ (after the gust hit), this is acceleration region is reduced.

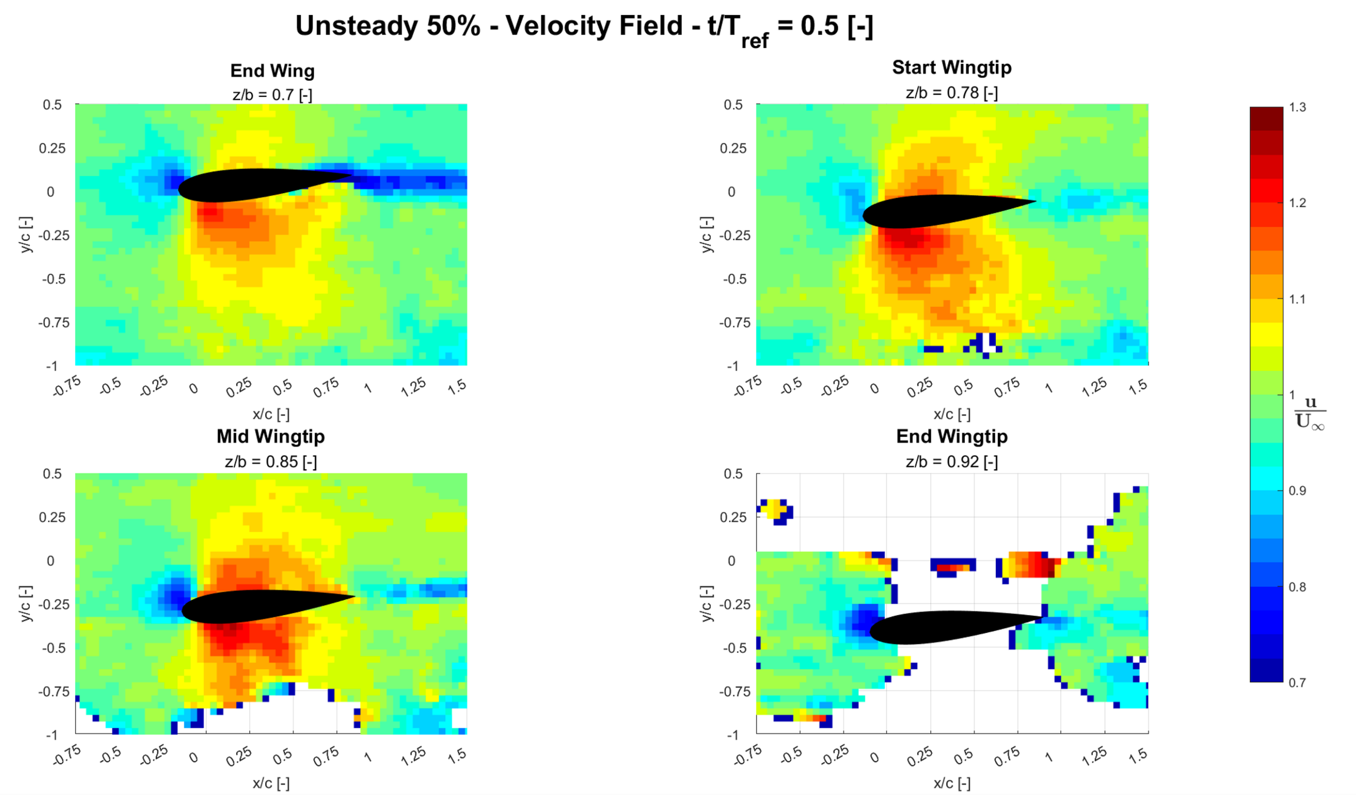

Figure 5.14: Flow field for the unsteady 50% condition, $t/T_{ref} = 0.5$ [-], (50 time steps).

The flow development at regions where more significant structural deformations occur (end of the wingtip) does not present significant differences with respect to the other spanwise locations. In some cases, in particular, at the wingtip, where both degrees of freedom (bending moment coefficient and wingtip deflection angle) are used in the structural reconstruction, some position deviations are visible between the flow-field and the location of the airfoil. This is caused by the reconstruction position of the wing/wingtip that does not coincide with a 100% accuracy with respect to the actual position, as visible in Figure 5.9.

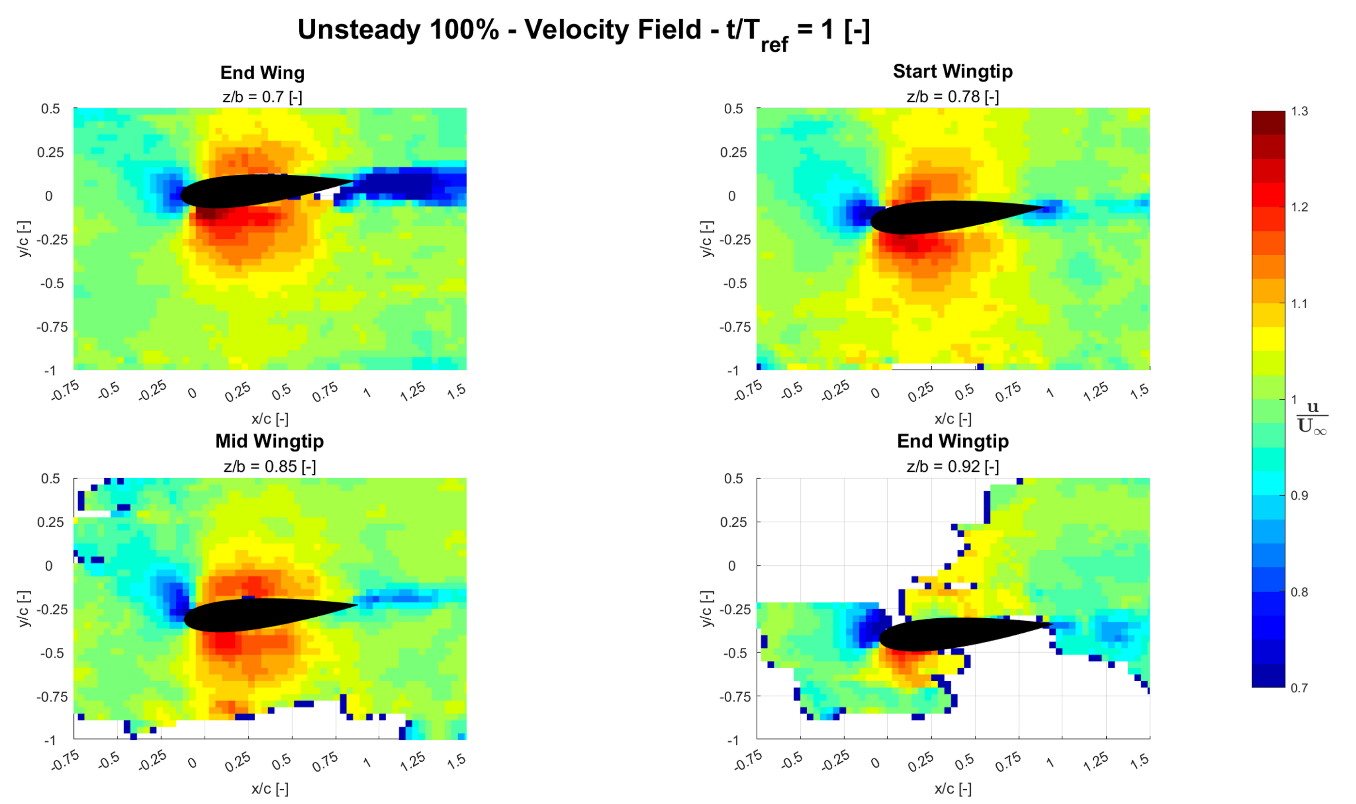

Figure 5.15: Flow field for the unsteady 100% condition, t/T_{ref} = 1 [-], (50 time steps).

The results of the three different phases suggest that the measured flow field follows the movement of the wingtip coherently, thus providing a qualitative confirmation of the consistency of the measurements taken during the wind tunnel experiment.

In Figure 5.16, the 3D wing/wingtip structure reconstruction with the velocity field at the four planes shown above is displayed for all the unsteady cases. A good match is visible between the reconstructed wing structure (averaged with the 50 time steps closer to the t/T_{ref} selected: 0, 0.5 and 1) and the flow field features. The only minor deviations present (more pronounced here with respect to the steady cases) are caused by the position of the reconstructed wing, which is a bit off.

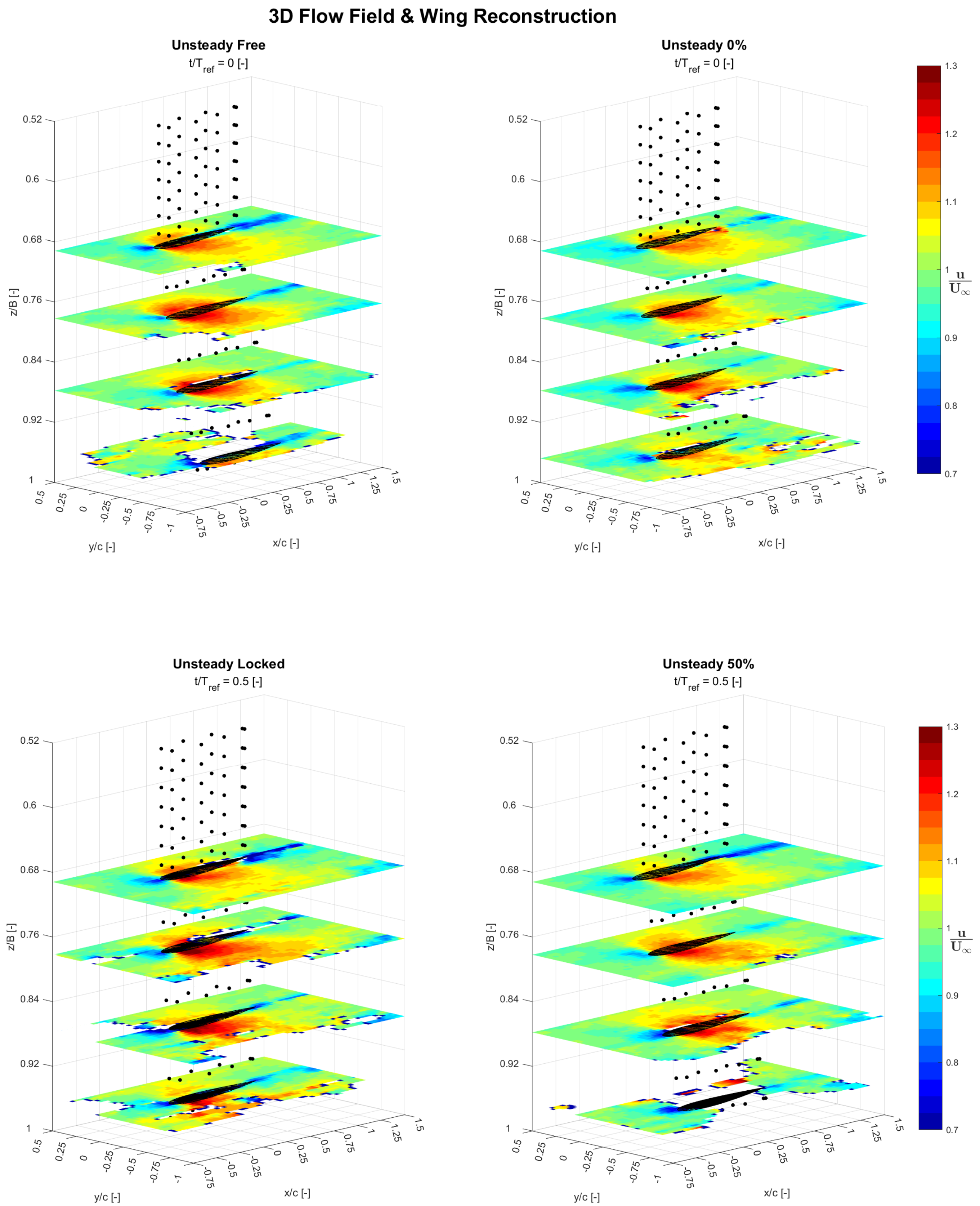
3D Flow Field & Wing Reconstruction
Unsteady Free
t/T_ref = 0 [-]
Unsteady 0%
t/T_ref = 0 [-]
Unsteady Locked
t/T_ref = 0.5 [-]
Unsteady 50%
t/T_ref = 0.5 [-]
z/B [-]
y/c [-]
x/c [-]
u/U∞

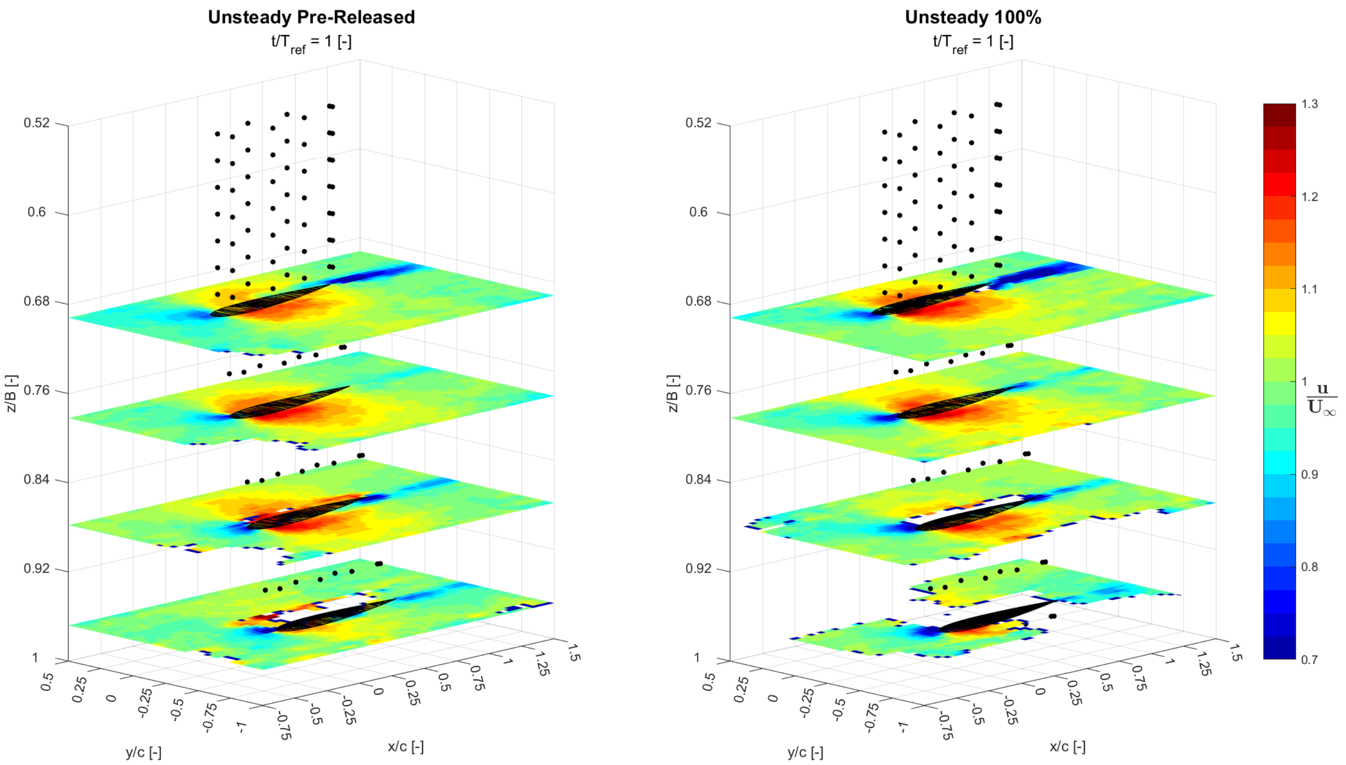

Figure 5.16: 3D flow field and wing reconstruction for the unsteady cases.

5.2.2 STRUCTURAL BEHAVIOUR

Also, the last two degrees of freedom determined from the conventional sensors placed on the wing are represented for the unsteady conditions. In Figure 5.17, the wingtip deflection angle (θ) given by the potentiometer for each time instant is illustrated.

As expected, for all the conditions, the wingtip angles start around zero and then oscillate around 10° after the gust arrives and the hinge is released. This is not true for the locked case where the fixed hinge causes a wingtip angle to stay closer to zero values, but also for the free condition where due to the released hinge from the beginning of the measurement, it starts around 10° and then oscillates around this value after the gust.

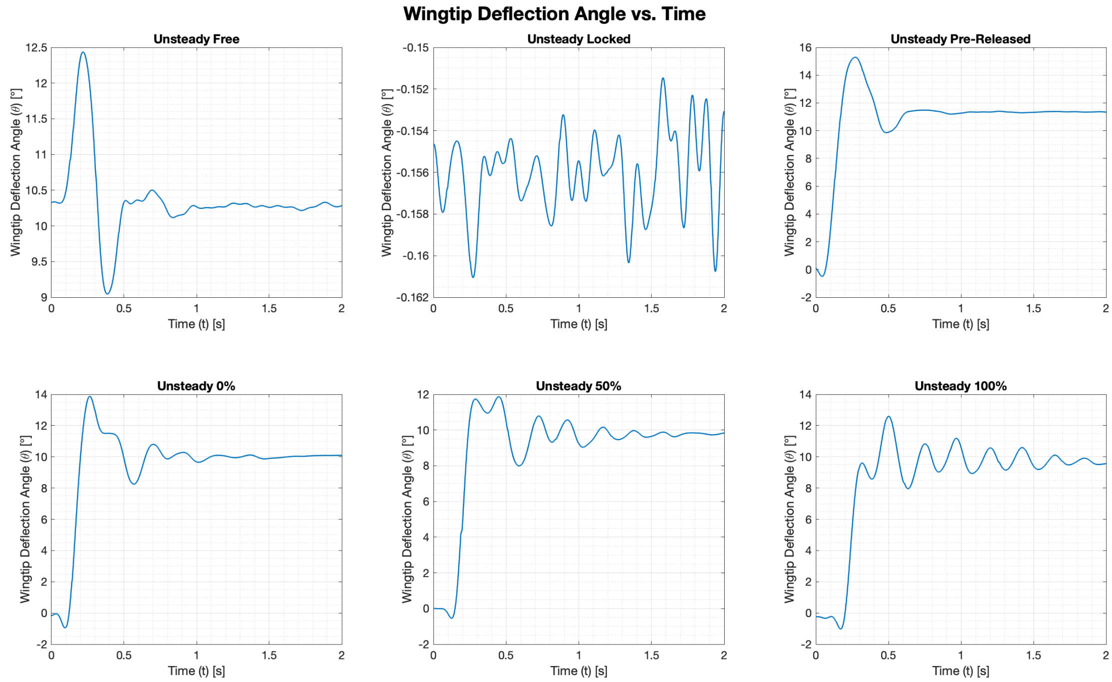

Figure 5.17: Wingtip angle (θ) for the unsteady conditions measured with the potentiometer.

While in Figure 5.18, the bending moment coefficient (C_B) calculated using the electric signal recorded by the strain gauges rosette is displayed. For all the different conditions, C_B stays around the zero value and then starts oscillating when the gust is encountered, with a decreasing amplitude over time. The trend is not visible for the unsteady free condition, where the wingtip is free to oscillate from the beginning to the end of the recorded time, and for the pre-released condition, where the oscillation is smaller compared to all the other conditions.

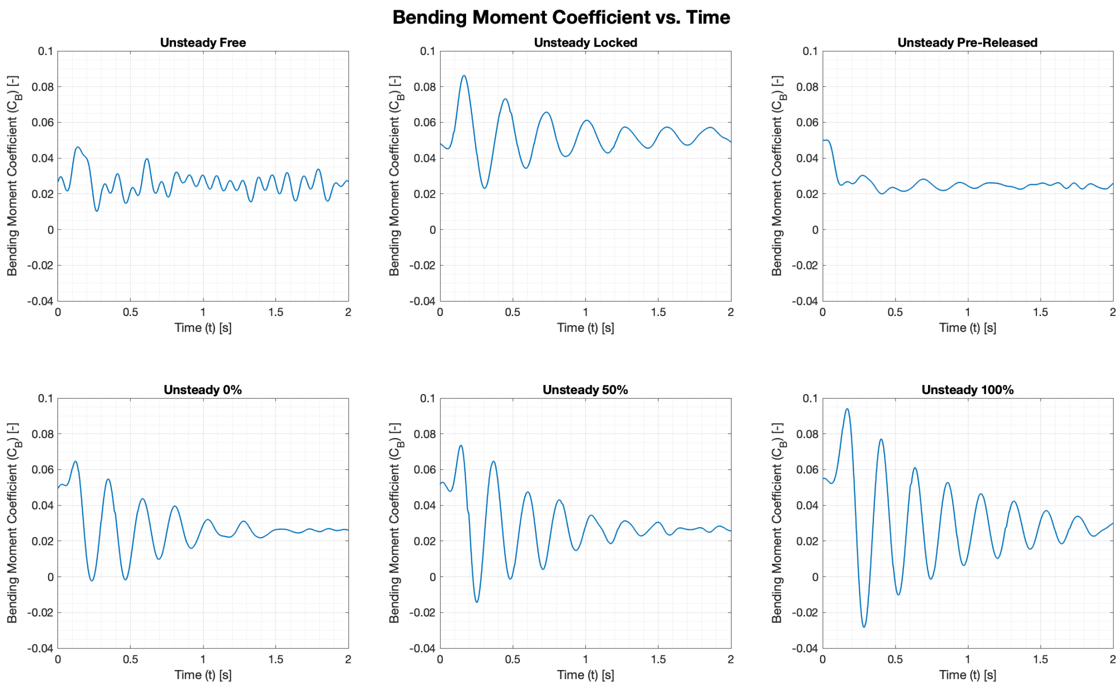

Figure 5.18: Bending moment coefficient (C_B) for the unsteady conditions measured with the strain gauges.

To better understand what these degrees of freedom represent in reality, the complete 3D wing/wingtip is reconstructed based on these two coefficients shown above. This was done for all six different hinge conditions for $t = 0$s ($t/T_{ref} = 0$ [-]), $t = 1.08$s ($t/T_{ref} = 0.5$ [-]) and $t = 2.02$s ($t/T_{ref} = 1$ [-]), using $T_{ref} = 2$s. Visible respectively in Figure 5.19. The wing reconstructed model that uses the two degrees of freedom (from the conventional sensors) matches very well with the IPR tracked fiducial markers painted on the wing. Indeed both the wing bending (based on C_B) and the wingtip deflection angle (θ) are consistent and coincide, when combined, in an accurate way with the IPR tracked markers (red markers).

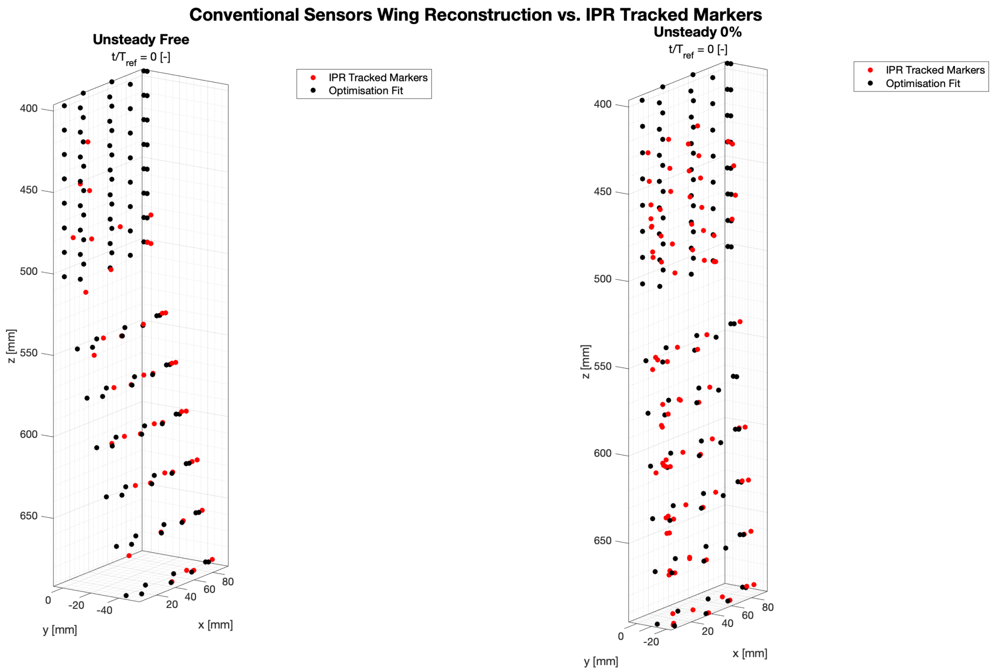

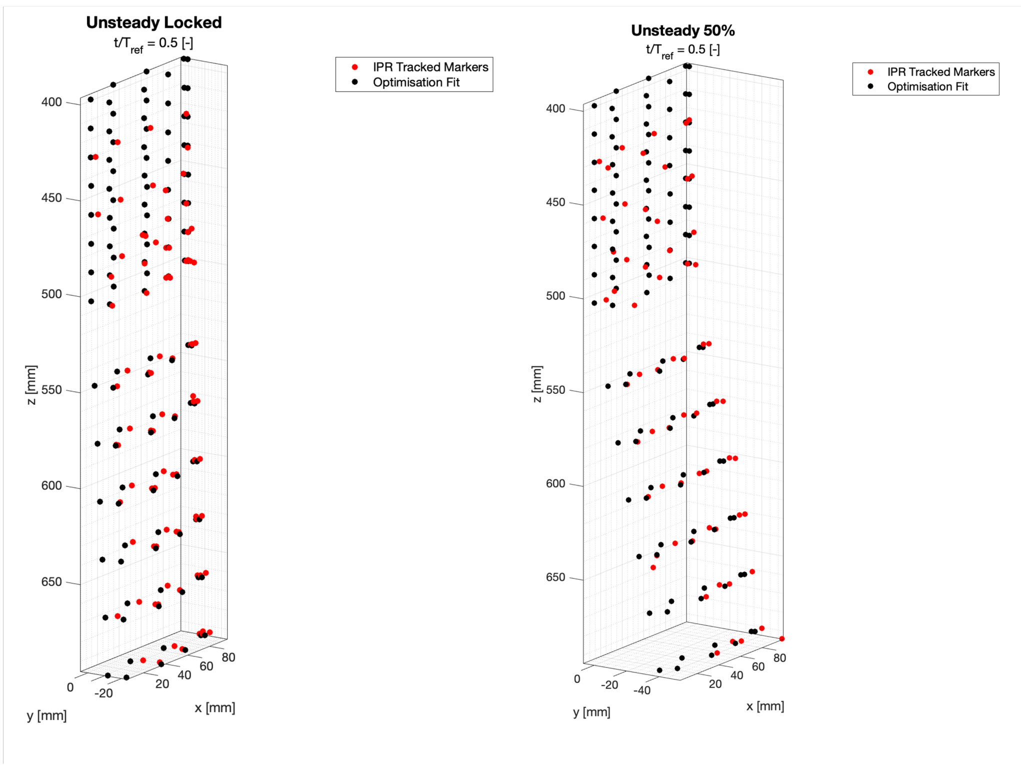

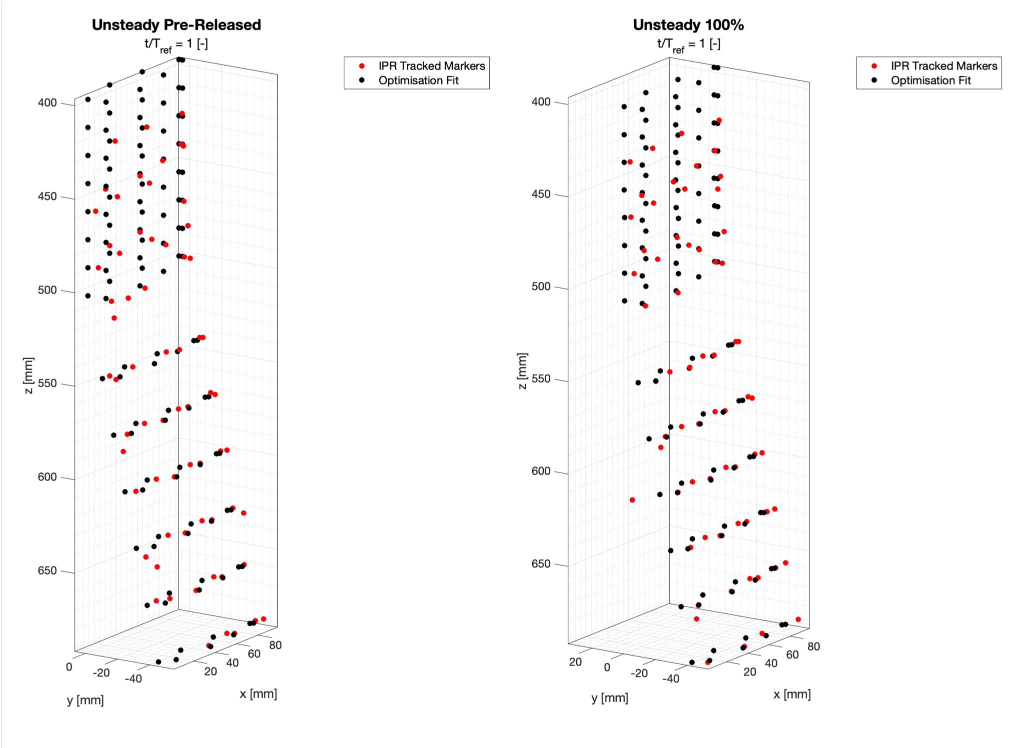

Figure 5.19: Wing reconstruction vs. IPR.

Most of the painted markers on the wing are tracked over the total acquisition time. However, some deviations between results are present due to disturbances and surface reflection acquired during the wind tunnel experiment and not appropriately cancelled in the image pre-processing steps. Furthermore, positional uncertainty due to the deviation of the marker's shape and intensity plays a role. As for the steady case, also now, on the wing, where only the bending degree of freedom is used for the wing reconstruction method, the matching with the tracked markers with the IPR post-processing is accurate. Instead, for the wingtip, where beyond the bending, also the wingtip deflection angle degree of freedom is used in the optimisation fit, a more pronounced deviation is visible compared to the IPR tracked markers, in particular at the tip of the wingtip, caused by the combination of these two degrees of freedom that are leading to positioning errors.

To quantify the distance difference between the IPR tracked markers that are painted on the wing and the reconstructed wing using the two degrees of freedom gathered from the conventional sensors (potentiometer and strain gauges), the same algorithm used for the steady conditions and already described in subsection 5.1.2 was used. This was done for the separated wing and wingtip, first for each time step and then for the total average. The average distances results are illustrated in Figure 5.20, while the total averages are listed in Table 5.2.

Table 5.2: Markers mean values of the average distance difference.

	Unsteady Free	Unsteady Locked	Unsteady Pre-Released	Unsteady 0%	Unsteady 50%	Unsteady 100%	Unit
Wing	0.794	0.482	1.335	0.941	0.963	0.873	mm
Wingtip	1.353	0.947	1.693	1.192	1.493	1.155	mm

Looking at the figure and the table containing the average values, it is possible to state that overall the two sets of markers are very close in all the different unsteady conditions. In particular, this deviation is a bit more pronounced for the wingtip, where both the bending and wingtip deflection angle degrees of freedom are employed, with respect to the wing, where only the bending is used in the wing reconstruction optimisation procedure. A low matching is visible for the initial time steps on the wing due to a low amount of tracked particles. In general, for all the different cases, the average distance for the wing is around 1mm, while 1.5mm for the wingtip, with the best results reached for the unsteady locked case where the markers are tracked precisely. Instead, the worst correlation was found in the pre-released hinge release for both the wing and the wingtip. These deviations are caused by errors experienced during the acquisition and IPR post-processing phases. This was visible before the outlier removal process, where missing markers and many outliers were present in the raw dataset for this hinge condition.

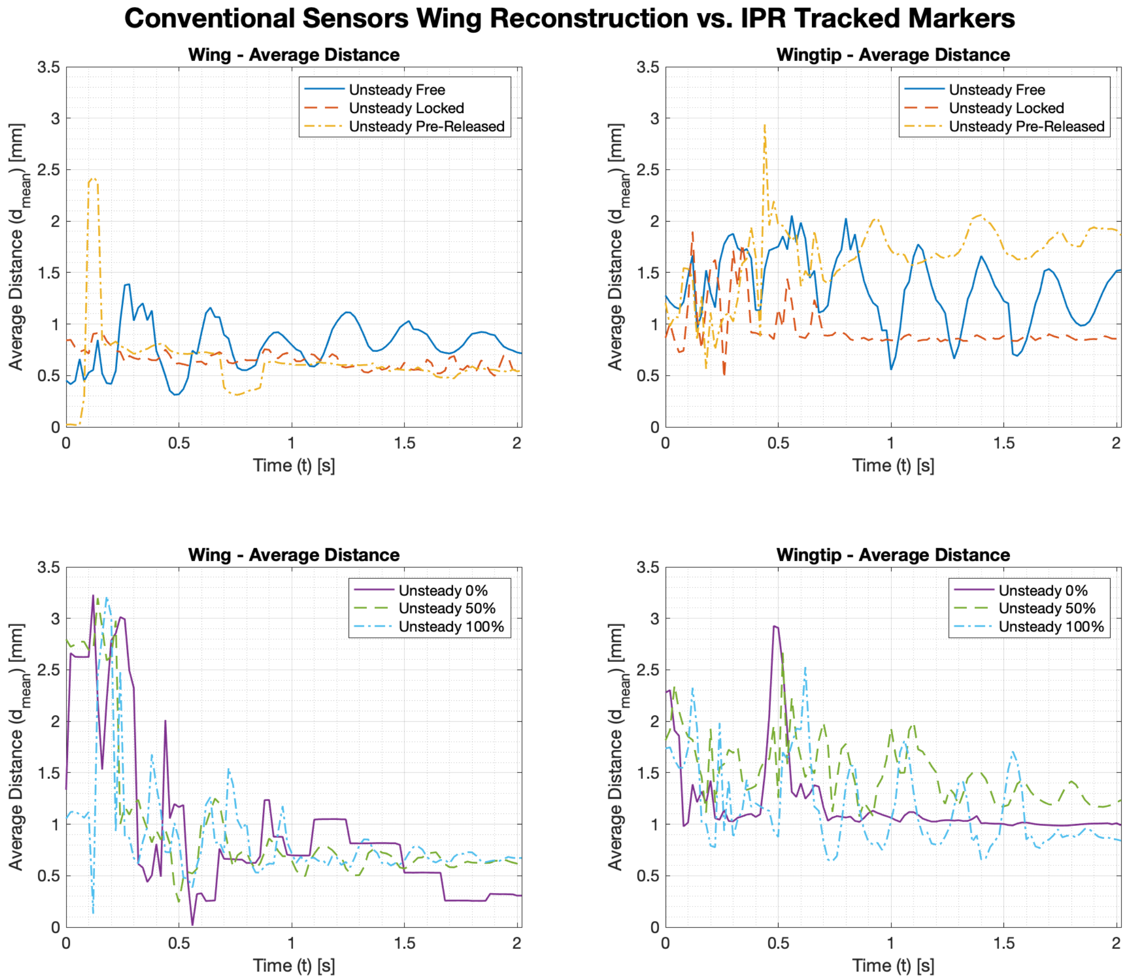

Figure 5.20: Markers average distance difference.

To easily visualise the Gust Load Alleviation (GLA) performance of the six different hinge release conditions (for the unsteady cases), the peak load and Root-Mean Square (RMS) normalised with the locked hinge conditions are used. These are found using the formulas presented in Equation 4.3 and Equation 4.3, and using the values from the strain gauges are illustrated in Figure 5.21 and Figure 5.22 respectively. In contrast, the resulting values are listed in Table 5.3.

First, the following considerations can be drawn by looking at the relative peak load in Figure 5.21. The best results are obtained when the hinge is released in advance. Indeed the free hinge produces a peak load reduction of -40.43%, while the pre-released hinge condition (released with the gust generator trigger signal before the gust hits the wing) reaches a value close to -99.93%. Then, the peak load reduction is reduced with the delay in the hinge release, as the wing is allowed to achieve higher loads before the hinge is released. Indeed, at 0% hinge release (release when the gust hits the wing), the peak load reduction was reduced to a value equal to -65.47%, then -26.69% for the 50% hinge release (released when the load achieves 50% of its peak load). While for the 100% hinge release condition (release at the peak load), the HFW increases the peak load with respect to the locked-hinge condition by 19.53%. Overall, it is possible to state that the peak load reduction is conditioned by the correct timing of the hinge release (also taking into account the fast gust generated (8Hz)) since releasing the hinge at high load thresholds (100%) aggravates the peak loads instead of alleviating them. Indeed, when the hinge is released before the gust, the HFW oscillates towards a steady state, reducing the peak load. Then, once the gust hits the wing/wingtip, the increase in load caused by the gust is compensated by the load relief caused by the HFW movement, leading to an alleviation of the peak load. Therefore, releasing the hinge at the time instant closer to the one when the gust hits the wing/wingtip provides the best gust load alleviation (also better than the free hinge condition).

Then, the relative RMS that is represented as an indication impact of the hinge release on the gust-induced oscillation on the wing/wingtip system is illustrated in Figure 5.22, and the following considerations can be done. The behaviour of the relative RMS is similar to that seen in the relative peak load. However, some main differences are present. Indeed, here, the best reduction in the oscillation is given by the free hinge condition, with a relative RMS of -40.41% with respect to the locked hinge condition. Then, the RMS reduction decreases with the increase of the hinge release threshold, with RMS values of 2.48% for the hinge pre-released (that was the beast condition for the relative peak load reduction) and 24.32% for the 0% hinge release. Now, the oscillation is aggravating, reaching an increase of 70.87%, with respect to the locked hinge condition, for the 50% hinge release, while a 14.62% is found for the 100% hinge release (that was the worst condition for the relative peak load reduction).

Table 5.3: Relative peak load and relative Root-Mean-Square (RMS).

	Unsteady Free	Unsteady Pre-Released	Unsteady 0%	Unsteady 50%	Unsteady 100%
Peak Load	-40.43%	-99.93%	-65.47%	-26.19%	19.53%
RMS	-40.41%	2.48%	24.32%	70.87%	14.62%

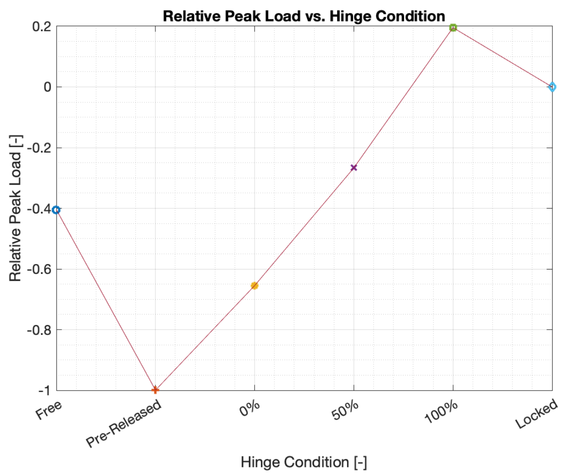

Figure 5.21: Relative peak load comparison.

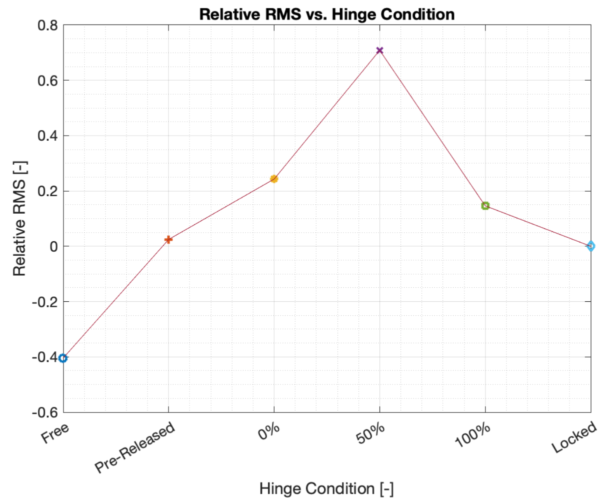

Figure 5.22: Relative Root-Mean-Square (RMS) comparison.

It is possible to conclude this peak load and RMS analyses stating that the best peak and oscillation reduction are reached when the hinge is released at the same time instant of the gust detection, while any delays aggravate the peak load experienced and oscillations created, which are damaging for the wing structure (fatigue effect) and the aircraft passenger. A similar analysis was conducted by Carrillo [18], and the results are in line with the ones presented in this thesis.

To also have a qualitative understanding of the flow velocity field at the time instant corresponding to the occurrence of the peak load, it was decided to plot that time instant in Figure 5.23 the flow field at the mid wingtip location ($z/b = 0.85$ or $z/b_{wingtip} = 0.5$) for each hinge release conditions. Again using the same parameters as before, a bin size of 15mm and 50 time bins (from 25 before to 25 after the time instant selected). Looking at the development of the flow, it is possible to find all the flow morphology features (stagnation point at the Leading Edge (LE), acceleration on the Suction Side (SS) of the airfoil and wake after the Trailing Edge (TE)). With respect to the cases displayed before, now that the peak load occurrence is illustrated, the flow tends to be more energetic and chaotic, with a higher acceleration on the SS, a more robust wake at the TE and a bit more noise all around on the surrounding flow field. This cause also a region of separated flow that is now visible in the mid-wingtip plane (before only at the end of the wing). Apart from this, no significant differences are visible with respect to the flow field displayed before, proving this wingtip design's excellent performance that does not present too severe aerodynamic problems in adverse conditions.

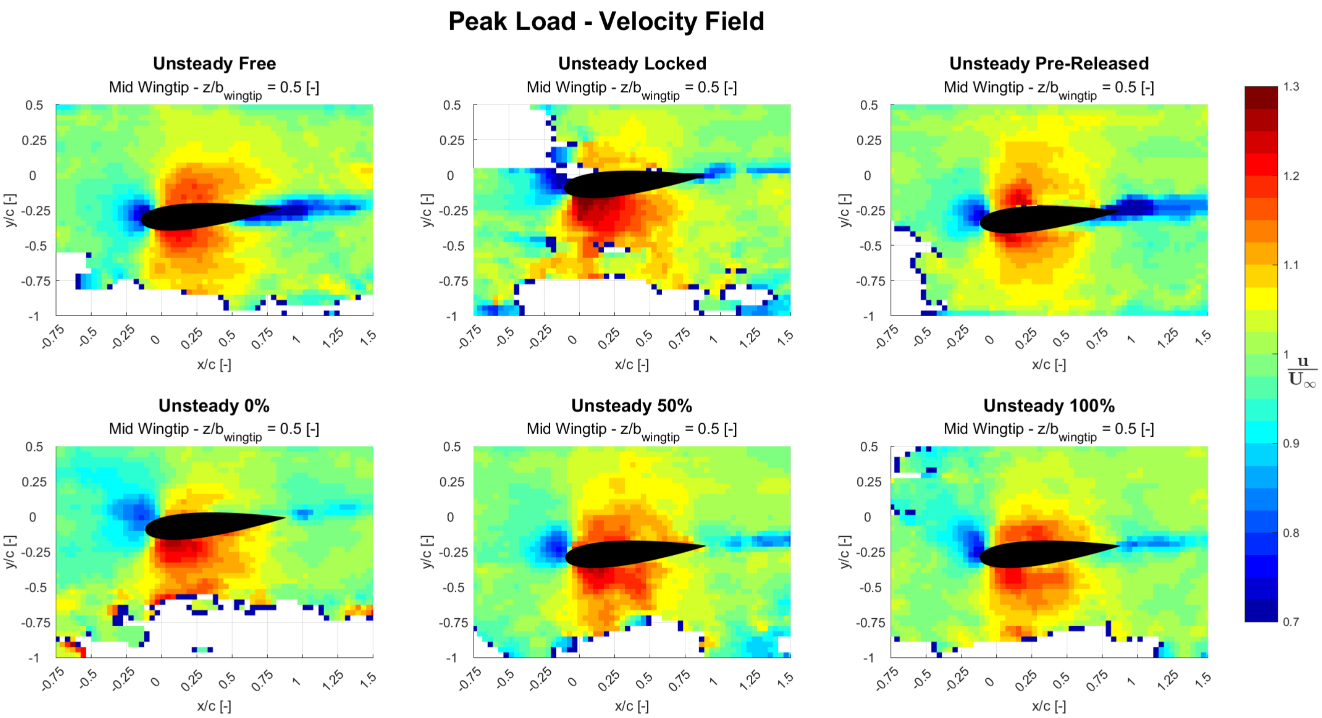

Figure 5.23: Velocity field at peak load time instant (15mm bin, 50 time steps).

Overall, it is possible to state that the quantitative and qualitative analysis performed on the combined results of phase-averaged flow and structure shows the potential of instantaneous large-scale particle image velocimetry for characterising the aeroelastic fluid-structure interaction phenomena.

6
Conclusions and Recommendations

6.1 Conclusions

The motivation of the research presented in this master thesis originates from the challenges of the current aviation industry regarding the reduction of emissions produced, going towards a greener future and fighting against climate change. To attenuate this problem and reach climate neutrality, a way is to improve the aerodynamic efficiency of the airliner, maximising the lift over drag value that will result in less energy consumed for a given flight. Reachable by increasing the wing span. Unfortunately, this is limited by the dimensions of the current gates that cannot meet these such extensive wingspan requirements and the structural weight that the fuselage can handle without encountering failure. For this reason, new solutions like the Hinged Folding Wingtip (HFWT) have been studied recently. This will increase the aircraft's wingspan during the flight but can be folded and closed when the aircraft is on the ground. At the same time can be used as a Gust Load Alleviation (GLA) device. Indeed, in case of a gust load hitting the wingtip, the hinge is released, letting the wingtip free to move and alleviating the root load created.

While reviewing the available literature, there was a lack of experimental studies for the aerodynamic dynamics and structural kinematics measurement, where most studies used numerical simulations. Furthermore, the results obtained by the Hinged Folding Wingtip device were not consistent between different studies. Indeed, experimental studies through wind tunnel campaigns are still needed for the verification of low-fidelity analytical methods, for identifying and understanding the physics underlying aeroelastic phenomena resulting from the combination of forces of different nature (inertial, elastic and aerodynamic), and for validation of computational tools employed to characterise complex Fluid-Structure Interaction (FSI) problems. Furthermore, achieving a complete aeroelastic characterisation is usually reached with the combination of two different measurement systems, one for the aerodynamic flow and one for the structure, leading to undesired effects limitations like low spatial resolution, complex set-up and intrusiveness of the instruments. Therefore, there is a need to develop a new measurement technique capable of overcoming all these limitations. This thesis is part of the research effort to overcome all these limitations of conventional measurement techniques and contributes to state-of-the-art wind tunnel aeroelastic experiments. This introduces and proposes a new, combined, integrated, non-intrusive, whole-field flow measurement technique using the instantaneous and large-scale tomographic Particle Image Velocimetry (PIV) using six cameras. This alternative method can provide simultaneous and integrated aerodynamic and structural measurement information allowing a complete characterisation of this HFWT model. This is needed to accurately understand this device's behaviour, in reality, eventually contributing to improving more sustainable aviation. To prove this, the following research question has been defined.

> Study the aerodynamic and structural behaviour of a hinged folding wingtip in both steady and unsteady conditions by means of an instantaneous large-scale particle image velocimetry wind tunnel experiment.

To achieve this research objective, a volumetric LPT approach for this large-scale aeroelastic investigation of the HFWT was demonstrated to be feasible by utilising a wind-tunnel experiment conducted in the W-tunnel at the Delft University of Technology. On the wing, several independent conventional sensors were included whose aeroelastic response measurements are taken as a reference. Indeed an accelerometer was used to track the wing's motion, a potentiometer for the wingtip rotation angle and a rosette of strain gauges to find the wing root bending moment. On the black wing/wingtip surface, a grid pattern of white fiducial markers was painted, allowing the structural response reconstruction from the images recorded by the six cameras. At the same time, the motion of Helium-Filled Soap Bubble (HFSB) tracer markers is tracked for flow field visualisation. Both steady and unsteady conditions are simulated, the latter using the gust generator mounted at the wind-tunnel nozzle that generates

1-cosine gusts.

After the experimental campaign, an extensive analysis was performed to extract meaningful structural and aerodynamic information from the raw images gathered with the PIV system. Indeed, these were pre-processed to isolate and separate the structure and flow markers using time-filtering operations, using the hypothesis that structural markers move slower than flow particles in the acquired images. Then, the structure images are processed using the Iterative Particle Reconstruction (IPR) algorithm to retrieve the position of the fiducial markers. While the flow images were processed using the Shake-The-Box (STB) algorithm to compute the tracks of the flow tracers.

A cubic polynomial equation fitting a simplified wing structural model based on a 1D Euler-Bernoulli beam theory was developed for the wing structural reconstruction. This was implemented with the data gathered by the potentiometer and the strain gauges to move the model with the two missing degrees of freedom, the wingtip angle and the bending coefficient. This was compared with the found marker position showing an excellent agreement and proving a clear correlation between marker-based tracked wingtip movement and the conventional sensors measurements. Indeed, for the steady conditions, the wing presents an average distance difference between the painted markers and the ones from the reconstruction of about 0.5mm, while the wingtip of about 1mm. The same trend was also visible for the unsteady conditions, with an average distance of 1mm for the wing and 1.5mm for the wingtip. This demonstrates that this approach is promising for reconstructing the aeroelastic response of the wing.

The Gust Load Alleviation (GLA) performance of the different hinge release conditions was addressed by computing the peak load, and Root-Mean-Square (RMS) both normalised by the locked hinge condition. It results in a significant effect on the hinge release timing on load alleviation. Indeed releasing the hinge at the same time as the gust detection (pre-released condition) can reduce the peak load by almost 100%. On the other hand, to minimise the wing-induced oscillations (visualised by the computed RMS), which are detrimental for the fatigue effects on wing structure and annoying for the passenger comfort, the hinge should be left free to oscillate (free condition), reaching a reduction of 40%. While releasing the hinge close to the maximum load (50% and 100% hinge conditions) increases both the peak load and oscillations, with an increment reaching almost 20% and 70% for peak load and oscillations, respectively. This shows the importance of detecting the gust on time and reacting immediately. Considering a trade-off between peak load reduction and oscillations, the best results are achieved if the hinge is released before the gust hits the wing.

While for the aerodynamic characterisation, the flow-field velocity distribution around the wing/wingtip was obtained using the tracer tracks found with the STB algorithm through ensemble averaging procedures. Two different methods were used, a spatial-average for the steady conditions and a phase average for the unsteady ones (using a time bin of 50 that leads to an uncertainty level equal to 5.138%). It was decided to use a bin size of 15 mm that gave an uncertainty level of 0.976% for the steady conditions while 4.654% for the unsteady ones. The flow field was visualised at different planes along the wing/wingtip span, showing all the typical aerodynamic features, including the stagnation point at the Leading Edge (LE), the acceleration on the Suction Side (SS), and the wake after the Trailing Edge (TE), including separation on the Pressure Side (PS) at the end wing region. This information were combined with the already found wing structural displacement reconstruction to reproduce the 3D visualisation of the FSI phenomenon. Showing good compliance between the structure and the flow-field features obtained with the ensemble-averaged procedure using the flow tracers tracks from STB.

Overall, this master thesis research study has fulfilled the proposed research goals, demonstrating the feasibility of performing a combined structural and aerodynamic characterisation of this Folding Hinged Wingtip (FHWT) through instantaneous, whole-field, non-intrusive and large-scale measurement systems for both steady and unsteady conditions. The accuracy of the PIV system used to conduct this fluid-structure aeroelastic study has been assessed, showing promising results and the potential to be an alternative to traditional measurement techniques. However, several limitations and points of improvement on this technique were identified (and presented in section 6.2); these can be addressed and overcome in future work.

6.2 Recommendations

This last section presents a series of recommendations that originate during the execution of this thesis research project. Indeed, although a first successful step in applying instantaneous large-scale Particle Image Velocimetry (PIV) for a combined aerodynamic and structural characterisation study, several improvements can be implemented. These recommendations should be considered and implemented for the future continuation of this study.

6.2.1 Experimental Set-Up, Data Analysis and Reduction Techniques

First, a new version of DaVis (that will be released later this year) should be used that allows the post-processing (through the STB and IPR algorithms) of all the images from the six different cameras on both sides of the wing (on both the Suction Side (SS) and Pressure Side (PS)) at the same time, without the need of splitting into two sets based on the side. This will permit more accurate results for both the tracked structural markers and velocity field distribution since the markers are tracked simultaneously by six different cameras. Furthermore, at the same time to reduce the processing time since now all the operations for the image pre-processing, Volume-Self Calibration (VSC), STB/IPR post-processing and ensemble average are done for both sides separated while having just one dataset will permit half the time needed.

The Helium-Filled Soap Bubble (HFSB) shape and seeding uniformity can be improved during the wind tunnel experiment. Indeed some nozzles were blocked while others were producing non-homogeneous shapes and concentration bubbles that caused the region of missing flow information (particularly on the sides of the measurement volume). This can be fixed by placing a finer turbulence grid before the exit of the wind tunnel to create a mixing of the produced bubbles but also checking that all the nozzles are not abstracted. Furthermore, the wing/wingtip model was placed vertically so that only the wingtip and a small part of the wing were hit by the flow generated from the W-tunnel wind tunnel. To have a more realistic aerodynamic and structural characterisation, the wing should be placed horizontally (so also the weight load is taken present), and at the same time, a bigger wind tunnel like the Open Jet Facility (OJF) should be used to have the entire span of the wing immersed in the flow.

The pre-processing image phase can be optimised to achieve better results. Indeed, in this study, the hypothesis that the movement of fiducial structural markers painted on the wing is, on average, much slower than the one of the Helium-Filled Soap Bubble (HFSB) was used to separate the flow and structure information from the recorded images. This can be a limiting factor in the case of flow separation and back-flow, where the flow tracers particles have a low velocity or in the case of non-linear structural phenomena (moving with high frequencies) like fluttering or Limit Cycle Oscillation (LCO), where the velocity of the structural fiducial markers increased drastically. This can be avoided by using a different shape for the markers painted on the wing model (different from the rounded shape of the tracers particles), so with the employment advanced tracking algorithm, it would be possible to distinguish flow tracers from the structural markers based on spatial filtering, without the usage of filtering techniques to separate the two sets.

The flow-field post-processing can be enhanced using a combination of the structured and unstructured volumetric grid, with non-regular bin sizes, for the ensemble averaging process based on the domain space position to account for the different discretisation requirements across the entire measurement volume and binning directions, preserving the object geometry. Indeed, the current process divides the volumetric flow-field domain into rectangular-shaped bins, which do not allow accurate reproduction of the shape of curved airfoil surfaces. This can be overcome by reconstructing the wing structure surface and then generating the unstructured volumetric grid in the vicinity of the wing surface, which is then connected to a generated structure one, imposing a priori the consistency between the flow and the structure. This would be similar to the mesh generation process around the surface of a body in the Computational Fluid Dynamics (CFD) simulations.

The fluid and structure interaction can be refined. Indeed the obtained flow field distribution and structural displacements are combined for visualisation purposes. However, the structural marker velocity is a boundary condition for the flow field distribution. Advanced techniques to retrieve boundary layer equations can be implemented to derive the actual velocity distribution between the object surface and the flow field, increasing the resolution of the measured velocity in the near wall region.

Finally, the model used to reconstruct the wing can be improved. Indeed, in this research, the wing is simplified using a One Dimensional (1D) Euler-Bernoulli beam model clamped at the root, fitted by a third-order polynomial equation. Assuming deflection in the direction perpendicular to the wing chord due to the lift, considered as a lateral point force located at the tip of the wing, and neglecting shear torsional deformation effects. Although promising results have been obtained, this model assumption is the cause of the discrepancies between the PIV recorded markers position and the reconstructed one through the optimisation process. The usage of a more precise structural model (at least a fourth-order polynomial equation) that takes into account also the torsion degree of freedom and model the lift as a distributed load with an elliptical shape is recommended for a future continuation of this study. To reconstruct the structural wing shape, the two missing degrees of freedom (wingtip angle and bending coefficient) can be directly computed through an optimisation algorithm that compares the structural markers tracked position from the IPR process with the ones painted on the wing (knowing their exact position), without using at all the information from the strain gauges and potentiometer. This new optimised structural model should permit the determination of the elastic structural forces just from the position of the painted fiducial markers, allowing a complete characterisation of the aeroelastic fluid-structure interaction problem using a single non-intrusive measurement system technique.

Future work should explore the exact range of application of this Hinged Folding Wingtip (HFWT) and evaluate the validity of the proposed model and the measurement technique. For example, using this described combined flow and structural PIV methodology involving higher wind speed, at Reynolds numbers closer to the real ones that the wing/wingtip will encounter in free-flight conditions when mounted on airliners.

This study can be extended with the implementation of the aerodynamic load determination, from the PIV gathered tracers information, of the wing/wingtip such as the lift produced due to the positive angle of attack (5°) used during the wind tunnel campaign. At the same time, the wing/wingtip aerodynamic and structural behaviour in different test cases can be evaluated, like at positive sideslip angles and the Limit Cycle Oscillation (LCO). These situations were tested during the wind tunnel experiment but were not analysed in this thesis report due to time limitations and can be explored in a future implementation of this study.

Bibliography

[1] *Reducing emissions from aviation,* `https://ec.europa.eu/clima/eu-action/transport-emissions/reducing-emissions-aviation_en` (2021), retrieved on 06/12/2021.

[2] *Trends in emissions that affect climate change,* `https://www.icao.int/environmental-protection/Pages/ClimateChange_Trends.aspx` (2021), retrieved on 06/12/2021.

[3] T. Wilson, A. Castrichini, A. Azabal, J.E. Cooper, R. Ajaj, M. Herring, *Aeroelastic Behaviour Of Hinged Wing Tips,* Tech. Rep. (International Forum on Aeroelasticity and Structural Dynamics, 2017).

[4] A. R. Collar, *The Expanding Domain of Aeroelasticity,* Tech. Rep. (Aeronautical Journal, 1946).

[5] Z. Wu, Y. Cao, M. Ismail, *Gust Loads on Aircraft,* Tech. Rep. (Cambridge University Press, 2019).

[6] H. H. Khodaparast, S. Coggon, M. I. Friswell, J. Cooper, *The Effects of Structural Nonlinearity on the Dynamic Response to Aeroelastic Gust Models,* Tech. Rep. (27th International Conference on Noise and Vibration Engineering, 2016).

[7] S. Guo, J. E. De Los Monteros, Y. Liu, *Gust Alleviation of a Large Aircraft with a Passive Twist Wingtip,* Tech. Rep. (Journal of Aerospace, 2015).

[8] J. Pattinson, T. Wilson, M. Herring, *High Fidelity Simulation of the Folding Wingtip for Loads Alleviation,* Tech. Rep. (15th International Forum on Aeroelasticity and Structural Dynamics, 2015).

[9] *Troubled flagship: Emirates' boeing 777x struggles,* `https://www.aerotime.aero/26573-emirates-boeing777x-struggles` (2021), retrieved on 09/12/2021.

[10] V. H. Siddaramaiah, D. E. Calderon, J.E. Cooper, T. Wilson, *Preliminary Studies in the Use of Folding Wing-Tips for Loads Alleviation,* Tech. Rep. (Applied Aerodynamics Conference, 2014).

[11] R. Cheung, D. Rezgui, D. Calderon, J. Cooper T. Wilson, *Testing of a Hinged Wingtip Device for Gust Loads Alleviation,* Tech. Rep. (Journal of Aircraft, 2018).

[12] R. Cheung, D. Rezgui, J. Cooper T. Wilson, *Testing of Folding Wingtip for Gust Load Alleviation of Flexible High-Aspect-Ratio Wing,* Tech. Rep. (Journal of Aircraft, 2019).

[13] F. Healy, R. Cheung, T. Neofet, M. Lowenberg, D. Rezgui, J. Cooper, A. Castrichini, T. Wilson, *Folding Wingtips for Improved Roll Performance,* Tech. Rep. (19th International Forum on Aeroelasticity and Structural Dynamics, 2021).

[14] *Albatrossone: Revolutionising aircraft wing design,* `https://www.youtube.com/watch?v=Rq2poT9pW3w` (2021), retrieved on 11/12/2021.

[15] S. A. Fazelzadeh, S. A. Fazelzadeh, H. Hoseini, *Nonlinear Flight Dynamics of a Flexible Aircraft Subjected to Aeroelastic and Gust Loads,* Tech. Rep. (Journal of Aerospace Engineering, 2012).

[16] A. Castrichini, T. Wilson, J. Cooper, *On the Dynamic Release of the Semi Aeroelastic Wing-Tip Hinge Device,* Tech. Rep. (The Aeronautical Journal, 2018).

[17] X. Carrillo Córcoles, J. Sodja, C. Mertens, A. Sciacchitano, B. W. van Oudheusden, R. De Breuker, *Experimental Investigation of Wing Stiffness and Hinge Release Load Threshold Effects on Folding Wingtip Performance,* Tech. Rep. (AIAA SciTech Forum, 2022).

[18] X. Carrillo Córcoles, *An experimental study on flared folding wingtips,* (2022).

[19] M.s Raffel, C. E. Willert, F. Scarano, C. J. Kähler, S. T. Wereley, *Particle Image Velocimetry: A Practical Guide* (Springer, Cham, Switzerland, 2018).

[20] A. Sciacchitano, *Ae4180 - flow measurement techniques, slides chaper 10: Particle image velocimetry,* (2021).

[21] G. E. Elsinga, F. Scarano, B. Wieneke, B. W. van Oudheusden , *Tomographic Particle Image Velocimetry*, Tech. Rep. (Experiments in Fluids, 2006).

[22] F. Scarano, *Tomographic PIV: Principles and Practice*, Tech. Rep. (Measurement Science And Technology, 2012).

[23] S. Ghaemi, F. Scarano, *Multi-Pass Light Amplification for Tomographic Particle Image Velocimetry Applications*, Tech. Rep. (Measurement Science And Technology, 2010).

[24] J. F. G. Schneiders , F. Scarano, C. Jux, A. Sciacchitano, *Coaxial Volumetric Velocimetry*, Tech. Rep. (Measurement Science and Technology, 2018).

[25] C. Jux, A. Sciacchitano, J. F. G. Schneiders, F. Scarano, *Robotic Volumetric PIV of a Full-Scale Cyclist*, Tech. Rep. (Experiments in Fluids, 2018).

[26] D. Schanz, S. Gesemann, A. Schröder, *Shake The Box': A Highly Efficient and Accurate Tomographic Particle Tracking Velocimetry (TOMO-PTV) Method Using Prediction of Particle Positions*, Tech. Rep. (10th International Symposium on Particle Image Velocimetry, 2013).

[27] L. Marimon Giovannetti, J. Banks, S. R. Turnock, S. W. Boyd, *Uncertainty Assessment of Coupled Digital Image Correlation and Particle Image Velocimetry for Fluid-Structure Interaction Wind Tunnel Experiments*, Tech. Rep. (Journal of Fluids and Structures, 2017).

[28] F. M. A. Mitrotta1, A. Sciacchitano, J. Sodja, R. De Breuker, B. W. van Oudheusden, *Experimental Investigation of the Fluid-Structure Interaction between a Flexible Plate and a Periodic Gust by Means of Robotic Volumetric PIV*, Tech. Rep. (13th International Symposium on Particle Image Velocimetry, 2019).

[29] C. Mertens, A. Sciacchitano, B.W. van Oudheusden, J. Sodja, *An Integrated Measurement Approach for the Determination of the Aerodynamic Loads and Structural Motion for Unsteady Airfoils*, Tech. Rep. (Journal of Fluids and Structures, 2021).

[30] C. Mertens, T. de Rojas Cordero, J. Sodja, A. Sciacchitano, B.W. van Oudheusden, *Determination of Collar's Triangle of Forces on a Flexible Wing based on Particle Tracking Velocimetry Measurements*, Tech. Rep. (AIAA SciTech Forum, 2021).

[31] C. Mertens, J. Sodja, A. Sciacchitano, B.W. van Oudheusden, *Experimental Aeroelastic Characterization of a Very Flexible Wing in Steady and Unsteady Inflow*, Tech. Rep. (Delft University of Technology, 2021).

[32] *W-tunnel,* `https://wiki.tudelft.nl/bin/view/Organisation/LR/WikiAero/ExperimentalWiki/TunnelsWiki/WTunnelWiki` (2022), retrieved on 03/03/2022.

[33] J- L. Costa Fernandez, *Aerodynamic load evaluation on a highly flexible wing by lagrangian particle tracking,* (2022).

[34] LaVision, *FlowMaster Shake-the-Box (4D PTV) - Product Manual* (LaVision GmbH, Göttingen, Germany, 2021).

[35] LaVision, *DaVis 10.2 Software - Product Manual* (LaVision GmbH, Göttingen, Germany, 2021).

[36] J. D. Anderson, *Fundamentals of Aerodynamics* (McGraw Hill Education, New York, US, 2017).

[37] ICAO, *International Standards And Recommended Practices Aerodromes* (International Civil Aviation Organization, New York, US, 1951).

[38] K. G. Pratt, *A Revised Formula for the Calculation of Gust Loads*, Tech. Rep. (National Advisory Committee for Aeronautics Collection, 1953).

[39] *Certification specifications and acceptable means of compliance for large aeroplanes cs25*, `https://www.easa.europa.eu/certification-specifications/cs-25-large-aeroplanes` (2021), retrieved on 07/12/2021.

[40] M. H. Shirk, T. J. Hertz, T. A. Weisshaar, *Aeroelastic Tailoring - Theory, Practice, and Promise*, Tech. Rep. (Journal of Aircraft, 2012).

[41] W. R. Krüger, J. Dillinger, R. De Breuker, K. Haydn, *Investigations of Passive Wing Technologies for Load Reduction*, Tech. Rep. (CEAS Aeronautical Journal, 2019).

[42] M. H. Smith, M.E. Renzelmann, A.D. Marx, *Folding Wing-Tip Systems*, Tech. Rep. (The Boeing Company, 1995).

[43] A. Castrichini, V.H. Siddaramaiah, D. Calderon, J. Cooper, T. Wilson, Lemmens Y, *Preliminary Investigation of Use of Flexible Folding Wing Tips for Static and Dynamic Load Alleviation*, Tech. Rep. (The Aeronautical Journal, 2016).

[44] A. Castrichini, Y. Lemmens, T. Wilson, *Nonlinear Folding Wing Tips for Gust Loads Alleviation*, Tech. Rep. (Journal of Aircraft, 2016).

[45] A. Castrichini, J.E. Cooper, *Nonlinear Negative Stiffness Wing-Tip Spring Device for Gust Loads Alleviation*, Tech. Rep. (Journal of Aircraft, 2016).

[46] G. Dussart, S. Yusuf, M. Lone, *Identification of In-Flight Wingtip Folding Effects on the Roll Characteristics of a Flexible Aircraft*, Tech. Rep. (Aerospace, 2019).

[47] T. Wilson, J. Kirk, J. Hobday, A. Castrichini, *Small Scale Flying Demonstration Of Semi Aeroelastic Hinged Wing Tips*, Tech. Rep. (International Forum on Aeroelasticity and Structural Dynamics, 2019).

[48] O. Avin, D. Raveh, A. Drachinsky, Y. Ben-Shmuel, *An Experimental Benchmark of a Very Flexible Wing*, Tech. Rep. (AIAA Scitech Forum, 2021).

[49] C. Kassapoglou, *Design and Analysis of Composite Structures: With Applications to Aerospace Structures* (John Wiley & Sons Ltd, New Jersey, US, 2013).

[50] *W-tunnel*, `https://www.tudelft.nl/lr/organisatie/afdelingen/aerodynamics-wind-energy` (2021), retrieved on 12/12/2021.

[51] F. Scarano, *Experimental Aerodynamics* (TUDelft, Deflt, The Netherlands, 2013).

[52] M. P. Arroyo, C. A. Greated, *Stereoscopic Particle Image Velocimetry*, Tech. Rep. (Measurement Science and Technology, 1991).

[53] G. T. Herman, A. Lent, *Iterative Reconstruction Algorithms*, Tech. Rep. (Computers in Biology and Medicine, 1976).

[54] J. Bosbach, M. Kühn, C. Wagner, *Large Scale Particle Image Velocimetry with Helium Filled Soap Bubbles*, Tech. Rep. (Experiments in Fluids, 2009).

[55] F. Scarano, S. Ghaemi, F. C. A. Caridi, J. Bosbach, U. Dierksheide, A. Sciacchitano, *On the Use of Helium-Filled Soap Bubbles for Large-Scale Tomographic PIV in Wind Tunnel Experiments*, Tech. Rep. (Experiments in Fluids, 2015).

[56] J. F. G. Schneiders, G. C. A. Caridi, A. Sciacchitano, F. Scarano, *Large-Scale Volumetric Pressure from Tomographic PTV with HFSB Tracers*, Tech. Rep. (Experiments in Fluids, 2016).

[57] D. Engler Faleiros, M. Tuinstra, A. Sciacchitano, F. Scarano, *Generation and Control of Helium-Filled Soap Bubbles for PIV*, Tech. Rep. (Experiments in Fluids, 2019).

[58] G. C. Alp Caridi, D. Ragni, A, Sciacchitano, F. Scarano, *HFSB-Seeding for Large-Scale Tomographic PIV in Wind Tunnels*, Tech. Rep. (Experiments in Fluids, 2016).

[59] C. Willert, B. Stasicki, J. Klinner, S. Moessner, *Pulsed Operation of High-Power Light Emitting Diodes for Imaging Flow Velocimetry*, Tech. Rep. (Measurement Science And Technology, 2010).

[60] D. Schanz, S. Gesemann, A. Schröder, *Shake-The-Box: Lagrangian Particle Tracking at High Particle Image Densities*, Tech. Rep. (Experiments in Fluids, 2016).

[61] B. Wieneke, *Iterative Reconstruction of Volumetric Particle Distribution*, Tech. Rep. (Measurement Science and Technology, 2012).

[62] N. Wiener, *Extrapolation, Interpolation, and Smoothing of Stationary Time Series With Engineering Applications* (Technology Press of the Massachusetts Institute of Technology, Boston, US, 1949).

[63] B. Pan, *Digital Image Correlation for Surface Deformation Measurement: Historical Developments, Recent Advances and Future Goals*, Tech. Rep. (Measurement Science and Technology, 2018).

[64] J. Baqersad, P. Poozesh, C. Niezrecki, P. Avitabile, *Photogrammetry and Optical Methods in Structural Dynamics – A Review*, Tech. Rep. (Mechanical Systems and Signal Processing, 2016).

[65] A. Timpe, Z. Zhang, J. Hubner, L. Ukeiley, *Passive Flow Control by Membrane Wings for Aerodynamic Benefit*, Tech. Rep. (Experiments in Fluids, 2013).

[66] R. Bleischwitz, R. de Kat, B. Ganapathisubramani, *On the Fluid-Structure Interaction of Flexible Membrane Wings for MAVs In and Out of Ground-Effect*, Tech. Rep. (Journal of Fluids and Structures, 2017).

[67] B. Wieneke, *Volume Self-Calibration for 3D Particle Image Velocimetry*, Tech. Rep. (Experiments in Fluids, 2008).

[68] D. Schanz, S. Gesemann, A. Schröder, M. Novara, *Non-Uniform Optical Transfer Functions in Particle Imaging: Calibration and Application to Tomographic Reconstruction*, Tech. Rep. (Measurement Science and Technology, 2012).

[69] C. Mertens, J- L. Costa Fernandez, A. Sciacchitano, B.W. van Oudheusden, J. Sodja, *Gridless Determination of Aerodynamic Loads Using Lagrangian Particle Tracks*, Tech. Rep. (14th International Symposium on Particle Image Velocimetry, 2021).

[70] *Hfsb fluid supply units (fsu)*, `https://wiki.tudelft.nl/bin/view/Organisation/LR/WikiAero/ExperimentalWiki/PIVsystemsWiki/HfsbFluidSupplyUnits` (2022), retrieved on 09/03/2022.

[71] *Led-flashlight 300*, `https://wiki.tudelft.nl/bin/view/Organisation/LR/WikiAero/ExperimentalWiki/PIVsystemsWiki/LEDWiki` (2022), retrieved on 08/03/2022.

[72] LaVision, *LED-Flashlight 300 - Product Manual* (LaVision GmbH, Göttingen, Germany, 2018).

[73] *Piv high speed acquisition system*, `https://wiki.tudelft.nl/bin/viewauth/Organisation/LR/WikiAero/ExperimentalWiki/PIVsystemsWiki/PhotronFastcamWiki` (2022), retrieved on 09/03/2022.

[74] LaVision, *HighSpeedStar - Product Manual* (LaVision GmbH, Göttingen, Germany, 2016).

[75] *Ethernet cable: Categories, types, performance pinout*, `https://www.electronics-notes.com/articles/connectivity/ethernet-ieee-802-3/cables-types-pinout-cat-5-5e-6.php` (2022), retrieved on 09/03/2022.

[76] LaVision, *FASTCAM Mini AX - Product Manual* (LaVision GmbH, Göttingen, Germany, 2021).

[77] *Air - density, specific weight and thermal expansion coefficient vs. temperature and pressure*, `https://www.engineeringtoolbox.com/air-density-specific-weight-d_600.html` (2021), retrieved on 18/01/2022.

[78] *Air - dynamic and kinematic viscosity*, `https://www.engineeringtoolbox.com/air-absolute-kinematic-viscosity-d_601.html` (2021), retrieved on 11/01/2022.

[79] David Engler Faleiros, *Soap Bubbes For Large-Scale PIV*, Ph.D. Thesis, Tu Delft (2021).

[80] *Intensity calibration,* `https://hcimage.com/help/Content/Viewing%20the%20Data/Sequence%20Data%20Document/Analysis/Intensity%20Calibration.htm#:~:text=The%20aim%20of%20this%20process,may%20have%20a%20nonlinear%20relationship.` (2022), retrieved on 11/03/2022.

[81] N. Agüera, G. Cafiero, T. Astarita, S. Discetti, *Ensemble 3D PTV for High Resolution Turbulent Statistics*, Tech. Rep. (Measurement Science and Technology, 2016).

[82] C. Jux, *Robotic volumetric particle tracking velocimetry by coaxial imaging and illumination,* (2017).

[83] T. de Rojas Cordero, *Integrated aerodynamic and structural measurements of the gust response of a flexible wing with robotic piv,* (2020).

[84] H. Wang, Q.-H. Qin, *Bernoulli Beam*, Tech. Rep. (Methods of Fundamental Solutions in Solid Mechanics, 2019).

[85] A. Sciacchitano, F. Scarano, *PIV Light Reflections Elimination Via Temporal High-Pass Filter*, Tech. Rep. (TUDelft, 2014).

A
Appendix A

A.1 Programmable Time Unit Connections

In order to connect the six cameras to the Programmable Time Unit (PTU), two connectors are attached to the back of the PTU, connector 1003832 on Port B and connector 1003832 on Port A. The Bayonet Neill Concelman (BNC) cables are used from these connectors. The following connections were set.

Cameras ———> PTU (connector 1003832 attached in PTU Port B)
Sync In Camera 1 ——-> EMon-1 1003832
Sync In Camera 2 ——-> EMon-2 1003832
Sync In Camera 3 ——-> ADC Start 1003832
Sync In Camera 4 ——-> ADC CLK 1003832

Gen In Camera 1 ———> PHO 0 1003832
Gen In Camera 2 ———> PHO 1 1003832
Gen In Camera 3 ———> PHO 0 1003832
Gen In Camera 4 ———> PHO 1 1003832

Gen Out Camera 1 ——-> In1/In3 1003832

Cameras ———> PTU (connector 1003832 attached in PTU Port A)
Sync In Camera 5 ——-> EMon-1 1003832
Gen In Camera 5 ——-> EMon-2 1003832
Sync In Camera 6 ——-> ADC Start 1003832
Gen In Camera 6 ——-> ADC CLK 1003832

In DaVis, it was selected the 1004716 connector in the hardware setup for Port B and the 1003518 connector for Port A, although you have 2 x 1003832 physically connected.

Instead, the trigger connector 100285 was used and inserted into the Trigger Input Port at the back of the PTU and cabled with the BNC coming from the gust generator.

Gust Generator ———> PTU (connector 100285 attached in PTU Trigger Input Port)
Trigger Gust Generator ——-> Trigger 100285
For the LEDs, the Laser Port at the back of the PTU is used with an extension cable connector; then, from this, the 1003831 connector is attached and connected with a splitter to the BNC coming from both LEDs.

LED ———> PTU (connector 1003831 attached in PTU Laser Port)
Ext. Trigger Input LED 1 ——-> Q1 1003831
Ext. Trigger Input LED 2 ——-> Q1 1003831

B
Appendix B

B.1 Image Pre-Processing

Since DaVis 10.2.1 (the latest version) cannot deal with the data from six cameras during the IPR and STB process, it handles the reconstruction within a multi-camera set-up in such a way that a particle must be seen by N-1 cameras simultaneously. This is not possible in the thesis experiment since the tracer on one side of the wing can be seen just by 3 cameras and not 5 (as required by the software). The first step of the image pre-processing is to split them into two sides, the ones from camera 1/2/3 and the ones from camera 4/5/6. This was done with the command Delete or Change Order of Frames in DaVis, with the settings imaged in Figure B.1.

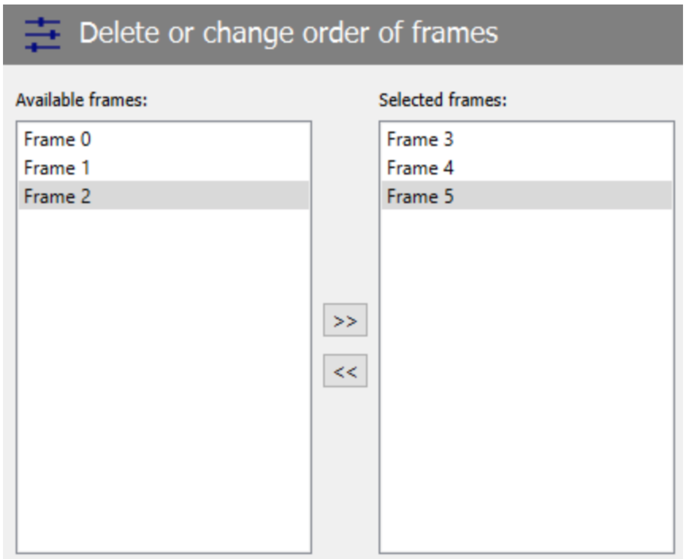

Figure B.1: Delete or change order of frames settings.

Then, since the images contain both the flow and structural markers, the next step is to separate both pieces of information. Two filters are used on the original (un-filtered images), visible in Figure B.2. To remove the fiducial markers painted on the wing, the Butterworth high pass filter (subtract time filter) was performed, resulting in the flow filtered images illustrated in Figure B.3. This filter, introduced by Sciacchitano et al. [85], used the hypothesis that structural markers are slower with respect to the flow tracers. It is based on the signal of the pixel intensity decomposition in the frequency domain. Then it removes the low-frequency spectrum corresponding to unwanted reflections on the wing skin, background noise and fiducial structure markers. A kernel of 7 images was selected after several tests since it gives a good trade-off between the structural markers removal and the introduction of ghost particles. While removing all the flow markers, a symmetrical minimum filter (time filter) was applied, giving the filtered structure images in Figure B.4. This is based on the holding operation of minimum light intensity for each pixel for a set filter length (kernel of 3 consecutive images was selected) since the structural fiducial markers occupy the same pixel position for a more significant amount of images with respect to the flow tracers particles.

Figure B.2: Unfiltered image.

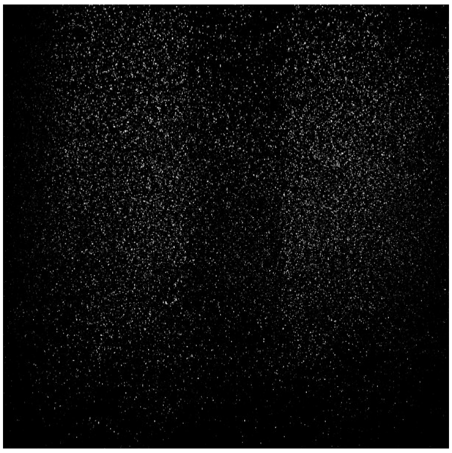

Figure B.3: Flow filtered image.

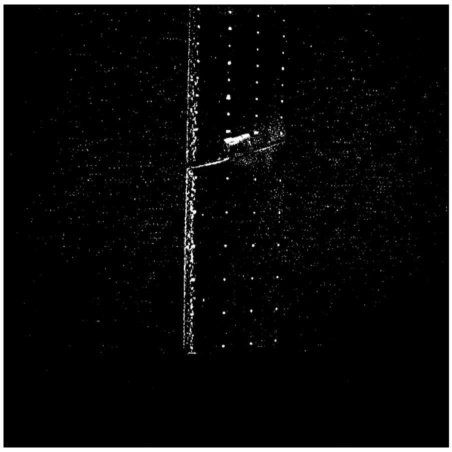

Figure B.4: Structure filtered image.

Both the filter parameters used are listed in Figure B.5 and Figure B.6.

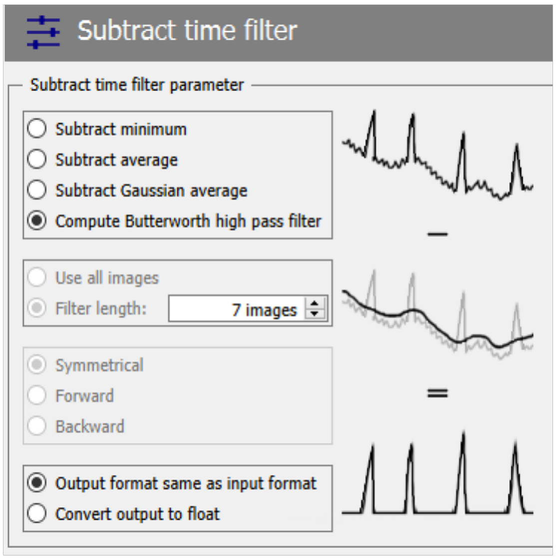

Figure B.5: Butterworth high pass filter Settings.

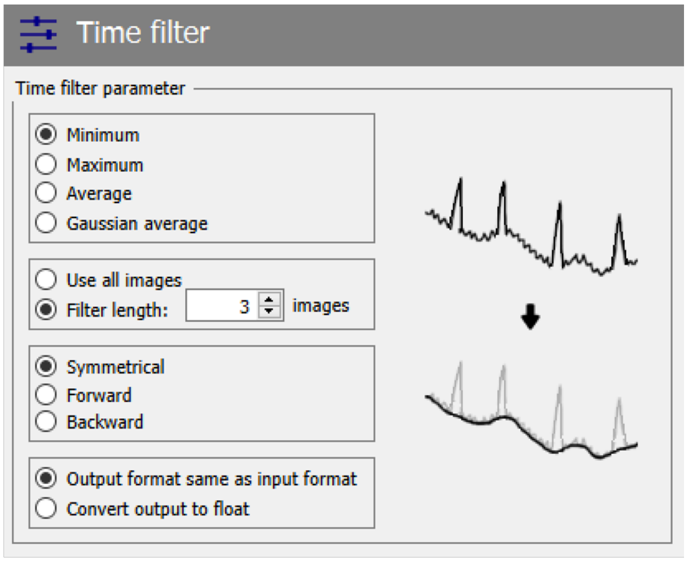

Figure B.6: Minimum filter settings.

The flow isolated images were directly used for the Shake-the-Box LPT algorithm since no further pre-processing steps were required. Further steps were necessary on the structure isolated images before applying the LPT algorithm to achieve rounded-shaped fiducial markers without any background reflections and noise.

First, a subtract sliding minimum filter is used (with a kernel of 12 pixels) to remove the image background by subtracting the local minimum from each pixel [35], the influence of remaining undesired noise and the surface reflections. Then a Gaussian smoothing (with a 3 x 3 pixels kernel) is applied to uniformise the markers' shape and increase the sizes. It eliminates the high-frequency noise by taking an average over the neighbourhood of a pixel [35], with the drawback of increasing the number of overlapping particles. Then the average standard deviation intensity normalisation filter is applied (with a kernel area of 40 x 40 pixels) to have a homogeneous intensity distribution, resulting in images with zero local mean intensity and a fixed dynamic range everywhere [35]. Since the intensity of the particles was lowered due to the previous pre-processing steps (in particular, the sliding minimum subtraction), the intensity of each pixel was multiplied by a constant value (1.1) to compensate for it. Lastly, a geometric mask (set outside rectangle constant) is used to only have visible the markers on the wing, removing the remained noise and reflection outside the desired illuminated wing, setting the outside region to a constant value (completely black), the rectangle was drawn to contain the wing in each camera view. All these operations are visible from Figure B.7 to Figure B.12. As visible from Figure B.12, the soap concentration at the wing's leading edge is still present. This was not a problem for the results since it was removed in the post-processing phase; more details are presented in subsection B.3.2.

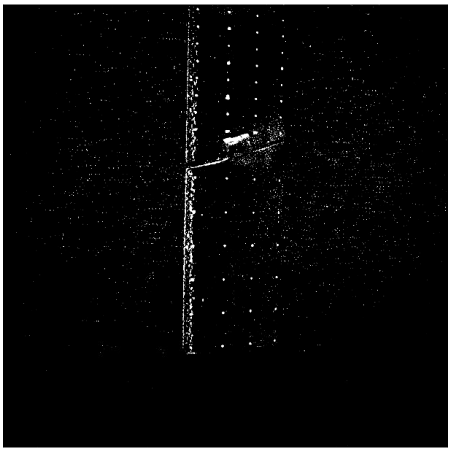

Figure B.7: Structure image.

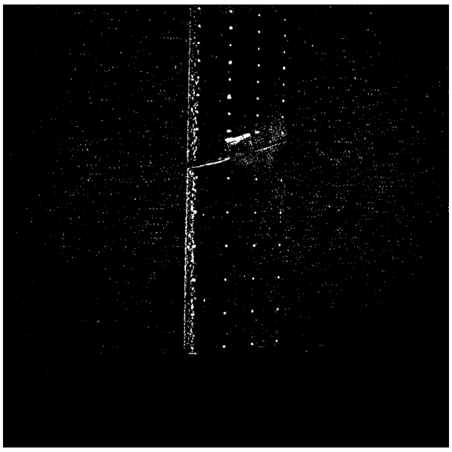

Figure B.8: Subtract sliding.

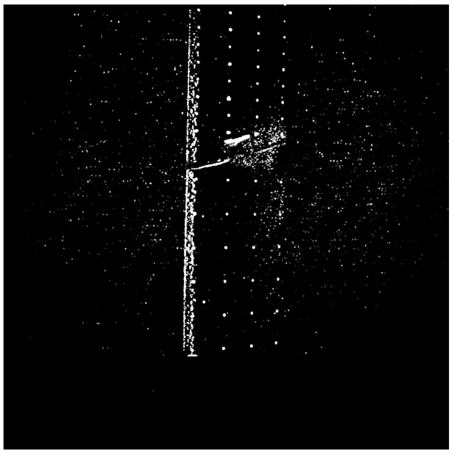

Figure B.9: Smoothing.

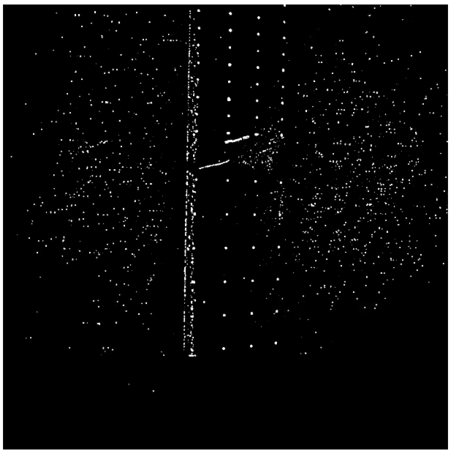

Figure B.10: Intensity normalisation.

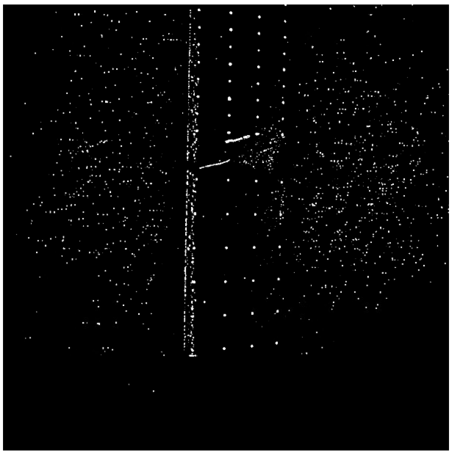

Figure B.11: Multiply.

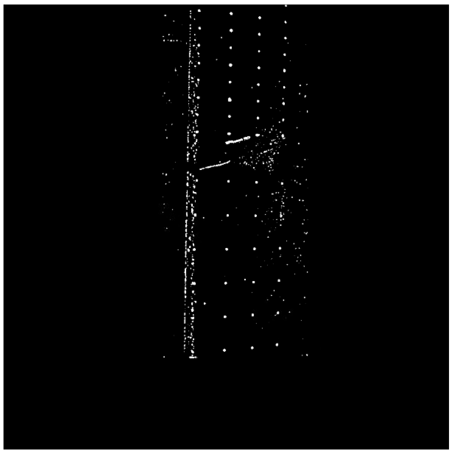

Figure B.12: Geometric mask.

The parameters used for the image pre-processing of the structure fiducial markers are displayed from Figure B.13 to Figure B.17.

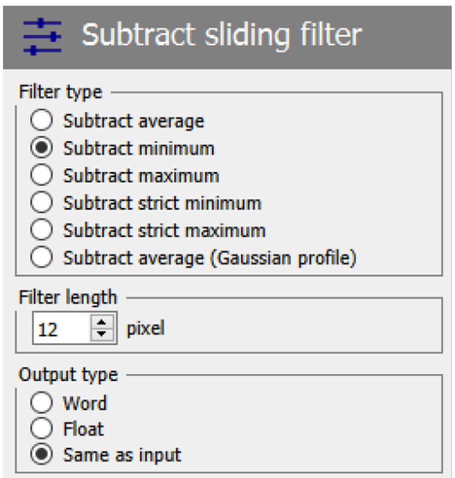

Figure B.13: Subtract sliding settings.

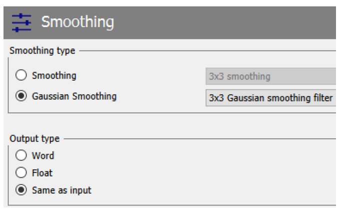

Figure B.14: Smoothing settings.

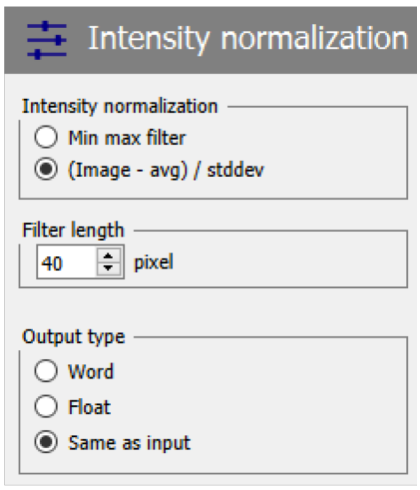

Figure B.15: Intensity normalisation settings.

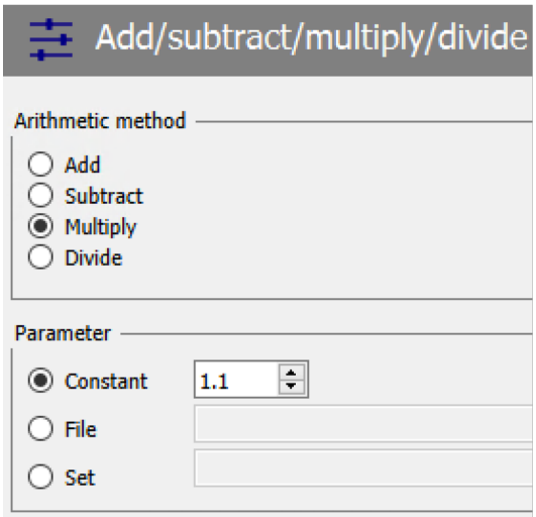

Figure B.16: Multiply settings.

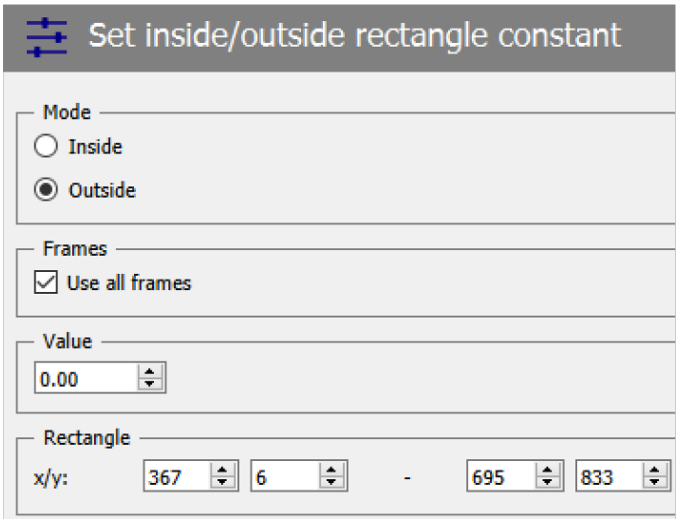

Figure B.17: Geometric mask settings.

B.2 VOLUME SELF-CALIBRATION

The next step was the Volume Self-Calibration (VSC) [67], which has the purpose of removing any residual calibration disparities using recorded particle images [34]. It includes two steps repeated iteratively for each non-overlapping sub-volume (until the disparity is below 0.1 voxels): calculate the disparity vector map for each particle, which is then used to correct the perspective calibration (mapping function). During this process, 100 images (the pre-processed ones) are used for each test case, spanning the entire dataset. Initially, the undisturbed flow stream images were used, but then it was discovered that better results were achieved with the images for each test case. Two sets of VSC were performed, one with the flow tracers particle images and another one with the structure markers images.

The settings used for the first and last iteration of the volume self-calibration are displayed in Figure B.18 and Figure B.19.

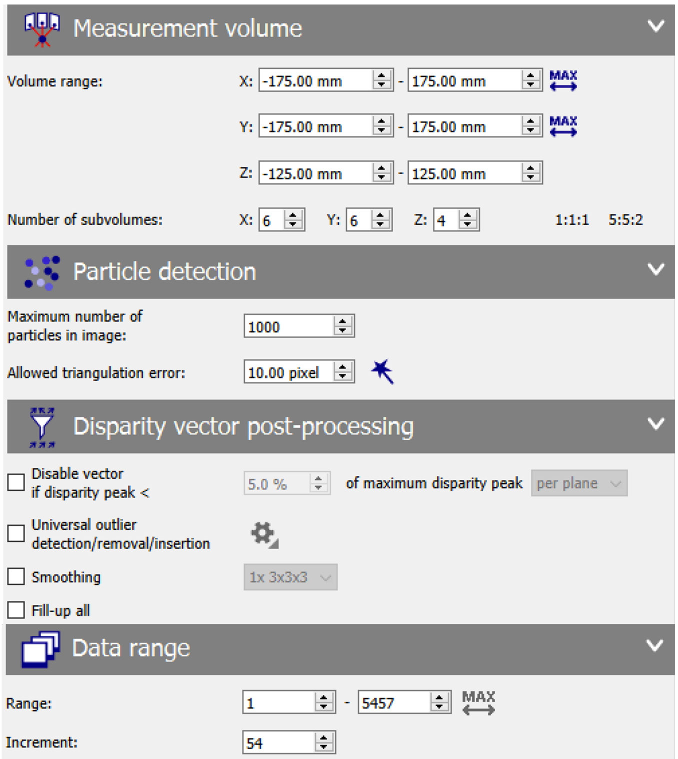

Figure B.18: Volume self-calibration initial settings.

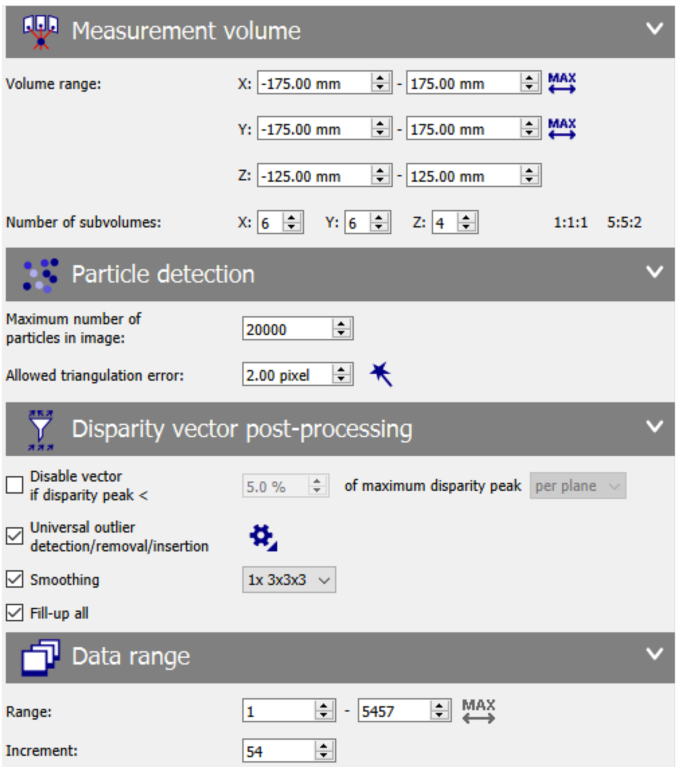

Figure B.19: Volume self-calibration final settings.

The first iterations of volume self-calibration started with a big allowed triangulation error (10) and a small number of tracer particles (1000) to capture the large initial disparities, limiting the number of ghost particles. For each camera, 6 x 6 x 4 sub-volumes were selected. The disparity vectors indicate the errors in the perspective calibration due to the lines of sight of a single particle from the different cameras that do not intersect in a single point in space [35]. Indeed, there will always be some deviations that are quantified for each tracer particle by the average length of the disparity vectors, called the triangulation error. Indeed, VSC is based on the triangulation that denotes the position detection of individual particles in 3D space from multiple camera images [35]. The allowed triangulation error setting indicates the maximum deviation that is tolerated in the lines-of-sight, where all the particles that have a triangulation error smaller are used to construct the disparity map [35].

Then after this first iteration, the number of tracer particles is increased to 5000 and then by steps of 5000, reaching the maximum value of 20000 for the fifth iteration, while the allowed triangulation error is decreased by 2 until the final iteration using 2. From the second iteration onwards, the following disparity post-processing settings were set on: universal outlier detection/removal/insertion, fill-up all and smoothing 3x3x3. After all these refinement iterations, the resulting calibration was accepted. Then, the Optical Transfer Function (OTF) [68] was calculated, disabling all the disparity vector post-processing settings and putting the allowed triangulation error equal to 1 to ensure that only the very well-fitting tracer particles are used for the OTF calculation.

B.3 LAGRANGIAN PARTICLE TRACKING OPERATIONS

After completing the image pre-processing operations and Volume Self-Calibration illustrated in the previous subsection, several processing steps were also needed to transform the recorded images into tracer particles and fiducial markers track data. Two approaches are used for the flow and structure markers explained in subsection B.3.1 and subsection B.3.2 respectively.

B.3.1 FLOW POST-PROCESSING - SHAKE-THE-BOX

For the flow HFSB, tracer particles tracking, the algorithm used is the Shake-The-Box (STB). This requires the Volume Self-Calibration (VSC) [67] and Optical Transfer Function (OTF) [68] both from the pre-processed isolated flow images for each test case dataset. The parameters for applying the STB algorithm to trace the flow particles are summarised in Figure B.20. These were selected doing a trade-off between the amount of tracked particles and the quality of the resulting tracks.

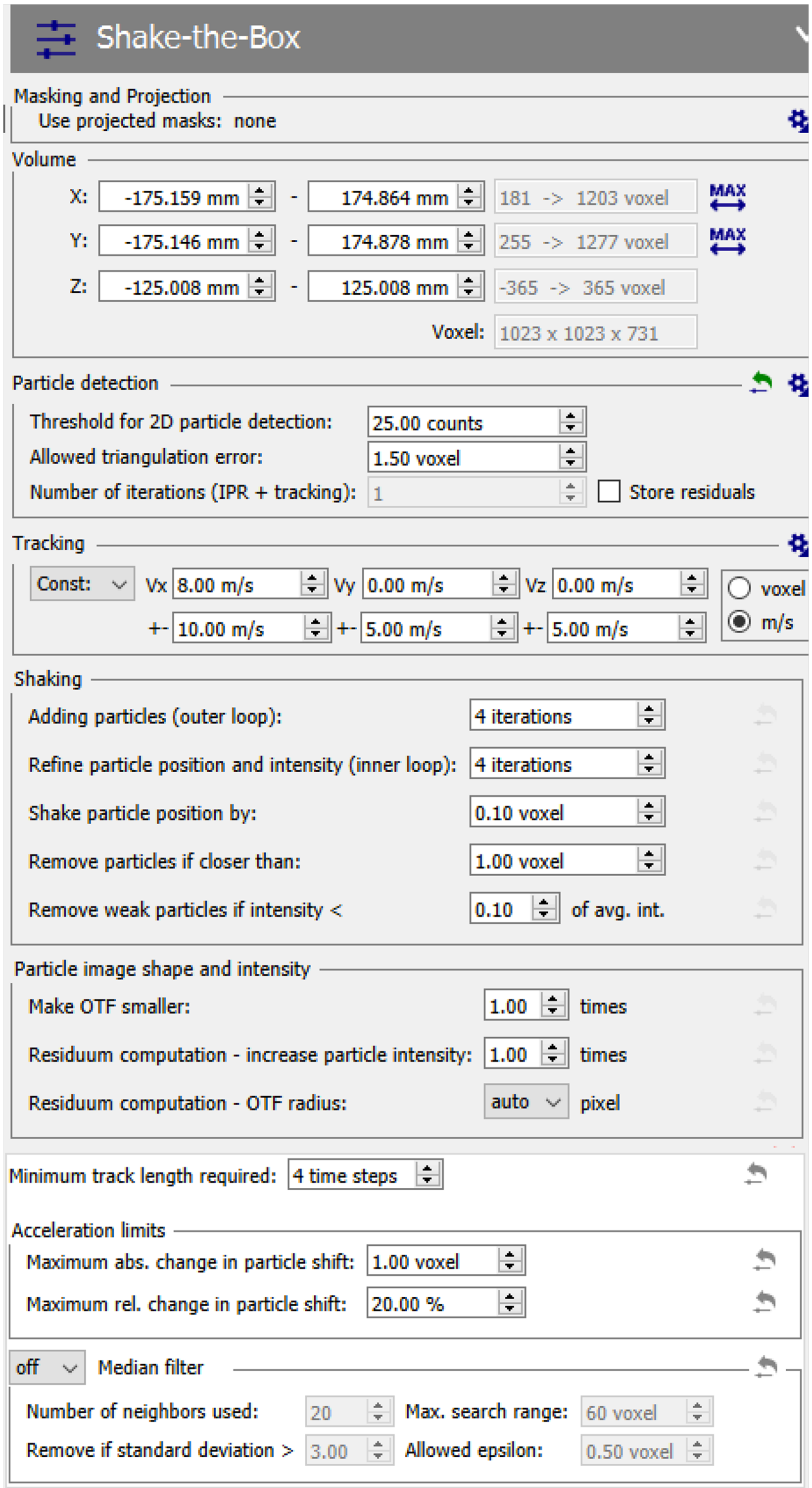

Figure B.20: Shake-the-box settings.

As listed in Figure B.20, the STB was performed in the entire measurement volume 350 x 350 x 250mm, same as the volume specified for volume self-calibration. With particles tracked if their intensity peak is higher than 25 (the threshold for 2D particle detection), this was set higher than any potential noise peak to detect true particle tracers, removing all the noisy background. Moreover, to detect only well-matching particles, a maximum allowed triangulation error tolerated by accepting particle matches from different cameras was set equal to 1.5. The velocity limits (including the dynamic range) used to capture all existing particle shifts (for the steady and unsteady cases) in the flow was set to $V_x = 8 \pm 10\,\mathrm{m\,s^{-1}}$, $V_y = 0 \pm 5\,\mathrm{m\,s^{-1}}$ and $V_z = 0 \pm 5\,\mathrm{m\,s^{-1}}$, the higher velocity is the one in x-direction due to the wind tunnel speed direction, while the velocity in z-direction is generated by the presence of the gust. Higher velocity is set for the x-direction with respect to the free-stream one due to the wing that can accelerate the flow locally. Also, negative velocities are accepted since these can be generated in the back-flow region around the airfoil. To avoid the detection of particles too close to the already existing ones, which often results from triangulation of some left-over intensity peaks in the residuum of the other particle [34], all the particles closer than 1 voxel between each other are discarded (considering a scale factor of 2.92 pixels/mm).

B.3.2 STRUCTURE POST-PROCESSING - ITERATIVE PARTICLE RECONSTRUCTION

Instead, the LPT used for the structure of fiducial markers painted on the wing was the Iterative Particle Reconstruction (IPR) because the use of the Shake-The-Box algorithm results in missing the majority of the fiducial markers painted on the wing, in particular near the tip of the wing with the consequence of an inaccurate structure reconstruction. Instead, the IPR algorithm worked well, tracking many markers. The IPR algorithm, introduced by Wieneke et al. [61], is the fundamental base where STB is constructed. Still, it does not include the 4D-PTV algorithm that uses the time information for track reconstruction. This LPT algorithm used a non-uniform Optical Transfer Function (OTF) and a Volume Self-Calibration (VSC) to decrease the errors in the tracking reconstruction process. Nevertheless, in this case, contrary to flow one, the OTF and the VSC are from two sets of images (pre-processed). Indeed, the OTF used is generated from the isolated structure markers images, while the VSC are from the isolated flow markers images (from the same test case dataset). This was done to achieve better results. The settings used for the iterative particle reconstruction algorithm are illustrated in Figure B.21.

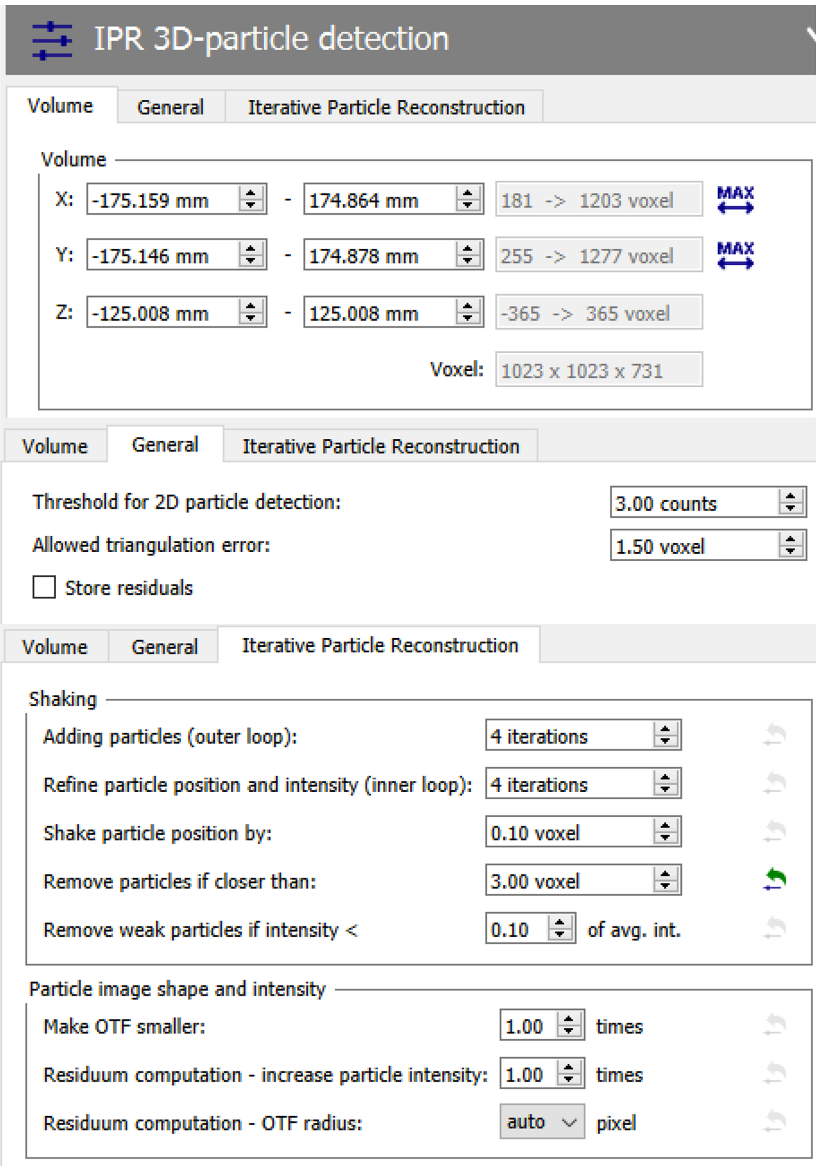

Figure B.21: Iterative particle reconstruction settings.

As visible in Figure B.21 the main setting difference with respect to the STB algorithm is on the threshold for 2D particle detection that now results in a value (3) way lower with respect to the STB one (25), allowing the detection of weakest in intensity structure markers, this is because all the image pre-processing steps actuated on the structure images reduced the intensity of the markers, even if the multiply by a constant filter was used to mitigate this effect. Another difference is that the particles closer than 3 voxels are now discarded (which correspond to a cube with a side equal to 8.76mm) because the distance between each fiducial marker painted on the wing (30mm) is bigger with respect to the one between the flow HFSB tracers, so this was done to eliminate all the noise from the soap concentrating at the LE of the wing. As the STB algorithm used all the 5457 images in the track reconstruction, the same number was also used for IPR one. This did not increase the computational cost and processing time due to the low number of tracks (low number of markers painted).

Once all these steps were actuated, the IPR and STB results were downloaded from the DaVis software using the command Export to Tecplot. This generates a .dat file with the coordinates of all the markers tracked for each time step. This .dat file was then converted to a .mat file with an own-made script.